Universität Bonn
Physikalisches Institut

$W \to \tau\nu_\tau$ Cross Section Measurement and Search for the Standard Model Higgs Boson in the $\tau_{\text{lep}}\,\tau_{\text{had}}$ Final State with the ATLAS Detector

Jana Kraus

Two measurements based on proton-proton collisions recorded with the ATLAS experiment at the LHC with τ leptons and missing transverse energy in the final state are presented.
The W boson production cross section with subsequent $W \to \tau\nu_\tau$ decay is measured based on 2010 ATLAS data at a centre-of-mass energy of $\sqrt{s} = 7$ TeV corresponding to an integrated luminosity of 34 pb^{-1}. The product of the W production cross section and branching ratio is measured to be $\sigma_W^{\text{tot}} \times \text{BR}(W \to \tau\nu_\tau) = (11.1 \pm 0.3\,(\text{stat.}) \pm 1.7\,(\text{syst.}) \pm 0.4\,(\text{lumi.}))$ nb. This is the first measurement of the $W \to \tau\nu_\tau$ process at the LHC. It is one of the first analyses to successfully validate the reconstruction and identification techniques for hadronically decaying τ leptons and missing transverse energy.
A search for the Standard Model Higgs boson decaying to a pair of τ leptons is performed with a leptonically and hadronically decaying τ lepton in the final state. The analysis is carried out on the full 2012 ATLAS data sample at a centre-of-mass energy of $\sqrt{s} = 8$ TeV corresponding to an integrated luminosity of 20.3 fb^{-1}. The selection of data events is based on the kinematic properties of a Higgs boson produced via vector-boson fusion or a boosted Higgs boson resulting mainly from gluon fusion. A deviation from the predicted background is found in data with an observed (expected) significance of 1 (1.7) σ at $m_H = 125$ GeV. The measured ratio of the signal strength to the Standard Model expectation is $\mu = 0.4 \pm 0.6$. In the combination of all $H \to \tau\tau$ decay modes an excess in data over the predicted background with a significance of 3.2 (2.5) σ at $m_H = 125$ GeV is found with a relative signal strength of $\mu = 1.4\,^{+0.6}_{-0.5}$. This result constitutes evidence that the recently discovered Higgs boson directly couples to fermions consistent with the expectation from the Standard Model. In particular the compatibility with a mass of $m_H = 125$ GeV is confirmed with this analysis.

Physikalisches Institut der
Universität Bonn
Nussallee 12
D-53115 Bonn

BONN-IR-2015-02
February 2015
ISSN-0172-8741

$W \to \tau\nu_\tau$ Cross Section Measurement and Search for the Standard Model Higgs Boson in the $\tau_{\text{lep}}\,\tau_{\text{had}}$ Final State with the ATLAS Detector

Dissertation
zur
Erlangung des Doktorgrades (Dr. rer. nat.)
der
Mathematisch-Naturwissenschaftlichen Fakultät
der
Rheinischen Friedrich-Wilhelms-Universität Bonn

von
Jana Kraus
aus
Bonn

Bonn, 2014

Dieser Forschungsbericht wurde als Dissertation von der Mathematisch-Naturwissenschaftlichen Fakultät der Universität Bonn angenommen und ist auf dem Hochschulschriftenserver der ULB Bonn http://hss.ulb.uni-bonn.de/diss_online elektronisch publiziert.

1. Gutachter:	Prof. Dr. Norbert Wermes
2. Gutachter:	Prof. Dr. Klaus Desch
Tag der Promotion:	23.02.2015
Erscheinungsjahr:	2015

Contents

CHAPTER 1

Introduction

Particle physicists aim to understand matter at its most fundamental level. A theory that explains most physics phenomena very elegantly is the Standard Model of Particle Physics. It comprises all known elementary particles with their interactions and groups them into fermions (quarks and leptons with half spin) and bosons (the mediators of the particle interactions with integer spin). In the last decades its predictions were confirmed in multiple experiments up to remarkable precision, for instance through the discovery of the W and Z bosons at the Super Proton Synchrotron at CERN in 1983, the top quark at the Tevatron in 1995 and the τ neutrino at the DONUT experiment in 2000. However, one crucial prediction of the Standard Model could not be experimentally confirmed for a long time: The existence of the massive scalar Higgs boson. The existence of this particle is implied by the Higgs Mechanism which gives masses to the bosons and fermions in the Standard Model.

The Large Hadron Collider (LHC) at CERN in Geneva reaches the highest-ever luminosity and centre-of-mass energy in proton-proton collisions. One of its major goals is to observe the Standard Model Higgs boson through its decay to bosons and fermions and measure its properties or to disprove its existence. Finally, in July 2012 two of its experiments, ATLAS and CMS, could claim the discovery of a new particle at a mass of about 125 GeV. All of its properties that could be measured in the following far agree with the predictions for a the Standard Model Higgs boson. For this outstanding success the inventors of the Higgs mechanism, Peter Higgs and François Englert, were awarded the Nobel Prize in Physics in 2013.

The discovery, however, so far only proved the Higgs boson decay to bosons. It is therefore crucial to also provide evidence for the direct coupling of the Higgs boson to fermions in order to verify the prediction of the Standard Model for the origin of fermion masses. The decay of the Higgs boson into a pair of τ leptons is the most promising final state at the LHC that allows an observation of the direct coupling of the discovered Higgs boson to fermions. This decay is studied in this thesis.

The analysis of this channel is challenging, since the τ leptons quickly decay to lighter leptons (electrons or muons) or hadrons accompanied by neutrinos. It requires dedicated techniques to reconstruct the visible hadronic decay products and distinguish them from leptons or jets originating from quarks or gluons. The neutrinos can only be measured indirectly through the missing transverse energy. Therefore, numerous sources of background mimic the $H \to \tau\tau$ signal and, moreover, the resolution of the invariant $\tau\tau$ mass is limited. The analysis of $H \to \tau\tau$ decays is divided into three different final states resulting from the τ decays to leptons or hadrons.

In order to detect a new phenomenon like a Higgs boson signal, it is crucial that all measurement parameters are determined precisely and that all background processes are well understood. Since the LHC operates at extremely high luminosity and in an energy range that has never been reached before, this can only be ensured through intensive preparative studies. The preparation for the $H \to \tau\tau$ search requires the optimisation and validation of the reconstruction and identification of hadronically decaying τ leptons and missing transverse energy in particular. For this purpose, several studies are performed in this thesis, e.g. the optimisation of the missing transverse energy reconstruction in events with τ leptons in ATLAS.

With the first LHC data, measurements of known Standard Model processes are performed. Besides improving the precision of the measurement results these can also be used to probe the performance of the detector and analysis methods as a preparation for the search for new physics phenomena. For the $H \to \tau\tau$ search the investigation of $W \to \tau\nu_\tau$ and $Z \to \tau\tau$ processes is an important prerequisite since they have the same signature of missing transverse energy and τ leptons in the final state.

In this thesis the measurement of the W production cross section with subsequent decay to $W \to \tau\nu_\tau$ is presented. It is based on ATLAS data recorded in 2010 at $\sqrt{s} = 7$ TeV corresponding to an integrated luminosity of 34 pb^{-1}. The investigation of $W \to \tau\nu_\tau$ decays complements the measurements of the W production cross section with subsequent decays to electrons and muons and is also the first measurement of this process at the LHC. In addition, due to its relatively large cross section, the $W \to \tau\nu_\tau$ process is the first process with which the performance of τ lepton and missing transverse energy reconstruction and identification can be validated in ATLAS. Therefore, this measurement also constitutes an important preparation for the search for $H \to \tau\tau$ decays.

A search for the decay of the Standard Model Higgs boson to a leptonically and hadronically decaying pair of τ leptons is performed in this thesis. It is based the full 2012 data set recorded with the ATLAS detector at a centre-of-mass energy of $\sqrt{s} = 8$ TeV corresponding to an integrated luminosity of 20.3 fb^{-1}. It provides the highest Higgs signal sensitivity among the three $H \to \tau\tau$ decay channels since it is the most frequent τ pair decay and combines the clear signature of a light lepton in the detector with the more probable hadronic τ decay. The $H \to \tau_{\text{lep}}\tau_{\text{had}}$ analysis is designed to select signal events resulting from vector-boson fusion since the characteristic high-energy jets resulting from this production process can be used to suppress background processes efficiently. Moreover, signal events resulting from a boosted Higgs boson mainly produced via gluon fusion are selected to reach a better mass resolution. The compatibility of data with the signal and background expectation is tested by comparing the invariant $\tau\tau$ mass distributions with a profile likelihood fit.

This analysis constitutes one of two independent and complementary search strategies that are pursued on the same ATLAS data set to search for $H \to \tau\tau$ decays. With both methods a first observation of the decay of the Higgs boson to τ leptons is made in the combination of all $H \to \tau\tau$ decay channels. These results provide the first evidence for the direct coupling of the discovered Higgs boson to fermions in ATLAS as predicted by the Standard Model. The analysis presented in this thesis provides a major contribution to this important achievement.

The thesis is organised as follows: In Chap. 2 the theoretical foundations of the Standard Model and of proton-proton collisions are discussed. The LHC, the ATLAS experiment and methods for the reconstruction and simulation of physics processes are explained in Chap. 3. Chapter 4 outlines important concepts for the analysis of W and Higgs decays and summarises the production mechanisms and previous measurements. The reconstruction of hadronically decaying τ leptons and missing transverse energy together with two performance and optimisation studies are discussed in Chap. 5. The cross section measurement of the $W \to \tau\nu_\tau$ decay is described in Chap 6. The search for $H \to \tau_{\text{lep}}\tau_{\text{had}}$ decays is presented in Chap. 7. A combination with other $H \to \tau\tau$ channels and a comparison to the results obtained with the alternative analysis method is provided in Chap. 8. Chapter 9 gives an outlook on future developments of $H \to \tau\tau$ analyses. Finally, all results are summarised in Chap. 10.

CHAPTER 2

Theoretical Framework

The Standard Model describes the elementary particles and their interactions studied in this thesis. The studied particles are produced and investigated in proton-proton collisions at the Large Hadron Collider in Switzerland. This chapter gives a brief introduction into the theoretical foundations of the Standard Model and the physics of proton-proton interactions.

Section 2.1 lists the characteristics of the Standard Model relevant for this thesis. It focusses on the formalism of electroweak interactions and the Higgs mechanism, which generates masses for the Standard Model particles and predicts the existence of a new scalar particle, the Higgs boson.

Section 2.2 outlines the theoretical framework of proton-proton collisions. Since protons are no elementary particles, the energy exchange takes place between their constituents, quarks and gluons. Therefore, the following relevant aspects are described in this section: The underlying theory of Quantum Chromodynamics, the parton distribution functions that model the quark/gluon interactions within the proton and the modelling of parton showers and of hadronisation.

2.1 The Standard Model

The Standard Model (SM) describes all known elementary particles that form matter and their interactions [1, 2].

The first group of particles are *fermions* which have a spin of 1/2 and follow the Pauli principle. They form the basic constituents of matter and are classified into leptons and quarks. The known leptons are electrons, muons and τ leptons (e, μ, τ), that carry an integer electric charge of -1 (in units of the elementary charge e). To each charged lepton a neutrino (ν_e, ν_μ, ν_τ) is associated which has no charge and is nearly massless. Quarks exist in six known flavours: Up, down, charm, strange, top, bottom (u, d, c, s, t, b). They have an electric charge of 2/3 or -1/3. In addition, they carry another quantum number, the so called *colour* charge, and can therefore have three additional degrees of freedom: green, red and blue. Each of the fermions has a counterpart, an *anti-particle* which has exactly the same properties, but the opposite quantum numbers. In nature quarks are confined to hadrons, such as protons or neutrons. Two types of hadrons exist: Baryons and mesons. Baryons are formed by three quarks, for example the proton (uud), while mesons are formed by one quark and an anti-quark, e.g. pions ($u\bar{d}$ or $\bar{u}d$). All these hadrons are colourless, no colour singlet has been observed so far.

In the Standard Model the two types of fermions are each grouped into three generations with increasing masses. These groups are based on the properties the fermions have in common and help to

classify different types of interactions between them. The generations and properties are summarised in Tab. 2.1. All stable matter in nature can be described by the particles of the first generation: Electrons, u and d quarks.

The interaction of fermions is based on three fundamental forces: The electromagnetic, weak and strong force. The electromagnetic force acts on all particles carrying electric charge, i.e. quarks and charged leptons. The strong force only appears between quarks carrying the colour charge and is responsible for their binding to hadrons. All fermions take part in the weak interaction. A mediator is associated to each force, together they form the second group of elementary particles in the Standard Model: The *bosons* with spin 1. The massless photon is exchanged in electromagnetic interactions. Eight different massless gluons are responsible for the strong interaction, they also carry a colour charge. Finally, the massive vector bosons, W^+, W^- and Z, are the mediators of the weak interaction. Table 2.2 shows the basic properties of the Standard Model bosons.

A fourth interaction, gravity, is not incorporated in the Standard Model since it is negligibly weak on the particle energy scale compared to the other forces. Advanced models describing this interaction by a mediation of the so called graviton were developed, but no proof of its existence was found so far.

The Standard Model provides a unified framework describing interactions and particles based on quantum field theory. Within this theory the dynamics of a system are described by the Lagrangian density, $\mathcal{L}$. Symmetries in a system are in general equivalent to the invariance under a gauge transformation [3]. *Global* gauge symmetries always come along with a conserved quantity, for instance the charge. A *local* (i.e. space-time dependent) invariance of the Lagrangian under a gauge transformation requires the introduction of *gauge fields*, which add the interaction of initially free particles to the theory. The form of the associated gauge fields depends on the characteristics of the underlying symmetry group. The number of gauge fields is equal to the number of its generators. The gauge fields of the Standard Model, which is a local gauge invariant theory, correspond to the three fundamental interactions explained above. It is fully described by a combination of these gauge groups:

$$\mathrm{SU(3)_C} \times \mathrm{SU(2)_L} \times \mathrm{U(1)_Y}$$

$\mathrm{SU(3)_C}$ is the symmetry group on which the strong interaction of quarks is based, its underlying theory is the so called theory of Quantum Chromodynamics (QCD). The subscript C denotes the colour charge that generates this transformation group, associated to it are eight gauge fields which correspond to the eight gluons. The group is non-abelian which enables the self-interaction of gluons. The strong coupling increases with larger distance, which causes quarks to be confined in hadrons. QCD plays an important role in the description of processes at the Large Hadron Collider, relevant aspects of it are therefore be discussed in Sec. 2.2.

The $\mathrm{SU(2)_L} \times \mathrm{U(1)_Y}$ group represents the symmetry group of the electroweak theory which unifies the weak and electromagnetic interaction. The subscript L indicates that the SU(2) group only acts on left-handed fermions. The subscript Y denotes the generator of the U(1) group, the weak hypercharge. The mediators of the electromagnetic and the weak force (photon, $W^\pm$ and Z boson) are a mixture of the four gauge fields associated to this group. The symmetry group $\mathrm{U(1)_{em}}$, describing the electromagnetic interaction based on the theory of Quantum Electrodynamics (QED), is thus a subgroup of this unified electroweak group. The fact that the vector bosons have masses, while the photon is massless, can be explained by a spontaneous symmetry breaking of this gauge group, which leads to the postulation of a new field and a particle associated to it, the Higgs boson.

The formalism of the electroweak theory as well as the spontaneous symmetry breaking and the Higgs mechanism are discussed in the following.

Leptons				Quarks			
Gen.	Particle	Charge [e]	Mass	Gen.	Particle	Charge [e]	Mass
1st	e	-1	511 keV	1st	u	$\frac{2}{3}$	2.3 MeV
	ν_e	0	< 2 eV		d	$-\frac{1}{3}$	4.8 MeV
2nd	μ	-1	105.7 MeV	2nd	c	$\frac{2}{3}$	1.28 GeV
	ν_μ	0	< 0.19 MeV		s	$-\frac{1}{3}$	95 MeV
3rd	τ	-1	1.78 GeV	3rd	t	$\frac{2}{3}$	173.1 GeV
	ν_τ	0	< 18.2 MeV		b	$-\frac{1}{3}$	4.18 GeV

Table 2.1: Fermions and their properties in the Standard Model [2].

Interaction	Boson	Charge [e]	Mass
Electromagnetic	γ	0	0
Strong	g_i, $i \in \{1,..,8\}$	0	0
Weak	W^+, W^-	± 1	80.4 GeV
Weak	Z	0	91.2 GeV

Table 2.2: Mediators of fundamental interactions (bosons) and their properties in the Standard Model [2].

2.1.1 The Theory of Electroweak Interactions

In the electroweak theory all fermions of the Standard Model are separated into left-handed and right-handed particles[1]. They are obtained from the fermion fields via $f_{L,R} = \frac{1}{2}(1 \mp \gamma^5)f$, where γ^5 is the product of the Dirac matrices [1, 3].

Only left-handed fermions couple to the charged components of the weak interaction. They are grouped into doublets of the $SU(2)_L$ symmetry group. The right-handed fermions form a singlet (f_R) of this group. The generator of this group is the so-called weak isospin. It has three components $T_a = \sigma_a/2$, where $a = 1, 2, 3$ and σ_a denote the Pauli matrices. One could associate the third component of the weak isospin to the neutral weak or electromagnetic interaction, however experiments have shown that both also have a component coupling to right-handed particles.

Therefore, to be able to fully include these neutral currents in the electroweak theory, the group $U(1)_Y$ is included, which involves couplings to both chiral states of the fermions. The corresponding charge of this group is the weak hypercharge Y, which relates to the third component of the isospin T_3 and the electric charge Q of the particle by $Y = 2(Q + T_3)$. From this new component, the neutral weak current and electromagnetic current are obtained as orthogonal combinations of the currents, which correspond to the third weak isospin component of the $SU(2)_L$ and the hypercharge of the $U(1)_Y$ group.

The groups of left-handed and right-handed fermions and their quantum numbers of the electroweak interaction are listed in Tab. 2.3.

[1] These two *chiral* states correspond to an helicity of +1 (right-handed) and -1 (left-handed) in the high relativistic case, where $E \gg mc^2$.

Fermion	T	T_3	Y
$q_L = \begin{pmatrix} u \\ d' \end{pmatrix}$	$\frac{1}{2}$	$+\frac{1}{2}$	$+\frac{1}{3}$
	$\frac{1}{2}$	$-\frac{1}{2}$	$+\frac{1}{3}$
u_R	0	0	$+\frac{4}{3}$
d'_R	0	0	$-\frac{2}{3}$
$l_L = \begin{pmatrix} \nu_\ell \\ \ell \end{pmatrix}$	$\frac{1}{2}$	$+\frac{1}{2}$	-1
	$\frac{1}{2}$	$-\frac{1}{2}$	-1
l_R	0	0	-2

Table 2.3: Chiral fermion doublets (singlets) of left-(right-)handed quarks (q) and leptons (l) together with their electroweak quantum numbers. u and d' summarise all up- and down-type quarks, where the latter are in their electroweak eigenstate (see text) [3].

In this case the down-type quarks (denoted with d') are in their electroweak state, rather than in their mass state (as in Tab. 2.1)[2].

The formal introduction of the gauge fields in the Lagrangian density through the condition of local gauge invariance is outlined in the following. The Lagrangian density for all free fermions (keeping them massless for the moment) is [4, 5]:

$$\mathcal{L}_f = \sum_{f=l,q} \bar{f}_L i\gamma^\mu \partial_\mu f_L + \sum_{f=l,q} \bar{f}_R i\gamma^\mu \partial_\mu f_R \tag{2.1}$$

Here f_L and f_R denote all left- and right-handed fermions according to Tab. 2.3, γ^μ the γ matrices and ∂_μ the derivative. The condition of the local gauge invariance requires, that the Lagrangian stays invariant under the following gauge transformations:

$$f_L \to e^{i\alpha_a(x)T^a + iY\beta(x)} f_L, f_R \to e^{iY\beta(x)} f_R \tag{2.2}$$

The initial Lagrangian of the free fermions (Eq. 2.1) is not invariant under local gauge transformations. To enforce this requirement, the derivative is replaced by the *covariant* derivative:

$$D_\mu f = \left(\partial_\mu - ig\vec{T}\vec{W}_\mu - ig'\frac{Y}{2}B_\mu\right) f \tag{2.3}$$

It introduces the four gauge fields $W_{\mu,i}$ ($i = 1, 2, 3$) and B_μ associated to the gauge groups $\mathrm{SU(2)_L}$ and $\mathrm{U(1)_Y}$. g and g' denote the corresponding coupling constants.

One obtains the Lagrangian of the electroweak interaction, invariant under local gauge transformation

[2] Electroweak and mass eigenstate are transferred into one another by the 3×3 *Cabibbo-Kobayashi-Maskawa matrix*, $d'_i = \sum_j V_{ij} d_j$. The quark states that couple to the charged weak interaction are thus in fact a mixture of different physical quark states. The individual matrix entries V_{ij} denote the coupling strength between different quark types [2].

and including interaction with these new fields:

$$\mathcal{L}_{f+G} = \sum_{f=l,q} \bar{f}_L i\gamma^\mu \left(\partial_\mu - ig\vec{T}\vec{W}_\mu - ig'\frac{Y}{2}B_\mu\right) f_L + \sum_{f=l,q} \bar{f}_R i\gamma^\mu \left(\partial_\mu - ig'\frac{Y}{2}B_\mu\right) f_R$$
$$- \frac{1}{4}W^a_{\mu\nu}W^{\mu\nu}_a - \frac{1}{4}B_{\mu\nu}B^{\mu\nu} \tag{2.4}$$

One can clearly see in the first row, that in addition to the free particle terms interaction terms between left-handed fermions and the W_μ and B_μ fields, as well as the interaction of right-handed fermions with the B_μ field, have been generated. The terms in the second row denote the gauge fields strength tensors $W^a_{\mu\nu} = \partial_\mu W^a_\nu - \partial_\nu W^a_\mu + g\epsilon^{ajk}W^j_\mu W^k_\nu$ and $B_{\mu\nu} = \partial_\mu B_\nu - \partial_\nu B_\mu$. They show the additional properties of the fields: The resulting cubic and quartic terms in the Lagrangian denote the self-interaction of the W^a resulting from the non-abelian property of $\mathrm{SU(2)_L}$.

The physical fields, the two charged $W^\pm$ bosons, the neutral Z boson and the photon denoted by A, are in fact mixed states of the electroweak fields W^a and B and are derived in the following way:

$$W^\pm_\mu = \frac{1}{\sqrt{2}}\left(W^1_\mu \mp iW^2_\mu\right) \tag{2.5}$$

$$\begin{pmatrix} Z_\mu \\ A_\mu \end{pmatrix} = \begin{pmatrix} \cos\theta_W & \sin\theta_W \\ -\sin\theta_W & \cos\theta_W \end{pmatrix} \begin{pmatrix} W^3_\mu \\ B_\mu \end{pmatrix} \tag{2.6}$$

The electroweak mixing angle θ_W is defined by the ratio of the coupling constants: $\sin\theta_W = g'/\sqrt{g'^2 + g^2}$, $\sin^2\theta_W \simeq 0.23$. The mixing of W^3_μ and B_μ to Z_μ and A_μ also reestablishes the coupling as it is observed in nature: The photon does not couple to neutrinos and the Z boson couples to both left-handed and right-handed particles, unlike B_μ and W^3_μ. With respect to the self-coupling of these physical fields the terms in Eq. 2.4 change in a way, that in each term at least a pair of W bosons is contained, thus a self-coupling of only photons or Z bosons does not occur.

Consequently, all electroweak interactions are well described by this theory. However, masses for both fermions and the gauge bosons are not included, and an inclusion would destroy the local gauge invariance of the theory. This clearly contradicts the experimental evidence that fermions and the weak gauge bosons have masses. An elegant solution to this problem is provided by the Higgs mechanism, which allows particles to acquire masses.

2.1.2 The Higgs Mechanism

The Higgs mechanism [6–8], which generates the masses of the particles, is based on the concept of spontaneous symmetry breaking. In order for this phenomenon to emerge, the system described by the Lagrangian must be invariant under a group of transformations, and, at the same time, feature a set of *multiple* ground (*vacuum*) states, i.e. field configurations with minimum energy. As soon as one of these states is selected as ground state of the system, the symmetry is broken since this vacuum state does not share the symmetry of the initial Lagrangian [1, 9]. The breaking of a global continuous symmetry always implies the existence of massless scalar (spin-0) particles associated to each broken generator of the symmetry group, which are called *Goldstone bosons* [10].

The Higgs mechanism combines this principle of the spontaneous symmetry breaking with the *local* gauge invariance of the Standard Model. The latter allows for transformations which remove the Goldstone bosons and generate mass terms for the gauge bosons of the electroweak theory, $W^\pm$ and Z, while the photon remains massless. This mechanism will be outlined in the following.

A $SU(2)_L$ doublet of two complex scalar fields (ϕ^+ and ϕ^0) with hypercharge $Y = +1$ is introduced [3, 4]:

$$\Phi = \begin{pmatrix} \phi^+ \\ \phi^0 \end{pmatrix} \tag{2.7}$$

The superscripts indicate the electric charge. The Lagrangian describing the dynamics of this system is given by:

$$\mathcal{L}_\Phi = (iD_\mu \Phi)^\dagger (iD^\mu \Phi) - V(\Phi) \tag{2.8}$$

D_μ denotes the covariant derivative as defined in Eq. 2.3. The potential $V(\Phi)$ is parametrised as:

$$V(\Phi) = \mu^2 \Phi^\dagger \Phi + \lambda (\Phi^\dagger \Phi)^2 \tag{2.9}$$

If $\mu^2 < 0$ (with $\lambda > 0$) the potential reaches a minimum at:

$$< 0|\Phi|0 >^2 \equiv \Phi_0^2 = \frac{-\mu^2}{2\lambda} \equiv \frac{v^2}{2} \tag{2.10}$$

It has thus an infinite number of ground states with a non-vanishing *vacuum expectation value*. The shape of the potential for one complex field is depicted in Fig. 2.1. All points on the circle with radius $v/\sqrt{2}$ represent the minimum of the potential.

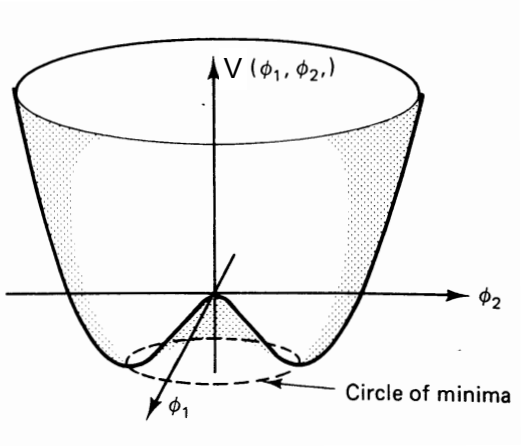

Figure 2.1: Potential function of a complex scalar field $\phi = \phi_1 + i\phi_2$. The vacuum states with minimum energy lie on a circle [1].

For the calculation of the Lagrangian any of these points can be chosen as ground state. An appropriate choice is:

$$\Phi_0 = \begin{pmatrix} 0 \\ \frac{v}{\sqrt{2}} \end{pmatrix} \tag{2.11}$$

At this point the symmetry breaking takes effect: The selected ground state no longer shares the symmetry of the Lagrangian. This choice of Φ_0 in particular breaks the symmetry of $SU(2)_L \times U(1)_Y$, while it still preserves the symmetry of $U(1)_{em}$, which allows for the photon to remain massless in the end.

In order to correctly interpret the theory under these new aspects, the scalar field in the Lagrangian is parametrised by expanding it around the chosen ground state. For this purpose, four real fields θ_a

($a = 1, 2, 3$) and H are introduced, and the scalar field doublet at first order is then given by:

$$\Phi(x) = \begin{pmatrix} \theta_2 + i\theta_1 \\ \frac{1}{\sqrt{2}}(v + H(x)) - i\theta_3 \end{pmatrix} = e^{iT^a(x)\theta_a(x)/v} \begin{pmatrix} 0 \\ \frac{1}{\sqrt{2}}(v + H(x)) \end{pmatrix} \tag{2.12}$$

The three fields θ_i correspond to the generators that are spontaneously broken, and thus to the three massless Goldstone bosons, which occur as a consequence of the symmetry breaking.

On the basis of the local gauge invariance of the initial Lagrangian under $SU(2)_L$ transformations a gauge transformation $\Phi(x) \rightarrow e^{-iT^a(x)\theta_a(x)/v}\Phi(x)$ can be applied, which completely eliminates any dependence on the three fields θ_i. Inserting this field parametrisation at the so-called *unitary gauge* into Eq. 2.8 yields:

$$\begin{aligned} \mathcal{L}_G = &\frac{1}{2}(\partial_\mu H)^2 + \frac{1}{8}g^2(v + H)^2 \left|W_\mu^1 + iW_\mu^2\right|^2 + \frac{1}{8}(v + H)^2 \left|gW_\mu^3 - g'B_\mu\right|^2 \\ &- \frac{1}{2}\lambda v^2(v + H)^2 - \frac{1}{4}\lambda(v + H)^4 \end{aligned} \tag{2.13}$$

If the physical gauge bosons $W^\pm$ and Z are included in this equation (according to Eq. 2.6), it results in Lagrangian terms of the form:

$$\mathcal{L}_G = \left(\frac{g^2v^2}{4}\right) W_\mu^+ W^{\mu-} + \frac{1}{2}\left(\frac{(g^2 + g'^2)v^2}{4}\right) Z_\mu Z^\mu + ... \tag{2.14}$$

These are the desired mass terms of the three weak gauge bosons, with the masses given by:

$$m_W = \frac{gv}{2}, \quad m_Z = \frac{\sqrt{g^2 + g'^2}v}{2} \tag{2.15}$$

No mass term for the photon is included in $\mathcal{L}$.

In conclusion, the Higgs mechanism generates masses of the heavy gauge bosons without breaking the symmetry of the Lagrangian. By choosing a particular ground state of the field Φ, spontaneous symmetry breaking of $SU(2)_L \times U(1)_Y$ takes place. Due to the local gauge invariance an appropriate gauge can be chosen, at which the resulting massless Goldstone bosons are eliminated from the Lagrangian and the gauge bosons $W^\pm$ and Z acquire mass. Also the degrees of freedom in the system are conserved within this mechanism: As soon as the weak interaction bosons acquire mass they gain each an additional degree of freedom, the longitudinal polarisation. These three additional degrees of freedom were formerly held by the three massless Goldstone bosons, which simultaneously vanish from the Lagrangian.

The last degree of freedom associated to the field $H(x)$ manifests in a new scalar particle with spin 0, whose kinematics are described by these terms of Eq. 2.13:

$$\mathcal{L}_{\text{Higgs}} = \frac{1}{2}(\partial^\mu H)^2 - \lambda v^2 H^2 - \lambda v H^3 - \frac{\lambda}{4}H^4 \tag{2.16}$$

Interpreting the individual terms, this leads to the conclusion that this new elementary particle, called the *Higgs boson*, is a massive particle with self-couplings in third and fourth order. Its mass can be read off from the second term in Eq. 2.16 and the couplings to the gauge bosons g_{HVV} and g_{HHVV} from the

interaction terms of the Higgs boson with the vector bosons in Eq. 2.13:

$$m_H = 2\lambda v^2 = -2\mu^2 \tag{2.17}$$

$$g_{HVV} = \frac{2m_V^2}{v}, \quad g_{HHVV} = \frac{2m_V^2}{v^2} \tag{2.18}$$

Here V denotes $W^{\pm}$ or Z.

In order to generate the fermion masses the same scalar field Φ can be used to introduce the so called *Yukawa* coupling of the Higgs field to fermions in the Lagrangian (here only displayed for the first fermion generation, using the parametrisation of Tab. 2.3) [4]:

$$\mathcal{L}_{\mathrm{YK}} = -\lambda_e \bar{l}_L \Phi e_R - \lambda_d \bar{q}_L \Phi d'_R - \lambda_u \bar{q}_L \tilde{\Phi} u_R \tag{2.19}$$

In the equation $\tilde{\Phi}$ is equal to $i\sigma_2\Phi^*$.

By expanding the field around its vacuum state and using the unitary gauge in the same way as described above, the mass terms and interaction terms of the fermions with the Higgs field are generated, with:

$$m_f = \frac{\lambda_f v}{\sqrt{2}} \tag{2.20}$$

$$g_{Hff} = \frac{m_f}{v} \tag{2.21}$$

Here f denotes all types of massive fermions.

The couplings of the Higgs field to fermions and gauge bosons is proportional to the particle masses (Eqs. 2.21 and 2.18). The Higgs boson will therefore decay predominantly to the particles with the highest mass. Since the couplings can be expressed only in terms of v, m_V, m_f and m_H, the Higgs production and decay mechanisms can be predicted very precisely. This will be explained further in Sec. 4.1.2 [3]. The mass of the Higgs boson, however, cannot be directly predicted by the Standard Model, since μ is an unknown parameter. It is therefore a major goal of particle experiments, to prove the existence of the Higgs boson, since this verifies the Higgs mechanism which generates the particle masses.

Considerations on the consistency of the theory impose upper and lower bounds on the Higgs mass, dependent on the energy scale up to which the Standard Model is valid, and thus define the loose range of the search for a Higgs boson in experiments [4]. As soon as particle colliders with high enough centre-of-mass energy were built, direct experimental search for a Higgs boson in the accessible mass range has been performed. These search results leading to the discovery of the Higgs boson with the Large Hadron Collider experiments in 2012 are reviewed in Sec. 4.1.3.

[3] The vacuum expectation value v is related to the Fermi constant G_F which can be measured in muon decays, $v = \frac{2M_W}{g} = (\sqrt{2}G_F)^{-1/2} \approx 246$ GeV [4].

2.2 Phenomenology of Proton-Proton Collisions

Particles of interest for this thesis, such as heavy bosons, are created in high-energy proton-proton (pp) collisions at the LHC and are identified through their decay particles in the detector. In order to make accurate predictions on relevant physics processes, a fundamental understanding of the inelastic scattering of protons is vital.

The pp collisions involve colour charge exchange, and are therefore based on the strong interaction described by the theory of QCD. According to the theory, protons consist of three valence quarks (u, u, d) and a sea of other quarks and gluons. During a collision energy is exchanged between two of these constituents, summarised as *partons*. From this interaction the particles of interest are produced and recorded in the detector.

The strength of the parton interaction is quantified by the strong coupling constant $\alpha_S(Q^2)$ depending on the energy scale Q^2. This energy dependence of α_S determines the nature of the strong interaction: At small energy scales, equivalent to large distances, the coupling gets large. This feature called *confinement* is responsible for the fact that quarks and gluons can only be detected confined in bound states in the detector [1]. It is thus not possible to study the interaction of the partons directly in the experiment.

The transition of an initial state to a particular final state, due to the energy transfer during the parton interaction, can be calculated based on the *Feynman rules* derived from the QCD Lagrangian [1]. They are visualised by Feynman diagrams (e.g. Fig. 2.2). The sum of all Feynman graphs defines the total transition amplitude for the considered process, the so called *Matrix element*. The cross section, denoting the probability for the occurrence of a certain process during a collision, can be calculated from the square of the Matrix element: $d\sigma \propto |\mathcal{M}|^2 d\rho$. The variable $d\rho$ denotes the phase space density, i.e. all possible kinematic states that can be assumed.

To fully derive the cross section of a pp collision the following aspects have to be taken into account [11]:

- The interacting partons carry an unknown fraction of the total proton momentum. In order to derive the cross section, all momentum fractions for all possible combinations of initial partons must be integrated over. The probability distribution is given by the so-called *Parton density functions* (PDFs).
- The incoming and outgoing partons can emit gluons, the so called initial and final state radiation (ISR and FSR, respectively), which themselves initialise an emission of gluons and quark-antiquark pairs. This is referred to as *parton shower* and treated separately from the main parton interaction.
- Due to the strong confinement forces at small energies, the partons form bound states with hadrons after the shower process which emerge as particle bundles (*jets*) in the detector. This process is called *hadronisation*.
- In a proton collision additional interaction of partons with a much lower energy exchange compared to the main parton collision take place. This is referred to as *underlying event*.

A prediction on the observables of any type of physics process produced in the hadron collision is done with the help of simulations provided by Monte Carlo (MC) generators. They model the complete chain of interactions addressing each of the above mentioned issues with different methods. A few of the theoretical concepts to describe these phenomena are therefore outlined in the following. A further description of different generator types will be given in Sec. 3.5.

2.2.1 Essentials of Perturbative QCD

The calculation of the matrix element is performed based on *perturbative* QCD by expanding it in orders of the strong coupling constant $\alpha_S(Q^2)$, which is equivalent to the number of vertices in the summed Feynman graphs [12]. At leading order (LO) the diagrams with the minimal number of vertices contribute, an example is shown in Fig. 2.2a. For processes of higher order additional vertices have to be taken into account, which result from contributions of quarks or gluons to real emissions and virtual loops[4], see Figs. 2.2b and 2.2c.

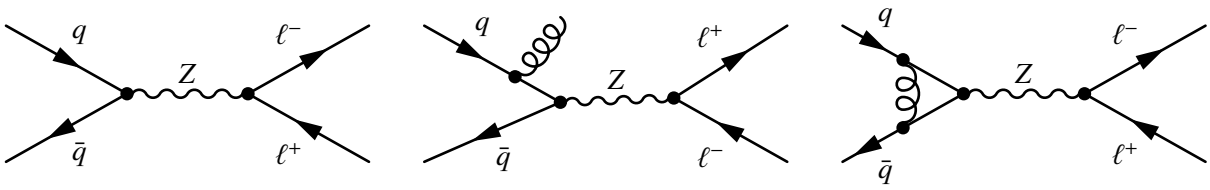

(a) (b) (c)

Figure 2.2: Basic Feynman graphs of a parton interaction resulting in a Z boson production and a subsequent decay to a pair of leptons. (a) Leading order diagram and two examples for higher order QCD corrections, (b) real gluon emission (ISR), (c) virtual loop.

Pertubative calculations of QCD processes can only be performed at small values of $\alpha_S(Q^2)$, corresponding to high energy scales and small distances of partons. As soon as the energy scale gets too small and α_S too large, the perturbation theory is no longer applicable. The parton scattering at the LHC with a high energy transfer, often referred to as the *hard* process, falls in the range where precise perturbative calculations are possible. *Soft* processes at smaller energy scales, e.g. the hadronisation process, can only be described by phenomenological models.

In addition, at smaller α_S there are limits to the QCD perturbative calculation: In the case when a gluon is emitted collinear to the initial parton or with very low energy (compare Fig. 2.2b), the corresponding real corrections in perturbation theory diverge [11].

In principle, if a complete perturbative calculation is performed, all divergent terms of real corrections cancel out with divergences of virtual corrections [13, 14]. In practice however, the proper arrangement of terms in order to cancel out becomes far too complex at higher perturbation orders. Therefore, the matrix element calculation is truncated at a certain order, e.g. NLO or NNLO (next-to-leading-order and so forth), and used as an approximation.

Calculations to much higher orders can be performed at *tree-level*, i.e. by excluding any virtual corrections, but since in this case real divergent terms remain in the calculation, they have to be restricted to a phase space region avoiding these soft/collinear divergences [1, 11]. This restriction is not feasible for a full description of proton-proton collisions, therefore, to cover the full phase space region, other approximate models have to be used in combination with the fixed-order perturbative calculations, which will be explained in the next subsection.

Another consequence of these fixed-order calculations is their dependency of the calculation on the renormalisation scale μ_R [15]. This scale is in general a result of renormalisability of the SM according

[4] Virtual particles is the general notation for particles which are produced intermediately in an interaction. According to the Feynman rules they do not necessarily need to have their rest mass, i.e. they are normally not on their mass shell [1].

to theory [1]: The divergences of virtual loops in the perturbative approach can be removed by additions to physical quantities defined in theory, such as mass or coupling constants. The key points are, that the divergences are associated to non-observable bare quantities and subtracted from the result, and that the resulting renormalised quantities are in fact the ones measurable by experiment. This procedure introduces the renormalisation scale, at which these subtractions of divergences are done. In the case of QCD the strong coupling constant is thus in fact dependent on μ_R. While a complete perturbative calculation is independent of μ_R, this is not the case for truncated calculations at lower orders. In this case a specific scale has to be chosen depending on the experiment [13].

2.2.2 Parton Density Functions

The principle of a hard scattering process is illustrated in Fig. 2.3: When the two protons (h_1, h_2) collide, their partons (a and b) interact with each other and new particles (c and d) are produced from the interaction. Each of the initial partons carries an unknown fraction of the total proton momentum $x_1 p_{h_1}$ and $x_2 p_{h_2}$. The squared transferred energy in the interaction is thus $\hat{s} = x_1 x_2 s$, with s being the squared centre-of-mass energy of the two protons.

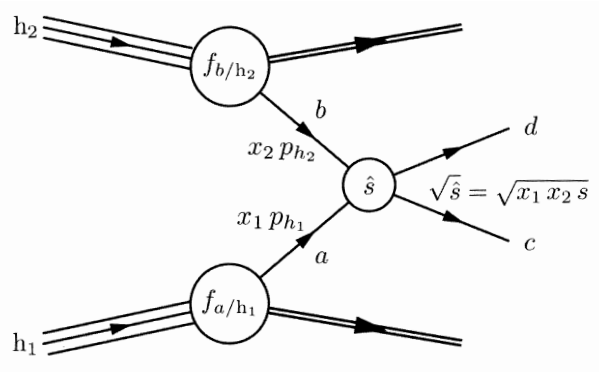

Figure 2.3: Basic Feynman diagram to describe the process of a proton-proton collision [11].

The probability function to find a parton with a certain momentum fraction is given by the parton density functions $f_{a/h_1}(x_{1,a})$ and $f_{b/h_2}(x_{2,b})$, where a and b denote the different parton types inside the interacting proton. The total hadronic cross section is thus defined by the cross section of the partonic process $\hat{\sigma}_{ab\to X}$ weighted by the two PDFs, integrated over the momentum fractions and summed over all combinations of parton pairs [13]:

$$\sigma_{pp\to X} = \sum_{ab} \int_0^1 \int_0^1 \mathrm{d}x_{1,a}\mathrm{d}x_{2,b} f_{a/h_1}(x_{1,a}) f_{b/h_2}(x_{2,b})\, \hat{\sigma}_{ab\to X} \tag{2.22}$$

This simple multiplication of parton cross section and PDFs in this formula is possible by virtue of the factorisation theorem [14, 16]: As explained before the hadron collision consists of parton processes at high and at low energy scales. The hard interaction of the partons is quantified by $\hat{\sigma}_{ab\to X}$ which can be precisely calculated by perturbative QCD up to a fixed order. The soft QCD-phenomena, like the interactions of the partons within the proton, cause a divergence of the perturbative expansion. The factorisation theorem states that all such divergences at a specific energy scale Q^2 are absorbed in the PDFs. The PDF is thus dependent on the energy scale, $f_i(x_{1,i}, Q^2)$. The explicit scale separating the soft and the hard regimes in the hadron scattering process is called *factorisation scale* μ_F.

Therefore, the cross section calculation in this form now depends on two scales, the factorisation scale μ_F and the renormalisation scale μ_R (see previous section). Usually they are chosen to be at the typical energy scale of the parton scattering $\hat{s}$, equivalent to the invariant mass of the final state particles [13].

The PDFs consequently can not be obtained from exact calculations, but have to be measured in the experiment instead. Since the PDFs are solely dependent on the energy scale, they are universal for different hard scattering processes [13, 14]. The determination of the PDFs for hadron colliders like the LHC can therefore be derived from various previous experiments at lower energy scales [17], e.g. by fitting the data of deep inelastic scattering (e on protons) at HERA [18]. Based on the results of these data fits, the PDFs can be calculated for the energy scale at the LHC. An example of a set of PDFs, the so called MSTW [17] set, determined at low energy scale and transferred to a high scale, is shown in Fig. 2.4.

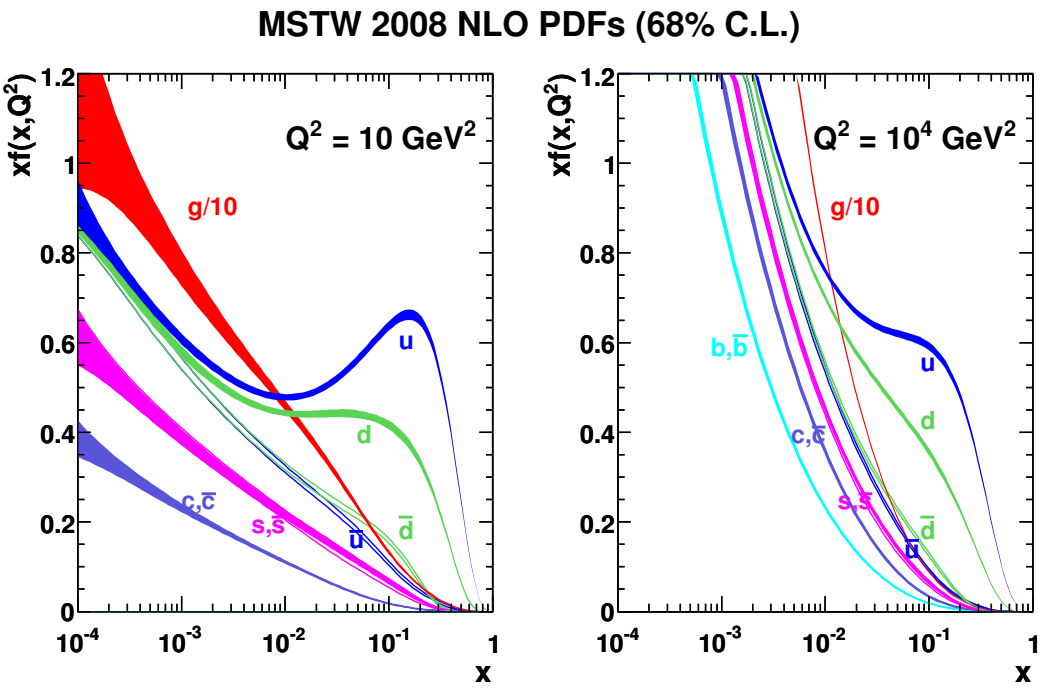

Figure 2.4: MSTW 2008 NLO set of PDFs at energy scales of $Q^2 = 10$ GeV^2 and $Q^2 = 10^4$ GeV^2. Also included are the one-σ confidence level uncertainty bands [17].

2.2.3 Parton Shower

Ingoing and outgoing partons, if present, can emit gluons (ISR and FSR). These themselves can further emit gluons or quark-antiquark pairs, and a parton shower evolves. This interaction with multiple partons goes beyond the fixed-order QCD perturbation theory. An exact calculation of this shower development is therefore not possible. An approximative method is used instead, the so called *parton shower* model, which is widely used by Monte Carlo generators [11, 13]. These approximate calculations can again be factorised with the matrix element of the hard interaction to describe the full proton-proton collision.

The model describes the evolution of a parton from the energy scale of the hard interaction down to a multiparton state at the scale of hadronisation through successive $1 \rightarrow 2$ splittings of the type $q \rightarrow gq$,

$g \to q\bar{q}$ and $g \to gg$. The probability for these splittings is obtained from approximate calculations. The dominating terms contributing to these splittings are determined at all orders and are added as corrections to the fixed-order matrix element. Those mainly result from the cases of collinear parton splitting and soft gluon emission (see above).

The evolution of splittings is usually parametrised in one observable: The increasing virtuality of the parton, its decrease of transverse momentum or its change of emission angle [13]. Different generators use different observables, as explained in Sec. 3.5.

A problem of this method are the divergent terms from collinear and soft contributions, resulting in probabilities for the parton splitting greater than one. This is solved by inclusion of the so called *Sudakov* form factor [11, 13]: It quantifies the probability, that a splitting does *not* happen at the transfer of a parton from a high energy scale Q_1^2 to a lower one Q_2^2. Included in the corrections added to the matrix element it can be seen as the respective virtual correction of each order handling the cancellation of real divergent terms.

If the shower evolution reaches a minimum energy scale threshold Q_0^2, usually around 1 GeV^2, the shower modelling is terminated [16].

In the parton shower model it is important to avoid double counting of phase space regions which have already been taken into account in the matrix element calculation. Different methods exist to perform a proper matching of these two [12, 14].

2.2.4 Hadronisation

After the parton shower evolution the final set of partons must undergo a hadronisation process to form a set of colourless hadrons according to the rules of confinement. In this non-perturbative regime the hadronisation process can only be accessed by phenomenological models. Two common models exist which are used by different generators [14, 16]:

The *string model* uses the confinement principle as a starting point. When the distance between the partons becomes larger, the potential energy between them increases and forms a colour flux string between them which is assumed to be uniform along its length. If the potential energy is high enough, the colour string can break to create a $q\bar{q}$ pair, each of them connected to the initial quark via a separate colour string. This mechanism continues until all quarks and anti-quarks are combined to colour-neutral hadrons, where each hadron corresponds to a small fraction of the initial string.

An alternative model, the *cluster model*, assumes that all gluons resulting from the parton shower split into quark-antiquark pairs. Quarks/anti-quarks from adjacent shower branches then form colour singlets together. These clusters are then combined to form the hadrons.

CHAPTER 3

The Large Hadron Collider and the ATLAS Experiment

As explained in the previous chapter heavy particles are produced in collider experiments. In order to produce the particle of interest a centre-of-mass energy $\sqrt{s}$ higher than the rest mass of the particles of interest must be achieved. Moreover, due to their small production cross sections a high number of collisions is needed to collect an sufficiently high amount of data for an investigation of the particles.

This thesis is based on data recorded at the Large Hadron Collider, a proton-proton-collider situated at the *Conseil Européen pour la Recherche Nucléaire* (CERN) near Geneva in Switzerland. The LHC reaches both the highest energy and the largest collision rate in the world. The data is taken by the ATLAS detector, one of the four experiments at the collision points of the LHC, which is able to cope with these large energies and data flow due to advanced detection technologies.

This chapter gives an overview of the experiment, the LHC and the ATLAS detector (Secs. 3.1 and 3.2). Emphasis is put on the detector parts relevant for detection of the event signatures investigated in this thesis. Moreover, the trigger system is explained in Sec. 3.3 and the event and particle reconstruction from the detector information is discussed briefly in Sec. 3.4 also focussing on the particles relevant for this thesis. Finally, in Sec. 3.5 the event generation and the simulation of the detector response are explained, which provide an important tool to make predictions of the different processes recorded with the ATLAS detector.

3.1 The Large Hadron Collider

The LHC is a circular collider with a circumference of about 27 km, situated in a tunnel about 100 m below the surface [19]. In two adjacent tubes with ultra-high vacuum two proton beams circulate in opposite directions at a design centre-of-mass energy of $\sqrt{s} = 14$ TeV (7 TeV per beam) and are brought to collision at four points, where four detectors (ATLAS, CMS, ALICE and LHCb) are situated to record the collision output[1]. A sketch of the LHC ring and the four experiments is shown in Fig. 3.1.

Each of the four experiments is designed for a different purpose providing a wide potential for physics research. ALICE [21] investigates mainly heavy-ion collisions to produce quark-gluon-plasma. LHCb [22] is dedicated to studies of b quark decays to find clues for the matter-antimatter imbalance in the universe. ATLAS [23] and CMS [24] are meant to investigate a wide range of physics processes at

[1] Instead of proton beams also heavy ions can be injected and brought to collision.

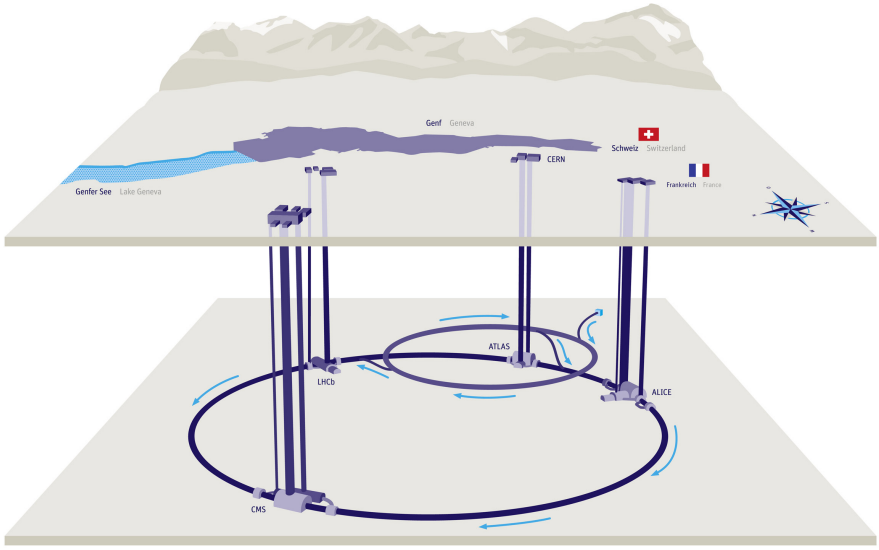

Figure 3.1: Sketch of the Large Hadron Collider and its four main experiments [20].

the TeV scale, including precision measurements of Standard Model parameters and the search for new physics phenomena such as the Higgs boson production.

The protons are pre-accelerated in a system of different smaller circular and linear accelerators and brought to an energy of 450 GeV before being injected into the LHC. In the LHC ring the protons are further accelerated to their final energy through superconducting radio-frequency cavities. Large superconducting dipole magnets with field strengths of up to 8 Tesla force the particles on their circular trajectories, while quadrupole and higher order magnets focus the beam to up to 16 μm near the collision points. In order to maintain the superconductivity of magnets and cavities the LHC ring is kept at a constant temperature of 1.9 K during operation by superfluid liquid helium.

The luminosity describes the number of protons that can interact per unit area and second. It is defined as $L = \dot{N}/\sigma$, where $\dot{N}$ denotes the event rate and σ the cross section. Pulsed by the radio-frequency cavities the protons are injected in packets (*bunches*) into the LHC ring, each bunch containing up to 10^{11} protons. The bunch spacing of the LHC operated at the design setup is 25 ns or 7 m. The aspired luminosity is $L = 10^{34}$ cm^{-2}s^{-1}. With these beam parameters the luminosity can be rewritten for the crossing of two bunches as $L = fn^2/A$, with f denoting the frequency of the collision of two bunches, n the number of protons in each bunch (assuming them to be equal) and A the effective transverse area, in which the beams are colliding [25]. Obviously a highly focussed beam and a high collision rate lead to higher luminosities.

A higher luminosity however also increases the problem of multiple proton-proton collisions, generally summarised as *pile-up* effects: In addition to the main proton-proton interaction in one bunch crossing, more interactions of protons in the same bunch take place simultaneously. Although the momenta of the produced particles of these additional reactions are generally lower than in the main *hard* interaction, a disentanglement from the collision of interest poses a challenge for the detection and analysis of the data events. For instance, in the LHC data set taken in 2012 (see below) the average mean number of interactions during one bunch crossing is about 20. This phenomenon is referred to as *in-time* pile-up. In addition, with smaller bunch spacing also *out-of-time* pile-up effects become more of a problem: This refers to the interactions from previous and subsequent bunch crossings, which are recorded together with the considered collision event, since the detector response time is larger than the

bunch spacing.

The operation of the LHC and the experiments started end of 2009. The first collisions of high energies with a centre-of-mass energy of $\sqrt{s} = 7$ TeV took place in March 2010 and the data taking continued until end of 2012 at centre-of-mass energies of $\sqrt{s} = 7$ TeV and $\sqrt{s} = 8$ TeV (this operation period is summarised as Run 1). This data forms the basis for the results obtained in this thesis. The luminosity was also chosen to be lower in the beginning with a bunch spacing of 50 to 75 ns. It was increased continuously, until it came very close to its design value end of 2012. Figure 3.2a shows the accumulative integrated luminosity $\mathcal{L} = \int L dt$ collected with the ATLAS detector in the first three years of operation as a function of time.

Figure 3.2b shows the distribution of the mean number of interactions per bunch crossing (in-time pile-up) throughout the data taking periods in 2011 and 2012. After a longer shutdown from the beginning of 2013 a next operation phase is planned for early 2015 (Run 2), with a centre-of-mass energy of $\sqrt{s} = 13$ TeV, close to the design value, and the design luminosity, in order to collect a multiple times larger data sample. Table 3.1 summarises the centre-of-mass energies, integrated luminosities[2] and average mean number of interactions within one bunch crossing for the three years of data taking relevant for this thesis.

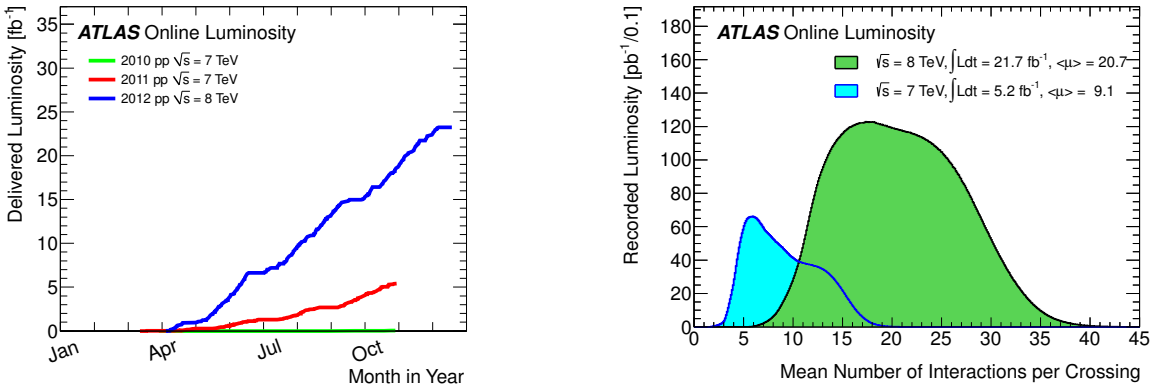

(a) (b)

Figure 3.2: (a) Integrated luminosity as a function of time for the LHC data taking periods of Run 1 in 2010, 2011 and 2012 recorded with ATLAS. (b) Mean number of interactions per bunch crossing in the 2011 and 2012 data set weighted by the luminosity [26].

Year	$\sqrt{s}$ [TeV]	$\int L dt$	$< \mu >$
2010	7	34 pb^{-1}	3
2011	7	4.6 fb^{-1}	9.1
2012	8	20.3 fb^{-1}	20.7

Table 3.1: Centre-of-mass energies, total integrated luminosity usable for the physics analysis in this thesis and the average mean number of interactions per bunch crossing $< \mu >$ recorded with ATLAS for the three LHC operation periods in Run 1 [27, 28].

[2] The integrated luminosity usable for data analysis is slightly smaller than the one delivered by the LHC. It only contains events that have been recorded when all detector elements were fully operational and a good reconstruction of all physics objects was possible.

3.2 The ATLAS Detector

The ATLAS detector (**A** **T**oroidal **L**HC **A**pparatu**S**) is designed to record the high multiplicity of particles delivered by the LHC collisions and provide precise measurements of their energies and momenta [23]. It is 44 m long and 25 m high and has a cylindrical shape, centred at the collision point of the proton beams, which covers nearly the full angular space around the beam axis. ATLAS consists of three main detector subsystems arranged in concentric layers: Closest to the interaction point lies the inner detector (ID), followed by an electromagnetic and hadronic calorimeter (ECal and HCal) and the muon spectrometer (MS). A sketch of the detector layout can be seen in Fig. 3.3.

A summary of all detector components will be given in the following, as well as a list of the commonly used variables and coordinates to describe particles within the ATLAS detector geometry.

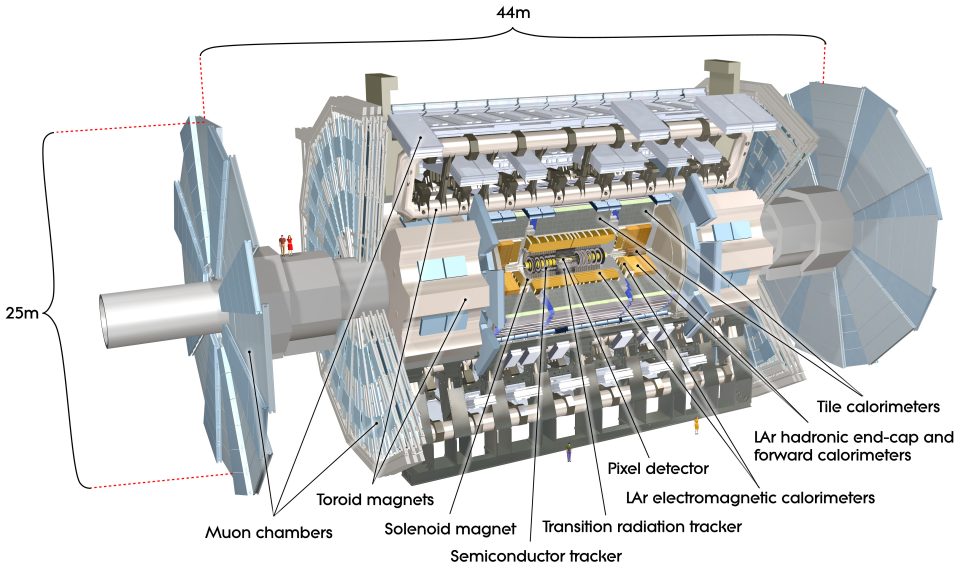

Figure 3.3: The ATLAS detector [23].

Important variables

A right-handed cylindrical coordinate system is used for the ATLAS detector, the origin being defined as the interaction point of the two protons in the centre. The direction of the proton beam inside the beam-pipe is defined as the z-axis. The x-axis is pointing towards the centre of the LHC ring and the y-axis points upwards. In the transverse plane of the detector the radial distance from the beam axis R and the azimuthal angle ϕ are used to describe the particle direction. The pseudorapidity $\eta = -\ln\tan\theta/2$ is used as a measure for the polar angle θ with respect to the z-axis. This quantity has the advantage that differences in pseudorapidity are invariant under longitudinal Lorentz-boosts for particles with negligible rest mass, which is a valid assumption for particles produced in the energy range of the LHC. A general measure for angular distances in ATLAS is therefore $\Delta R = \sqrt{\Delta\phi^2 + \Delta\eta^2}$.

Momenta and energies of particles are preferably investigated in the transverse plane, where the total momentum can be assumed to be zero due to momentum conservation during the collision. The variables $p_T = \sqrt{p_x^2 + p_y^2}$ or E_T denote the transverse momentum or energy.

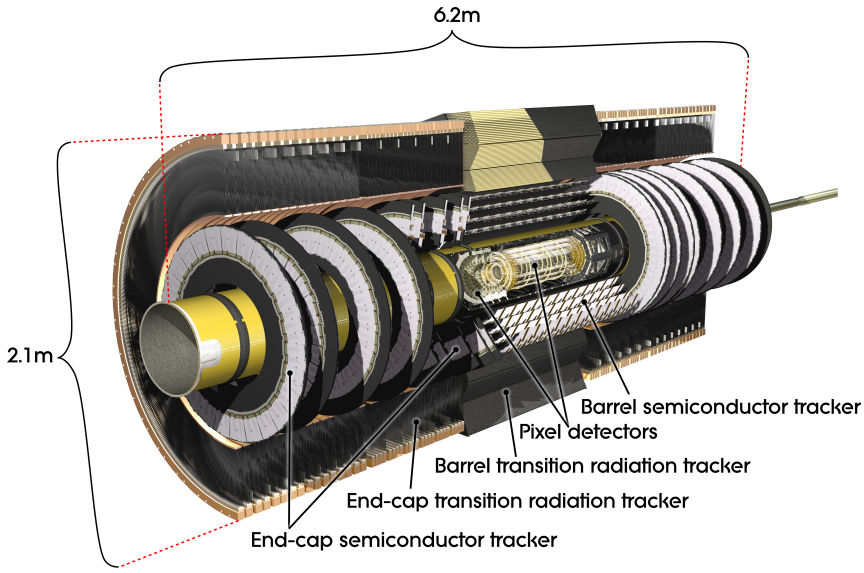

Figure 3.4: Cut away view of the inner detector [23].

Inner Detector

The inner detector provides a precise measurement of charged particle trajectories coming from the collision point. It is enclosed by a solenoid magnet which constitutes a field of 2 Tesla parallel to the beam axis. This causes a bending of the particle trajectories in the transverse plane, and allows a momentum and charge measurement from the curvature of the particle track. The ID consists of three detection subsystems, separated into a central region (*barrel*) and two front and rear regions (*end-caps*). A sketch is shown in Fig. 3.4. Its total radius is about 1.1 m and it covers the full azimuthal range and a pseudorapidity of $|\eta| < 2.5$, except for the transition radiation tracker which reaches only up to $|\eta| < 2$.

The particles traversing the detector leave electric signals in the individual detector layers (*hits*), which can be combined to reconstruct the particle *tracks*. Moreover, by extrapolating the tracks their point of origin in the beam-pipe (*vertex*) can be precisely reconstructed. This is particularly important to detect long-living particles such as b-quark hadrons or τ leptons, since their decay takes place at a different position (*secondary vertex*) than the original collision (*primary vertex*). For the reconstruction of hadronically decaying τ, which are investigated in this thesis, a good spacial resolution of the inner detector is crucial to reconstruct the often very close-by tracks of the τ decay products.

The **pixel detector**, a silicon-based semiconductor detector, is situated closest to the beam axis [29]. It consists of three cylindrical layers in the barrel region and three disks in each end-cap region. With a total of 80 million readout channels and a pixel size of $50 \times 400\ \mu\text{m}^2$ (in $R - \phi \times z$) it provides a very good spacial resolution of 10 μm ($R-\phi$) and 115 μm (z) [30]. This allows precise measurements of track parameters, which is crucial due to the high density of tracks close to the collision point. In particular, it enables the distinction of multiple vertices from pile-up and reconstruction of secondary vertices of b-quark hadrons or τ leptons.

The next sub-detector is also a silicon-based semiconductor detector, the **semiconductor tracker** (SCT). It consists of four layers of microstrips in the barrel region parallel to the beam axis and nine disks at each side in the end-caps. Each strip has a pitch of 80 μm. They provide a precise position measurement in the $R - \phi$ plane. A measurement of the z coordinate is obtained via a small stereo

angle between the two surfaces of each layer. It provides a measurement accuracy of 17 μm ($R-\phi$) and 580 μm (z).

The outermost part of the ID is the large **transition radiation tracker** (TRT). It consists of more than 300000 straw tubes with a diameter of 4 mm, filled with a Xenon-based gas mixture and based on the measurement principle of proportional drift tubes [29]. In the barrel region they are aligned parallel to the beam axis and have a length of 144 cm, while in the end-cap region they have a length of 37 cm and are aligned radially. Thus, the TRT only provides an $R-\phi$ information on the particle track in the barrel region, with a granularity of 130 μm per straw. Due to the large amount of space points measured by the TRT (typically 36) and the large track path covered by it, it also improves the momentum resolution. In combination with the fine granularity semiconductor trackers (with in total 7 space points) an accurate track reconstruction and high momentum resolution is provided by the ID.

In addition, the TRT allows particle identification through the detection of transition radiation. For this purpose polypropylene fibres or foils surround the tubes which cause the emission of transition radiation by the traversing particles [2]. The transition radiation photons are also detected inside the straw tubes and cause a signal with a higher amplitude than the signal of the ionising particles themselves. Since the emission probability depends on the particle's Lorentz-boost factor $\gamma = E/m$, it helps to differentiate between for instance pions and electrons, which plays an important role in the identification of hadronically decaying τ leptons studied in this thesis.

Calorimeters

The calorimeters which are situated outside the inner detector and solenoid, are essential for precise energy measurements of different kinds of particles. Neutral and charged particles reaching the calorimeters are absorbed by its dense matter, where they initiate a shower of secondary particles due to different kinds of interactions with the materials [2].

Two different calorimeter systems are included in ATLAS optimised for different particles: An electromagnetic calorimeter used for the detection of electrons and photons and a hadronic calorimeter to collect energy depositions of hadrons contained in quark/gluon jets or hadronically decaying τ leptons. All calorimeters in ATLAS are so called *sampling* calorimeters where passive and active material for absorption and detection of showering particles are arranged in alternating order. A schematic view of the calorimeter system can be seen in Fig. 3.5a.

The calorimeters need to consist of very dense material to guarantee that the full energy of particles is contained and can be measured. In addition, it must be as hermetic as possible to be able to measure the energy depositions in all possible directions and reconstruct the energy of all particles of the collision. This is in particular important for an accurate reconstruction of the missing transverse energy carried away by neutrinos, which is indirectly measured from the sum of all energy depositions in the calorimeters (see Sec. 5.3). The ATLAS calorimeters are covering therefore an area up to $|\eta| < 4.9$.

The inner **electromagnetic calorimeter** with a very fine granularity serves as a measurement device for electrons and photons. It makes use of their high interaction probability via pair production and bremsstrahlung at high energies in matter [2]. This causes the formation of particle cascades (*showers*) which are detected. The radiation length (X_0) is a measure for the longitudinal extension of the shower and depends on the material [29]. The total thickness of the ECal is about 24 X_0 in the barrel ($|\eta| < 1.475$) and 26 X_0 in the end-caps ($1.375 < |\eta| < 3.2$). The ECal is designed in a special accordion shape which provides short drift paths and is thus suited for high particle rates [31]. The active material consists of chambers filled with liquid argon (LAr) in which the ionising particles of the showers are detected. The passive absorption material is lead.

The ECal barrel consists of three layers in depth with finely segmented cells and strips to allow

a precise reconstruction of the transversal and longitudinal extension of the shower. The ECal end-caps consist of two layers with a slightly coarser granularity. An additional presampler in front of the calorimeter is used to correct for the energy losses in the inner detector and the solenoid region. A sketch of the detailed ECal barrel segmentation can be seen in Fig. 3.5b. The fine granularity of the ECal allows in particular to separate nearby photons from neutral pion decays, which occur in hadronic decays of τ leptons, studied in this thesis.

The coarser and larger **hadronic calorimeter** is used for energy measurements of the hadronic components of jets and τ leptons, such as pions, protons and neutrons. The hadronic interactions with the material cause a hadronic particle shower. In the barrel region ($|\eta| < 1.7$) tiles of scintillators are used as detection material and steel is used as absorber material. In the end-cap regions ($1.5 < |\eta| < 3.2$) the HCal consists of copper and LAr. The barrel detector has three layers in depth, and each end-cap consists of two wheels of calorimeter material with two layers.

The amount of material needed to stop a hadronic particle is quantified with the so-called interaction length λ [29]. The hadronic calorimeters provide a thickness of $> 7\lambda$, enough to absorb also high-energy hadrons.

In the forward and backward detector region ($3.1 < |\eta| < 4.9$) an additional calorimeter, the **LAr forward calorimeter** (FCal), is installed. Its first layer consists of copper and the second and third layers consist of tungsten absorber material for electromagnetic and hadronic shower production. It contains in total about 10λ of material. This detector element collects the energy of particles which are emitted very close to the beam axis. This is important for the accurate detection of forward jets occurring for instance in the vector-boson fusion production of a Higgs boson (see Sec. 4.1.2).

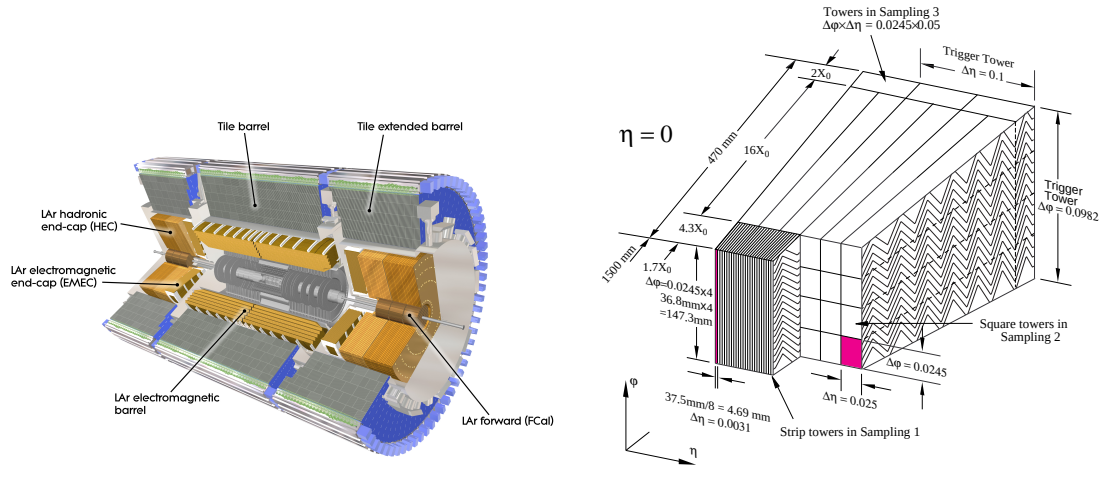

(a) (b)

Figure 3.5: (a) Cut-away view of the ATLAS calorimeter system. (b) Section of the ECal barrel showing the three layers and the granularity of cells or strips [23].

Muon Spectrometer

The outermost part of the ATLAS detector is the **muon spectrometer**. It was designed for precision momentum and position measurements of muons, as all other visible particles should have lost their complete energy by showering in the calorimeters before [23, 32]. Due to their large mass, muons lose their energy primarily by ionisation and leave only a small fraction of their energy in the inner parts of the detector.

A plan view of the MS is shown in Fig. 3.6. The muon spectrometer is interspersed with eight superconducting air-core toroid magnets with a magnetic field strength of 4 Tesla. They cause a deflection of the muon trajectories dependent on their charge and momentum, which provides an independent precise momentum measurement that can be combined with the inner detector measurement. In the MS a muon traverses either three chambers in the barrel, which are arranged in cylindrical shells around the beam axis, or four wheels perpendicular to the beam axis in the end-caps. The total coverage of the MS in pseudorapidity is $|\eta| < 2.7$.

In the central region the particle trajectories are detected with the help of **monitored drift tubes** (MTDs), while at large pseudorapidities ($|\eta| > 2$) **cathode strip chambers** (CSCs) are used. The latter are multiwire proportional chambers with strip cathodes which can handle higher counting rates [29]. Additional chambers provide measurements for the trigger system (Sec. 3.3): In the barrel this is done by **resistive plate chambers** (RPCs), which consist of two plates with a gas mixture in between. They provide very fast detection of muon tracks. In the end-caps **thin gap chambers** (TGCs) are used, a special type of multiwire proportional chambers, which in addition to the high rate capacity also have a very short response time.

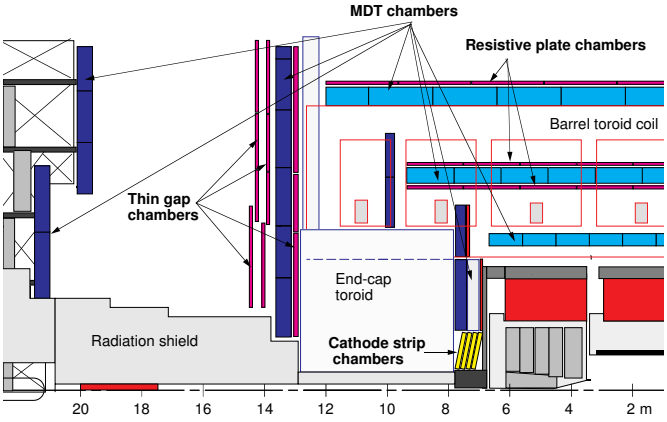

Figure 3.6: Quarter section of the ATLAS muon spectrometer [33].

Energy and momentum resolution

The **energy resolution** in the calorimeters is parametrised as the quadratic sum of different components in the following way [34]:

$$\frac{\sigma_E}{E} = \frac{a}{\sqrt{E}} \oplus \frac{b}{E} \oplus c \tag{3.1}$$

The first (*sampling*) term with coefficient a accounts for statistical fluctuations of the number of particles produced in a shower. The second (*noise*) term with coefficient b includes effects due to electronic noise and pile-up. The third (*constant*) term with coefficient c accounts for inhomogeneities of the energy measurement due to differences between cells and the material distribution in the detector.

The intrinsic **resolution of the transverse momentum** inside a magnetic field is given by [29]:

$$\frac{\sigma_{p_\mathrm{T}}}{p_\mathrm{T}} = \sqrt{\frac{720}{N+4}} \frac{\sigma_x p_\mathrm{T}}{0.3BL^2} \tag{3.2}$$

In this equation σ_x denotes the error of a single measurement point, N the number of measurement points, B the magnetic field strength and L the length of the track. The resolution in the tracking detector is affected by multiple scattering (MS) [29] of the traversing particles. The transverse momentum resolution is degraded by:

$$\left.\frac{\sigma_{p_\mathrm{T}}}{p_\mathrm{T}}\right|_{\mathrm{MS}} = 0.045 \frac{1}{\beta} \frac{1}{B\sqrt{LX_0}} \tag{3.3}$$

Here X_0 denotes the radiation length of the material and β the relative particle velocity. This term is thus dominant at low momenta. An overview of the resolution of the ATLAS detector components is given in Tab. 3.2.

Detector system	Energy/momentum resolution
Inner detector	$\sigma_{p_\mathrm{T}}/p_\mathrm{T} \sim 0.05\% p_\mathrm{T} \oplus 1\%$
Electromagnetic calorimeter	$\sigma_E/E \sim 10\%/\sqrt{E} \oplus 0.7\%$
Hadronic calorimeter	$\sigma_E/E \sim 50\%/\sqrt{E} \oplus 3\%$
Muon spectrometer	$\sigma_{p_\mathrm{T}}/p_\mathrm{T} \sim 2\%$ (at 50 GeV), $\sim 10\%$ (at 1 TeV)

Table 3.2: Approximate energy and momentum resolutions of the ATLAS detector components. The units of E and p_T are in GeV [23].

3.3 The ATLAS Trigger System

The cross section for the production of particles that are potentially interesting for the physics program of ATLAS is relatively small. Therefore, they are only produced in a small fraction of the proton collisions. In addition, the collision event rate delivered to ATLAS is far too large to be handled by any available storage system. Consequently, a trigger system is used to filter the events by instantly applying selection criteria to the recorded collisions in order to decide if an event is stored or discarded. At the ATLAS detector this procedure is performed in three levels where each level refines the selection criteria compared to the previous level by using more detector information [23, 35].

The level-1 (L1) trigger needs to make fast decisions in a time less than 2.5 μs. Therefore, it applies simple algorithms on reduced granularity information from the calorimeters and muon chambers to search for muons, electron/photon clusters, hadronically decaying τ and jet candidates. The energy of the particles is determined from the sum of energy depositions within so called *trigger towers* that stretch longitudinally over the calorimeters with a size 0.1×0.1 in $\Delta\eta \times \Delta\phi$. A hadronically decaying τ candidate is for example defined as a square of 2×2 towers and its energy summed within these towers in ECal and HCal. Also, its isolation is quantified based on the energy sum between 2×2 and 4×4 towers around the τ candidate [36].

In addition, the L1 trigger defines regions of interest (RoI) of the geometrical η and ϕ position of these detected particles. A central trigger processor combines the information from calorimeters and muon chambers and makes the final decision on whether the event is kept or deleted. In the former case the trigger acceptance signal is transferred to the higher trigger levels together with the regions of interest information.

The level-2 (L2) trigger uses the RoIs from L1 as seeds to investigate the events further and make more sophisticated decisions. It uses the full detector granularity including the track information from the inner detector. But as it only evaluates detector information locally in the RoIs and applies sequentially processed algorithms and selection criteria, it can still take the trigger decision very fast, within about 40 ms.

The subsequent Event Filter (EF) trigger uses the full detector information and applies a improved event reconstruction. Therefore it achieves the highest background rejection. Its decision time is in the order of four seconds. For instance in the case of hadronically decaying τ leptons calibration and reconstruction algorithms are applied which are very similar to the final *offline* reconstruction (Sec. 3.4) [36].

If an event is finally accepted after the three trigger steps, it is passed to the final data storage. The full trigger system manages to reduce the initial collision event rate of 40 MHz (in the design setup) to 200 Hz storable data.

In the initial phase of the ATLAS data taking the luminosity was relatively low, allowing for very loose trigger selection criteria. With increasing luminosity the filter conditions, such as p_{T} thresholds, had to be tightened constantly on all three levels in order to maintain the trigger rate for a storage of data[3].

For hadronically decaying τ leptons this causes the following problem: They can not be well distinguished from the background of quark/gluon jets, in contrast to electron or muons (Sec. 3.4). Substantially higher p_{T} thresholds must therefore be applied in the trigger selection already at L1 and L2 to be able to maintain the required trigger rates.

Figure 3.7 shows the trigger *response function*, i.e. the trigger efficiency as a function of the offline reconstructed transverse momentum of the investigated particle, for all three levels of a muon and a τ trigger used in 2012 data. Typically, the trigger efficiency rises around the momentum threshold (*turn-on curve*) until it reaches a plateau at higher momenta. Due to the reduced granularity a lower energy resolution at L1 and L2 can be observed, resulting in a less steep turn-on curve. While in the case of a muon trigger the EF level is not affected by this, the τ trigger also shows a slow turn-on at EF level.

These tight trigger conditions also limit the kinematic range in which physics studies with τ decays can be performed. However, the τ selection can be combined with other objects in the trigger filter condition, such as $E_{\mathrm{T}}^{\mathrm{miss}}$ or light leptons. This allows for lower p_{T} thresholds on both objects.

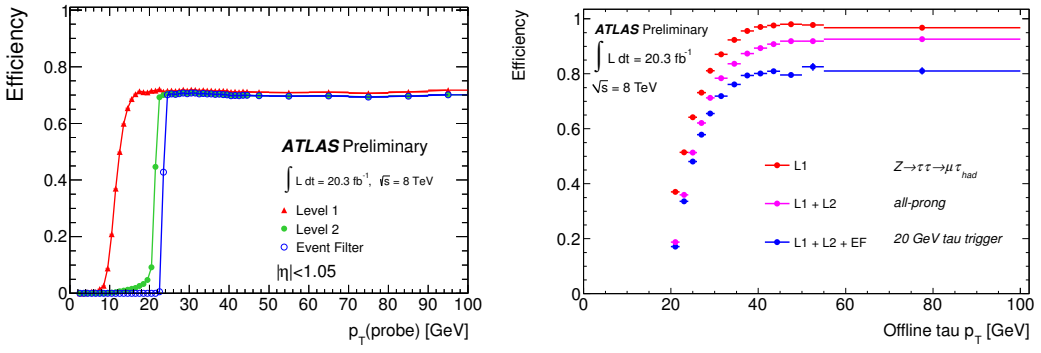

(a) (b)

Figure 3.7: Trigger response after each trigger level of two different triggers used in 2012 data. (a) Efficiency of a muon trigger combination ($p_{\mathrm{T}} > 24$ GeV or $p_{\mathrm{T}} > 36$ GeV) as a function of the offline reconstructed muon momentum within $|\eta| < 1.05$. (b) Efficiency of a hadronically decaying τ trigger ($p_{\mathrm{T}} > 20$ GeV) as a function of the offline reconstructed τ p_{T} [37].

[3] If too many events are selected by too loose filter criteria, only a fraction of them is stored, e.g. every third event. The factor by which the events are rejected is called *pre-scale*.

3.4 Event Reconstruction

For an analysis of the collision events recorded by ATLAS, the information of the different sub-detectors, such as the energy depositions in the calorimeters and the hits in the tracking detectors, are combined to form *physics objects* that represent the different particles resulting from the pp collision.

For this purpose the data is subjected to different reconstruction algorithms. Additional identification algorithms are applied to better define the objects and separate them from one another, for instance an electron and a pion, which both leave a track in the inner detector and a matching calorimeter shower. All algorithms relevant for the final state particles investigated in this thesis are reviewed briefly in the following. Since the algorithms are under constant development, only a snapshot of their implementation at the end of the LHC data taking period in 2012 is given. Only important differences with respect to previous states used for the analysis of the earlier data are mentioned.

The reconstruction of τ leptons and missing transverse energy, which play a major role in both the $H \to \tau_{\text{lep}}\tau_{\text{had}}$ search and $W \to \tau\nu_\tau$ cross section measurement, is summarised here and covered more extensively in Chap. 5.

Track Fitting

As a first step the hits (space points/drift circles) of the particle trajectories recorded in the ID and the MS are combined to particle tracks. The measured hits are therefore extrapolated from inside to outside starting from three measured space points in the innermost pixel and SCT layers [38]. A fit connects the innermost hits to a track segment, extends it to the outer layers by adding additional hits subsequently and determines the parameters of the track: the momentum p and charge q of the track (q/p), its angular direction in ϕ and θ evaluated at the point of closest approach of the track to the detector origin and the so called impact points d_0 and z_0 which denote the distance of this point from the detector origin in transverse and longitudinal direction.

Quality criteria are applied to the tracks, e.g. the number of hits, to reduce fake tracks from pile-up efficiently [39]. In a second step, primary and secondary vertices are reconstructed from the tracks, by associating different tracks to a common vertex via a fit.

Similarly, the hits in the muon spectrometer are fitted to form tracks either individually or combined with the ID hit measurements.

Clustering

To quantify and locate the energy depositions of various particles in the calorimeters, a scan for clusterings of energy depositions, resulting from an electromagnetic or hadronic shower, is performed. Depending on the type of particle two different algorithms are applied in ATLAS to reconstruct these energy clusters [40].

The *sliding window algorithm* reconstructs clusters from electrons and photons in the ECal. It uses a rectangular window with a fixed size and sums the energy depositions of the contained cells to find local energy maxima and to define the cluster. This clustering method allows for a very precise energy calibration.

In contrast, the *topological clustering* reconstructs clusters (*topoclusters*) with a variable size. It starts from a single cell with a significant energy deposition and iteratively adds neighbouring cells (in all three dimensions) to the cluster, provided that the deposited energy is above the expected noise threshold. In ATLAS this algorithm is used for hadronically decaying τ leptons, jets and missing transverse energy,

since it provides efficient suppression of noise, including pile-up, for clusters with a large number of cells.

All reconstructed clusters are calibrated to provide a precise energy measurement of the particle. The calibration procedure is optimised for each particle individually.

Electron

Electrons leave a track in the inner detector and an energy deposition in the electromagnetic calorimeter. The calorimeter cluster is reconstructed with the sliding window algorithm: The ECal is scanned for energy depositions above 2.5 GeV summed within a $\eta \times \phi = 0.025 \times 0.025$ window (corresponding to the size 3×5 cells in the second ECal layer, compare Fig. 3.5b [41]. If a cluster is found, the algorithm searches for a matching track in the inner detector. This track is required to have $p_{\mathrm{T}} > 0.5$ GeV and its extrapolated impact point in the second layer of the calorimeter must lie within $|\Delta\eta| < 0.05$ and $|\Delta\phi| < 0.05$ ($|\Delta\phi| < 0.1$ in the bending direction of the electron) of the cluster barycentre. If no track can be associated to the cluster, the object is considered as unconverted photon.

In 2012 data, the track reconstruction for electrons is improved by an incorporation of their high bremsstrahlung emission probability in the fit, which increases the reconstruction efficiency and results in a better track parameter measurement [42]. For this purpose, the cluster extension is redefined in each layer individually to match its expected lateral and longitudinal shape more precisely. The reconstruction efficiency for electrons with $p_{\mathrm{T}} > 15$ GeV is $\sim 97\%$, while only about 9% of the main source of background (hadronic jets) are reconstructed as electrons [41].

An energy calibration is applied to the reconstructed clusters to adjust the energy to its true value according to Monte Carlo simulations, including a correction for energy depositions and losses in front of the calorimeter, and around and behind the cluster window [43].

To further separate signal electrons from background (hadronic jets, photon conversions and non-isolated electrons within jets produced from hadron decays), further quality criteria are applied to the reconstructed electron candidates based on the expected longitudinal and lateral shower shapes and track properties. They are combined to a selection with three different working points, having an increasing background rejection and decreasing signal efficiency [41]:

Loose The selection criteria are based on the shower shape in the first and second layer of the ECal. In addition, information on the (small) leakage of the shower into the hadronic calorimeter is used. Quality criteria for the track and track-cluster matching further increase the background rejection.

Medium Tighter cuts on the *loose* identification criteria are applied and criteria based on the shower in the third ECal layer are added. Furthermore, a hit in the innermost pixel layer to reject photon conversions is required and a high amount of measured transition radiation.

Tight Besides stricter requirements on the *medium* selection, photon conversions matched to the electron are excluded. Additionally, it is required that the ratio of cluster energy to track momentum is around one as expected for genuine electrons.

These criteria vary slightly for each data taking period. In general a focus on more pile-up resistant variables for the selection criteria was introduced for the 2011 and 2012 data taking periods to prevent a degradation of the efficiency under high-luminosity conditions [44, 45]. The signal identification efficiency of the *tight* working point in 2012 data is $\sim 78\%$ for energies within 20–50 GeV, with a background rejection by a factor of 200 [41].

Muon

Muons leave the unique signature of a track in the ID and MS and, as they are minimum ionising particles, a small energy deposit in the calorimeters. Several algorithms exist in ATLAS to reconstruct muons in the full pseudorapidity range and energy spectrum [46, 47]. Depending on the combination of the information from the different sub-detector components four muon types are defined during reconstruction:

Stand Alone These muons are only reconstructed from the muon trajectories in the MS (from at least two hits). The muon track is extrapolated to the point of closest approach to the beam axis and the track parameters are determined taking into account the energy loss in the calorimeters. Essentially, they enlarge the acceptance for muon candidates outside the ID range within $2.5 < |\eta| < 2.7$.

Combined The muon track is reconstructed independently in the muon spectrometer and in the ID. The final estimation of the track parameters is then obtained from a combination of the two measurements. This is the most efficient muon reconstruction type, providing a good suppression of muons resulting from kaon or pion decays in the detector and the best track parameter resolution.

Segment-tagged The ID track is extrapolated to the MS and combined with track segments measured in at least one of the muon chambers. This helps to increase the acceptance for low p_{T} muons or muons in regions with a low MS acceptance.

Calorimeter tagged A reconstructed ID track is extrapolated to the calorimeter and matched to a cluster consistent with the energy deposition of a minimal ionising particle. Regions where no MS measurement is possible, e.g. at $\eta \approx 0$, are covered with this algorithm.

To ensure that the track is well-reconstructed quality criteria on the number of hits in different ID sub-detectors are applied to the ID tracks that are used for muon reconstruction.

Two different algorithm strategies exist in ATLAS, which are used to reconstruct these types of muons using different methods. The method chosen for the muon definition in this thesis is the *Staco* algorithm. In the case of combined muons it merges the ID and MS track measurement by calculating their weighted sum based on the covariance matrices of both. The reconstruction efficiency for muons with $p_{\mathrm{T}} > 10$ GeV taking into account all types is uniformly about 99% in the whole detector region.

Jet

A jet resulting from a quark or gluon in the pp collision (see Sec. 2.2) is composed of a variety of hadrons (protons, neutrons, pions), which produce a large shower with electromagnetic and hadronic components in the calorimeters. In addition, its charged components leave numerous tracks in the ID.

The reconstruction therefore starts in the calorimeters, where clusters are formed via the topological clustering algorithm. The topological clusters are the input to a dedicated jet reconstruction algorithm deciding which clusters belong to the jet and forming the final jet object.

The standard algorithm used in ATLAS is the *anti-kt* algorithm [48]. It sequentially merges the clusters depending on their relative distance from one another ΔR (Sec. 3.2) and their relative transverse momentum. A distance measure is defined for each pair of clusters i and j as:

$$d_{ij} = \min\left(\frac{1}{k^2_{\mathrm{T},i}}, \frac{1}{k^2_{\mathrm{T},j}}\right)\frac{\Delta R^2_{ij}}{R^2} \tag{3.4}$$

Here ΔR_{ij} is the distance between the two clusters, $k_{T,i}$ the transverse momentum of cluster i and R the so called distance parameter. Moreover the distance measure $d_{iB} = 1/k^2_{T,i}$ is defined for each particle. The clustering proceeds by finding the minima of all possible d_{ij} and d_{iB} values. If a d_{ij} is identified as minimum the two clusters i and j are merged by adding their four-momenta. If d_{iB} is found as a minimum the merging is stopped and the final jet candidate is defined. The distance parameter R indicates therefore the resolution at which two jets can be resolved from one another. For the jet definition used in this thesis a parameter of $R = 0.4$ is chosen. This algorithm has the advantage, that the jet is geometrically well defined and its boundaries are robust against soft radiation since the soft clusters are merged first with the hard ones.

The initial topoclusters are calibrated based on the local cluster weighting calibration scheme (LCW). It classifies clusters as hadronic or electromagnetic and corrects them individually taking into account their different responses and also energy depositions outside the cluster. The final jet candidates are subjected to a further dedicated calibration to recover the true energy scale of the particles contained. Energy and pseudorapidity are corrected based on response functions measured by simulation [49, 50]. The increasing luminosity in 2011 and 2012 demanded the inclusion of elaborate corrections of the jet energy for pile-up effects, basically treating pile-up as uniform diffuse background within the jet area which adds energy to the signal [51].

Additional reduction of pile-up jets in an investigated event can be achieved by using information from the tracks associated to the jet[4]. The so-called jet vertex fraction, determines the fraction of the jet's tracks resulting from the primary vertex (PV) of the hard scattering:

$$\mathrm{JVF} = \frac{\sum_{\text{jet tracks resulting from PV}} p_{\mathrm{T}}^{\mathrm{trk}}}{\sum_{\text{all jet tracks}} p_{\mathrm{T}}^{\mathrm{trk}}} \tag{3.5}$$

The sum includes tracks above a p_{T} threshold of 500 MeV. Therefore, jets with a small JVF are more likely to be pile-up jets not resulting from a parton of the main hard interaction and can be excluded from the analysis.

b-tagging

b-hadrons that consist of *b* quarks are relatively long-lived and thus decay at a secondary vertex dislocated from their origin in the detector. Different *b*-tagging algorithms exist in ATLAS to identify these *b*-hadron decays and to separate these *b*-quark jets from jets originating from light or *c* quarks: The *IP3D* algorithm focusses on the impact parameter significance (d_0/σ_{d_0}, z_0/σ_{z_0}) of tracks within jets, the *SV1* algorithm reconstructs secondary vertices within the jet, and the more complex *JetFitter* algorithm aims to reconstruct the topology of the *b*- and subsequent *c*-hadron decays [52].

The information of these algorithms is combined in an artificial neural network by the *MV1* algorithm to create a more powerful discriminant. Its output is a tagging weight, indicating the probability that a *b* or a light-flavour jet is found. Different efficiency points are defined. At an efficiency of 70% for identifying a *b*-jet with p_{T} >20 GeV correctly, the background of *c* jets is reduced by a factor of 5, and the light-flavoured jet background is rejected by a factor of 150 [53].

[4] This information can therefore only be accessed within the acceptance of the ID, thus within $|\eta| < 2.5$.

τ leptons

τ leptons decay in the beam-pipe, thus only their decay products are detected. For the τ decay to leptons the electron/muon reconstruction methods are used. The majority of τ leptons ($\sim 65\%$) decay to hadrons, which form collimated jets in the detector. Therefore, the reconstruction of these hadronic τ decay products starts from a reconstructed jet (see above). Characteristically they form narrow isolated showers in the calorimeter, have a low track multiplicity and a remote τ decay vertex. These properties form the basis for further reconstruction, identification and calibration algorithms, which are applied to define the final τ objects and distinguish them from the background of quark/gluon jets or leptons. These algorithms are explained in detail in Chap. 5.

Missing Transverse Energy

Neutrinos and other undetectable particles are indirectly measured through the missing transverse energy $E_{\mathrm{T}}^{\mathrm{miss}}$. Under the assumption that the total momentum in the plane transverse to the beam-pipe is zero in the pp collision, the total missing momentum is determined by the vectorial sum of all transverse momenta measured in the detector. Therefore, $E_{\mathrm{T}}^{\mathrm{miss}}$ is reconstructed from the energy depositions in the calorimeters and the muon spectrometer. A dedicated calibration is applied to ensure an accurate measurement. In addition, pile-up corrections are crucial to maintain the $E_{\mathrm{T}}^{\mathrm{miss}}$ resolution at high luminosity. The details of the $E_{\mathrm{T}}^{\mathrm{miss}}$ reconstruction are explained in detail in Chap. 5.

3.5 Simulation of Events

To investigate and interpret data from LHC pp collisions, it is important to compare data with simulations of individual physics processes. They are provided by *Monte Carlo* generators, which simulate these processes based on the theoretical calculation and modelling methods discussed in Sec. 2.2.

A variety of generators exists, some provide a fully generated proton collision, while others focus on a certain part of the scattering process. Commonly used are the general-purpose event generators Pythia [54, 55] and Herwig [56]. They implement leading-order matrix element calculation of the hard interaction together with the modelling of the various additional components of the collision event [57, 58].

Pythia uses the parton shower evolution based on the change of parton virtuality and the string model for hadronisation, while Herwig models the parton shower with the angular emission as evolution parameter and the cluster model for hadronisation (see Sec. 2.2 for details). Both can also simulate underlying event processes, however, Herwig is usually interfaced with the separate tool Jimmy [59] used for the underlying event modelling.

These generators are well suited to simulate the direct emission of vector bosons, e.g. in the processes investigated for the measurement of the $W \to \tau\nu_\tau$ cross section in Chap. 6. On the other hand, they fail to model processes with higher jet multiplicities accurately, since the parton shower does not model jet momentum spectra precisely enough [12].

For such cases other generators exist, which perform the exact matrix element calculations for several emitted hard partons at tree-level (not including virtual corrections, see Sec. 2.2). An example is Alpgen [60] which calculates up to five additional emitted hard partons. This exact calculation is then interfaced with Herwig and Pythia, which handle the additional modelling of parton shower, hadronisation and underlying event. Different dedicated methods are applied for a proper matching of parton shower and matrix element calculations [14, 61]. In the search for a $H \to \tau_{\mathrm{lep}}\tau_{\mathrm{had}}$ decay (Chap. 7) these

types of generators are used for the simulation of W and Z bosons in association with jets, since here final states with high jet multiplicities are investigated.

More complex processes like top quark pair production (Fig. 7.7a) or Higgs production mechanisms like gluon fusion and vector-boson fusion (Figs. 4.4a and 4.4b) cannot be simulated accurately enough at leading order or higher-order tree-level [57]. Generators providing full NLO calculations including virtual corrections are therefore used instead to simulate these processes, such as POWHEG [62] or MC@NLO [63], interfaced with PYTHIA or HERWIG, respectively.

Separate tools are interfaced with these generators, TAUOLA [64] and PHOTOS [65], which handle the decay of τ leptons and emission of photons, respectively. TAUOLA is in particular important to correctly incorporate polarisation of the decaying resonances in the τ lepton decay.

Different sets of PDFs that can be interfaced with these generators exist, each using a different parametrisation of these functions. Common sets used for simulated samples at the LHC are e.g. MSTW [17], CTEQ [66] or CT10 [67].

In addition to the kinematics of the main pp collision, pile-up effects resulting from the bunch structure of the proton beams in the LHC ring (see Sec. 3.1) must be accounted for in the simulation. These additional interactions of other protons mainly result in a pair of jets with low transverse momentum, often referred to as *minimum-bias*[5]. For a simulation of in-time pile-up and out-of-time pile-up effects these minimum bias events are simulated or taken from data and a certain amount of them is overlaid with the hard interaction following a Poisson-distribution [58].

Moreover, the following effects are also taken into account in the event simulation: The radiation background of neutrons and photons in the ATLAS underground cavern, interactions of protons with residual gas atoms in the beam-pipe (beam-gas) and interactions of protons with upstream material like collimators (beam-halo) [68].

All generators produce basically a set of four-vectors of the particles resulting from a certain physics process after hadronisation. These are then passed through a full geometrical simulation of the detector, provided by the program GEANT4 [69]. It simulates the interaction of the particles with the detector material, their propagation and energy losses in the detector and the signals created in the detector subsystems, such as hits and energy depositions [68].

After a *digitisation* step, where the hits and energy depositions are transformed to the response of the different detector components, the output of this simulation can be subjected to the same reconstruction algorithms as real data (Sec. 3.4) to define the final physics objects.

[5] Minimum bias in general summarises all events that are collected in the detector with minimum transverse momentum requirements to provide a selection of events that is as inclusive as possible. They are dominated by these soft dijet events.

CHAPTER 4

Concepts of Higgs and W Boson Analyses

The investigation of the $W \to \tau\nu_\tau$ decay and the search for a Higgs boson decaying to a pair of τ leptons with the ATLAS detector require a detailed investigation of all signal and background processes and dedicated analysis methods.

The characteristics and challenges of the production and decay of Higgs and W bosons at the LHC are explained in Sec. 4.1, focussing in particular on the processes that are investigated in the framework of this thesis. Moreover, in order to put the measurements of this thesis into context, previous measurements of Higgs and W boson processes are summarised in this section, in particular the discovery of the Higgs boson at the LHC.

In Sec. 4.2 the methods used for a statistical analysis of data in this thesis are discussed and compared to each other. The methodology to determine the cross section of the $W \to \tau\nu_\tau$ decay from the measurement parameters is explained. In addition, the profile likelihood fit is described that is used to perform statistical tests on data in order to quantify how compatible it is with a $H \to \tau\tau$ signal.

Finally, Sec. 4.3 describes a data-based method to model important background processes in both analyses: The embedding technique. It is used to model the dominant $Z \to \tau\tau$ background in the $H \to \tau\tau$ search and to validate the modelling of W and Z processes in the $W \to \tau\nu_\tau$ cross section measurement.

4.1 Higgs and W Physics at the LHC

Figure 4.1 gives an overview of the production cross sections of different physics processes at the LHC and other proton-(anti)proton collisions at different energies. The W and Higgs boson production cross sections are by orders of magnitude smaller than the total proton-proton cross section. The latter is dominated by minimum bias events and also purely hadronic processes, where high-p_{T} jets resulting from quark/gluon production are produced[1]. The Higgs boson production cross section is in addition much smaller than the ones of other Standard Model processes, like W, Z and top quark production. This shows clearly the challenges for an the analysis of these physics processes:

- A large amount of data is needed to select a statistically significant amount of the collision events of interest.

[1] These hadronic processes will be referred to as *QCD* or *multijet* background throughout this thesis.

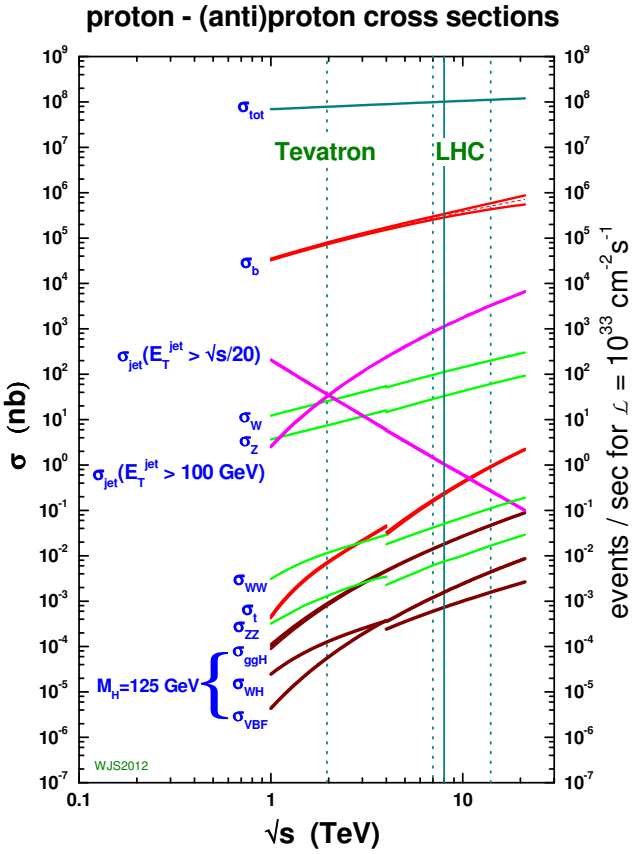

Figure 4.1: Cross sections and event rates of different Standard Model particles produced at proton-(anti)proton collisions as a function of the centre-of-mass energy $\sqrt{s}$ [70].

- The huge background must be filtered out to a large extent (by trigger and offline selection criteria) and be well understood.

This also dictates the order in which the measurements are performed at the LHC: In the early data taking phase, large enough samples of W bosons and other electroweak processes can be collected to perform precise measurements. These measurements are at the same time a preparation for the Higgs search, where electroweak processes also are large sources of background. A significant signal of a Higgs boson can only be measured in a much larger data sample towards the end of the Run 1 period of the LHC (Tab. 3.1).

An overview of the W and Higgs production and decay processes is given in the following. The relevance of different background processes for the studied decays will be discussed in detail in the respective analysis chapters (Chaps. 6 and 7).

4.1.1 W Production and Decay

At the LHC, W bosons are produced at leading order through a quark-antiquark pair. The corresponding Feynman graph can be seen in Fig. 4.2a. The processes $u\bar{d} \rightarrow W^+$ and $d\bar{u} \rightarrow W^-$ dominate at leading order, where the quark is a valence quark of one proton and the anti-quark is a sea quark of the other proton (compare Sec. 2.2). Based on this process alone, it would be expected that in proton-proton colliders positively charged W bosons occur roughly twice as much as negatively charged ones, due to

the valence quark distribution in the protons. This is in contrast to proton-antiproton colliders, where the anti-quark can also be a valence quark.

However, as can also be seen in Figs. 4.2b–4.2d, also contributions from pure sea-quark interactions (e.g. $u\bar{d}$, $s\bar{c}$) and processes of higher order like $q(\bar{q})g$ interactions need to be taken into account for the cross section calculation [71, 72]. A precise knowledge of the parton density functions (Sec. 2.2.2) is thus crucial for an accurate cross section calculation.

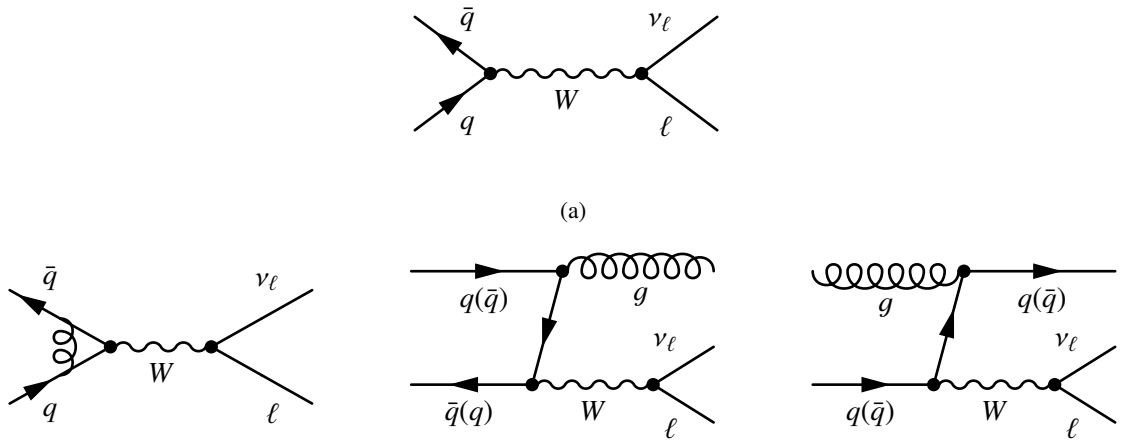

Figure 4.2: Feynman diagrams in (a) leading order and (b, c, d) next-to-leading-order contributing to the W production with subsequent decay to a lepton and neutrino.

The W boson either decays to quarks with a branching ratio of 0.674 ± 0.003 or a charged lepton (e, μ, τ) and neutrino with an average branching ratio of 0.109 ± 0.001 [2]. Due to the large QCD background, only the leptonic decay modes of W bosons are exploited for a cross section measurement.

The W production cross section times leptonic branching ratio as a function of the centre-of-mass energy is shown in Fig. 4.3 for pp and $p\bar{p}$ collisions. Shown are also the experimental measurements of the cross section with subsequent decay to electrons and muons performed at different energies, including the results from ATLAS and CMS with the first data at $\sqrt{s} = 7$ TeV [73, 74].

Previous measurements of the W production cross section at hadron colliders with subsequent decay $W \to \tau\nu_\tau$ were reported at the UA1 experiment (at energies of $\sqrt{s} = 546$ GeV and $\sqrt{s} = 630$ GeV) [75] and later at CDF and D0 ($\sqrt{s} = 1.8$ TeV) [76–78]. The measurement of the $W \to \tau\nu_\tau$ cross section presented in this thesis is thus the first result of this channel obtained at the LHC and complements the measurements in the other leptonic decay channels.

4.1.2 Higgs Production and Decay

As explained in Sec. 2.1.2, the mass of the Higgs boson is a free parameter in the Standard Model. Together with the particle masses it determines the strength of the couplings. Therefore, the Higgs boson production cross section and decay branching ratios can be determined as a function of its mass m_H. This is a key information for collider experiments to determine which productions mechanisms and decay channels can be searched for and which are the most important channels to focus on with the highest discovery potential. Four main types of Higgs boson production mechanisms exist [4]: *gluon fusion* (ggF), *vector-boson fusion* (VBF), *associated production with a vector boson* (VH) and

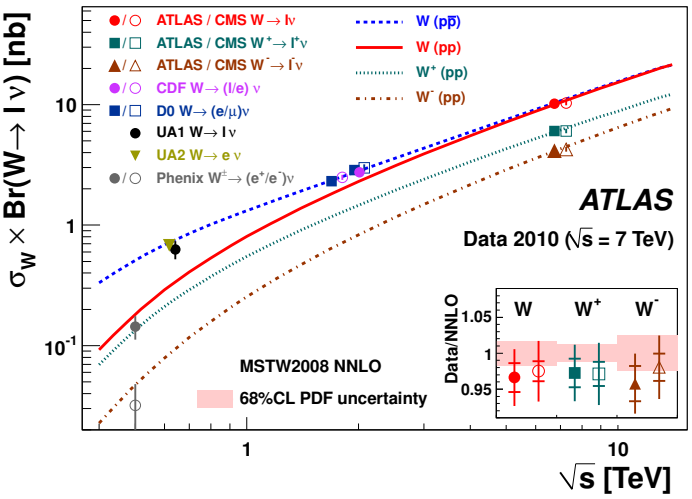

Figure 4.3: Theoretical NNLO prediction of the cross section times branching ratio of $W \to \ell\nu$ ($\ell = \mu, e$) for pp and $p\bar{p}$ colliders as a function of the centre-of-mass energy, split also into the different charges W^+ and W^- for pp colliders. The measurement results at different experiments including ATLAS and CMS are also shown. The small inset shows the results at for the ATLAS and CMS collaborations as ratio of measurement to NNLO prediction and its uncertainty, where the inner error bars denote all but the luminosity uncertainty and the outer error bars the total uncertainty [73].

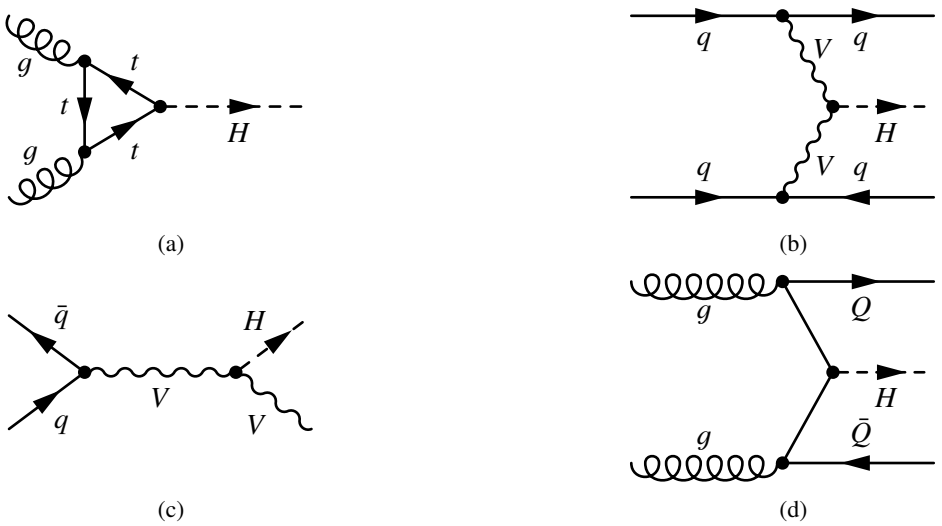

Figure 4.4: Feynman graphs of the main Higgs boson production processes at leading order: (a) gluon-gluon fusion, (b) vector-boson fusion, (c) associated production with a vector boson and (d) associated production with a heavy quark pair.

associated production with a heavy quark pair (ttH). The Feynman graphs of the production processes at leading order are shown in Fig. 4.4.

At the LHC the dominant production process is gluon fusion $gg \to H$ over the full investigated mass range (100–600 GeV). The main contributions to the loop are coming from top and bottom quarks, since the coupling of the Higgs boson is proportional to the particle masses (Eqs. 2.18 and 2.21). The production process with the second largest cross section is the vector-boson fusion ($qq \to qq + H$). Its production rate is one order of magnitude smaller than the one of ggF, but it features a clear signature through the additional quarks in the final state, which is useful to distinguish it from the large QCD background (Fig. 4.1). The associated production with a vector boson ($q\bar{q} \to VH$, with $V = W, Z$) has the third largest production cross section and also features additional particles from W, Z decays in the final state. The smallest contribution to the Higgs production comes from the associated production with a heavy quark pair, dominantly a $t\bar{t}$ pair ($gg \to t\bar{t}$). Figure 4.5 shows the cross sections at $\sqrt{s} = 7$ TeV and $\sqrt{s} = 8$ TeV (centre-of-mass energies of the LHC data taking periods in 2011 and 2012, respectively) as a function of the Higgs mass.

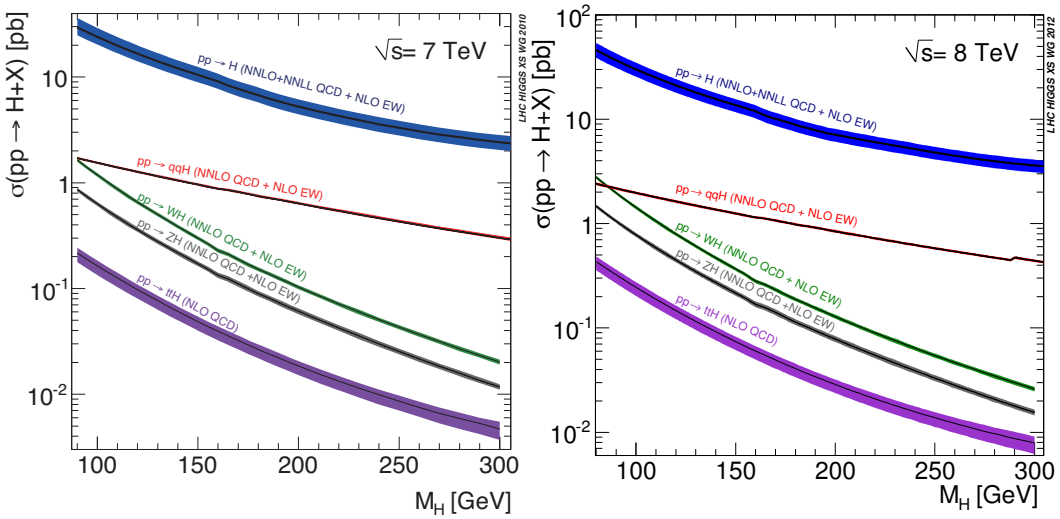

(a) (b)

Figure 4.5: Standard Model Higgs cross section at the LHC in total and split into the four main production processes as a function of the Higgs mass for a centre-of-mass energy of (a) $\sqrt{s} = 7$ TeV and (b) $\sqrt{s} = 8$ TeV [79].

Since the Higgs boson decays quickly after having been produced in a collision, it can only be detected by its decay products. Due to the proportionality of the Higgs boson coupling to the particle masses it decays predominantly to the heaviest particles that are allowed in the accessible phase space. As a consequence, the different final states are sensitive to different mass regions of m_H. Figure 4.6a shows the branching ratios for the dominant decay processes as a function of m_H.

Roughly above the threshold $m_H > 2m_W$ ($V = W, Z$) the decays to pairs of these vector bosons are most dominant. The decay to W bosons has always the largest branching ratio since W^+ and W^- are two separate particles which contribute both to the decay, in contrast to the neutral Z boson[2]. At lower masses ($m_H < 130$ GeV) the branching ratios of the decays to $b\bar{b}$, $\tau\tau$, $c\bar{c}$, gg and $\gamma\gamma$ increase. Although the last two of those are massless particles and thus do not couple to the Higgs boson directly, they contribute with significant branching ratio through decays containing loops with heavy particles.

[2] The decay to a pair of top-quarks only plays a role at much higher Higgs masses ($m_H \geq m_T$) and is therefore not visible in this graph.

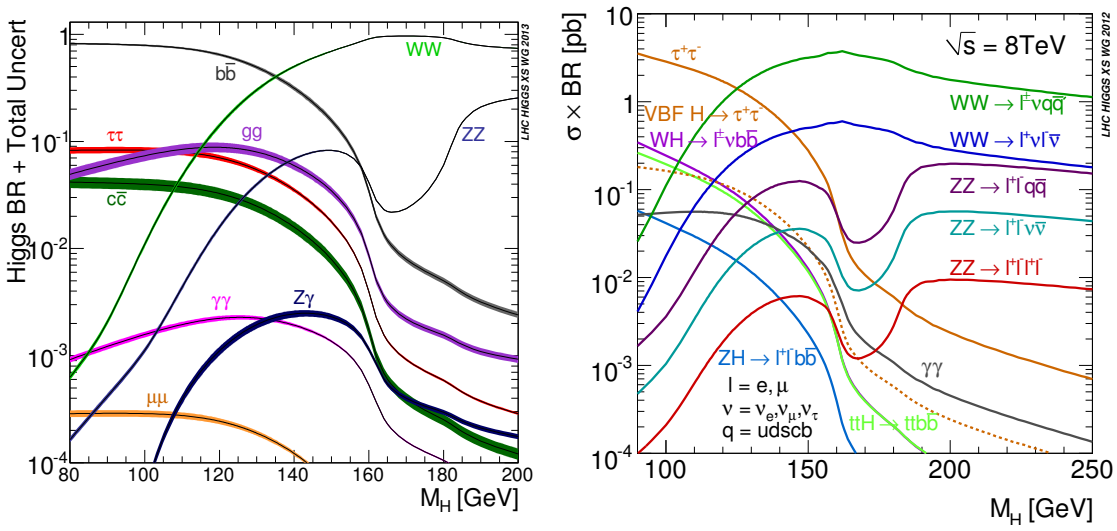

(a) (b)

Figure 4.6: (a) Branching ratio of the Standard Model Higgs boson as a function of the Higgs mass, (b) branching ratio times cross section at $\sqrt{s} = 8$ TeV [79].

To obtain an estimate of the experimental sensitivity for these decays processes, not only the production cross sections times branching ratio is decisive. In addition, it has to be taken into account how well particles resulting from the Higgs production and decay and their subsequent decay particles can be identified in the detector and distinguished from background. In the case of the LHC experiment, the hadronic activity at proton-proton collisions makes a detection of quark and gluon final states very difficult. gg and $c\bar{c}$ can hardly be separated from the large multi-jet background, neither can hadronic decay products of WW and ZZ pairs. The decay to $b\bar{b}$ can be investigated at the LHC due to its large branching ratio and b-tagging techniques to identify b-quark jets (Sec. 3.4). However, this is only possible in the production mode together with a leptonically decaying W or Z boson, where the lepton can be used in the trigger selection.

In contrast, the Higgs boson decay to leptons with the largest branching ratio, a pair of τ leptons or photons, can be much better distinguished from the multijet background. This allows also the investigation of production processes with a larger cross section: ggF and VBF. Figure 4.6b shows the product of Higgs production cross section and branching ratio, for all final states that can be well-enough separated from background at the LHC, as a function of m_H for $\sqrt{s} = 8$ TeV data (the distribution is very similar for data with $\sqrt{s} = 7$ TeV). It is clearly visible that of all identifiable event signatures at the LHC, the decay to a pair of τ leptons via ggF has by far the highest cross section times branching ratio at low masses ($m_H < 130$ GeV). Also the $H \to \tau\tau$ decay resulting from VBF production has a large contribution in this mass range. Consequently, this decay channel offers a high experimental sensitivity on a Higgs bosons with a low mass, which is why it is studied in this thesis.

In summary, the main search channels at the LHC are $H \to WW^{(*)}$ and $H \to ZZ^{(*)}$, completed at lower masses ($m_H < 150$ GeV) by $H \to \gamma\gamma$, $H \to b\bar{b}$ and $H \to \tau\tau$, in the identifiable production and final state modes.

A more detailed review of the characteristics of the production mechanisms and the decay channels of $H \to \tau\tau$ relevant for this thesis is presented in Sec. 7.2.

4.1.3 Discovery of the Higgs Boson at the LHC

First searches for a Standard Model Higgs boson were performed with the experiments at LEP and Tevatron. A direct upper limit on the Higgs mass at 95% CL could be established by the LEP experiments of $m_H > 114.4$ GeV [80]. The Tevatron experiments with a centre-of-mass energy of $\sqrt{s} = 1.96$ GeV were able to investigate a mass range of 90–200 GeV. In 2011 they achieved an exclusion of the region $156 < m_H < 177$ GeV at 95% CL [81].

Due to its high luminosity and large centre-of-mass energy compared all other previous experiments, first search results were obtained very fast with the LHC: Large m_H ranges were excluded, narrowing down the region where a Higgs boson could exist to a small window at low mass. Finally, in July 2012 a significant excess around a mass of 125 GeV could be observed in data by the ATLAS and CMS experiments, establishing the discovery of a new neutral boson decaying to bosons as predicted for a Standard Model Higgs boson [82, 83]. It was first discovered in the decay channels of $\gamma\gamma$, $ZZ \to 4\ell$ and $WW \to \ell\nu\ell\nu$ which all individually showed a consistent excess[3].

The combined observed significance found with ATLAS was 5.9σ at a mass of 125 GeV. Figures 4.7a and 4.7b show the excess observed in the spectrum of the invariant mass in the $H \to \gamma\gamma$ and the $H \to ZZ^{(*)} \to 4\ell$ channels. The observed and expected p_0 value as a function of the mass for the combination and the individual Higgs channels is shown in Fig. 4.7c [4]. CMS came to a similar observation of the new particle, the resulting p_0 distribution can be seen in Fig. 4.7d.

Afterwards, also the Tevatron experiments reported an excess between 120 and 135 GeV in their total recorded data with a largest significance of 3.3σ consistent with the discovery [84].

Subsequent analyses performed with the full LHC data of Run 1 collected until end of 2012 (Tab. 3.1) consolidated the discovery with an even more significant signal of the new particle [85, 86]. Although the discovered boson is very consistent in its coupling to boson pairs with a Standard Model Higgs boson, a complete conclusion on the nature of the discovered particle can only be drawn after more of its properties are proven in the experiment.

The next large achievement was the measurement of the spin and parity quantum numbers of the new boson by both experiments in summer 2013. This measurement provides evidence that the discovered boson has a spin of 0 and a positive parity, and is indeed consistent with the scalar Higgs boson predicted by the Standard Model [87, 88].

However, no significant excess in the fermionic decay channels $H \to bb$ and $H \to \tau\tau$ could be observed until that point. The analysis of these final states is more complex since the signature with b-jets or the combination of τ leptons and missing transverse energy (Chap. 5) are difficult to disentangle from QCD background and result in a poor mass resolution. In order to prove that the discovered Higgs boson also couples to fermions as predicted by the Standard Model, the observation of a decay to fermions is of crucial importance.

Due to the relatively high cross section times branching ratio (Fig. 4.6b) in the Higgs production processes that can be studied at the LHC, the $H \to \tau\tau$ channel offers the largest experimental sensitivity among the fermionic decays, therefore it is the topic of this thesis.

[3] The diphoton and $ZZ^{(*)} \to 4\ell$ decay channels have the highest discovery potential, since they have a very clean signature in the detector consisting of only leptons and photons, which can be well separated from hadronic background processes, and which leads to a very good resolution of the invariant mass.

[4] For an explanation of the statistical analysis of data in the context of a Higgs boson search see Sec. 4.2.2.

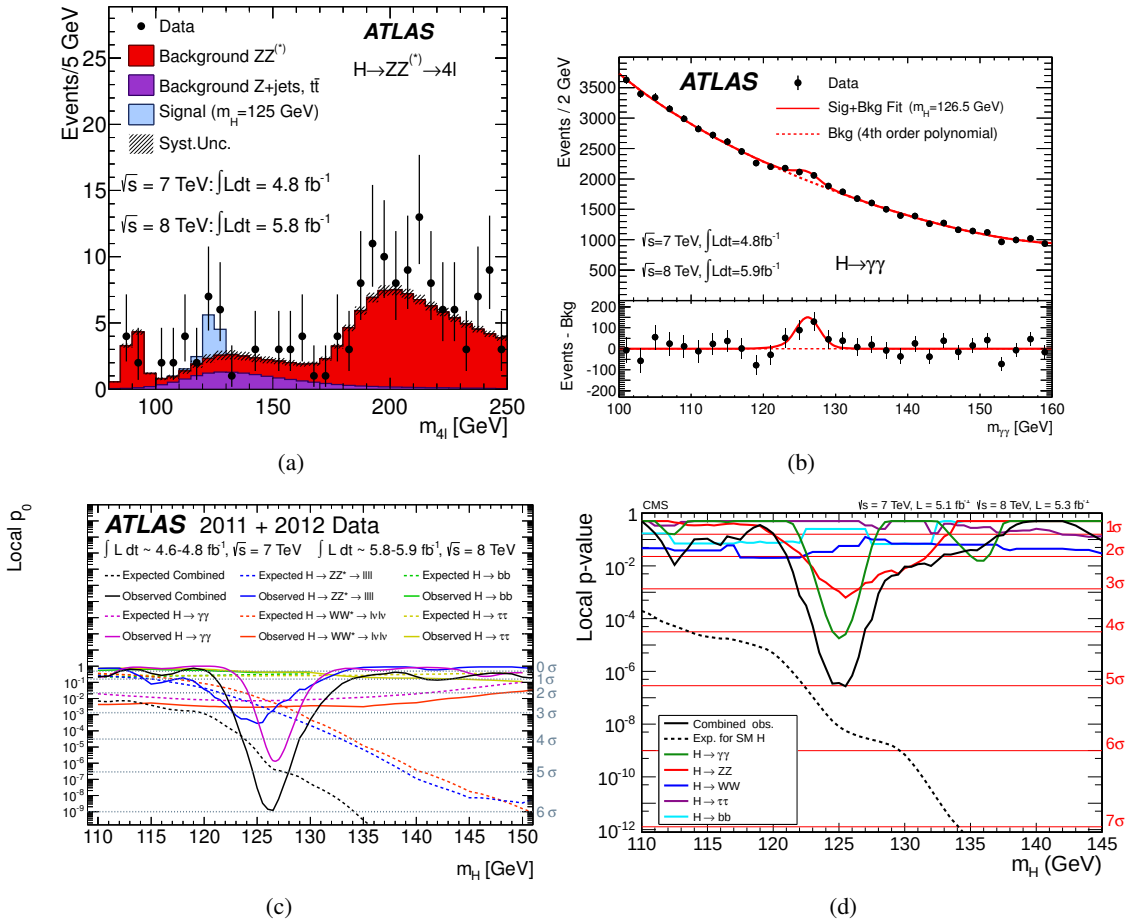

Figure 4.7: Discovery of a Higgs-like particle at the LHC in combined data with $\sqrt{s}$ = 7 TeV and $\sqrt{s}$ = 8 TeV. (a) Invariant mass distribution of the $H \to ZZ^{(*)} \to 4\ell$ candidates at ATLAS. The background and signal expectation for m_H = 125 GeV are compared to data. (b) The invariant diphoton mass of $H \to \gamma\gamma$ candidates at ATLAS. A fit of signal+background and background is compared to data. The bottom shows the residuals of data after a subtraction of the fitted background. (c) and (d): Observed local p_0 value as a function of the hypothesised Higgs mass for the individual Higgs decay channels and their combination for ATLAS (c) and CMS (d). The dashed lines show the expected p_0 values [82, 83].

4.2 Statistical Methods

The different statistical methods implemented to derive the $W \to \tau\nu_\tau$ cross section and to search for a $H \to \tau\tau$ signal in data will be outlined in the following.

In general, due to the simple relation $\sigma = N/\mathcal{L}$, a cross section of a process can be derived by counting the number of signal events in a data sample. In order to test the compatibility of data with a signal of a Higgs boson, a fit is performed on a binned distribution that separates signal from background. A high signal-to-background ratio in the selected data sample is desirable to increase the statistical significance of the result. The Higgs cross section is very small and it is overwhelmed by numerous sources of background in data (Fig. 4.1). These can only be reduced by selecting a very small phase space region where the signal is expected. Consequently, statistical uncertainties play a larger role in this analysis than in the cross section measurement of the W production, where a signal dominated sample can be defined much easier.

In both methods it is crucial to reduce systematic uncertainties associated to the measured observables such as background contributions or efficiencies as far as possible, since they affect the precision of the calculated or fitted parameters of interest.

4.2.1 Methodology of a Cross Section Measurement

The measurement of the production cross section times branching ratio of a physics process, as it is done for the $W \to \tau\nu_\tau$ process in this thesis, is based on a sample with a high-purity of selected signal events.

The total cross section is defined as [33]:

$$\sigma^{\text{tot}} \equiv \sigma^{\text{prod}} \times \text{BR} = \frac{N_{\text{obs}} - N_{\text{bkg}}}{AC\mathcal{L}} \tag{4.1}$$

According to this equation the following parameters have to be determined including their statistical and systematic uncertainties, respectively:

- N_{obs} is the number of observed events in the data sample.
- N_{bkg} is the number of background events in the data sample.
- $\mathcal{L}$ is the integrated luminosity.
- A is the so called *fiducial acceptance factor*, which refers to the fraction of events in the phase space region defined by the geometrical acceptance of the detector and by the kinematic selection of the analysis:

  $$A = \frac{N_{\text{gen, kin/geom}}}{N_{\text{gen, all}}} \tag{4.2}$$

  Here $N_{\text{gen, all}}$ denotes the total number of simulated signal events and $N_{\text{gen, kin/geom}}$ denotes the number of simulated signal events within the fiducial acceptance region.

- C is the so called *correction factor* that takes into account the trigger, reconstruction and identification efficiencies of the final state particles and the efficiency of all selection criteria of an analysis within the fiducial acceptance:

  $$C = \frac{N_{\text{reco, all cuts}}}{N_{\text{gen, kin/geom}}} \tag{4.3}$$

  Here $N_{\text{reco, all cuts}}$ is the number of fully simulated signal events passing the reconstruction, trigger and the selection criteria of the analysis.

Since the A factor is calculated without using experimental data, the measurement result is often given in form of the fiducial cross section:

$$\sigma^{\text{fid}} \equiv A \cdot \sigma^{\text{tot}} = \frac{N_{\text{obs}} - N_{\text{bkg}}}{C\mathcal{L}} \tag{4.4}$$

4.2.2 Statistical Tests with a Profile Likelihood Fit

In order to quantify the compatibility of the analysed data with a Higgs boson signal, it is evaluated with the help of statistical tests. An upper limit on the Higgs production cross section extractable from a data sample can be set when testing the compatibility of the hypothesis containing a signal with a certain signal strength and background (H_1). A discovery of a signal on the other hand is established if the background-only hypothesis (H_0) can be rejected in data.

In the search for the $H \to \tau\tau$ decay presented in this thesis the hypothesis test is done by a binned maximum likelihood fit. The likelihood function is built from the observed and expected number of events for each bin of the invariant $m_{\tau\tau}$ mass distribution, an observable which separates signal and background well from each other (Sec. 7.3). The expected number of events in the ith bin is defined by the sum of expected signal (s_i) and background (b_i) events:

$$E[n_i] = \mu s_i + b_i \tag{4.5}$$

The parameter μ denotes the signal strength and is a free parameter in the likelihood fit. A signal strength $\mu = 1$ corresponds to the exact prediction of the signal of a Standard Model Higgs boson, while $\mu = 0$ corresponds to the background-only model[5].

The *likelihood function* has the following form [89, 90]:

$$L(\boldsymbol{n}|\mu, \boldsymbol{\theta}) = \prod_{i=1}^{N} \text{Pois}(n_i|\mu s_i + b_i) \prod_{j=1}^{M} f(\tilde{\theta}_j|\theta_j) \tag{4.6}$$

Here $\boldsymbol{n} = (n_1,...,n_N)$ denotes the set of the observed number of events in data distributed over N bins and the product of $\text{Pois}(n_i|\mu s_i + b_i)$ stands for the Poisson probabilities of observing n_i events with the expectation $\mu s_i + b_i$ in each bin.

The additional set of parameters $\boldsymbol{\theta} = (\theta_1,...,\theta_M)$ are the so-called *nuisance parameters* (NP). They account for the fact, that the prediction of signal and background are affected by systematic uncertainties in the experiment, and thus data might not being perfectly described by the model. These can be e.g. the uncertainty of the energy scale, a selection efficiency or a theoretical cross section[6]. The nuisance parameters increase the degrees of freedom in the fit and allow the model to have more flexibility in this enlarged parameter space. As a consequence, these additional parameters improve the description of data, but result at the same time in larger uncertainties on the estimated parameters of interest (μ in this case).

Constraints on the nuisance parameters are obtained by the estimation of the size of the systematic uncertainty in auxiliary measurements (e.g. in control regions or by calibration measurements). It can be assumed that the repetition of these experiments yields a probability distribution function (PDF) for each NP in form of a Gaussian with a central value 0 (defined as no systematic bias) and a width of ±1 (systematic effect included as up or down variation) [89, 91]. This is reflected by the second term in Eq. 4.6: It includes the product of the PDFs $f(\tilde{\theta}_j|\theta_j)$, denoting the respective auxiliary measurement $\tilde{\theta}_j$ which constrains the nuisance parameter θ_j. Due to this way of incorporating nuisance parameters in the likelihood function it is often referred to as *profile likelihood*.

[5] The signal is always specified for a certain fixed mass of the Higgs boson and only the signal strength is estimated in the fit, since this analysis has only little sensitivity to the mass. The hypothesis test is repeated however for several mass points within the sensitive range.

[6] Also the statistical uncertainties of the signal and background samples per bin are included as nuisance parameters since they also influence the modelling of the fitted mass distribution.

To test a hypothesised value of μ, the *profile likelihood ratio* is used [92]:

$$\lambda(\mu) = \frac{L(\mu, \hat{\hat{\boldsymbol{\theta}}})}{L(\hat{\mu}, \hat{\boldsymbol{\theta}})} \tag{4.7}$$

In this formula the $\hat{\mu}$ and $\hat{\boldsymbol{\theta}}$ in the denominator denote the values that maximise L when they are varied simultaneously, thus they are the optimal values of the μ and θ parameters obtained for a given data set. The numerator contains the hypothesised μ value that is being tested. $\hat{\hat{\boldsymbol{\theta}}}$ is the maximum likelihood estimator of $\boldsymbol{\theta}$ that maximises L for this specific μ and is thus a function of μ. The final *test statistic* for the test of a certain hypothesis is defined as:

$$q_\mu = -2 \ln \lambda(\mu) \tag{4.8}$$

If $\hat{\mu}$ is very close to μ, i.e. if the data is consistent with the tested hypothesis, q_μ is 0, while for increasing incompatibility between the data and the hypothesis the value of q_μ gets larger. The exact quantification of the degree of incompatibility is given by the so-called p-value, which is defined as:

$$p_\mu = \int_{q_{\mu,\text{obs}}}^{\infty} f(q_\mu|\mu) \mathrm{d}q_\mu \tag{4.9}$$

In this equation $f(q_\mu|\mu)$ denotes the PDF of this test statistic, which is the distribution of q_μ obtained after numerous tests under the assumption of a signal strength μ. $q_{\mu,\text{obs}}$ is the test statistic obtained from the actual fit to data and thus denotes one point on this distribution. The integral from this point to infinity thus denotes the probability of finding a data set with equal or greater incompatibility with the predictions of the hypothesis. This is also illustrated in Fig. 4.8a. A hypothesis can be regarded as excluded, if the corresponding p value is below a certain threshold.

The p-value is often transformed to the equivalent *significance* Z, defining the p-value in units of the standard deviations σ of a Gaussian distribution above its mean. Consequently, it is defined as $Z = \Phi^{-1}(1 - p)$, Φ^{-1} being the inverse cumulative distribution of a Gaussian [2, 92]. A discovery of a new signal is by convention required to have a significance of at least 5σ, equivalent to $p = 2.87 \times 10^{-7}$. To define an upper limit on the signal strength, a threshold value of $p = 0.05$, i.e. a 95% confidence level (CL), is commonly used which corresponds to $Z = 1.64$[7].

An example for the calculation of these values is the test of the background-only hypothesis in data for the purpose of discovering a signal: If a signal is present in data, H_0 will be found incompatible with data. For this hypothesis test, the test statistic is defined as:

$$q_0 = \begin{cases} -2 \ln \lambda(0) & \hat{\mu} \geq 0 \\ 0 & \hat{\mu} < 0 \end{cases} \tag{4.10}$$

This incorporates the prerequisite that a negative q_0 can only result from a downward background fluctuation. An approximation of the PDF $f(q_0|0)$ entering Eq. 4.9 can be obtained for a large enough data set by a convolution of a delta-function and a one-dimensional χ^2 distribution [2, 92]. Using Eq. 4.9 p_0

[7] An adjustment is made for cases where the expected signal is much smaller than the background $s + b \approx b$. To avoid the exclusion of a signal due to large downwards fluctuation of data (as it might happen when using Eq. 4.9), the CL_s procedure is used instead. A signal strength μ is regarded as excluded at 95% CL if $\text{CL}_\text{s} = p_\mu/(1 - p_0) < 0.05$.

If the experiment is sensitive to the signal, the denominator is close to one. However, if it is not or only slightly sensitive, p_μ and $1 - p_0$ have a similar size since the PDFs of both are almost overlapping. As a consequence CL_s is large, which prevents the signal hypothesis to be excluded [90].

can be calculated as $p_0 = 1 - \Phi^{-1}(q_0|0)$ which yields a significance of:

$$Z_0 = \sqrt{q_0} \tag{4.11}$$

To estimate the significance to be *expected* for the purpose of a discovery or the exclusion of μ values in data, a *median test statistic* $\text{med}[q_\mu|\mu']$ and consequently a median p-value and significance Z can be determined. This is illustrated in Fig. 4.8b. To determine the expected p-value and significance for the tested hypothesis of a signal strength μ, the PDF for assuming both the tested signal strength μ and a different value μ' in data are derived, $f(q_\mu|\mu)$ and $f(q_\mu|\mu')$. The median of $f(q_\mu|\mu')$ is thus the expected test statistic, which would be obtained in data if it contained a signal with strength μ'.

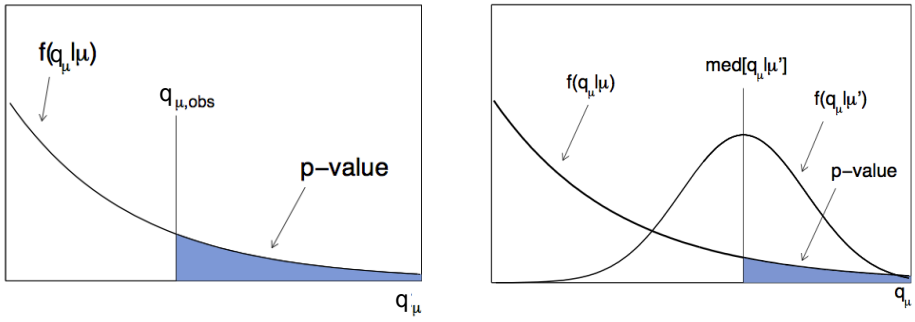

(a) (b)

Figure 4.8: (a) PDF of the test statistic q_μ and the p-value obtained for an observed test statistic q_μ^{obs}, (b) PDF of the test statistic q_μ and the median (expected) p-value obtained for a test statistic assuming a signal strength μ' [92].

The median of the test statistic can be obtained from the so called *Asimov* data set [92]. To define this data set it is assumed that every bin entry is at its expected value, thus statistical fluctuations in data are not considered. The measured maximum likelihood estimators $\hat{\mu}$ and $\hat{\boldsymbol{\theta}}$ in the profile likelihood ratio (Eq. 4.6) are equal to the true parameters μ' and $\boldsymbol{\theta}$ in the Asimov data set. Therefore, the test statistic $q_{\mu,A}$ is equivalent to the median of $f(q_\mu, \mu')$. Considering again the test of the H_0 hypothesis for the purpose of a signal discovery, the expected significance (assuming a signal strength μ') is [92]:

$$\text{med}[Z_0|\mu'] = \sqrt{q_{0,A}} \tag{4.12}$$

The error bands ($N\sigma$) that give an estimate of the expected variation of the significance in data, when statistical fluctuations are present, are defined as:

$$\text{med}[Z_0|\mu' + N\sigma] = \sqrt{q_{0,A}} + N \tag{4.13}$$

$$\text{med}[Z_0|\mu' - N\sigma] = \max[\sqrt{q_{0,A}} - N, 0] \tag{4.14}$$

As a first approximation to estimate the expected significance of a data sample one can consider the total number of data events n in one single bin, following a Poisson distribution with the expectation value $E[n] = \mu s + b$, where the background value b is assumed to be known. The median significance assuming a signal with $\mu = 1$ is then [92]:

$$\text{med}\,[Z_0|1] = \sqrt{2((s+b)\ln(1+s/b) - s} \tag{4.15}$$

If $s \ll b$ this can be reduced to $\text{med}\,[Z_0|1] \approx s/\sqrt{b}$.

4.3 An Embedding Technique to Model $Z \to \tau\tau$ and $W \to \tau\nu_\tau$ Decays

For the physics measurements presented in this thesis a reliable and accurate estimation of the relevant signal and background processes is critical to obtain a precise result. For this, it is desirable to rely as little as possible on simulations, since a modelling of a full collision event, in particular of pile-up and underlying event processes, is very complex and results in large systematic uncertainties. Instead, the preferred way is to investigate individual processes directly from measured data.

The dominant background in the search for the $H \to \tau\tau$ decay presented in this thesis (Chap. 7) is the $Z \to \tau\tau$ process. Its final state particles are identical to those of the signal process, which originate also from a resonant mass. Thus, a $H \to \tau\tau$ signal is expected in the tail of the $Z \to \tau\tau$ invariant mass distribution, which makes it difficult to find a clean control region in the data to investigate this background without a significant signal contamination. In addition, this makes an accurate modelling of the mass and thus $E_{\mathrm{T}}^{\mathrm{miss}}$ crucial for the final extraction of a signal (more details on the properties of these decay channels are given in Sec. 7.2).

For a measurement of the $W \to \tau\nu_\tau$ cross section (presented in Chap. 6), the precision of the result depends to a large extend on an accurate modelling of missing transverse energy, which uses the full detector information for the reconstruction.

The *embedding* technique is a powerful tool to address these problems. It was first developed for the modelling of the $Z \to \tau\tau$ background [93–95]: It starts from a sample of $Z \to \mu\mu$ events in ATLAS data, a decay process which can be selected with high efficiency and purity in ATLAS. Apart from differences in the mass between muon and τ lepton, this process is kinematically identical to $Z \to \tau\tau$. Moreover, due to the small branching ratio of $H \to \mu\mu$ the signal contamination is negligible (Fig 4.6a). The muons in this sample are replaced by simulated τ leptons resulting from a $Z \to \tau\tau$ decay. The rest of the event, including jet and pile-up kinematics, is taken directly from the $Z \to \mu\mu$ data. Thus it provides a much better estimate of the jet kinematics and $E_{\mathrm{T}}^{\mathrm{miss}}$, since only the well-understood signal process is simulated, while the rest of the event is based on data.

An embedded sample to model the $W \to \tau\nu_\tau$ decay can simultaneously be derived from $W \to \mu\nu_\mu$ data with the same technique [96].

The embedding procedure is performed in the following steps, illustrated also in Fig. 4.9 for an embedding of $Z \to \tau\tau/W \to \tau\nu_\tau$ events:

Selection of $Z \to \mu\mu/W \to \mu\nu_\mu$ events in data A pure sample of $Z \to \mu\mu$ data is selected by requiring at least two isolated well-reconstructed muon candidates with opposite charge within $|\eta| < 2.5$ and one muon with $p_{\mathrm{T}} > 20$ GeV and one with $p_{\mathrm{T}} > 15$ GeV. For the $W \to \mu\nu_\mu$ selection one muon within also $|\eta| < 2.5$ and $p_{\mathrm{T}} > 20$ GeV and a significant amount of $E_{\mathrm{T}}^{\mathrm{miss}}$ is required. In addition, the $Z \to \mu\mu$ invariant mass (the $W \to \mu\nu_\mu$ transverse mass, Eq. 6.2) is required to be close to the Z (W) resonance. (A detailed description of the characteristics of these processes is provided in Secs. 7.2 and 6.2)

Simulation of the $Z \to \tau\tau/W \to \tau\nu_\tau$ decay From the reconstructed muons the kinematics of the $Z \to \mu\mu$ ($W \to \mu\nu_\mu$) decay are derived and they thereafter are replaced by τ leptons. For this step, the mass difference of the two leptons is taken into account by rescaling the four-momenta based on the relation $|p_\tau| = \sqrt{E_\mu^2 - m_\tau^2}$. In the $W \to \mu\nu_\mu$ case the full kinematic reconstruction is not possible since the neutrino cannot be directly detected. Therefore, among the two possible solutions for the longitudinal component of the neutrino momentum one is randomly chosen. The resulting $Z \to \tau\tau$ ($W \to \tau\nu_\tau$) kinematics are subjected to Tauola and Photos (Sec. 3.5), to simulate the τ decay, taking into account polarisation and spin correlations of the τ leptons resulting

from Z (W) bosons. This resulting $Z \to \tau\tau$ ($W \to \tau\nu_\tau$) signal event is then passed to the ATLAS detector simulation, digitisation and reconstruction[8].

Removal of muons in $Z \to \mu\mu/W \to \mu\nu_\mu$ data The selected muons are erased from the $Z \to \mu\mu$ ($W \to \mu\nu_\mu$) data by removing all tracks associated to them. In addition, also the energy depositions in the calorimeter are subtracted: The passage of the muons through the calorimeter is simulated without underlying event or pile-up effects and the expected cell energy depositions are subtracted in the $Z \to \mu\mu$ ($W \to \mu\nu_\mu$) data event.

Merging of data and simulated signal Subsequently, the simulated $Z \to \tau\tau$ ($W \to \tau\nu_\tau$) signal is inserted in the rest of the $Z \to \mu\mu$ ($W \to \mu\nu_\mu$) event by adding the simulated tracks and energy depositions in the calorimeters. This hybrid event is then again subjected to a full reconstruction to correctly calculate all objects and $E_{\mathrm{T}}^{\mathrm{miss}}$ with the full event information.

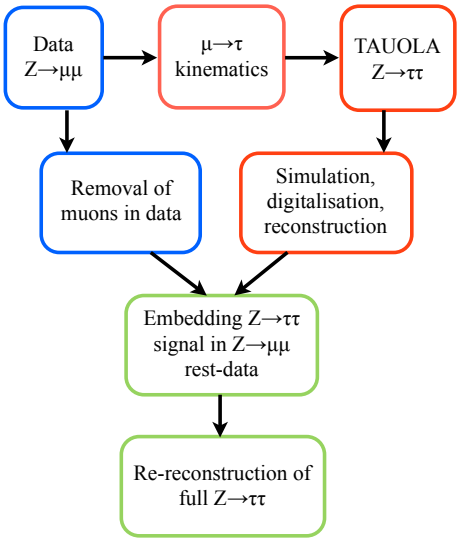

Figure 4.9: Flowchart of the embedding procedure for $Z \to \tau\tau$ events.

Due to the complexity of this procedure careful validation of each of these steps has been performed, validating the robustness and accuracy of the procedure [96–98]. The statistical size of the τ-embedded sample is naturally determined by the size of the $Z \to \mu\mu/W \to \mu\nu_\mu$ data sample and thus increases over the data taking time[9]. Only the trigger response cannot be emulated with the embedding method due to missing information in the used data format. This fact has to be taken into account for an investigation of kinematic quantities and the sample normalisation within the respective analysis.

To summarise, for the $W \to \tau\nu_\tau$ cross section measurement these samples are implemented to validate in particular the modelling of pile-up and underlying events in simulated signal and background processes (Sec. 6.3). For the $H \to \tau\tau$ search the embedded sample is used for the estimation of the $Z \to \tau\tau$ background. In this case corrections are applied to compensate for an influence of the muon selection criteria on the τ kinematics and to account for the missing trigger information. This will be explained in more detail in Sec. 7.5.

[8] Calorimeter noise is switched off in this step to avoid double counting.

[9] For the efficient use of all data events, a kinematic filter is applied at generator level to only use generated $Z \to \tau\tau$ events, that fall into the kinematic range of typical physics analyses.

CHAPTER 5

τ Leptons and Missing Transverse Energy in ATLAS

The search for $H \rightarrow \tau\tau$ presented in this thesis is performed in the $\tau_{\text{lep}}\,\tau_{\text{had}}$ decay channel with the visible decay products of the leptonically and hadronically decaying τ leptons and three neutrinos in the final state. Also the $W \rightarrow \tau\nu_\tau$ cross section is measured in the final state with a hadronically decaying τ lepton and a neutrino. The accuracy of the analysis results depends strongly on the reconstruction efficiency, the background rejection and the calibration of τ leptons and $E_{\text{T}}^{\text{miss}}$. The optimisation and validation of these algorithms in the first ATLAS data is therefore an important prerequisite for a successful performance of physics analyses.

The characteristics of τ leptons relevant for the analysis are discussed in Sec. 5.1. While in reconstruction leptonically decaying τ leptons are treated equivalent to prompt electrons and muons, a dedicated algorithm is needed for the visible decay products of hadronically decaying τ leptons. The hadronic decay products of the τ leptons are often mimicked by QCD jets and light leptons. A strong suppression of these misidentifications is important for the physics analyses presented in this thesis since processes with QCD jets and leptons constitute the major sources of background. A detailed discussion of the τ_{had} reconstruction and identification algorithms is given in Sec. 5.2. An example for a validation and measurement of the τ_{had} identification algorithms in data is outlined in Sec. 5.2.1: A method to measure the misidentification probability of electrons in data and simulation.

For the reconstruction of the missing transverse energy, in particular for the $H \rightarrow \tau\tau$ search, it is most important to optimise the resolution: It directly influences the accuracy of the invariant $m_{\tau\tau}$ mass reconstruction, which is crucial to determine the sensitivity in data to a $H \rightarrow \tau\tau$ signal. The $E_{\text{T}}^{\text{miss}}$ reconstruction and calibration methods are therefore described in Sec. 5.3. Moreover, in Sec. 5.3.1 studies to optimise the treatment of hadronically decaying τ leptons in $E_{\text{T}}^{\text{miss}}$ and harmonise it with the τ selection in the analysis are described. This allows to profit from a refined $E_{\text{T}}^{\text{miss}}$ calibration with improved resolution.

5.1 Properties of τ Leptons

The τ lepton is by far the heaviest lepton with a mass of (1776.8 ± 0.2) MeV (compare Sec. 2.1) and is the only one that can decay into lighter leptons and quarks (hadrons). Its lifetime is thus only $(290.3 \pm 0.5) \times 10^{-15}$ s, corresponding to a mean decay length of 87.1 μm [2]. Therefore, in the ATLAS

detector the τ decay takes place in the beam-pipe and only the decay products can be investigated in the detector. The branching ratio for *leptonically* decaying τ leptons is about 35%, while the fraction of τ lepton decaying *hadronically*, i.e. to pions (π) and more rarely to kaons (K), is about 65% [1]. Due to charge conservation only odd numbers of charged decay particles occur. In the hadronic decay modes additional neutral hadrons, mostly pions (π^0), can also be produced (in about 78% of the hadronic τ decays). The individual decay modes and branching ratios for a negatively charged τ lepton are summarised in Tab. 5.1.

Decay mode	Γ_i/Γ
$\tau^- \rightarrow e^-\bar{\nu}_e\nu_\tau$	17.83%
$\tau^- \rightarrow \mu^-\bar{\nu}_\mu\nu_\tau$	17.41%
$\tau^- \rightarrow h^-\nu_\tau + \geq 0h^0$ (*one-prong*)	49.46%
$\tau^- \rightarrow h^-h^-h^+\nu_\tau + \geq 0h^0$ (*three-prong*)	15.20%
$\tau^- \rightarrow h^-h^-h^-h^+h^+\nu_\tau + \geq 0h^0$ (*five-prong*)	0.10%

Table 5.1: Decay modes of a τ^- lepton and the corresponding branching ratios Γ_i/Γ. $h^\pm$ denotes a $\pi^\pm$ or a $K^\pm$, while h^0 denotes additional neutral hadrons, mainly π^0 particles [2].

Leptonically decaying τ leptons are as explained above reconstructed and identified in the same way as electrons and muons (Sec. 3.4). The reconstruction and identification of hadronically decaying τ leptons is a challenge since their signature is similar to QCD jets, which have much larger production cross sections (Fig. 4.1). In addition, also electrons and to a smaller extend muons can mimic the signature of hadronically decaying τ leptons mostly with one track. However, several shower and track characteristics distinguish them from these sources of background:

- A low track multiplicity, i.e. one or three tracks situated in a narrow cone
- A narrow calorimetric shower (with a width R $\sim 1/p_T$), often with a large electromagnetic component due to the decays of the neutral pions to photons
- The τ decay products are well isolated from the rest of the event
- A small invariant mass of the size of the τ mass
- A τ decay vertex displaced from the primary vertex

These properties form the basis for the reconstruction and identification methods of hadronically decaying τ leptons.

5.2 τ_{had} Reconstruction and Identification

Reconstruction

The reconstruction algorithm aims to reconstruct the sum of four-momenta of all visible decay products of a hadronically decaying τ lepton using cluster and track information. The algorithm starts from

[1] In this thesis leptonically decaying τ leptons are denoted as τ_{lep} and hadronically decaying ones as τ_{had}. Referring to the *reconstructed objects* of the τ decay, this includes per definition only the *visible* decay products since neutrinos are reconstructed separately in E_T^{miss}. In contrast, referring to the τ *decay modes* such as $H \rightarrow \tau_{lep}\tau_{had}$ or $W \rightarrow \tau_{had}\nu_\tau$ the τ_{lep} and τ_{had} notations include *all* τ decay products.

jets with $p_T > 10$ GeV and $|\eta| < 2.5$ which are reconstructed by the anti-k_t algorithm with a distance parameter $R = 0.4$ and are based on topological clusters (Sec. 3.4) [99]. To reduce effects of high pile-up in 2011 and 2012 data and increase the reconstruction efficiency the τ decay vertex is reconstructed with a dedicated algorithm. It selects the vertex with the highest fraction of transverse momentum summing the transverse momenta of all well-reconstructed tracks that are matched to the jet candidate within $\Delta R < 0.2$.

The resulting four-momentum of the τ_{had} candidate is defined with respect to this τ vertex. The directions (η, ϕ) and the transverse momentum p_T are calculated from the sum of clusters within the *core-cone* $\Delta R = 0.2$ of the cluster barycentre. The mass of the τ candidate is defined to be zero, thus p_T is equivalent to the transverse energy E_T.

The τ_{had} energy is calibrated to a specific τ *energy scale* (TES) [100]. This calibration takes into account the special mix of neutral and charged pions which determines the energy distribution in ECal and HCal for τ_{had} candidates. Additionally, this calibration corrects for energy losses in front of the calorimeters and outside the τ cone. To correct the energy for pile-up and underlying event contributions an offset term dependent on the mean number of interactions is subtracted.

Finally, tracks are associated to the clusters if they are within $\Delta R < 0.2$ of the τ_{had} direction and satisfy the following selection criteria [99]: $p_T \geq 1$ GeV, the number of silicon (pixel) detector hits ≥ 7 (2), $|d_0| \leq 1.0$ mm and $|z_0 \sin\theta| \leq 1.5$ mm. The number of tracks in the core-cone defines the classification as *one-prong*, *three-prong* or *multi-prong* candidates[2]. The sum of the track charges is equivalent to the τ_{had} charge.

The τ_{had} reconstruction itself does not provide much rejection against the background of QCD jets or electron and muons. Therefore, in a second step, dedicated identification algorithms are applied to distinguish the true τ_{had} candidates from these background processes.

Discrimination against QCD Jets

In order to separate genuine τ leptons from the large background of QCD jets, criteria based on the characteristic properties of τ_{had} decay products in the calorimeter and inner detector are defined [99, 101]. A few important ones are listed here:

- The energy/p_T-weighted distance of tracks/energy depositions associated to the τ_{had} candidate
- The momentum fraction of the leading τ_{had} track
- The energy fraction deposited within a narrow cone of $\Delta R < 0.1$ with respect to the τ_{had} axis
- The energy fraction deposited in the ECal
- The number of tracks in the isolation cone $0.2 < \Delta R < 0.4$ around the τ_{had} axis
- The decay length of the τ_{had} vertex in the transverse plane
- The invariant mass of clusters and tracks associated to the τ_{had} candidate

The full list and exact definition of all identification variables is given in Appendix A. Two example distributions of important discriminating variables are shown for τ_{had} signal events compared to the QCD background in Fig. 5.1. The identification (ID) variables are combined in three different discriminants to select genuine τ candidates efficiently and to reject QCD jets. The simplest discriminant is based on

[2] Tracks in an outer (*isolation*) cone ($0.2 < \Delta R < 0.4$) are also subjected to the same track identification criteria and are used for the calculation of several kinematic observables in the identification algorithms.

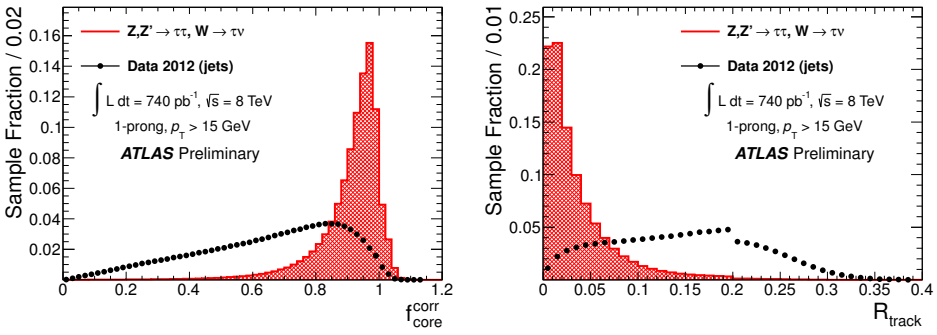

(a) (b)

Figure 5.1: Two τ_{had} identification variables used for a τ_{had}-jet separation. The distributions of genuine τ leptons for simulated $Z \to \tau\tau$, $W \to \tau\nu_\tau$ and $Z' \to \tau\tau$ events (red) is compared to the background of QCD jets obtained from data at $\sqrt{s} = 8$ TeV (black points). (a) $f_{\text{core}}^{\text{corr}}$, the ratio between the energy deposited in a cone $\Delta R < 0.1$ around the τ_{had} axis and the energy deposited in a cone $\Delta R < 0.4$ corrected for pile-up. (b) R_{track}, p_{T}-weighted distance of the tracks from the τ_{had} axis [100].

a *cut-based* algorithm, where p_{T} dependent selection criteria are applied on some of the characteristic variables. In addition, two further discriminants are defined by using multivariate algorithms: A *boosted decision tree* method (BDT) and a *projected likelihood* method (LLH)[3] [101–103]. Given the same signal efficiency they achieve a better background rejection than the cut-based algorithm.

The set of variables used in the three identification algorithms changes continuously during the ATLAS data taking periods. Due to the increasing luminosity in 2011 and 2012 data, several improvements are introduced to ensure a stable performance of the τ_{had} identification also under conditions of high pile-up. More track-based variables are used, while calorimeter-based ones are omitted since they are very sensitive to additional cell energy entries from pile-up. In addition, corrections depending on the number of vertices in the event are applied [99]. A table of the variables used in the BDT and cut-based algorithms for the different data sets investigated in this thesis can be found in Appendix A.

All ID algorithms define three working points (*loose*, *medium*, *tight*) with decreasing signal efficiency and increasing background rejection. For the analyses presented in this thesis, the *BDT medium* working point is used for the τ_{had} identification since it provides a compromise between a high signal efficiency and a good background rejection. The corresponding efficiencies and background rejection factors for the analyses of the 2010, 2011 and 2012 data sets are summarised in Tab. 5.2.

Data set	τ_{had} ID	Signal efficiency		Background rejection	
		one-prong	three-prong	one-prong	three-prong
2010	BDT medium	30%	35%	~ 100	~ 300
2011	BDT medium	50%	55%	~ 30	~ 60
2012	BDT medium	60%	55%	~ 40	~ 100

Table 5.2: Signal and inverse background efficiencies of the τ_{had} ID working points for $20 < p_{\text{T}}^{\tau_{\text{had}}} < 40$ GeV implemented in this thesis for the analyses of the 2010, 2011 and 2012 data sets[4] [99, 101, 104, 105].

[3] These algorithms combine a set of variables to provide an output value between 0 (background-like) and 1 (signal-like) with a continuous gradient of signal and background efficiency.

[4] The efficiency is here defined as the fraction of all reconstructed τ_{had} candidates that pass the τ_{had} identification.

Discrimination against Electrons

Hadronically decaying τ leptons can also be mimicked by electrons: The signature of an electron in the detector is very similar to a one-prong τ_{had} candidate since it also features a track in the inner detector and an associated calorimeter cluster. The algorithms applied for the separation of τ_{had} and QCD jets are not efficient enough to suppress these misidentified electrons. An additional *electron veto* is applied to further reduce this background.

Several characteristic shower and track properties can be used to distinguish τ_{had} and e from each other [99, 106]. The most important difference is that electrons emit transition radiation in the TRT with much higher probability compared to pions and kaons from τ_{had} decays due to their higher Lorentz factor γ (Sec. 3.2). Also the form of the calorimetric shower is different. In contrast to electron showers, τ_{had} showers are much longer and wider since they deposit a high fraction of energy in the HCal and the shower is widened through the additional energy depositions of the neutral pions in the τ_{had} decay.

Based on these features several identification variables are defined, such as the fraction of transition radiation hits in the TRT, the ratio of the track momentum to the energy deposited in ECal and HCal, or the energy fraction deposited in a ring of $0.1 < \Delta R < 0.2$ around the τ_{had} axis. A detailed list of the *electron veto* variables can be found in Appendix A. Two example distributions of discriminative variables are shown for electrons and true τ_{had} candidates in Fig 5.2.

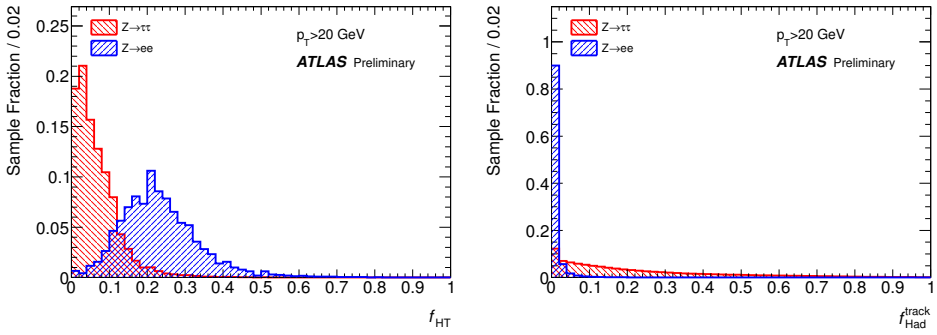

(a) (b)

Figure 5.2: Two variables used for a τ_{had}-electron separation. The distributions of genuine τ leptons for simulated $Z \to \tau\tau$ events (red) is compared to the background of electrons in simulated $Z \to ee$ events (blue). (a) f_{HT}, the ratio of high-threshold to low-threshold hits in the TRT of the leading track indicating transition radiation. (b) $f_{\text{Had}}^{\text{track}}$, the ratio of energy deposited in the first HCal layer to the momentum of the leading τ_{had} track [107].

In the analysis of the 2010 data for the $W \to \tau\nu_\tau$ cross section an electron veto based on simple selection criteria using these discriminative variables is applied. For the $H \to \tau_{\text{lep}}\tau_{\text{had}}$ search in 2011 and 2012 data, a BDT-based electron veto is applied to achieve a better background rejection. The algorithm has been continuously optimised during data taking to adjust to the different luminosity conditions in data. Different working points (*loose*, *medium*, *tight*) of the electron veto are defined. The corresponding efficiencies of the working points implemented in this thesis are summarised in Tab. 5.3.

The probability of electrons misidentified as three-prong τ_{had} candidates[5] is very small ($< 1\%$) and thus no dedicated algorithm has been developed to suppress this background. However, a non-negligible number of such events are found as a background in the $H \to \tau_{\text{lep}}\tau_{\text{had}}$ search. Therefore, an additional

[5] The additional tracks arise from radiated photons that undergo conversion in the inner detector or from underlying event processes.

Data set	e-veto	Signal efficiency		Background rejection	
		one-prong	three-prong	one-prong	three-prong
2010	cut-based tight	85%	-	~ 60–80	-
2011	BDT medium	85%	-	~ 100–200	-
2012	BDT medium	85%	97%	~ 100–200	~ 10

Table 5.3: Signal efficiencies and inverse electron background efficiency of the τ_{had} electron veto working points implemented in this thesis for the analyses of the 2010, 2011 and 2012 data sets [99, 104, 108, 109].

veto for these three-prong candidates is applied. It is derived from the BDT algorithm developed for one-prong $e \rightarrow \tau_{\text{had}}$ misidentifications (Tab. 5.3).

Discrimination against Muons

Muons can mimic hadronically decaying τ leptons only in rare cases, when they leave an exceptionally large energy in the calorimeter and the muon reconstruction fails. For these misidentified muons the fraction of energy in the electromagnetic calorimeter is either very small since the muon deposits a large part of its energy in the HCal, or very large if the muon emits a photon in the inner detector. In addition, the momentum fraction of the leading track is usually very large for misidentified muons. Based on these properties a *muon veto* is developed to reject these misidentified muons. The exact definitions of the muon veto variables can be found in Appendix A. A signal efficiency of 96% is achieved for true τ_{had} candidates, while about 40% of the misidentified muons can be rejected by the muon veto.

5.2.1 Measurement of the $e \rightarrow \tau_{\text{had}}$ Misidentification Probability

A precise knowledge of the number of misidentified τ_{had} candidates is important to estimate the background in physics measurements involving τ leptons, such as the $W \rightarrow \tau\nu_\tau$ cross section or the search for the Higgs boson in the $H \rightarrow \tau\tau$ decay. Therefore, the probability of QCD jets and electrons being misidentified as hadronically decaying τ leptons is measured and compared to simulation.

A first measurement of that kind in ATLAS performed on the τ_{had} electron veto with a so-called *tag-and-probe* method will be described here. It is based on 37 pb^{-1} of $\sqrt{s} = 7$ TeV data [106, 109]. The results of this method are included in the $W \rightarrow \tau\nu_\tau$ cross section measurement presented in Chap. 6.

$Z \rightarrow ee$ events are selected in data to have a pure sample of electrons and to extract the misidentification probability $e \rightarrow \tau_{\text{had}}$. Events that pass an electron trigger requirement are selected and a well-identified electron is defined as the *tag* object. This electron is required to have $p_{\text{T}} > 30$GeV, be reconstructed inside $|\eta| < 2.47$ (excluding the transition region $1.37 < |\eta| < 1.52$ [6]), pass the tight electron identification (Sec. 3.4) and be isolated from the rest of the event. A second *probe* object is required to have exactly one track, $p_{\text{T}} > 15$ GeV and lie within $|\eta| < 2.5$. If more than one of such tag-and-probe pairs are found, the one with the highest scalar p_{T} sum is chosen. In addition, the invariant mass of the pair is required to fall in the mass window $80 < m_{ee} < 100$ GeV and the pair must have charges of opposite sign. An additional requirement of $E_{\text{T}}^{\text{miss}} < 20$ GeV suppresses the remaining background, mainly from $W \rightarrow e\nu$.

Figure 5.3a shows the invariant mass distribution in data and simulation of the tag-and-probe pairs after all described selection criteria except for the invariant mass requirement. It can be seen that a very pure sample with a very small background contamination has been selected.

[6] In this detector region the electron reconstruction is less efficient and not well modelled in simulation [45].

Finally, τ_{had} identification and electron veto requirements are applied to the probe candidate. The misidentification probability is defined as:

$$f_{\text{ID}} = \frac{\text{Number of probe candidates passing the electron veto and } \tau_{\text{had}} \text{ identification}}{\text{Number of probe candidates}} \tag{5.1}$$

It is evaluated as a function of p_{T} and $|\eta|$ of the probe candidate in data and simulation.

Systematic effects of this method are also evaluated. Since the background contamination gets larger when veto and identification criteria are applied, the influence on f_{ID} is evaluated. The background contamination is derived from data control regions by inverting the charge product and/or requiring more than one track. An overall correction factor is calculated and considered as systematic uncertainty. Additional sources of systematic uncertainties are the electron energy scale and the choice of the invariant mass window.

Figure 5.3b shows the misidentfication probability measured in data compared to simulation for the cut-based electron veto as a function of $|\eta|$ of the probe candidate. The medium BDT τ_{had} identification is applied in addition (Sec. 5.2). This is the configuration which is used in the $W \to \tau\nu_\tau$ cross section measurement. In the transition region of the detector ($1.37 < |\eta| < 1.52$) the prediction from simulation does not agree with data. This is due to the fact that some of the identification variables, e.g. amount of transition radiation in the TRT, are not well modelled in simulations in these detector regions. Therefore, scale factors are derived from the seen discrepancies to correct the efficiency in simulation to the one in data in the analysis.

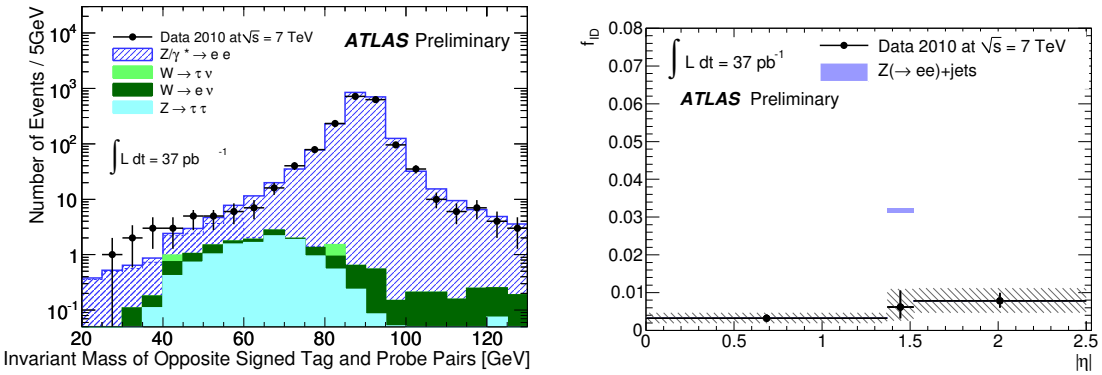

(a) (b)

Figure 5.3: (a) Distribution of the invariant mass of the $Z \to ee$ tag-and-probe pair. Data (black points) is compared to the expectation from simulation (stacked). (b) $e \to \tau_{\text{had}}$ misidentification probabilities as a function of the tau pseudorapidity for the tight cut-based electron veto and medium BDT τ_{had} ID. Data (black points) is compared to simulated $Z \to ee$ events including uncertainties (blue). The error bars indicate the statistical uncertainty on the data measurement, while the shaded area indicates the total uncertainty including the systematic one.

5.3 Reconstruction of Missing Transverse Energy

The missing transverse energy $E_{\mathrm{T}}^{\mathrm{miss}}$ in the ATLAS experiment is defined as the momentum imbalance in the transverse plane of the beam axis. It results from neutrinos or other weakly interacting particles that cannot be directly measured in the detector. Based on momentum conservation it is calculated as the negative vectorial sum of the transverse momenta of all particles detected in one pp collision. It is thus a vectorial quantity with the magnitude $E_{\mathrm{T}}^{\mathrm{miss}}$ [7].

Since $E_{\mathrm{T}}^{\mathrm{miss}}$ is only indirectly measured it is a challenge to reconstruct it precisely with a good resolution. Mismeasurements due to finite detector coverage, dead material or noise need to be minimised. The missing transverse energy is in general measured by the sum of energy deposited in the cells of the calorimeter and the energy deposited in the muon spectrometer:

$$E_{x(y)}^{\mathrm{miss}} = E_{x(y)}^{\mathrm{miss,calo}} + E_{x(y)}^{\mathrm{miss,muon}} \tag{5.2}$$

$$E_{\mathrm{T}}^{\mathrm{miss}} = \sqrt{E_x^{\mathrm{miss}\,2} + E_y^{\mathrm{miss}\,2}} \tag{5.3}$$

The missing transverse energy in the calorimeter is defined as the total negative sum of the cell energies associated to topoclusters (Sec. 3.4) within $|\eta| < 4.9$:

$$E_x^{\mathrm{miss,calo}} = -\sum_{i=0}^{N_{\mathrm{cells}}} E_i \sin\theta_i \cos\phi_i \;,\; E_y^{\mathrm{miss,calo}} = -\sum_{i=0}^{N_{\mathrm{cells}}} E_i \sin\theta_i \sin\phi_i \tag{5.4}$$

In this formula E_i is the energy of the ith cell and θ_i, ϕ_i its polar and azimuthal angle. The scalar total sum of energy depositions is defined as:

$$\sum E_{\mathrm{T}}^{\mathrm{miss,calo}} = \sum_{i=0}^{N_{\mathrm{cells}}} E_{\mathrm{T},i} \tag{5.5}$$

The muon term of $E_{\mathrm{T}}^{\mathrm{miss}}$ is calculated from the negative sum of momenta of all good quality muons measured in the muon spectrometer within the range $|\eta| < 2.7$. Up to $|\eta| < 2.5$ the combined measurement of muon momentum from ID and MS is used, which takes into account the energy loss of the muon in the calorimeter. Outside this region the measurement in the MS is used (compare Sec. 3.4).

A calibration is applied to $E_{\mathrm{T}}^{\mathrm{miss}}$ to ensure an accurate measurement and to prevent a degradation of the resolution due to dead material and varying responses of different areas of the calorimeter. A simple and robust calibration is provided by the *LCW calibration* scheme (Sec. 3.4) which is equally applied to all topoclusters [110, 111]. This energy calibration is used for the measurement of the $W \to \tau\nu_\tau$ cross section in this thesis.

The most important variable to quantify the accuracy of $E_{\mathrm{T}}^{\mathrm{miss}}$ is the resolution. It is evaluated as a function of $\sum E_{\mathrm{T}}$. The Gaussian width of the fitted E_x^{miss} and E_y^{miss} distribution is evaluated for each bin of $\sum E_{\mathrm{T}}$. The resulting resolution function can be approximately described with $\sigma = k \times \sqrt{\sum E_{\mathrm{T}}}$. For minimum bias events in 2010 data a resolution with $k \approx 0.5\ \sqrt{\mathrm{GeV}}$ is measured [110]. The resolution is shown a function of $\sum E_{\mathrm{T}}$ in Fig. 5.4a.

A more refined calibration of $E_{\mathrm{T}}^{\mathrm{miss}}$ is defined by assigning the cells within topoclusters to a high-p_{T} parent object and applying the calibration of these objects to the cells [111, 112]. This significantly

[7] Since it is a vectorial quantity it is also referred to as *missing transverse momentum*. However, to stress the fact that it is calculated based on the energy depositions of the particles in the calorimeter, it will be referred to as *missing transverse energy* throughout this thesis.

improves the $E_{\mathrm{T}}^{\mathrm{miss}}$ accuracy and also minimises systematic uncertainties on the energy scale. The calorimeter cells are assigned to the parent objects in the following order to avoid double counting of cells: Electrons, photons, hadronically decaying τ leptons, high and low p_{T} jets and muons. Cells not associated with any of these objects are also taken into account. The calorimeter $E_{\mathrm{T}}^{\mathrm{miss}}$ term is then calculated as:

$$E_{x(y)}^{\mathrm{miss,calo}} = E_{x(y)}^{\mathrm{miss},e} + E_{x(y)}^{\mathrm{miss},\gamma} + E_{x(y)}^{\mathrm{miss},\tau} + E_{x(y)}^{\mathrm{miss,jets}} + (E_{x(y)}^{\mathrm{miss,calo},\mu}) + E_{x(y)}^{\mathrm{miss,SoftTerm}} \tag{5.6}$$

The individual terms are:

- $E_{x(y)}^{\mathrm{miss},e}$ is reconstructed from cells in clusters associated to good quality electrons with $p_{\mathrm{T}} > 10$ GeV and calibrated using the electron calibration.
- $E_{x(y)}^{\mathrm{miss},\gamma}$ is reconstructed from cells in clusters associated to good quality photons with $p_{\mathrm{T}} > 10$ GeV at the electromagnetic (EM) scale[8].
- $E_{x(y)}^{\mathrm{miss},\tau}$ is reconstructed from cells in clusters associated to good quality τ leptons with $p_{\mathrm{T}} > 20$ GeV and calibrated to the τ energy scale. The development and optimisation of the τ term is described in Sec. 5.3.1.
- $E_{x(y)}^{\mathrm{miss,jets}}$ is reconstructed from cells in clusters associated to jets with $p_{\mathrm{T}} > 20$ GeV. They are calibrated to the jet energy scale (Sec. 3.4).
- $E_{x(y)}^{\mathrm{miss,calo},\mu}$ is a term resulting from the calorimeter entries of muons. It is only added if the muon is reconstructed with the Standalone algorithm or when the muon is not isolated and the energy measurement cannot be disentangled from the surrounding jet.
- $E_{x(y)}^{\mathrm{miss,SoftTerm}}$ is calculated from cells of clusters associated to low-p_{T} jets with $10 < p_{\mathrm{T}} < 20$ GeV and from all topoclusters outside the above physics objects applying the LCW calibration. Momenta of tracks in the ID are added to this term to account for very low-p_{T} objects that do not reach the calorimeter. Furthermore, for clusters that can be associated to a track the cluster energy is replaced by the track momentum which provides a better resolution [113].

The search for the $H \to \tau_{\mathrm{lep}}\tau_{\mathrm{had}}$ decay based on 2011 and 2012 data presented in this thesis implements the object-based calibration and profits from the improved $E_{\mathrm{T}}^{\mathrm{miss}}$ resolution.

Due to the increasing luminosity dedicated algorithms are included to suppress pile-up effects. Pile-up effects lead to a significant degradation of the $E_{\mathrm{T}}^{\mathrm{miss}}$ measurement since additional pile-up clusters are also picked up by the $E_{\mathrm{T}}^{\mathrm{miss}}$ calculation [113, 114]. The implemented method focusses on the pile-up suppression in all terms with hadronic energy as they are most affected. For $E_{x(y)}^{\mathrm{miss},\tau}$ and $E_{x(y)}^{\mathrm{miss,jets}}$ the pile-up correction is already applied to the initial objects and is thus transferred to the $E_{\mathrm{T}}^{\mathrm{miss}}$ calculation (Secs. 3.4 and 5.2). Furthermore, a threshold on the jet vertex fraction is applied to jets in order to discard jets that are not associated to a hard scattering vertex (Sec. 3.4). For the $E_{x(y)}^{\mathrm{miss,SoftTerm}}$ term the track information is used to suppress pile-up effects. Similar to the JVF a *soft term vertex fraction* is derived (STVF):

$$\mathrm{STVF} = \frac{\sum_{N_{\mathrm{tracks(SoftTerm),\,PV}}} p_{\mathrm{T}}}{\sum_{N_{\mathrm{tracks(SoftTerm)}}} p_{\mathrm{T}}} \tag{5.7}$$

[8] The EM scale is the initial energy scale of clusters, before the LCW or any object-specific calibration is applied. It correctly measures the energy in the ECal, not taking into account dead material.

All tracks which are not matched to physics objects are summed in the denominator, while in the numerator only the ones associated to the primary vertex (PV) are included. The $E_{x(y)}^{\text{miss,SoftTerm}}$ term is then scaled by STVF to give a lower weight to pile-up contributions.

Figure 5.4b shows the final resolution as a function of $\sum E_{\text{T}}$ before and after the implementation of the STVF method measured in 2012 $Z \rightarrow \mu\mu$ data and simulation. With the STVF method a clear improvement can be seen. The resolution is close to the one in the absence of pile-up [113].

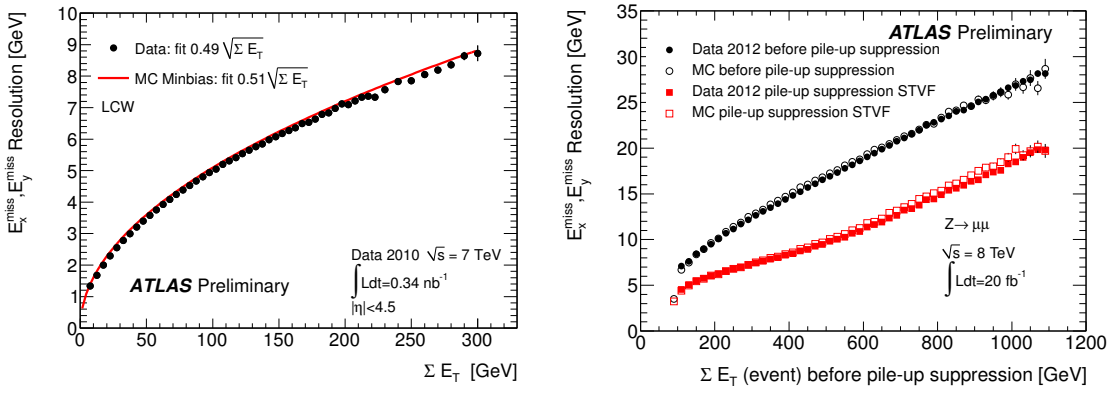

(a) (b)

Figure 5.4: E_x^{miss} and E_y^{miss} resolution as a function of the total transverse energy sum $\sum E_{\text{T}}$ (a) for minimum-bias events in $\sqrt{s} = 7$ TeV data (black points) and simulation (red curve) using LCW calibration, (b) for $Z \rightarrow \mu\mu$ events in $\sqrt{s} = 8$ TeV data (filled points) and simulation (empty points) using the object-based calibration before (black) and after (red) pile-up suppression with the STVF method [110, 113].

5.3.1 Inclusion of τ Leptons in $E_{\text{T}}^{\text{miss}}$

As explained before, the refined object-based calibration provides a better accuracy of $E_{\text{T}}^{\text{miss}}$ with a higher resolution compared to the LCW calibration. Energy scales and systematic uncertainties of physics objects are directly transferred to $E_{\text{T}}^{\text{miss}}$ and can therefore be much better optimised or reduced, respectively. In addition, a better pile-up stability can be achieved since each $E_{\text{T}}^{\text{miss}}$ term can be corrected individually. To be able to implement the refined $E_{\text{T}}^{\text{miss}}$ reconstruction in the search for the $H \rightarrow \tau\tau$ decay and in general analyses involving τ leptons a identical definition of the $E_{x(y)}^{\text{miss},\tau}$ term and τ leptons in the analysis is crucial. Studies to adjust and optimise the τ selection and calibration in $E_{\text{T}}^{\text{miss}}$ based on simulated $W \rightarrow \tau\nu_\tau$ and $Z \rightarrow \tau\tau$ processes at $\sqrt{s} = 7$ TeV are presented in this section.

At first, selection criteria for the definition of τ_{had} objects in $E_{\text{T}}^{\text{miss}}$ are developed. The purpose is to select a pure sample of clusters associated to genuine hadronically decaying τ leptons and minimise the fraction of misclassified clusters: If too many misidentified lepton/QCD jet clusters are included in $E_{x(y)}^{\text{miss},\tau}$ or too many genuine τ_{had} candidates are associated to $E_{\text{T}}^{\text{miss}}$ terms with a different calibration (Eq. 5.6), the accuracy of $E_{\text{T}}^{\text{miss}}$ degrades. The influence of different working points of the τ_{had} identification algorithms (BDT, LLH and cut-based) on the $E_{\text{T}}^{\text{miss}}$ reconstruction is tested. A p_{T} threshold of 20 GeV for τ_{had} candidates significantly reduces misidentified candidates in the τ_{had} term. This threshold is also conform to the energy range of τ leptons used in the $H \rightarrow \tau\tau$ and other analyses. In addition, an inclusion of misidentified electrons or muons in the $E_{x(y)}^{\text{miss},\tau}$ can be reduced by the application of e and μ veto (Sec. 5.2).

Besides the resolution another variable is defined to quantify the accuracy of $E_{\mathrm{T}}^{\mathrm{miss}}$: The *linearity* is defined as the ratio $(E_{\mathrm{T}}^{\mathrm{miss}} - E_{T}^{\mathrm{miss,True}})/E_{T}^{\mathrm{miss,True}}$ measured as a function of $E_{T}^{\mathrm{miss,True}}$ [112]. If $E_{\mathrm{T}}^{\mathrm{miss}}$ has the correct scale, the linearity is close to zero. At small $E_{T}^{\mathrm{miss,True}}$ values a deviation is expected due to the finite resolution of $E_{\mathrm{T}}^{\mathrm{miss}}$.

Figure 5.5 shows the resolution and linearity measured in a simulated $W \rightarrow \tau\nu_{\tau}$ sample for different τ_{had} ID working points. Lepton vetoes and the $p_{\mathrm{T}} > 20$ GeV requirement are included to define the $E_{x(y)}^{\mathrm{miss},\tau}$ term. The luminosity conditions in the simulated sample correspond to the data taking period of 2011 at ATLAS (Tab. 3.1). For comparison also the LCW-calibrated $E_{\mathrm{T}}^{\mathrm{miss}}$ is included. A significantly better resolution and linearity can be observed for the object-based calibration compared to the LCW calibration[9]. The linearity lies within 5% for high $E_{\mathrm{T}}^{\mathrm{miss}}$, while the LCW-calibrated $E_{\mathrm{T}}^{\mathrm{miss}}$ differs up to 10% from its true value. Obviously, a good and unambiguous selection of τ_{had} candidates is found, which provide an accurate calculation of the refined $E_{\mathrm{T}}^{\mathrm{miss}}$. Only small differences can be observed between the τ_{had} ID algorithms. This is important for a consistent event reconstruction in τ_{had} analyses: The $E_{\mathrm{T}}^{\mathrm{miss}}$ reconstruction is compatible with any τ_{had} ID algorithm that is used to select τ_{had} objects in the analysis. For the final $E_{\mathrm{T}}^{\mathrm{miss}}$ definition the BDT medium working point is chosen, which is conform to the $H \rightarrow \tau\tau$ search.

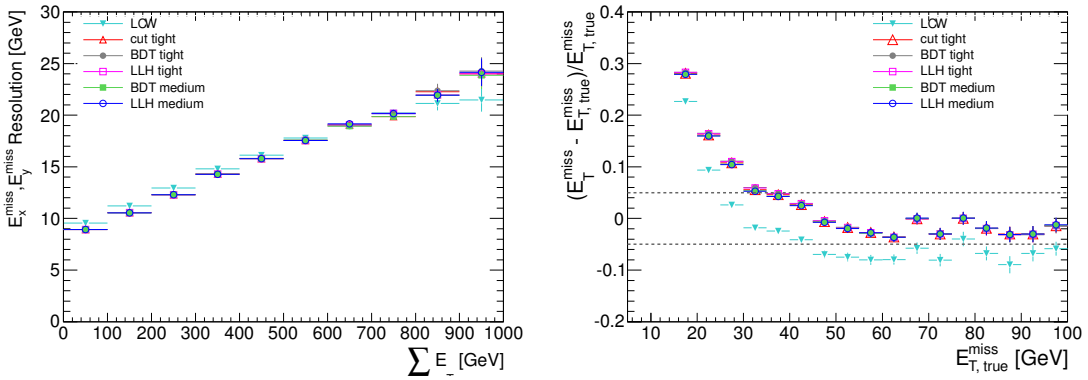

(a) (b)

Figure 5.5: (a) E_{x}^{miss} and E_{y}^{miss} resolution as a function of $\sum E_{\mathrm{T}}$ and (b) $E_{\mathrm{T}}^{\mathrm{miss}}$ linearity as a function of $E_{T}^{\mathrm{miss,True}}$ in a simulated $W \rightarrow \tau\nu_{\tau}$ sample at $\sqrt{s} = 7$ TeV. Different τ_{had} identification working points implemented in the object-calibrated $E_{\mathrm{T}}^{\mathrm{miss}}$ reconstruction are shown. For comparison also the LCW-calibrated $E_{\mathrm{T}}^{\mathrm{miss}}$ is shown (turquoise).

Another important study carried out is the implementation of the TES for the topoclusters associated to the $E_{x(y)}^{\mathrm{miss},\tau}$ term. This ensures a conformity of $E_{\mathrm{T}}^{\mathrm{miss}}$ with τ_{had} objects in the analysis, allowing a common treatment of systematic uncertainties and pile-up suppression. In this context the optimal cone size needs to be found within which topoclusters are associated to $E_{x(y)}^{\mathrm{miss},\tau}$. Two different cones are defined: The fixed τ_{had}-cone in which the TES calibration is applied ($\Delta R = 0.2$, see Sec. 5.2) and the $E_{\mathrm{T}}^{\mathrm{miss}}$-cone which contains the clusters associated to the $E_{x(y)}^{\mathrm{miss},\tau}$ that are *not* associated to other $E_{\mathrm{T}}^{\mathrm{miss}}$ terms. When a too large $E_{\mathrm{T}}^{\mathrm{miss}}$-cone is chosen, topoclusters in the vicinity of the τ_{had} axis are not included in other $E_{\mathrm{T}}^{\mathrm{miss}}$ terms for a correct $E_{\mathrm{T}}^{\mathrm{miss}}$ calculation. This is illustrated in Fig. 5.6.

[9] Only at high $\sum E_{\mathrm{T}}$ the object-based resolution seems slightly worse. This is due to the fact, that the STVF pile-up suppression was still under development at the point of these studies and is not yet included. As Fig. 5.4 shows, this improves the resolution of the object-based $E_{\mathrm{T}}^{\mathrm{miss}}$ even at large $\sum E_{\mathrm{T}}$.

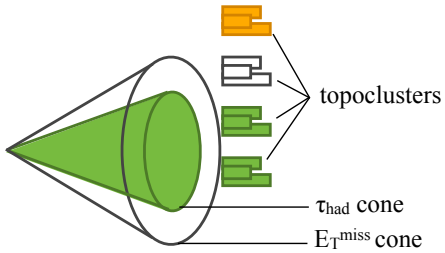

Figure 5.6: Illustration of association and calibration of topoclusters to the $E_{x(y)}^{\text{miss},\tau}$ term (example of a wide $E_{\text{T}}^{\text{miss}}$-cone). The green clusters are included in the TES calibration within the τ_{had}-cone. Yellow clusters outside the $E_{\text{T}}^{\text{miss}}$-cone are associated to other $E_{\text{T}}^{\text{miss}}$ terms with a different calibration. The white clusters within the $E_{\text{T}}^{\text{miss}}$-cone and outside the TES calibration cone are not considered for the $E_{\text{T}}^{\text{miss}}$ calculation.

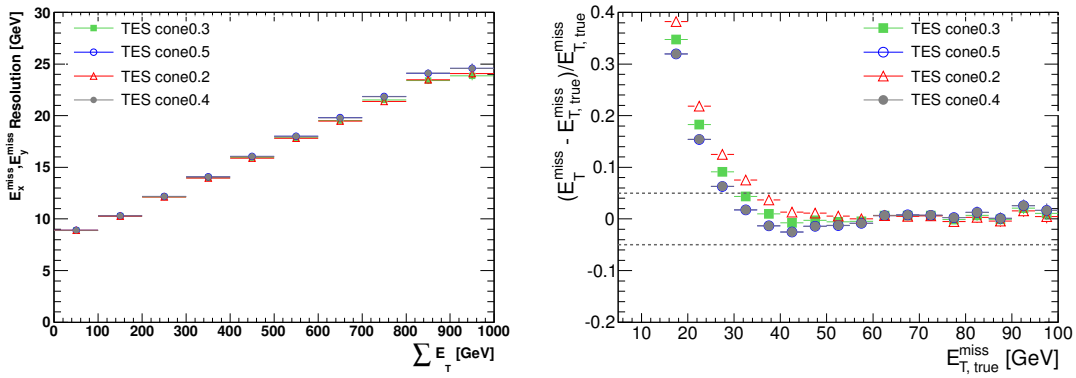

(a) (b)

Figure 5.7: (a) E_x^{miss} and E_y^{miss} resolution as a function of $\sum E_{\text{T}}$ and (b) $E_{\text{T}}^{\text{miss}}$ linearity as a function of $E_T^{\text{miss,True}}$ in a simulated $W \to \tau\nu_\tau$ sample at $\sqrt{s} = 7$ TeV. The object-calibrated $E_{\text{T}}^{\text{miss}}$ using different $E_{\text{T}}^{\text{miss}}$-cone sizes ΔR for the definition of the $E_{x(y)}^{\text{miss},\tau}$ term which is calibrated to the τ energy scale is shown. Only events are included, where a BDT medium τ_{had} candidate with $p_{\text{T}} > 20$ GeV is found.

The TES calibration also corrects for energy depositions outside the τ_{had}-cone. If hence a too small $E_{\text{T}}^{\text{miss}}$-cone is defined, energy depositions might be double-counted in the TES calibration and in other $E_{\text{T}}^{\text{miss}}$ terms.

In Fig. 5.7 the resolution and linearity of $E_{\text{T}}^{\text{miss}}$ reconstructed using a TES calibration for $E_{x(y)}^{\text{miss},\tau}$ are compared in the simulated $W \to \tau\nu_\tau$ sample using different $E_{\text{T}}^{\text{miss}}$-cone sizes. Only events are considered where a hadronic τ_{had} candidate fulfilling the above defined selection criteria is found. While the resolution is very similar in all cases, clear differences in the linearity can be seen. An $E_{\text{T}}^{\text{miss}}$-cone size of $\Delta R = 0.3$ results in a linearity close to zero for $E_T^{\text{miss,True}} > 30$ GeV. With smaller (larger) $E_{\text{T}}^{\text{miss}}$-cone sizes $E_{\text{T}}^{\text{miss}}$ is over-(under-)estimated due to double-counting(neglecting) of topoclusters. Therefore, $\Delta R = 0.3$ is chosen as the size of the $E_{\text{T}}^{\text{miss}}$-cone for the calculation of the $E_{x(y)}^{\text{miss},\tau}$ term.

After the above described optimisation of the $E_{x(y)}^{\text{miss},\tau}$ term, the refined $E_{\text{T}}^{\text{miss}}$ reconstruction can be implemented in the $H \to \tau\tau$ search. The analysis profits from the improved resolution and a proper and consistent treatment of τ_{had} objects and $E_{\text{T}}^{\text{miss}}$ in the event reconstruction (Chap. 7).

CHAPTER 6

Measurement of the $W \to \tau\nu_\tau$ Cross Section

In this chapter the first measurement of the $W \to \tau\nu_\tau$ cross section with ATLAS is presented, based on 2010 $\sqrt{s} = 7$ TeV data corresponding to a total amount of 34 pb^{-1}. It is the first measurement performed at the LHC and complements the measurements of the W production cross section in the light lepton decay channels (Sec. 4.1.1).

Decays of W and Z bosons, in particular to τ leptons, are a major source of background in searches for new physics including the search for the Standard Model $H \to \tau\tau$ decay, which is presented in the next chapter.

A precise cross section measurement of these processes is thus an essential prerequisite to study the compatibility of data with a possible signal of a new particle on top of the expected background.

Moreover, due to its relatively large cross section, the $W \to \tau\nu_\tau$ decay offers the possibility to study final states with τ_{had} and $E_{\text{T}}^{\text{miss}}$ in the first ATLAS data and to validate the performance of their reconstruction and identification algorithms. This is a vital preparation for an analysis of these final states in the $H \to \tau\tau$ and other new physics searches.

In Sec. 6.1 the analysis strategy is outlined. Characteristics of the signal and background processes in the $W \to \tau\nu_\tau$ analysis are discussed in Sec. 6.2, together with the simulated samples used to investigate these processes in the analysis. Section 6.3 describes and motivates the choice of criteria applied to select a pure sample of signal events in data. The different methods to estimate the contribution of background processes to this selected data sample are explained in Sec. 6.4. The composition of the selected sample and the important kinematic distributions are investigated in Sec. 6.5. The determination of the cross section, including the measurement of efficiency correction and acceptance factors, is summarised in Sec. 6.6. It also describes the validation of the results through several alterations to the main analysis method. A detailed investigation of the sources of systematic uncertainties is performed in Sec. 6.7. Finally, in Sec. 6.8 the results of the $W \to \tau\nu_\tau$ cross section measurement are presented and interpreted.

6.1 Outline of the Analysis Strategy

The measurement of the $W \to \tau\nu_\tau$ cross section (Eq. 4.1) requires the selection of a pure sample of signal events with large statistics. To obtain the exact number of signal events in this sample, the number of background events must be precisely estimated and subtracted. In addition, the selected signal events must be corrected for trigger, reconstruction and selection efficiency and the kinematic and geometrical acceptance in the detector. Finally, a detailed investigation of all sources of systematic uncertainties is

necessary to determine the precision of the measurement.

The measurement of the $W \to \tau\nu_\tau$ cross section presented in this chapter is only performed with hadronically decaying τ leptons, since leptonic τ decays cannot easily be distinguished from prompt $W \to e\nu_e$ and $W \to \mu\nu_\mu$ decays in the detector.

This complex final state of a hadronically decaying τ lepton and $E_{\mathrm{T}}^{\mathrm{miss}}$ poses the following challenges to the analysis:

- The τ_{had} and $E_{\mathrm{T}}^{\mathrm{miss}}$ usually have very low momenta.
- The cross section of QCD background processes is several orders of magnitude higher compared to the signal cross section (Fig. 4.1).
- The $E_{\mathrm{T}}^{\mathrm{miss}}$ reconstruction is based on the full event information and can be affected by pile-up.

In order to select a sufficiently large amount of signal events in data, a dedicated trigger and event selection allowing low enough momentum thresholds is developed. The event selection criteria aim to efficiently suppress the large QCD background as well as the also significant background from other W and Z decays. At the same time the influence of the $E_{\mathrm{T}}^{\mathrm{miss}}$ resolution and pile-up dependency on the measurement are minimised by a careful choice of the selection criteria. Dedicated methods are applied to estimate or validate the different background contributions in data. This allows to avoid large systematic uncertainties, which are often associated to the modelling of different processes by simulation. Since this analysis is one of the first to probe the performance of τ_{had} and $E_{\mathrm{T}}^{\mathrm{miss}}$ reconstruction and identification, a careful validation of the consistency and stability of the results is crucial.

The analysis applied for the cross section measurement is a further development of a first simple analysis method applied in a much smaller data sample corresponding to an integrated luminosity of 546 nb^{-1} which led to the first observation of $W \to \tau\nu_\tau$ decays with ATLAS [115, 116]. The cross section measurement presented in this chapter is published in [117].

6.2 Signal and Background Processes

W production and $W \to \tau_{\mathrm{had}}\nu_\tau$ decay

The Feynman graphs of leading and next-to-leading order and the first measurements of W production have been discussed in Sec. 4.1.1. At next-to-next-to-leading order the $W \to \tau\nu_\tau$ signal is predicted to be produced at $\sqrt{s} = 7$ TeV with a cross section times branching ratio [72, 118, 119] of:

$$\sigma \times \mathrm{BR} \equiv \sigma^{\mathrm{NNLO}}_{W\to\tau\nu_\tau} = (10.46 \pm 0.52)\ \mathrm{nb} \tag{6.1}$$

The cross section times branching ratio for the two different charges are $\sigma^{\mathrm{NNLO}}_{W^+\to\tau^+\nu_\tau} = (6.16 \pm 0.31)$ nb and $\sigma^{\mathrm{NNLO}}_{W^-\to\tau^-\nu_\tau} = (4.30 \pm 0.21)$ nb.

The predicted branching ratio for the hadronic τ decay mode is 0.6479 ± 0.0007 [2]. The typical Feynman graph of this decay mode is shown in Fig. 6.1.

Events from $W \to \tau_{\mathrm{had}}\nu_\tau$ production at the LHC contain predominantly low-p_{T} W bosons. This results in typical transverse momenta between 10 and 40 GeV of the reconstructed τ_{had} [1]. The missing transverse energy results from the two neutrinos of the W and hadronic τ decays. The W decay neutrino is mostly emitted in the opposite direction compared to the τ lepton decay products. It usually carries a larger momentum fraction than the τ decay neutrino, hence $E_{\mathrm{T}}^{\mathrm{miss}}$ is also often found in the opposite

[1] As explained in Sec. 5.1, the reconstructed τ_{had} object is built from the visible τ decay products only, i.e. the sum of hadrons.

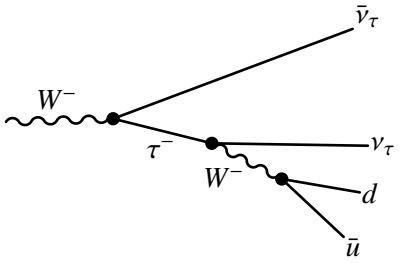

Figure 6.1: Feynman diagram of a W^- decay to a hadronically decaying τ lepton.

direction to the visible hadronic τ decay products. $E_{\mathrm{T}}^{\mathrm{miss}}$ has a maximum around 20 GeV and a significant tail up to about 80 GeV.

In Fig. 6.2a the reconstructed $E_{\mathrm{T}}^{\mathrm{miss}}$ of the $W \to \tau_{\mathrm{had}}\nu_\tau$ decay is compared to $W \to e\nu_e$ and $W \to \mu\nu_\mu$ decays[2]. Since only a small part of the muon energy is deposited in the calorimeter, $E_{\mathrm{T}}^{\mathrm{miss}}$ is very small in $W \to \mu\nu_\mu$ processes. The $W \to e\nu_e$ decay has a much harder calorimeter $E_{\mathrm{T}}^{\mathrm{miss}}$ spectrum compared to $W \to \tau_{\mathrm{had}}\nu_\tau$. This results from the fact that only one neutrino is produced in the $W \to e\nu_e$ decay, which balances the electron momentum. Also the τ_{had} momentum of the $W \to \tau_{\mathrm{had}}\nu_\tau$ decay is in general lower compared to the other W decays, since a fraction of the W decay momentum is carried away by the τ decay neutrino as illustrated in Fig. 6.2b.

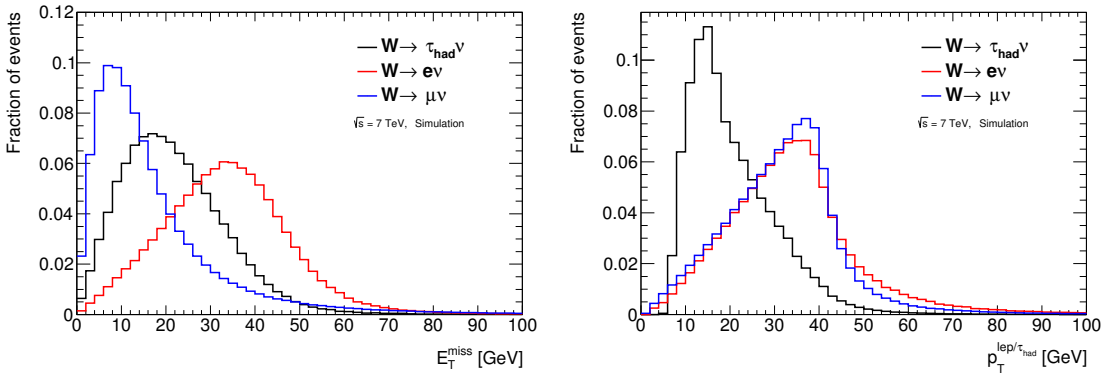

(a) (b)

Figure 6.2: (a) Reconstructed calorimeter $E_{\mathrm{T}}^{\mathrm{miss}}$ spectrum ($E_{\mathrm{T}}^{\mathrm{miss,calo}}$) and (b) reconstructed momentum of the τ_{had}/electron/muon of simulated $W \to e\nu_e$, $W \to \mu\nu_\mu$ and $W \to \tau_{\mathrm{had}}\nu_\tau$ decays based on simulations at $\sqrt{s} = 7$ TeV. Only events with good-quality $\tau_{\mathrm{had}}/e/\mu$ objects matched to a true particle are considered.

These characteristics of $E_{\mathrm{T}}^{\mathrm{miss}}$ and hadronically decaying τ leptons in $W \to \tau_{\mathrm{had}}\nu_\tau$ decays form the basis for a selection of these events in data.

Based on these observables the transverse mass of the W boson can be defined as:

$$m_{\mathrm{T}} = \sqrt{2 \cdot p_{\mathrm{T}}^{\tau_{\mathrm{had}}} \cdot E_{\mathrm{T}}^{\mathrm{miss}} \cdot \left(1 - \cos\Delta\phi\left(\tau_{\mathrm{had}}, E_{\mathrm{T}}^{\mathrm{miss}}\right)\right)} \tag{6.2}$$

Here, $\Delta\phi\left(\tau_{\mathrm{had}}, E_{\mathrm{T}}^{\mathrm{miss}}\right)$ denotes the angle between τ_{had} and $E_{\mathrm{T}}^{\mathrm{miss}}$ in the plane transverse to the beam axis. This quantity reaches its maximum at the mass of the W boson m_W.

In Fig. 6.3 an event display of a $W \to \tau_{\mathrm{had}}\nu_\tau$ decay candidate in the ATLAS detector is shown.

[2] For $E_{\mathrm{T}}^{\mathrm{miss}}$ the LCW calibration is used. Only energy depositions in the calorimeter ($E_{\mathrm{T}}^{\mathrm{miss,calo}}$) are taken into account (Sec. 5.3).

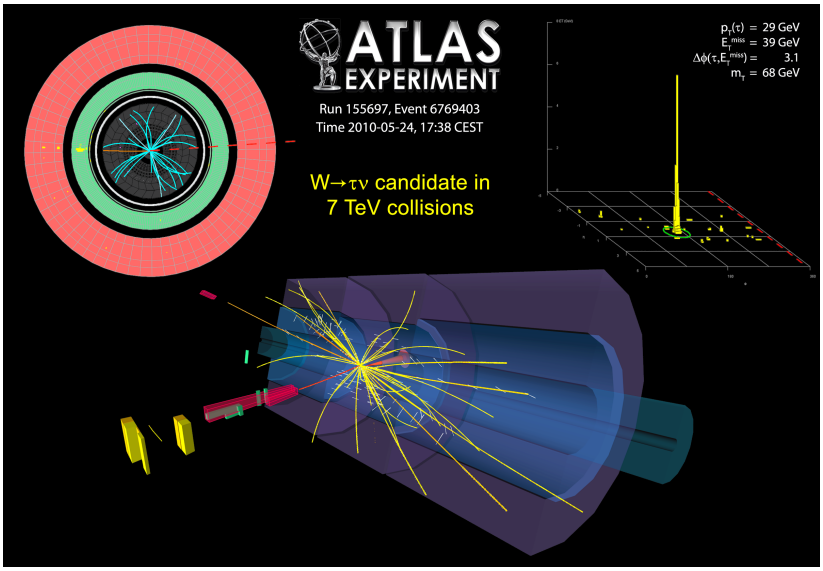

Figure 6.3: Event display of one of the first $W \to \tau_{\text{had}}\nu_\tau$ decay candidates observed in ATLAS. The hadronically decaying one-prong τ lepton is visible as red/orange track with an associated narrow cluster (pink) reconstructed from energy depositions in the calorimeter (yellow and green). $E_{\text{T}}^{\text{miss}}$ is reconstructed in the transverse plane opposite to the τ_{had} candidate (red arrow/dashed line). The top right view shows the size of the energy depositions in the calorimeter, the τ_{had} cone is indicated (green circle).

Background Processes

Several background processes can mimic the $W \to \tau_{\text{had}}\nu_\tau$ signal in the ATLAS detector:

QCD processes QCD production is the dominant source of background: One quark/gluon jet is incorrectly identified as a hadronically decaying τ lepton and a significant amount of missing transverse energy is measured due to incomplete event reconstruction. This false $E_{\text{T}}^{\text{miss}}$ calculation due to mismeasurements is referred to as *fake* $E_{\text{T}}^{\text{miss}}$ in the following. The cross section of the sum of QCD processes is several orders of magnitude larger than the signal cross section (compare Fig. 4.1). Therefore, an effective suppression and accurate estimation of these processes is crucial for the analysis.

$W \to e\nu/\mu\nu$ These processes also constitute a significant background. Two cases can occur: Either the lepton from the W boson decay ($\ell \to \tau_{\text{had}}$) or an accompanying jet is misidentified as a hadronically decaying τ lepton ($j \to \tau_{\text{had}}$), compare the Feynman graphs in Fig. 4.2. By vetoing reconstructed electrons or muons and ones that are misidentified as τ_{had} in the event both cases can be suppressed.

$W \to \tau\nu \to e\nu/\mu\nu$ Leptonic decay modes of τ leptons are difficult to distinguish from primary electrons and muons as explained above. Therefore, this process contributes also as a background to the $W \to \tau_{\text{had}}\nu_\tau$ signal and it is rejected in a similar way as $W \to e\nu_e$ and $W \to \mu\nu_\mu$.

$Z \to ee/\mu\mu$ This process poses a source of background if one of the decaying light leptons is incorrectly reconstructed as a hadronically decaying τ lepton and $E_{\text{T}}^{\text{miss}}$ is measured due to incomplete reconstruction of the second lepton or other objects. Similar to the background of other W decays described above, a rejection of events with an additional muon or electron can efficiently suppress this background. In addition, its cross section is one order of magnitude smaller than the one of the signal process, therefore, it is negligible in the analysis as will be shown in the following.

$Z \rightarrow \tau\tau$ If one of the τ leptons decays hadronically and the second one is incompletely reconstructed or lost, the $Z \rightarrow \tau\tau$ decay also constitutes a background for the $W \rightarrow \tau_{\text{had}}\nu_\tau$ signal.

Top pair production $t\bar{t}$ Top quarks decay with $\sim$ 100% branching ratio in Wb. The (semi)leptonic $t\bar{t}$ decay can contribute as a background if one of the W boson decay products is a τ_{had} and the other one decays into a pair of quarks or a light lepton that fails the reconstruction[3]. In addition, a decay of the W bosons to quarks only (hadronic $t\bar{t}$), where one of the resulting jets is misidentified as τ_{had} candidate, can also contribute as a background. But since the cross section of this process is much smaller than the signal process, it also can be neglected as will be shown in the following.

Data and Simulated Samples

The data used for this measurement is recorded at a centre-of-mass energy of $\sqrt{s} = 7$ TeV during the 2010 LHC run. The integrated luminosity of the data sample, considering only data-taking periods where all relevant detector subsystems are fully operational, is 34 pb^{-1} (Tab. 3.1).

The W, Z and $t\bar{t}$ decays are summarised as electroweak (EW) background in the following. They are modelled by simulation.

The production of W and Z bosons with additional jets is simulated with the Pythia generator using the modified PDF set MRSTLO* [120]. Underlying event and pile-up effects are adjusted to ATLAS data with the AMBT1 tune [121]. $t\bar{t}$ processes are generated with Mc@nlo interfaced with Herwig/Jimmy. For a description of the generators see Sec. 3.5. The theoretical cross sections are calculated up to NNLO, the values are summarised in Tab. 6.1 together with the size of each simulated sample. The effects of in-time pile-up (Sec. 3.1) are included in the simulation using a mean number of additional vertices $< n >= 2$ [4]. The vertex distribution of the simulated samples is reweighted to match it to the distribution in data.

The QCD background is directly estimated from data, as will be described in Sec. 6.4.

Physics process	$\sigma\times$ BR [nb]	$N_{\text{gen. events}}$
$W \rightarrow \tau\nu_\tau$	10.46 ± 0.52	1.0×10^6
$W \rightarrow e\nu_e$	10.46 ± 0.52	1.4×10^6
$W \rightarrow \mu\nu_\mu$	10.46 ± 0.52	1.4×10^6
$Z \rightarrow ee$	0.99 ± 0.05	1.0×10^6
$Z \rightarrow \mu\mu$	0.99 ± 0.05	1.0×10^6
$Z \rightarrow \tau\tau$	0.99 ± 0.05	1.0×10^6
$t\bar{t}$ (semi)leptonic decay	$(0.16 \pm 0.01) \times (0.546 \pm 0.006)$	2.0×10^5
$t\bar{t}$ hadronic decay	$(0.16 \pm 0.01) \times (0.454 \pm 0.004)$	3.0×10^4

Table 6.1: List of simulated signal and background samples used in the $W \rightarrow \tau_{\text{had}}\nu_\tau$ cross section measurement with their theoretical cross section times branching ratio at NNLO ($\sigma\times$ BR) and the number of events that are generated $N_{\text{gen. events}}$ [2, 72, 119, 122, 123].

[3] Note that for top decays, the notation *leptonic* includes decays to τ leptons, while the term *hadronic* only refers to decays to quarks.

[4] This pile-up simulation does not include out-of-time pile-up effects (Sec. 3.1). Suitable samples with this out-of-time pile-up simulation were not applicable to the analysis at the time. But the agreement of several pile-up sensitive distributions between data and simulation confirms that the inclusion of only in-time pile-up effects describes data accurately enough and thus out-of-time pile-up effects can be neglected for this analysis.

6.3 Event Selection

The physics objects in this analysis are reconstructed according to the algorithms described in Sec. 3.4. All jets are required to pass the threshold of $p_T > 20$ GeV and lie within $|\eta| < 4.5$. The LCW-calibrated E_T^{miss} is used only including calorimeter energy depositions (Sec. 5.3). The selection criteria that are applied to select a high-purity sample of $W \to \tau_{had}\nu_\tau$ events are discussed in the following.

Trigger The trigger chosen for the analysis combines the two main characteristics of $W \to \tau_{had}\nu_\tau$ decays: The presence of a hadronically decaying τ lepton and missing transverse energy.

The combination of the two objects in the trigger selection allows for a relatively low threshold on the momentum of both (Sec. 3.4). This is crucial to select a large fraction of signal events since they have usually very low transverse momenta, as explained above (Sec. 6.2). Due to the increasing luminosity the thresholds of the trigger are tightened for the later data taking period of 2010. Instead of applying the tighter trigger requirements to the full data sample, a mixture of both triggers is used for a selection of data in this analysis in order to achieve the largest possible signal yield: For the first data period corresponding to an integrated luminosity of ~ 11 pb^{-1} the events must pass the *looser* trigger requirements. In the second data taking period corresponding to an integrated luminosity of ~ 24 pb^{-1} the *tighter* trigger requirements are applied. Table 6.2 summarises the selection criteria included in these two triggers[5]. Also included are the signal efficiencies of these two triggers with respect to the full event selection estimated from simulation.

	$\int Ldt$	τ_{had}/E_T^{miss} trigger selection	ϵ_{trig} [%]
Looser trigger	11 pb^{-1}	BDT loose τ_{had}, $p_T > 12$ GeV $E_T^{miss} > 20$ GeV	81.3 ± 0.8
Tighter trigger	24 pb^{-1}	BDT medium τ_{had}, $p_T > 16$ GeV $E_T^{miss} > 22$ GeV	62.7 ± 0.7

Table 6.2: Overview of the two trigger selections used in the 2010 data sample at $\sqrt{s} = 7$ TeV for the $W \to \tau_{had}\nu_\tau$ selection (Logical OR). Listed are the integrated luminosity $\int Ldt$ in which the respective trigger is applied, the selection criteria on τ_{had} and E_T^{miss} reconstructed at trigger level and the trigger efficiency ϵ_{trig} (including statistical uncertainties) with respect to the full $W \to \tau_{had}\nu_\tau$ event selection measured in simulated signal samples.

The trigger responses of the separate τ_{had} and E_T^{miss} trigger requirements as a function of the τ_{had} momentum and E_T^{miss} are measured in data and simulation.

A pure data sample enriched with $W \to \tau\nu_\tau$ events is selected by applying the trigger requirement on τ_{had} (E_T^{miss}) and the most efficient event selection criteria, e.g. the τ_{had} identification criteria. Based on this sample, the response function of the other trigger requirement on E_T^{miss} (τ_{had}) is then derived. The same procedure is applied to the simulated signal sample. Figure 6.4 depicts the measured trigger response for simulation and data. Figure 6.4a shows the $E_T^{miss} > 20$ GeV trigger used in the first data period, while Fig. 6.4b shows the $E_T^{miss} > 22$ GeV trigger used the second data period as a function of the reconstructed E_T^{miss}.

The τ_{had} trigger response of the $p_T > 12$ GeV trigger used in the first data period is shown in Fig. 6.4c and the $p_T > 16$ GeV trigger used in the second data period is shown in Fig. 6.4d, evaluated as a function

[5] The reconstruction algorithms of τ_{had} and E_T^{miss} on trigger level are very similar to the offline reconstruction described in Secs. 5.3 and 5.2. For details see [124, 125].

of the reconstructed τ_{had} p_{T} in the p_{T} range of 20 to 60 GeV [6].

For the $E_{\text{T}}^{\text{miss}}$ trigger responses a steep turn-on of the efficiency at low $E_{\text{T}}^{\text{miss}}$ values can be observed, until it reaches a constant efficiency above $E_{\text{T}}^{\text{miss}} \approx 30$ GeV (compare Sec. 3.3). In this kinematic range small $E_{\text{T}}^{\text{miss}}$ changes correspond to large efficiency changes. Consequently, differences between data and simulation (as observed here) lead to large systematic uncertainties in the cross section measurement. Therefore the threshold on the $E_{\text{T}}^{\text{miss}}$ range that is included for the cross section measurement is chosen to lie above this turn-on region, as will be explained in the following.

A similar efficiency increase at low momenta is expected for the τ_{had} trigger (Sec. 3.3 and [124]). Therefore the kinematic range included for the cross section measurement is also chosen to be much higher than the trigger threshold. In Figs. 6.4c and 6.4d it can be seen that for $p_{\text{T}} > 20$ GeV the τ_{had} triggers have almost reached the efficiency plateau. The differences between data and simulation observed for all trigger components in the studied kinematic range are included as systematic uncertainties in the measurement (Sec. 6.7).

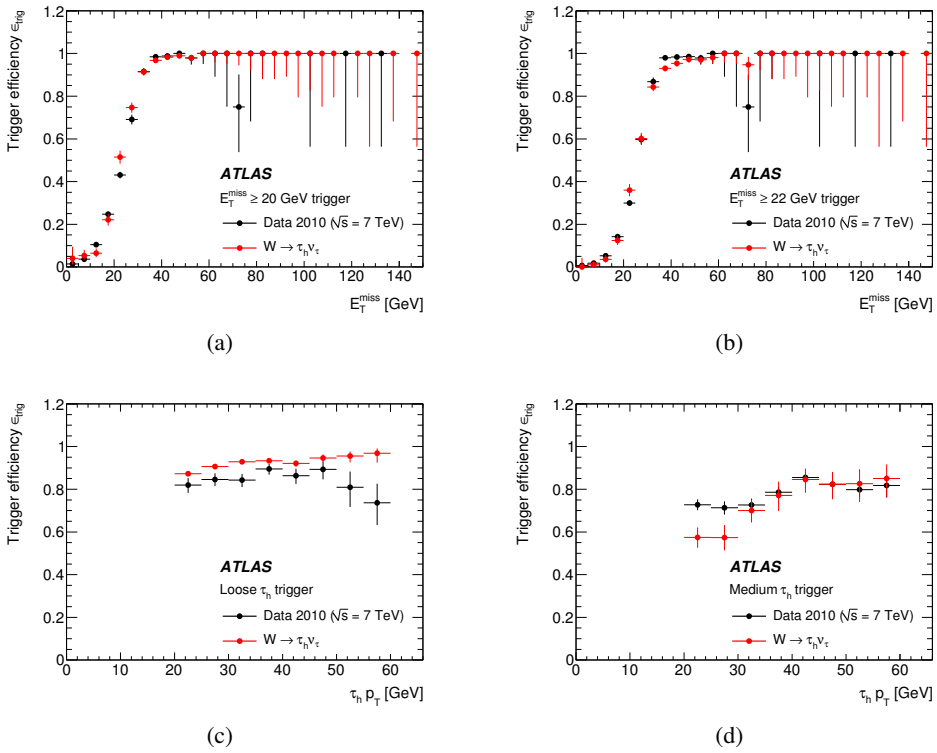

Figure 6.4: Trigger response of the trigger components used to select $W \rightarrow \tau\nu_{\tau}$ events measured in 2010 data at $\sqrt{s} = 7$ TeV (black) and simulated signal (red). Top: Response of the missing transverse energy trigger as a function of $E_{\text{T}}^{\text{miss}}$ for (a) the looser $E_{\text{T}}^{\text{miss}}$ trigger ($E_{\text{T}}^{\text{miss}} > 20$ GeV) and (b) the tighter $E_{\text{T}}^{\text{miss}}$ trigger ($E_{\text{T}}^{\text{miss}} > 22$ GeV). Only events are considered that pass a high-threshold τ_{had} trigger ($p_{\text{T}} > 38$ GeV, loose BDT ID) and several event selection criteria, as explained in the text. Bottom: Response of the τ_{had} trigger as a function of τ_{had} transverse momentum for (c) the looser τ_{had} trigger ($p_{\text{T}} > 12$ GeV) and (d) the tighter τ_{had} trigger ($p_{\text{T}} > 16$ GeV). Only events are considered that pass a high $E_{\text{T}}^{\text{miss}}$ trigger ($E_{\text{T}}^{\text{miss}} > 20$ GeV and $E_{\text{T}}^{\text{miss}} > 40$ GeV, respectively) and several event selection criteria [117].

[6] Since no signal-dominated sample can be obtained for very low or high transverse momenta in data, the trigger response is only studied in the p_{T} range that is investigated in the analysis (The τ_{had} selection is explained later in this section).

Event cleaning In order to include only events with well-reconstructed $E_{\mathrm{T}}^{\mathrm{miss}}$ for the measurement, several *cleaning* criteria are applied. Events are required to have at least one reconstructed vertex that is formed by three or more tracks with $p_{\mathrm{T}} > 150$ MeV.

Further selection requirements based on calorimeter information are applied to reject non-collision events and events containing jets that are incompletely reconstructed or significantly affected by electronic noise in the calorimeters [126].

In the transition region between barrel and end-cap of the detector the resolution of the jet energy degrades [50]. In order to ensure a uniformly good $E_{\mathrm{T}}^{\mathrm{miss}}$ resolution, events are rejected if a jet or a τ_{had} candidate is found within $1.3 < |\eta| < 1.7$.

In addition, if in an event $E_{\mathrm{T}}^{\mathrm{miss}}$ vector is found to be collinear to one of the jets, it originates very likely from an incomplete reconstruction of the jet. These cases are avoided by requiring a minimum separation of $\Delta\phi(\mathrm{jet}, E_{\mathrm{T}}^{\mathrm{miss}}) > 0.5$ for all selected jets in the event.

Event topology Further requirements are implemented to select events with the typical $W \to \tau_{\mathrm{had}}\nu_\tau$ signature, i.e. missing energy accompanied by a τ_{had} candidate.

A minimum **missing transverse energy** of 30 GeV is required. Although the $E_{\mathrm{T}}^{\mathrm{miss}}$ spectrum of the signal sample reaches its maximum at lower values (Fig. 6.2a), a higher selection threshold is chosen to avoid the turn-on range of the $E_{\mathrm{T}}^{\mathrm{miss}}$ trigger (as explained before). The background of fake $E_{\mathrm{T}}^{\mathrm{miss}}$ from QCD processes or Z decays can be significantly reduced by this selection criterion.

The reconstructed τ_{had} **candidates** are required to have at least one track and to satisfy the medium BDT identification (Sec. 5.2). The pseudorapidity must be within $|\eta| < 2.5$ and outside the detector transition region $1.3 < |\eta| < 1.7$ (as discussed before).

The τ_{had} candidate with the highest p_{T} is required to have a transverse momentum between 20 and 60 GeV, which is the typical signal range for τ leptons from $W \to \tau_{\mathrm{had}}\nu_\tau$ decays (Fig. 6.2b). The lower threshold is again limited by the trigger turn-on curve. In addition, the rejection of misidentified QCD jets is less efficient at lower momentum thresholds [106]. The upper threshold on the τ_{had} momentum suppresses the background of other W decays and QCD processes with higher p_{T} ranges.

Lepton vetoes In order to suppress the EW background containing leptons, a veto of light leptons is applied. Any identified *combined* muon or *tight* electron with $p_{\mathrm{T}} > 15$ GeV is rejected (Sec. 3.4). This mainly reduces the contribution of EW processes, where the τ_{had} candidates is a misidentified jet and the light lepton of the EW decay is also reconstructed. Events, where electrons or muons are misidentified as the τ_{had} candidates, are suppressed by the tight cut-based electron and muon veto of the τ_{had} identification (Sec. 5.2).

$E_{\mathrm{T}}^{\mathrm{miss}}$ significance In order to reject QCD events with a large $E_{\mathrm{T}}^{\mathrm{miss}}$ due to incomplete event reconstruction, the so-called $E_{\mathrm{T}}^{\mathrm{miss}}$ significance is defined:

$$S_{E_{\mathrm{T}}^{\mathrm{miss}}} = \frac{E_{\mathrm{T}}^{\mathrm{miss}}[\mathrm{GeV}]}{0.5\sqrt{\sum E_{\mathrm{T}}[\mathrm{GeV}]}} \tag{6.3}$$

The denominator is equivalent to the resolution of $E_{\mathrm{T}}^{\mathrm{miss}}$ measured in minimum bias events (Sec. 5.3). Events are selected if $S_{E_{\mathrm{T}}^{\mathrm{miss}}} > 6$.

This selection criterion efficiently rejects QCD background. This can be seen in Fig. 6.5. It shows the distribution of data and simulated $W \to \tau_{\mathrm{had}}\nu_\tau$ events in the two-dimensional plane of $\sqrt{\sum E_{\mathrm{T}}}$ and $E_{\mathrm{T}}^{\mathrm{miss}}$ after only trigger and event cleaning requirements have been applied. At this point the data is clearly

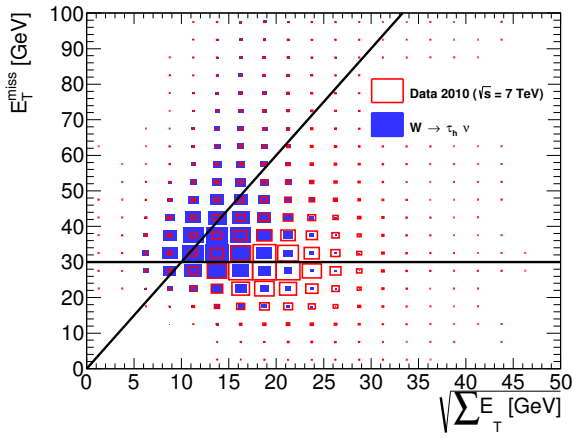

Figure 6.5: Distribution of the $W \to \tau_{\text{had}}\nu_\tau$ signal in the plane of $\sqrt{\sum E_{\text{T}}}$ and $E_{\text{T}}^{\text{miss}}$ as expected from simulation (blue) and data (red) at $\sqrt{s} = 7$ TeV corresponding to an integrated luminosity of 34 pb^{-1}. Only events that pass the trigger and event cleaning criteria are displayed. The distributions are normalised to unity and the box size is proportional to the fractional number of events in each bin. The selection thresholds on $S_{E_{\text{T}}^{\text{miss}}}$ and $E_{\text{T}}^{\text{miss}}$ used in the event selection are shown as solid lines.

dominated by QCD events. Comparing events with the same reconstructed $E_{\text{T}}^{\text{miss}}$ value one can see that $\sum E_{\text{T}}$ is usually larger in QCD events than for the $W \to \tau_{\text{had}}\nu_\tau$ process due to the higher hadronic energy depositions in QCD processes. The $E_{\text{T}}^{\text{miss}}$ selection criterion alone provides less separation between signal and background compared to the $S_{E_{\text{T}}^{\text{miss}}}$ criterion[7].

Summary of Event Selection Criteria

In summary, the following selection criteria are applied to obtain a sample rich in $W \to \tau_{\text{had}}\nu_\tau$ events:

- Loose trigger in first and tighter trigger in second data period combining $E_{\text{T}}^{\text{miss}}$ and τ_{had} triggers
- Event cleaning
- $E_{\text{T}}^{\text{miss}} > 30$ GeV
- τ_{had} selection: Leading-p_{T} candidate passing medium BDT τ_{had} ID, $|\eta| < 2.5$, $1.3 > |\eta| > 1.7$ and $20 < p_{\text{T}}^{\tau_{\text{had}}} < 60$ GeV
- Lepton vetoes: Rejection of events containing identified electrons and muons with $p_{\text{T}} > 15$ GeV and failing the tight τ_{had} electron veto and muon veto
- $S_{E_{\text{T}}^{\text{miss}}} > 6$

The number of events after each selection step is shown in Tab. 6.3 for data and simulated signal and EW background processes. The number of EW background events obtained from simulation are normalised to the integrated luminosity of 34 pb^{-1}.

In data 2335 events are found after the full event selection. This sample is clearly dominated by signal events: 1811 ± 25 $W \to \tau_{\text{had}}\nu_\tau$ signal events are expected to pass the selection according to

[7] It should be noted that data and simulated events are selected with the τ_{had} and $E_{\text{T}}^{\text{miss}}$ triggers, thus events with very low $E_{\text{T}}^{\text{miss}}$ values are already rejected and not displayable here.

	Data	$W \to \tau_{\text{had}}\nu_\tau$	$W \to \tau_{\text{lep}}\nu_\tau$	$W \to e\nu_e$	$W \to \mu\nu_\mu$	$Z \to \tau\tau$	$Z \to ee$	$Z \to \mu\mu$	$t\bar{t}$ (lep.)	$t\bar{t}$ (had.)
Events	165 757 532	232 377	126 672	358 359	358 656	340 334	34 644	33 917	2746	2186
Trigger	6 879 843	20 111 ± 81	7507 ± 50	175 936 ± 152	5620 ± 37	2664 ± 9	2306 ± 9	707 ± 5	1305 ± 3	395 ± 5
Event cleaning	2 421 757	15 327 ± 71	5771 ± 44	137 755 ± 148	4216 ± 32	1659 ± 7	656 ± 5	527 ± 4	376 ± 2	27.2 ± 1.6
$E_{\text{T}}^{\text{miss}} > 30$ GeV	350 444	11 899 ± 64	3718 ± 36	104 857 ± 138	3829 ± 31	1145 ± 6	19.3 ± 0.8	459 ± 4	349 ± 2	6.5 ± 0.8
τ_{had} selection	37 199	4790 ± 41	767 ± 16	19648 ± 69	280 ± 8	446 ± 4	3.2 ± 0.3	54.5 ± 1.4	50.9 ± 0.9	0.1 ± 0.1
Lepton vetoes	9604	3959 ± 38	29.4 ± 3.2	196 ± 7	111 ± 5	259 ± 3	< 0.1	2.9 ± 0.3	10.9 ± 0.4	0.1 ± 0.1
$S_{E_{\text{T}}^{\text{miss}}} > 6$	2335	1811 ± 25	15.1 ± 2.3	92.5 ± 4.9	56.1 ± 3.8	112 ± 2	< 0.1	1.4 ± 0.2	6.4 ± 0.3	< 0.1

Table 6.3: Number of events passing the selection criteria in 34 pb^{-1} of data at $\sqrt{s} = 7$ TeV and the expected numbers in the simulated signal and EW samples. They are normalised to the integrated data luminosity. Stated are also the statistical uncertainties.

simulation. For the rejection of the EW background the τ_{had} identification criteria and lepton vetoes are most efficient. The contribution of Z boson and $t\bar{t}$ processes is negligible after the selection.

The expected number of QCD events is not shown, since it can not reliably be estimated from simulation (Sec. 6.2). A rough estimate on the number of QCD events remaining after each selection step can be derived from the number of data events reduced by the expected signal and EW background events. The high QCD rejection efficiency of the event cleaning, $E_{\text{T}}^{\text{miss}}$, $S_{E_{\text{T}}^{\text{miss}}}$ and BDT τ_{had} identification criteria is then clearly visible. A method to estimate the precise contribution of QCD directly from data is discussed in the next section.

6.4 Background Estimation

In this section the different methods for a precise estimation of the background contribution to the selected data sample are explained. The different background processes are divided into two categories, the electroweak and QCD background.

Estimation of the Electroweak Background

The number of expected events from electroweak background processes is obtained from simulation. This is justified by the good agreement observed between data and simulation for the cross sections of W, Z and $t\bar{t}$ production measured through the decays to light leptons in the first ATLAS data [73, 122].

Two of the most important kinematic observables in the selection, $E_{\text{T}}^{\text{miss}}$ and $S_{E_{\text{T}}^{\text{miss}}}$, are calculated from information of the full event. Therefore, it is important to validate that all processes, in particular pile-up and underlying event effects, are accurately modelled by simulation.

For this purpose the $W \rightarrow \tau_{\text{had}}\nu_\tau$ process is modelled with an embedding technique (Sec. 4.3). In a high-purity $W \rightarrow \mu\nu_\mu$ data sample the muon is replaced with a simulated τ_{had} candidate with the same kinematics. Consequently, only the τ decay products and the corresponding detector response are simulated, while all other properties of the event, including pile-up and underlying event, are taken directly from data. Details of this method are described in Sec. 4.3 and [96].

The distributions of the analysis-relevant quantities are shown for the τ_{had}-embedded data sample and the simulated $W \rightarrow \tau_{\text{had}}\nu_\tau$ events after the application of the event selection. Several key distributions characteristic for the $W \rightarrow \tau_{\text{had}}\nu_\tau$ decay are investigated. Figure 6.6 shows a few examples: The $S_{E_{\text{T}}^{\text{miss}}}$ and τ_{had} p_{T} distribution, the separation in ϕ of $E_{\text{T}}^{\text{miss}}$ and τ_{had}, and the W transverse mass (Eq. 6.2) for both samples[8]. A good agreement is observed within the statistical uncertainties for all kinematic quantities. This adds confidence in the event model provided by the simulation of signal and EW background processes.

Estimation of the QCD Background

The QCD background is estimated directly from data for this analysis. This choice is driven by the fact that the cross section of hadronic processes is high and only in a small fraction of them the signal signature is mimicked. Thus the modelling of $j \rightarrow \tau$ and fake $E_{\text{T}}^{\text{miss}}$ is associated with large systematic uncertainties. Moreover, the selection efficiency is low, which leads to the problem that an insufficient number of simulated QCD events is available resulting in large statistical uncertainties. Therefore, the QCD background contribution cannot be predicted reliably by simulation. Instead, an estimation of this

[8] It has to be noted that an emulation of the τ_{had} and $E_{\text{T}}^{\text{miss}}$ trigger efficiency and turn-on curve is not implemented in the embedded sample, since it is conceptually impossible (Sec. 4.3). Therefore the trigger selection is not applied to the $W \rightarrow \tau_{\text{had}}\nu_\tau$ sample either, in order to not bias the kinematic distributions for the comparison.

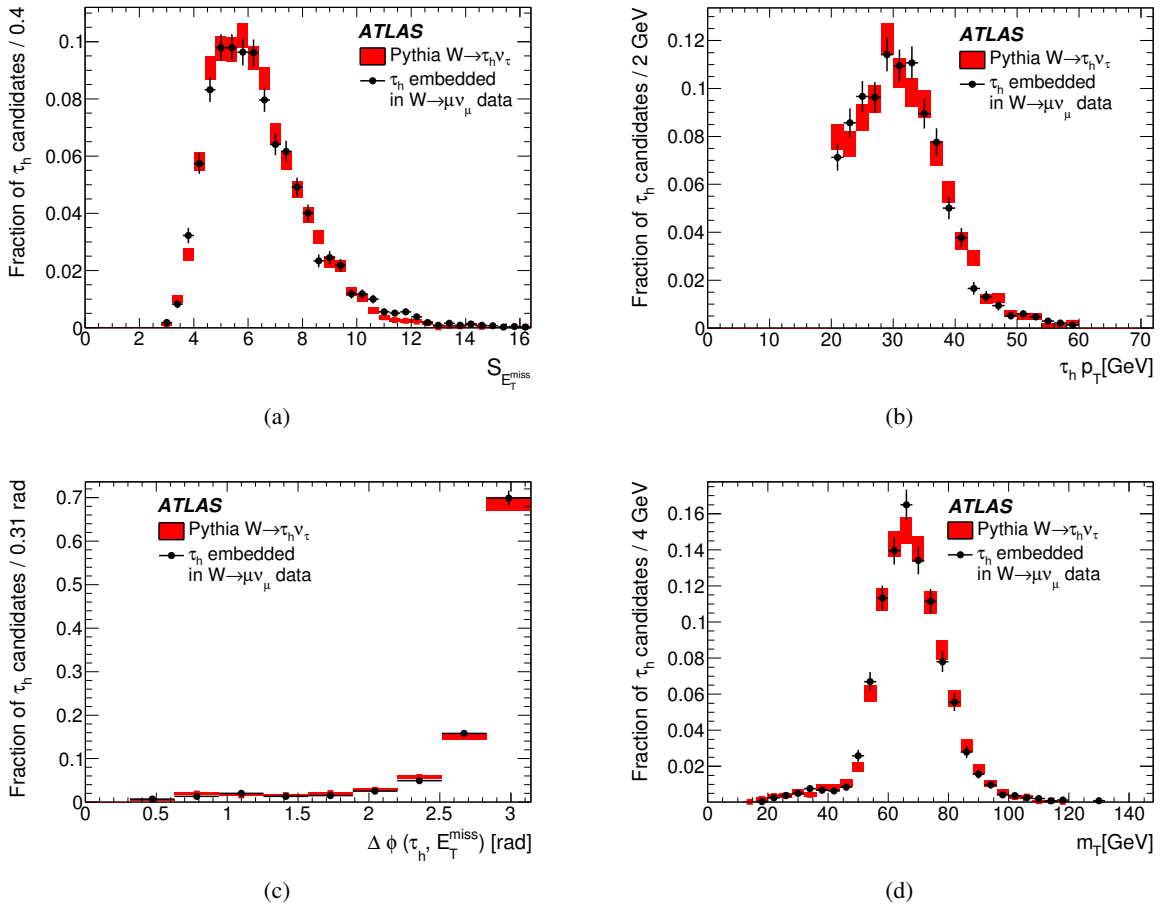

Figure 6.6: Comparison of kinematic observables for the τ_{had}-embedded $W \to \mu\nu_\mu$ data sample (points) and simulated $W \to \tau_{\text{had}}\nu_\tau$ events (histogram), including statistical uncertainties (red). (a) Missing transverse energy significance, (b) the transverse momentum of the τ_{had} candidate, (c) separation in ϕ between the τ_{had} candidate and $E_{\text{T}}^{\text{miss}}$ and (d) the transverse mass m_{T}. The full event selection without the trigger requirement is applied to both samples (apart from the $S_{E_{\text{T}}^{\text{miss}}}$ requirement in (a)) [117].

background is performed directly from data, which results in a more precise result with much smaller statistical and systematic uncertainties.

The method is based on the selection of four independent data samples: In addition to the selected sample enriched with $W \rightarrow \tau_{\text{had}}\nu_\tau$ signal events (A), three additional *control regions* (B, C, D) are defined which are dominated by the QCD background. These control regions are obtained by inverting the requirements on $S_{E_{\text{T}}^{\text{miss}}}$ and/or the τ_{had} identification, resulting in the following four samples:

- Region A: $S_{E_{\text{T}}^{\text{miss}}} > 6.0$ and τ_{had} candidates satisfying the signal τ_{had} ID requirements described in Sec. 6.3
- Region B: $S_{E_{\text{T}}^{\text{miss}}} < 4.5$ and τ_{had} candidates satisfying the signal-region τ_{had} ID requirements
- Region C: $S_{E_{\text{T}}^{\text{miss}}} > 6.0$ and τ_{had} candidates satisfying a looser BDT τ_{had} ID but failing the signal-region τ_{had} ID requirements
- Region D: $S_{E_{\text{T}}^{\text{miss}}} < 4.5$ and τ_{had} candidates satisfying a looser BDT τ_{had} ID but failing the signal-region τ_{had} ID requirements

Figure 6.7 sketches the definitions of the four regions.

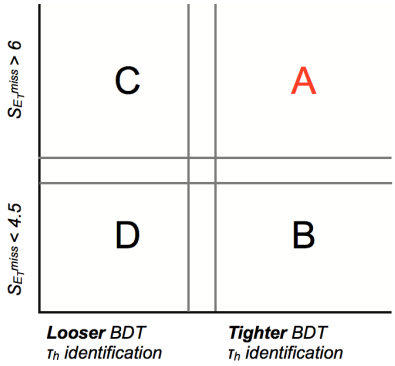

Figure 6.7: Sketch of the four regions used for the data-driven estimation of the QCD background (signal region A and three control regions B, C, D).

The exact thresholds defining the control regions are optimised to provide a sample with sufficient statistics and low contamination from EW background and signal.

Events in the range $4.5 < S_{E_{\text{T}}^{\text{miss}}} < 6$ are not considered for the background estimation, since this region contains a too large fraction of EW and signal processes.

In order to obtain the QCD-dominated control regions C and D, a very loose threshold on the BDT τ_{had} identification discriminant with a low background rejection is defined to select τ_{had} candidates[9]. If the predefined *BDT loose* working point is used, a too large fraction of signal and EW background is included, which is why an even looser requirement is chosen for these control regions. (Sec. 5.2).

Also the trigger selection is adjusted for these control regions with looser BDT τ_{had} ID to increase the yield of QCD background events: Since the tighter trigger applied in the second data period of 2010 contains a medium BDT τ_{had} selection on trigger level, the looser trigger of the first period is used instead (Tab. 6.2). This trigger is pre-scaled in the second data period (Sec. 3.4), which reduces the total

[9] The exact distribution of the τ_{had} ID BDT discriminant for signal and control region are shown in Appendix B.

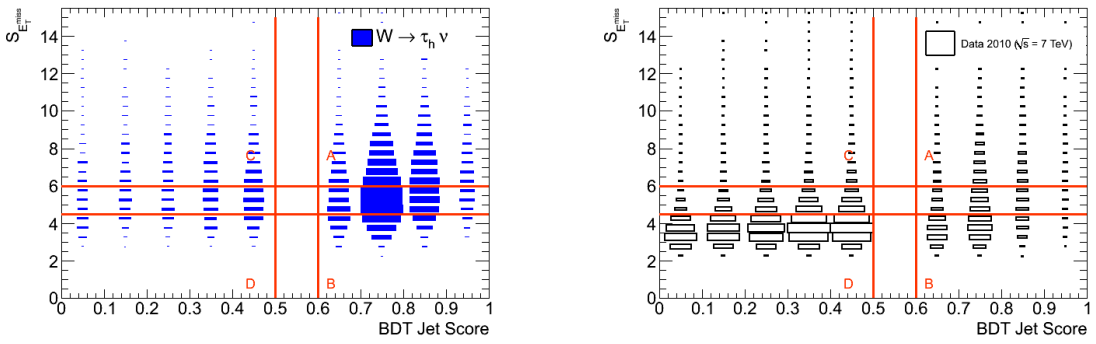

(a) (b)

Figure 6.8: Distribution of (a) $W \to \tau_{\text{had}}\nu_\tau$ signal and (b) 2010 data ($\sqrt{s}$ = 7 TeV, 34 pb^{-1}) in the four defined control regions A,B,C,D after the full event selection except for the $S_{E_T^{\text{miss}}}$ criterion. The area of the boxes is proportional to the fractional number of events in each bin.

integrated luminosity in the regions C and D to a total of 16.3 pb^{-1}. Since the statistics in these regions are very high, an accurate estimate can still be obtained from this smaller data sample.

In Fig. 6.8 the distribution of data and simulated signal events these four regions are shown. The domination of the QCD background in the three control regions is clearly visible.

The number of QCD events in the signal region $N^{\text{A}}_{\text{QCD}}$ can be estimated from the defined control regions in the following way:

$$N^{\text{A}}_{\text{QCD}} = N^{\text{B}} N^{\text{C}} / N^{\text{D}} \tag{6.4}$$

Here, N_i (i = B, C, D) denotes the number of data events found in the three control regions. This equation is only valid if these two assumptions are fulfilled:

- The shape of $S_{E_T^{\text{miss}}}$ is uncorrelated with the tightness of the τ_{had} ID selection, i.e. it is the same in the combined regions CD and AB.
- The contribution of signal and EW processes in the three control regions is negligible.

The choice of the variables for the control regions supports the first assumption: The $S_{E_T^{\text{miss}}}$ relies on global properties of the event, to which the τ_{had} candidate only contributes through its transverse momentum. The τ_{had} identification on the other hand is based on shower shape and track variables only connected to the τ_{had} candidate.

The independence of these two variables is verified by comparing the shape in the combined region AB with $S_{E_T^{\text{miss}}}$ shape in three subsamples of the combined region CD. The latter are defined by slices of the τ_{had} ID BDT discriminant with different background rejection within this region (compare Sec. 5.2). The comparison of the four shapes is shown in Fig. 6.9 after subtraction of the expected signal and EW background in each sample. No major difference in the $S_{E_T^{\text{miss}}}$ shape can be seen in any of the distributions, thus the assumption of a small correlation of the two variables is reasonable.

To ensure that the second assumption is fulfilled, the above explained gaps between signal and background regions are defined. The residual signal and EW background contamination in the control regions i = B, C, D is taken into account by replacing the number of selected events N^i in Eq. 6.4 by the expression $N^i - c_i(N^{\text{A}} - N^{\text{A}}_{\text{QCD}})$.

$$c_i = \frac{N^i{}_{\text{sig}} + N^i{}_{\text{EW}}}{N^{\text{A}}_{\text{sig}} + N^{\text{A}}_{\text{EW}}} \tag{6.5}$$

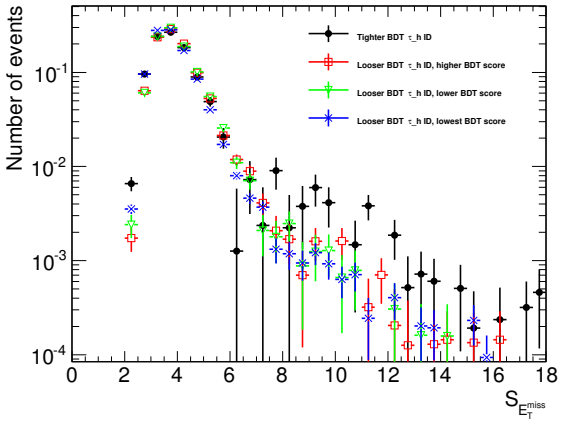

Figure 6.9: Shape of the $S_{E_{\mathrm{T}}^{\mathrm{miss}}}$ distribution in the combined signal and control region AB (black) and in the combined control regions CD divided into three regions of the BDT τ_{had} identification with different background rejection (red, green, blue). The expected signal and EW background contributions are subtracted.

This is the ratio of signal to EW background events in the control region i and the signal region as expected from simulation. With this substitution Eq. 6.4 becomes:

$$N^{\mathrm{A}}_{\mathrm{QCD}} = \frac{[N^{\mathrm{B}} - c_{\mathrm{B}}(N^{\mathrm{A}} - N^{\mathrm{A}}_{\mathrm{QCD}})][N^{\mathrm{C}} - c_{\mathrm{C}}(N^{\mathrm{A}} - N^{\mathrm{A}}_{\mathrm{QCD}})]}{N^{\mathrm{D}} - c_{\mathrm{D}}(N^{\mathrm{A}} - N^{\mathrm{A}}_{\mathrm{QCD}})} \tag{6.6}$$

Several alternative variables for a definition of suitable control regions have also been tested, including the number of jets in the event, the number of tracks associated to the τ_{had} candidate and $\sum E_{\mathrm{T}}$. Consistent results are obtained. However, the chosen variables yield the best results with respect to statistical uncertainties, the degree of signal and EW contamination and correlation.

6.5 Final Sample Decomposition

The resulting estimates of the sample compositions in the four regions are summarised in Tab. 6.4. The method predicts 127 ± 8 QCD events in the signal region after the full selection. For the EW background a total of 284 ± 7 events is expected based on simulation, while 1811 ± 25 $W \to \tau_{\mathrm{had}}\nu_\tau$ signal events are predicted after the full selection.

Several characteristic kinematic distributions are investigated in signal and control regions in order to test the agreement of the background model with data and to confirm that the selected events show the typical properties of $W \to \tau_{\mathrm{had}}\nu_\tau$ decays.

Combined signal and control region The accuary of the background model is tested by comparing the data to the summed prediction of simulated EW and signal background and to the estimated contribution of the QCD background in the combined signal and control regions. Signal and EW background are normalised to the theoretical cross section at NNLO.

Figure 6.10a shows the $S_{E_{\mathrm{T}}^{\mathrm{miss}}}$ distribution in the combined region A and B, extended over the full $S_{E_{\mathrm{T}}^{\mathrm{miss}}}$ spectrum. The full signal selection is applied except for the $S_{E_{\mathrm{T}}^{\mathrm{miss}}}$ requirement. The QCD background shape is taken from the combined region C and D and normalised according to Eq. 6.6. For the same combined region the modelling of signal and background is compared to data for the $E_{\mathrm{T}}^{\mathrm{miss}}$ and

	A	B	C	D
N^i (Data)	2335	4796	1577	27636
N^i_{sig} ($W \to \tau_{\text{had}}\nu_\tau$)	1811 ± 25	683 ± 16	269 ± 8	93 ± 5
N^i_{EW}	284 ± 7	118 ± 4	388 ± 9	90 ± 4
c_i		0.38 ± 0.01	0.31 ± 0.01	0.087 ± 0.003
N^i_{QCD}	127 ± 8	3953 ± 75	885 ± 45	27444 ± 166

Table 6.4: Estimated sample compositions and c_i factors (Eq. 6.5) in signal region A and control regions B, C, D [10].

$\sum E_{\text{T}}$ distribution in Figs. 6.10b and 6.10c.

In Figs. 6.10d and 6.10e the distributions of the most important τ_{had} identification variables R_{EM} and R_{track} included in the BDT algorithm are shown[11]. The data and the expected signal and background contribution in the combined regions A and C are compared. τ_{had} candidates in signal region A are identified by the medium BDT τ_{had} identification, while events in the control region C pass the looser BDT τ_{had} selection. The QCD background shape is taken from the combined region B and D and normalised according to Eq. 6.6. In all distributions a good agreement between data and the expectation from simulation and the QCD background estimation can be seen. This confirms the accuracy and consistency of the background estimation.

Signal region In addition, different characteristic distributions are investigated in the signal region A in data and compared to the expected signal and background distributions. Signal and EW background are normalised to the theoretical cross section at NNLO. The estimate of the QCD background shape is taken from one of the control regions B or C. The QCD background shape is taken from region C for $E_{\text{T}}^{\text{miss}}$ quantities since it is defined in the same $S_{E_{\text{T}}^{\text{miss}}}$ range as the signal region. For characteristic quantities of the τ_{had} candidate, the QCD estimate is taken from region B since it also contains events selected by the medium BDT τ_{had} identification[12].

In Fig. 6.11a the $E_{\text{T}}^{\text{miss}}$ spectrum in the signal region is shown. In Fig. 6.11b it is in addition displayed at logarithmic scale to investigate the agreement in the tail of the distribution. Figure 6.11c depicts the distribution of $\sum E_{\text{T}}$ in the selected events. As expected for $W \to \tau_{\text{had}}\nu_\tau$ decays, the $E_{\text{T}}^{\text{miss}}$ spectrum reaches at maximum around 40 GeV and has a significant tail up to 80 GeV. Figures 6.11d and 6.11e show the distribution of the two τ_{had} identification variables R_{EM} (left) and R_{track} in the signal region. The distance of tracks and calorimeter cells associated to the τ_{had} candidates is small, as expected for genuine hadronically decaying τ leptons.

Furthermore, the kinematic quantities of the τ_{had} candidates are investigated: The spectrum of the transverse momentum, the pseudorapidity, the number of tracks of the hadronic decay products of the τ and the sum of their charges are shown in Figs. 6.12a–6.12d. The τ_{had} candidates have relatively low momenta, as expected for signal events. Mainly events with one or three tracks associated to the τ_{had} candidates are found, which is typical for the hadronically decaying τ leptons (Sec. 5.1). More

[10] The statistical uncertainty on $N^{\text{A}}_{\text{QCD}}$ includes both the uncertainty on the calculation of the c_i coefficients, due to the statistical uncertainty of the simulated samples, and the statistical uncertainty of data in the four regions. For the cross section measurement this ΔN_{QCD} uncertainty is categorised as systematic uncertainty.

[11] These variables quantify the weighted distance of calorimeter energy depositions and tracks of τ_{had} candidates (Sec. 5.2), see Appendix A for the exact definition.

[12] The predictions of shape and normalisation of the QCD background are also tested using the corresponding alternative control region (B or C) for each variable and also a good agreement of the QCD background prediction in the signal region is found. This shows that the background estimation is robust and unbiased from these differences in selection [127].

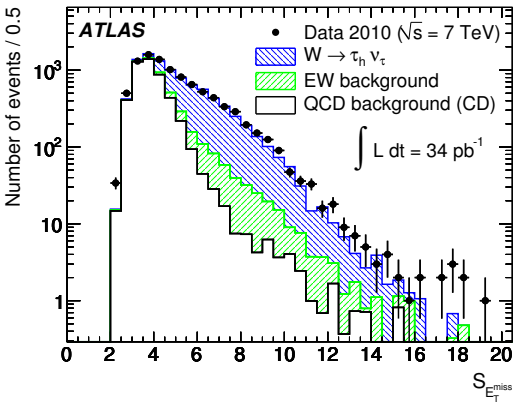

(a)

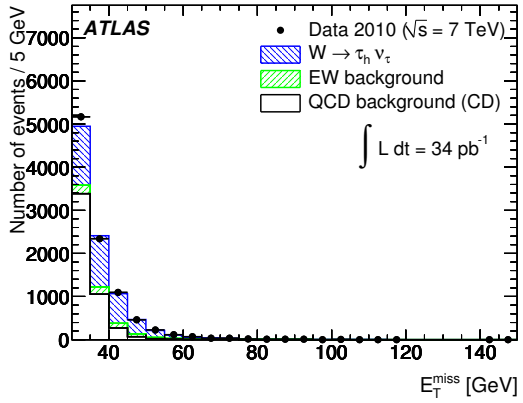

(b)

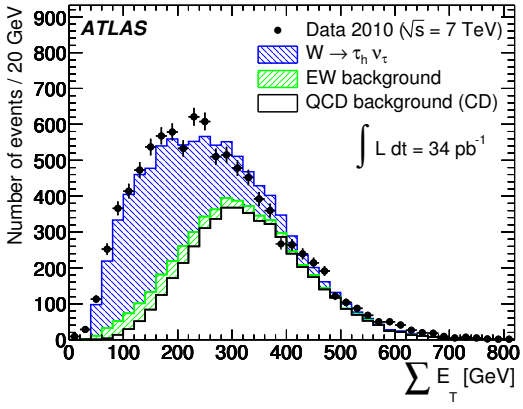

(c)

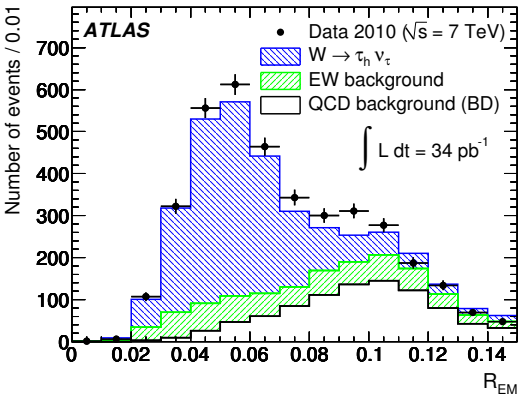

(d)

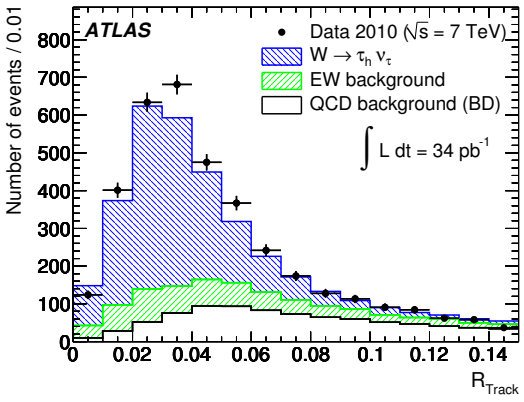

(e)

Figure 6.10: Distribution of (a) missing transverse energy significance, (b) missing transverse energy, (c) $\sum E_{\mathrm{T}}$ in the combined region AB (in (a) extended over the full $S_{E_{\mathrm{T}}^{\mathrm{miss}}}$ range). The QCD background shape has been extracted from the combined regions CD. Distribution of the two τ_{had} identification variables (d) R_{EM} and (e) R_{track} in the combined region AC. The QCD background shape has been extracted from the combined region BD. The expected signal and EW background contributions are also shown, normalised to the theoretical NNLO cross section.

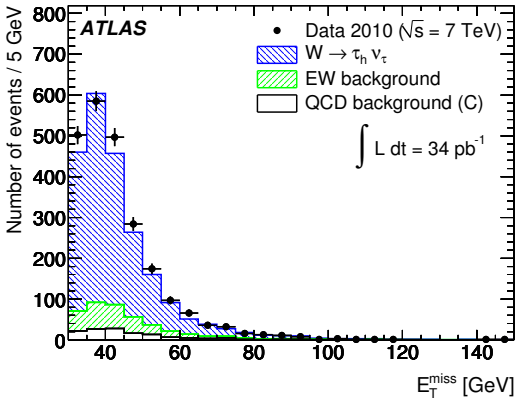

(a)

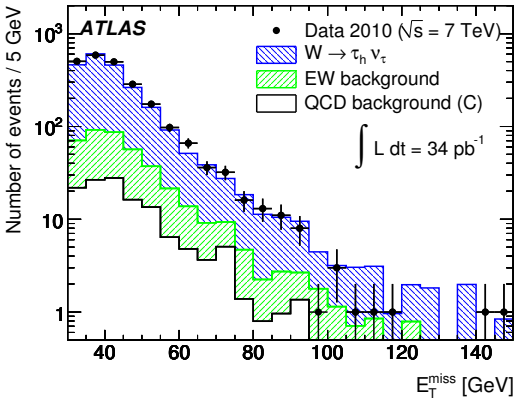

(b)

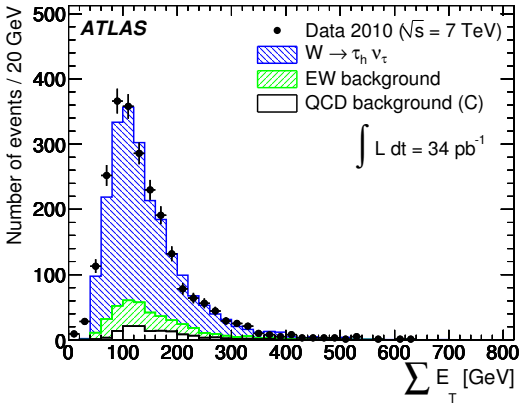

(c)

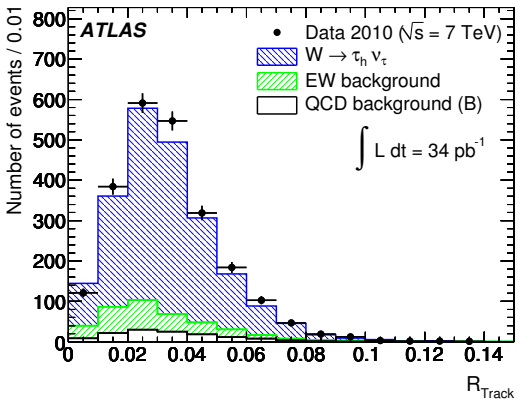

(d)

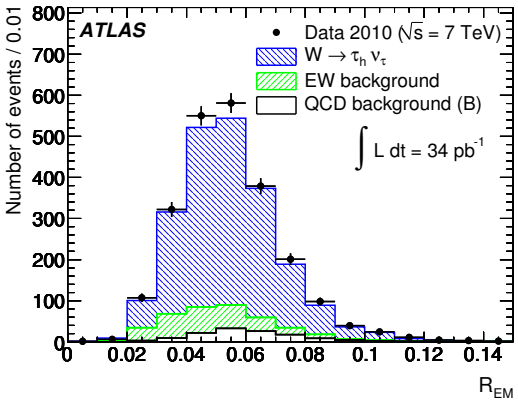

(e)

Figure 6.11: Distribution of missing transverse energy in (a) linear and (b) logarithmic scale, (c) $\sum E_{\mathrm{T}}$, two τ_{had} identification variables (d) R_{EM} and (e) R_{track} in the signal region A after the full event selection. The QCD background shape has been extracted from region C or B. The expected signal and EW background contribution in region A are also shown, normalised to the theoretical NNLO cross section.

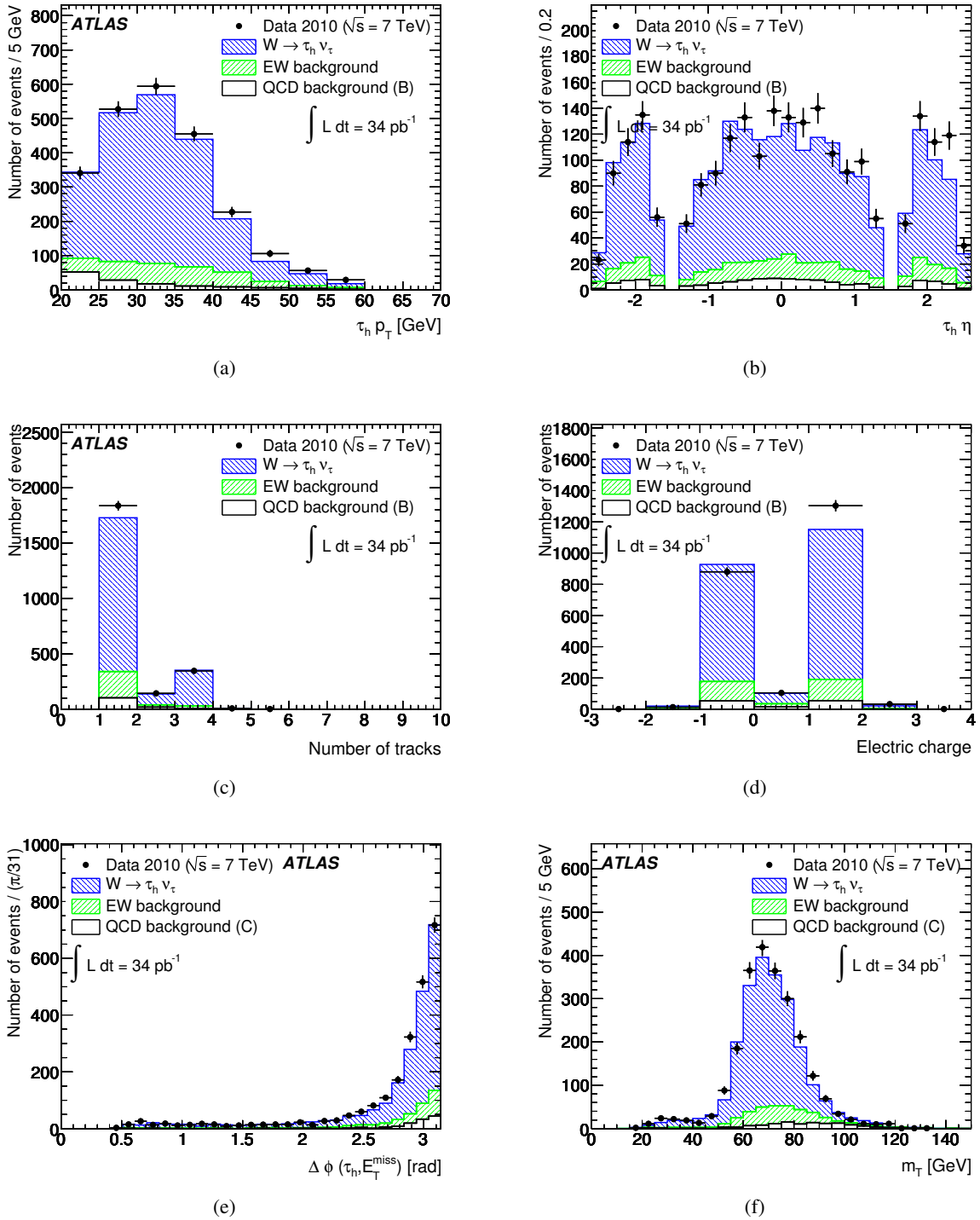

Figure 6.12: Distribution of (a) transverse momentum, (b) pseudorapidity and (c) the number of associated tracks and (d) the charge of the τ_{had} candidate, (e) $\Delta\phi$ between $E_{\text{T}}^{\text{miss}}$ and the τ_{had} candidate and (f) the transverse mass m_{T} in the signal region A after the full event selection. The QCD background shape has been extracted from region B or C. The expected signal and EW background contribution in region A are also shown, normalised to the theoretical NNLO cross section.

candidates are selected with a positive charge than with a negative charge. This results from the higher probability of W^+ production at pp colliders (Sec. 4.1.1).

Figures 6.12e and 6.12f show characteristic observables combining the $E_{\mathrm{T}}^{\mathrm{miss}}$ and τ_{had} quantities: The $\Delta\phi$ separation of $E_{\mathrm{T}}^{\mathrm{miss}}$ and the τ_{had} candidate, and the transverse mass (Eq. 6.2). The large separation in ϕ, typical for $W \to \tau_{\mathrm{had}}\nu_\tau$ decays, is clearly visible in data. As expected, the transverse mass has values between 60 and 80 GeV.

All kinematic observables show the typical behaviour of $W \to \tau_{\mathrm{had}}\nu_\tau$ decays, which further confirms that a clean sample of signal events has been selected in data. In all distributions reasonable agreement is found between data and the expectation of $W \to \tau_{\mathrm{had}}\nu_\tau$ signal and background. It is already visible, that the signal cross section measured in data is slightly higher than the theoretical prediction to which the simulated signal sample is normalised. The observed differences between data and model are covered by the combined systematic and statistical uncertainties of data and the background models, as shown in Appendix B.

A detailed analysis of all sources of systematic uncertainties is presented in Sec. 6.7.

6.6 Measurement of the Cross Section

The procedure for the cross section measurement has been explained in Sec. 4.2.1.

For the $W \to \tau_{\mathrm{had}}\nu_\tau$ signal process in particular, the total cross section is defined as the product of the W production cross section at the LHC, the branching ratio of the $W \to \tau\nu_\tau$ decay and the hadronically decaying τ lepton: $\sigma^{\mathrm{tot}}_{W\to\tau_{\mathrm{had}}\nu_\tau} \equiv \sigma^{\mathrm{tot}}_{W} \times \mathrm{BR}(W \to \tau\nu_\tau) \times \mathrm{BR}(\tau \to (\mathrm{had})\nu_\tau)$. According to Eqs. 4.1 and 4.4, the total and fiducial cross sections of the $W \to \tau_{\mathrm{had}}\nu_\tau$ decay are thus defined as:

$$\sigma^{\mathrm{tot}}_{W\to\tau_{\mathrm{had}}\nu_\tau} = \frac{N_{\mathrm{obs}} - N_{\mathrm{EW}} - N_{\mathrm{QCD}}}{A_W C_W \mathcal{L}}; \; \sigma^{\mathrm{fid}}_{W\to\tau_{\mathrm{had}}\nu_\tau} = \sigma^{\mathrm{tot}}_{W\to\tau_{\mathrm{had}}\nu_\tau} \cdot A_W \tag{6.7}$$

At this point of the analysis the number of data events and the estimated number of background events in the selected sample, N_{obs} and $N_{\mathrm{bkg}} = N_{\mathrm{EW}} + N_{\mathrm{QCD}}$, have been determined as stated in Tab. 6.4.

The phase space region in which the fiducial cross section is measured is derived from the geometrical acceptance of the detector and the kinematic selection of the analysis (Sec. 6.3). This region is defined based on the decay products from a simulated hadronic τ decay and corresponds to the following criteria at generator level, i.e. before detector simulation and reconstruction:

- $20 < p_{\mathrm{T}}^{\tau,\mathrm{vis}} < 60$ GeV
- $|\eta^{\tau,\mathrm{vis}}| < 2.5$, excluding $1.3 < |\eta^{\tau,\mathrm{vis}}| < 1.7$
- $(\sum p^{\nu})_{\mathrm{T}} > 30$ GeV
- $|\Delta\phi(p^{\tau,\mathrm{vis}}, \sum p^{\nu})| > 0.5$

Here, the visible τ momentum $p_{\mathrm{T}}^{\tau,\mathrm{vis}}$ and the pseudorapidity $\eta^{\tau,\mathrm{vis}}$ are calculated from the sum of the *truth* four-vectors of all *visible* hadronic τ decay products. This momentum also includes photons radiated both from the τ lepton and from the decay products themselves, considering only photons within $\Delta R < 0.4$ with respect to the τ lepton. The minimum $E_{\mathrm{T}}^{\mathrm{miss}}$ requirement translates into a momentum threshold on the transverse component of the sum of the simulated neutrino four-vectors $(\sum p^{\nu})_{\mathrm{T}}$. According to Eq. 4.2 the fiducial acceptance factor A_W is defined as the fraction of the total generated events found in this geometrical region.

The correction factor C_W (Eq. 4.3) is calculated as the fraction of all generated signal events within the fiducial region that passes the trigger requirements, the reconstruction and the full event selection.

The two factors are determined with the help of the PYTHIA Monte Carlo $W \to \tau_{\text{had}}\nu_\tau$ event sample (Sec. 6.2). The measured values A_W, C_W, $\sigma^{\text{tot}}_{W\to\tau_{\text{had}}\nu_\tau}$ and $\sigma^{\text{fid}}_{W\to\tau_{\text{had}}\nu_\tau}$ are listed in Tab. 6.5. The different sources of systematic uncertainties on these measured observables are investigated in the next section.

A_W	0.0975 ± 0.0004 (MC stat.)
C_W	0.0799 ± 0.0011 (MC stat.)
$\sigma^{\text{fid}}_{W\to\tau_{\text{had}}\nu_\tau}$	$(0.70 \pm 0.02$ (stat.)) nb
$\sigma^{\text{tot}}_{W\to\tau_{\text{had}}\nu_\tau}$	$(7.2 \pm 0.2$ (stat.)) nb

Table 6.5: Measured values of the fiducial acceptance factor A_W (Eq. 4.2), the correction factor C_W (Eq. 4.3) the fiducial and total cross section of the $W \to \tau_{\text{had}}\nu_\tau$ decay (Eq. 6.7). Stated are the statistical uncertainties of data (stat.) and simulation (MC stat.)[13].

Analysis Cross Checks

Since the $W \to \tau_{\text{had}}\nu_\tau$ cross section measurement as presented in this chapter is one of the first analyses that investigates final states with $E_{\text{T}}^{\text{miss}}$ and hadronically decaying τ leptons in ATLAS data, cross checks of the implemented analysis method are particularly important to confirm the obtained results.

Several modifications to selection and background estimation are studied, focussing on the two main aspects: Since the BDT τ_{had} identification algorithm is quite complex (Sec. 5.2), it is tested if the results are influenced by the τ_{had} selection method. Due to the increasing luminosity, it is investigated if the results are influenced by different pile-up conditions. The following alternations of the analysis have been studied:

- The simpler cut-based τ_{had} identification method is used for the selection and the definition of the control regions, which relies only on three variables to select τ_{had} candidates (Appendix A).
- The selected data sample is restricted to events with only one reconstructed primary vertex, to see if the pile-up effects influence the result.
- The selected data sample is split according to the number of tracks (one-prong and multi-prong) and charges (positive and negative) in order to confirm that a consistent result can be obtained with the two respective subsamples.
- Different BDT τ_{had} identification working points are tested for the selection of signal sample and background estimation.
- An alternative calculation of $S_{E_{\text{T}}^{\text{miss}}}$ using the sum of the track transverse momenta instead of calorimeter cell energies in the denominator of Eq. 6.3 is tested, since the track momentum measurement is in general less sensitive to pile-up effects.

[13] These uncertainties on A_W and C_W resulting from the limited size of simulated samples are categorised as systematic uncertainty for the cross section measurement.

All these alternative methods yield consistent results compared to the baseline analysis in terms of a good signal and background modelling and a consistent cross section within statistical uncertainties. The first two cross checks are explained more detail here[14].

Selection of events with the cut-based τ_{had} identification The same analysis as presented above is performed using the simple cut-based method for the τ_{had} identification instead of the BDT ID algorithm. Also the medium working point is used to achieve a comparable signal efficiency (Sec. 5.2).

The rest of the event selection and background estimation is applied in the same way as described in Secs. 6.3 and 6.4. To define the regions B and D for the QCD background estimation the *loose* working point of the cut-based τ_{had} ID algorithm is used.

Table 6.6 shows the resulting event yields for signal region A and the three control regions in data, as well as the expected signal and background contribution. The fraction of background is much higher after the full event selection compared to the main analysis with the BDT τ_{had} ID selection (Tab. 6.4), due to the much lower background rejection efficiency of the cut-based τ_{had} ID.

Figure 6.13a shows the $S_{E_{\text{T}}^{\text{miss}}}$ distribution in the combined region AB. Figures 6.13b–6.13d show a few examples of the main characteristic distributions of the $W \to \tau_{\text{had}}\nu_\tau$ decay in the signal region. More variables are shown in Appendix B.

All figures show reasonable agreement between data and the expected signal and background, similar to the standard method. The cross section calculated from the measured values agrees within statistical uncertainties with the result in Tab. 6.5. This alternative analysis thus further confirms the consistency of the analysis with different τ_{had} identification methods.

Study of events with one primary vertex As a second test the analysis is restricted to events with only one primary vertex. The definition of the background control regions and the selection of the signal region is exactly the same as in the main analysis (see above). The number of events in data and the expected signal and background contributions can be seen in Tab. 6.7.

Figure 6.14a shows the $S_{E_{\text{T}}^{\text{miss}}}$ distribution in the combined region AB. Figures 6.14b–6.14d show a few examples of the main characteristic distributions of the $W \to \tau_{\text{had}}\nu_\tau$ decay in the signal region. More variables are shown in Appendix B.

Reasonable agreement between data and the expectated signal, EW and QCD background can be seen, similar to the main analysis. The derived cross section agrees within statistical uncertainties with the result in Tab. 6.5. The consistency between the subsample with one vertex and the full sample with no restriction on the vertex multiplicity shows that the influence of pile-up effects on the result is small.

[14] The other cross checks are described in [127].

	A	B	C	D
N^i (Data)	3248	21435	1734	35437
N^i_{sig} $(W \to \tau_{\text{had}}\nu_\tau)$	2169 ± 28	2935 ± 32	578 ± 12	790 ± 14
N^i_{EW}	428 ± 9	501 ± 9	348 ± 8	269 ± 7
c_i		1.32 ± 0.02	0.36 ± 0.01	0.41 ± 0.01
N^A_{QCD}	363 ± 34			

Table 6.6: Estimated sample compositions and c_i factors (as defined in Eq. 6.5) in the signal region A and control regions B, C, and D. The cut-based τ_{had} identification is used for the selection of signal and control regions.

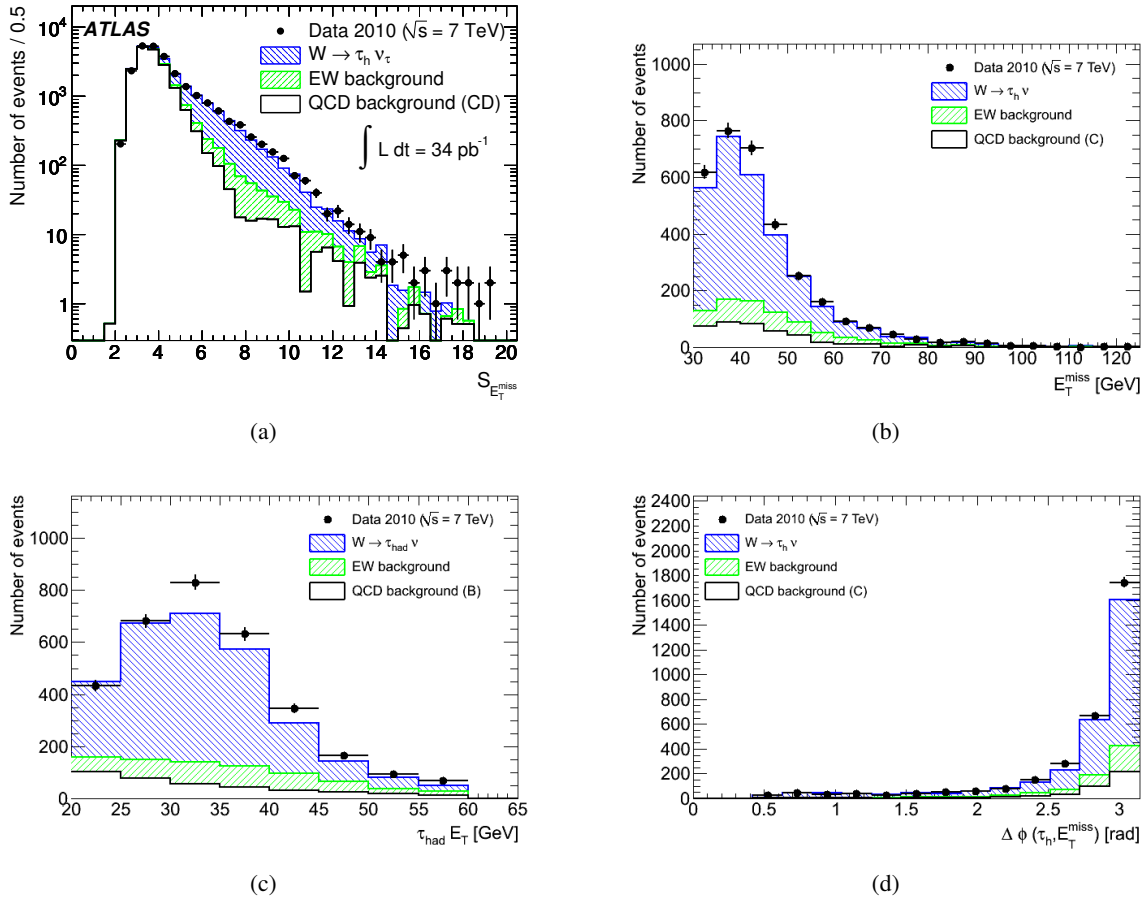

Figure 6.13: Analysis with the cut-based τ_{had} identification used for the selection of signal and control regions: (a) Distribution of missing transverse energy significance in the combined region AB, extended over the full $S_{E_{\text{T}}^{\text{miss}}}$ range. The QCD background shape has been extracted from the combined region CD. Distribution of (b) missing transverse energy, (c) τ_{had} transverse momentum and (d) $\Delta\phi$ between $E_{\text{T}}^{\text{miss}}$ and the τ_{had} candidate in the signal region A after the full event selection. The QCD background shape has been extracted from region B or C. The expected signal and EW background is also shown, normalised to the theoretical cross section at NNLO.

	A	B	C	D
N^i (Data)	1054	370	714	2710
N^i_{sig} ($W \to \tau_{\text{had}}\nu_\tau$)	778 ± 20	29 ± 4	103 ± 7	3.5 ± 1.0
N^i_{EW}	122 ± 5	4.7 ± 0.9	144 ± 7	7.5 ± 1.5
c_i		0.040 ± 0.002	0.27 ± 0.01	0.010 ± 0.001
N^A_{QCD}	54 ± 5			

Table 6.7: Estimated sample compositions and c_i factors (as defined in Eq. 6.5) in the signal region A and control regions B, C, and D for events with exactly one primary vertex.

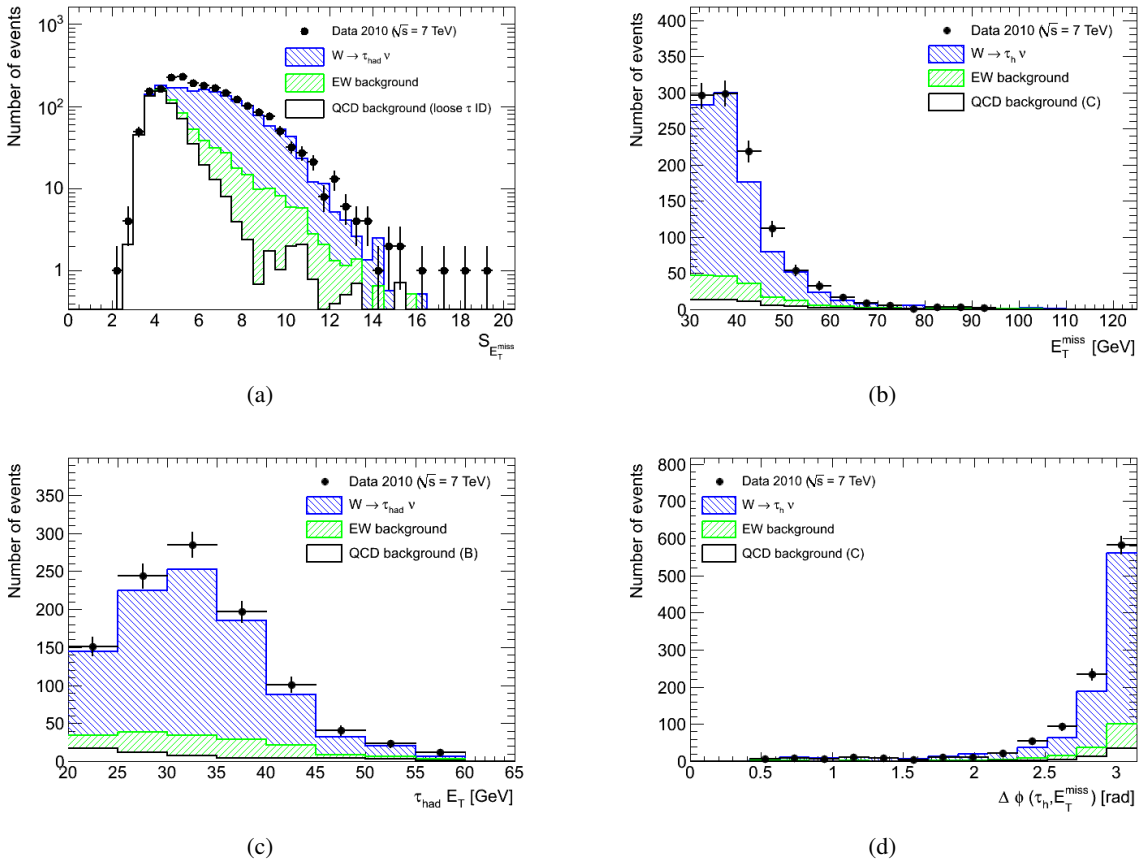

Figure 6.14: Analysis of events with one primary vertex: (a) Distribution of missing transverse energy significance in the combined region AB, extended over the full $S_{E_{\text{T}}^{\text{miss}}}$ range. The QCD background shape has been extracted from the combined region CD. Distribution of (b) missing transverse energy, (c) τ_{had} transverse momentum and (d) $\Delta\phi$ between $E_{\text{T}}^{\text{miss}}$ and the τ_{had} candidate in the signal region A after the full event selection. The QCD background shape has been extracted from region B or C. The expected signal and EW background is also shown, normalised to the theoretical cross section at NNLO.

6.7 Systematic Uncertainties

In this section the sources of systematic uncertainties that affect the cross section measurement are discussed. They can be grouped into three different types:

- Experimental uncertainties resulting from kinematic reconstruction of the event, object identification and selection efficiencies and affecting the measured physics objects (τ_{had}, leptons, $E_{\text{T}}^{\text{miss}}$).
- Uncertainties which are associated with the data-driven method used to model the QCD background and to determine the accuracy of the prediction of background shape and normalisation in the selected sample.
- Theoretical uncertainties that affect the background prediction of simulated samples and the calculation of the fiducial acceptance and correction factors.

In the following, they are listed individually for the different measured parameters, N_{EW}, N_{QCD}, C_W, A_W and luminosity.

Monte Carlo predictions (N_{EW} and C_W)

Two of the measured quantities are based on the prediction from detector simulation: The number of EW background events N_{EW} and the correction factor C_W. They are affected by the following systematic uncertainties:

Trigger The efficiency of the combined τ_{had}-$E_{\text{T}}^{\text{miss}}$ triggers used in the two data periods is measured with the help of simulation (Tab. 6.2). The systematic uncertainty is determined from the differences in the trigger responses of the individual trigger components observed between data and simulation (Fig. 6.4)[15].

For each component (τ_{had} and $E_{\text{T}}^{\text{miss}}$) of the two triggers, the uncertainty is derived from the observed differences integrated over the $E_{\text{T}}^{\text{miss}}$ and τ_{had} p_{T} range that is studied in this analysis. These uncertainties are combined to derive the systematic uncertainty of the looser and tighter trigger used in both data periods. The latter are finally combined and weighted by the integrated luminosity to obtain the total systematic uncertainty on the trigger efficiency. The different uncertainties of the individual trigger components are summarised in Tab. 6.8.

The correlation of the $E_{\text{T}}^{\text{miss}}$ and τ_{had} trigger components, which is not taken into account with this procedure, is studied by comparing the turn-on curves of the *combination* and *product* of both trigger components in simulation. It is found to be negligible [127].

τ_{had} identification efficiency The uncertainties on the modelling of the τ_{had} reconstruction and the BDT identification as a function of the number of tracks and vertex multiplicity are taken into account as well [101].

[15] The commonly used procedure to account for differences between data and simulation is to correct the simulated samples to the data efficiency and apply the uncertainty of the efficiency measurement as systematic uncertainty (as it is also done in the $H \to \tau_{\text{lep}}\tau_{\text{had}}$ analysis (Chap. 7). However, at this early stage of the ATLAS data taking the precise efficiency measurements in data are still under development, e.g. in the case of the trigger no estimate of the combined τ_{had}-$E_{\text{T}}^{\text{miss}}$ trigger efficiency in data is possible due to low statistics. Therefore, no corrections are applied to simulation in this $W \to \tau_{\text{had}}\nu_\tau$ analysis. The observed differences in efficiencies between simulation and data are applied as conservative estimate of the systematic uncertainty.

Trigger component	Systematic uncertainty
Looser trigger	
τ_{had} component	6.5%
$E_{\text{T}}^{\text{miss}}$ component	1.0%
Combined	6.6%
Tighter trigger	
τ_{had} component	5.0%
$E_{\text{T}}^{\text{miss}}$ component	3.2%
Combined	5.9%
Combination of both triggers	6.1%

Table 6.8: Summary of systematic uncertainties on the trigger efficiency.

Energy scale and resolution The signal and background acceptances depend on the energy scale of the clusters used for the computation of $E_{\text{T}}^{\text{miss}}$ and $S_{E_{\text{T}}^{\text{miss}}}$ and the energy scale of the τ_{had} candidates. The sources of systematic uncertainties affecting the τ_{had} and cluster energy in simulation are studied individually in the analysis and then combined: The energy scale uncertainty on clusters is evaluated separately in the central region of the detector ($|\eta| < 3.2$) and the forward region ($|\eta| > 3.2$). In the former case, also the energy scale uncertainty of τ_{had} candidates is studied simultaneously.

The uncertainty on the cluster energy calibrated with the LCW calibration (Sec. 5.3) within an detector region $|\eta| < 3.2$ is at most 10% for a p_{T} of 500 MeV and within 3% at higher p_{T} [111]. To account for these uncertainties, all topoclusters are rescaled by the factor $1 + a\,(1 + 1.2/p_{\text{T}})$ with $a = \pm 0.03$, and $E_{\text{T}}^{\text{miss}}$ and $\sum E_{\text{T}}$ are recomputed. At the same time the τ_{had} energy scale is varied according to its uncertainty, which ranges from 2.5% to 10%, depending on its p_{T}, η and number of tracks (Sec. 5.2 and [101]).

In a second test, the clusters in the forward region ($|\eta| > 3.2$) are varied within their uncertainty of 10% [111].

In addition, the effect of the $E_{\text{T}}^{\text{miss}}$ resolution on the signal and background efficiency is investigated. The $E_{\text{T}}^{\text{miss}}$ resolution is measured to be $0.5\sqrt{\sum E_{\text{T}}}$ for minimum bias events in data, but found to be slightly larger in the presence of high-p_{T} jets (Sec. 5.3 and [110]). Therefore x and y components of $E_{\text{T}}^{\text{miss}}$ are multiplied with an additional Gaussian function to model a resolution of up to $0.55\sqrt{\sum E_{\text{T}}}$, which covers this uncertainty.

Finally, the effect of an exclusion of the inner ring cells of the forward detector components in $|\eta| > 4.5$ for the $E_{\text{T}}^{\text{miss}}$ calculation is studied. This region is poorly modelled in simulation and is studied as separate source of systematic uncertainty [128].

For each of these variations the largest deviation from the nominal signal and EW background yield is determined and then combined to the total systematic uncertainty. The different systematic uncertainties are summarised for all affected samples in Tab. 6.9.

	$W \to \tau_{\text{had}}\nu_\tau$	$W \to e\nu_e$	$W \to \mu\nu_\mu$	$W \to \tau_{\text{lep}}\nu_\tau$	$Z \to \tau\tau$
Energy scale $\lvert\eta\rvert < 3.2$ (τ_{had}/cluster)	5.6%	9.1%	5.0%	6.0%	5.3%
Energy scale $\lvert\eta\rvert < 3.2$ (cluster)	2.4%	4.5%	2.3%	5.1%	2.3%
$E_{\text{T}}^{\text{miss}}$ resolution	2.7%	9.6%	2.3%	5.5%	2.6%
Excluding FCal inner ring	0.6%	2.8%	0.1%	0.6%	0.8%
Total systematic uncertainties	6.7%	14.1%	5.8%	9.6%	6.2%

Table 6.9: Relative variation of event selection efficiency due to uncertainties on the energy scale and resolution. The effect of each source of systematic uncertainty (energy scale uncertainty in central and forward detector region, $E_{\text{T}}^{\text{miss}}$ resolution and exclusion of the inner FCal ring) and the total systematic uncertainty for signal and EW background processes are shown. Only non-negligible EW background processes are investigated.

$e \to \tau_{\text{had}}$ and $j \to \tau_{\text{had}}$ misidentification The probability to misidentify a jet or lepton as τ_{had} candidate is evaluated in data and compared to the simulation in order to determine the systematic uncertainties. Table 6.10 shows the composition of the W background processes based on these different misidentification cases for all events that pass the full event selection. In order to measure the $j \to \tau_{\text{had}}$ misidentification probability, a sample of $W \to \ell\nu$ events (with $\ell = e, \mu$) with at least one additional jet is selected in data. In this sample, the fraction of QCD jets that are reconstructed and identified as τ_{had} candidates (according to the τ_{had} selection applied to this analysis) is measured. Comparing this misidentification probability to the one in simulation yields a difference of 31%. This is taken into account as systematic uncertainty for all events in which a jet is misidentified as electron in the EW background according to Tab. 6.10.

The $e \to \tau_{\text{had}}$ misidentification probability is measured in a $Z \to ee$ data sample with a tag-and-probe method. This method is explained in detail in Sec. 5.2.1. The difference that is found between data and simulation is taken into account as systematic uncertainty for the fraction of events, where the τ_{had} candidate is mimicked by an electron (Tab. 6.10). The systematic uncertainty is found to be 13.5% for the simulated $W \to e\nu_e$ sample.

Since the probability of a $\mu \to \tau_{\text{had}}$ misidentification is in general very small (Sec. 5.2) and only a small fraction of $W \to \mu\nu_\mu$ events pass the $W \to \tau_{\text{had}}\nu_\tau$ selection criteria on $E_{\text{T}}^{\text{miss}}$ and τ_{had} due to the low energy deposits of muons in the calorimeters, only a few events of this type remain after the full event selection (Tab. 6.3). The systematic uncertainty arising from the differences in simulation and data in the misidentification probability is therefore not further investigated in this analysis.

	$W \to e\nu_e$	$W \to \mu\nu_\mu$
$e \to \tau_{\text{had}}$	70%	-
$\mu \to \tau_{\text{had}}$	-	59%
$j \to \tau_{\text{had}}$	30%	41%

Table 6.10: Fraction of events passing the full $W \to \tau_{\text{had}}\nu_\tau$ event selection, where an electron, muon or jet is misidentified as τ_{had} candidate in $W \to \mu\nu_\mu$ and $W \to e\nu_e$ decays.

Electron and muon reconstruction/identification efficiency The uncertainties of the muon and electron reconstruction efficiencies are also taken into account, since they affect the veto of reconstructed/identified leptons in the event selection. The resulting differences in signal and background acceptance due to the different identification and reconstruction efficiencies in data and simulation is taken as systematic uncertainty in the analysis [45, 47].

Underlying event modelling In order to study the influence of the underlying event model, in particular on $E_{\mathrm{T}}^{\mathrm{miss}}$ quantities, alternative models to the AMBT1 tune (Sec. 6.2) are investigated. A Pythia sample with the Perugia2010 tune [129] is used for comparison. The resulting differences in the signal and EW background acceptance between the two tools are taken as systematic uncertainty. The good agreement of the $E_{\mathrm{T}}^{\mathrm{miss}}$ based quantities between the simulated signal and embedded samples (Fig. 6.6) further confirms that the underlying event is well modelled in simulation and no further uncertainties have to be considered.

Pile-up reweighting The procedure to correct for pile-up effects by reweighting the simulated samples to the vertex distribution in data is affected by the statistical uncertainties of data and simulation. The systematic uncertainty is evaluated by varying the weights within their statistical uncertainty and comparing the results after the event selection.

Cross section Since the event yields for each EW background sample are scaled according to the theoretical NNLO cross section, the uncertainties on these values also influence the precision of the $W \to \tau_{\mathrm{had}}\nu_\tau$ cross section measurement.

For the W and Z decays to light leptons and $t\bar{t}$ processes the uncertainties on the cross section are derived from the ATLAS measurements, they range from 3.8% to 9.7% [119, 122]. For $Z \to \tau\tau$ and $W \to \tau_{\mathrm{lep}}\nu_\tau$ decays no measurement results are available at the time of the analysis, thus the uncertainty on the theoretical NNLO calculation is used instead. It takes into account uncertainties on the proton PFDs, the coupling constant a_S and renormalisation and factorisation scales and is estimated to be 5% [17, 118].

QCD Background Estimation (N_{QCD})

In order to assess the systematic uncertainty on the number of QCD background events N_{QCD} estimated by the data-driven method (Sec. 6.4), the following sources of systematic uncertainties are taken into account:

Correlation of variables An assumption of the QCD estimation is that $S_{E_{\mathrm{T}}^{\mathrm{miss}}}$ and τ_{had} identification are not correlated. The small differences observed in Fig. 6.9 might result from a minimal correlation of the two variables. In order to quantify this correlation, the $S_{E_{\mathrm{T}}^{\mathrm{miss}}}$ threshold to define region B and D is varied between 4 and 6. The largest deviation of the resulting number of QCD background events estimated from these regions is taken as systematic uncertainty.

Correction for signal and EW background The correction for signal and EW background contributions in the QCD control regions is affected by the systematic and statistical uncertainties of the simulated samples. To investigate the systematic uncertainty the total signal and EW background yields in these regions are varied within the combination of their systematic and statistical uncertainty. The difference in the resulting QCD estimation is taken as systematic uncertainty.

Fiducial Acceptance (A_W)

Two sources of systematic uncertainties are studied for the measurement of the fiducial acceptance factor A_W:

Proton PDF The measurement is affected by the uncertainties on the proton PDFs. In order to estimate the effect on the analysis different PDF sets are compared. The signal sample using the MRSTLO* is reweighted to alternative PDF sets (CTEQ6.6 and HERAPDF1.0 [18], see Sec. 3.5). The maximum difference in the acceptance after the application of the fiducial selection criteria defined in Sec. 6.6 is used as systematic uncertainty.

Also the uncertainty due to the PDF fit itself is evaluated with the help of the CTEQ6.6 set. The signal sample is reweighted from the default set to the set where the individual PDF fit parameters have been varied within their uncertainty [127].

Modelling of W production The uncertainty on the modelling of the W production is evaluated by replacing the Pythia signal sample by a Mc@nlo sample (Sec. 3.5), where the parton shower is modelled by Herwig, and the change of the fiducial acceptance is investigated[16].

Luminosity $\mathcal{L}$

Also the uncertainty on the integrated luminosity influences the cross section measurement. It is measured to be 3.4% [27, 130].

Summary of Systematic Uncertainties

Table 6.11 summarises the systematic uncertainties that affect the quantities measured in the selected signal sample. Shown are all considered uncertainties for the number of EW background events N_{EW}, the QCD background events N_{QCD} and the correction factor C_W.

In the table also the effects of all systematic uncertainties on the accuracy of the fiducial cross section measurement are shown. For this calculation, the correlation of systematic uncertainties that affect several experimental observables simultaneously have been taken into account, e.g. in the case of the τ_{had} ID efficiency. Also the statistical uncertainties of the simulated signal and EW background and the QCD estimate (Tabs. 6.4 and 6.5) are included as further sources of systematic uncertainties affecting the cross section measurement.

For the calculation of the total cross section (Eq. 6.7) the theoretical uncertainties affecting the fiducial acceptance factor A_W are taken into account as well, they are summarised in Tab. 6.12.

The total systematic uncertainty on the fiducial cross section amounts to 15.1%. The largest sources of systematic uncertainties in the cross section measurement are the energy scale with 8% and the τ_{had} ID efficiency with 10.3%. This is expected since they are associated to the most important event selection criteria: The energy scale strongly influences $E_{\mathrm{T}}^{\mathrm{miss}}$, $S_{E_{\mathrm{T}}^{\mathrm{miss}}}$ and the τ_{had} momentum, the corresponding selection criteria provide an efficient suppression of the large QCD and EW background. In addition, also the τ_{had} identification plays a central role for the selection of a pure signal sample.

[16] Since Herwig in association with external generators does not handle the effects of τ polarisation correctly, the acceptance measured with the Mc@nlo is corrected for this effect [127].

	$\frac{\delta C_W}{C_W}$	$\frac{\delta N_{\mathrm{EW}}}{N_{\mathrm{EW}}}$	$\frac{\delta N_{\mathrm{QCD}}}{N_{\mathrm{QCD}}}$	$\frac{\delta\sigma^{\mathrm{fid}}_{W\to\tau_{\mathrm{had}}\nu_\tau}}{\sigma^{\mathrm{fid}}_{W\to\tau_{\mathrm{had}}\nu_\tau}}$
Trigger efficiency	6.1%	6.1%	-	7.0%
Energy scale	6.7%	8.7%	-	8.0%
τ_{had} ID efficiency	9.6%	4.1%	-	10.3%
$j \to \tau_{\mathrm{had}}$ misidentification	-	7.2%	-	1.1%
$e \to \tau_{\mathrm{had}}$ misidentification	-	4.5%	-	0.7%
Pile-up reweighting	1.4%	1.2%	-	1.6%
Electron reconstruction/identification	-	1.2%	-	0.2%
Muon reconstruction	-	0.3%	-	0.04%
Underlying event modelling	1.3%	1.1%	-	1.5%
Cross section	-	4.5%	-	0.7%
QCD estimation: Stability/correlation	-	-	2.7%	0.2%
QCD estimation: Sig./EW contamination	-	-	2.1%	0.1%
Statistical uncertainty (MC, QCD)	1.4%	2.4%	6.0%	1.5%
Total systematic uncertainty	13.4%	15.2%	6.9%	15.1%

Table 6.11: Summary of the systematic uncertainties affecting the measured quantities C_W, the correction factor, N_{EW} and N_{QCD}, the expected number of EW and QCD background events in the selected data sample. Also the effects of the uncertainties on the fiducial cross section (Eq. 6.7) are shown. For the calculation of this uncertainty correlations between the systematic uncertainties affecting C_W and N_{EW} have been taken into account.

	$\frac{\delta A_W}{A_W}$
PDF	1.9%
W production model	0.2%
Statistical uncertainty (MC)	0.4%
Total systematic uncertainty	2.0%

Table 6.12: Summary of systematic uncertainties affecting the fiducial acceptance factor A_W (Eq. 4.2).

6.8 Results and Interpretation

The final results on the measured observables relevant to the $W \to \tau_{\text{had}}\nu_\tau$ cross section measurement including their systematic uncertainties are listed in Tab. 6.13.

N_{obs}	2335
N_{QCD}	127 ± 9 (syst.)
N_{EW}	284 ± 43 (syst.)
A_W	0.0975 ± 0.0019 (syst.)
C_W	0.0799 ± 0.0107 (syst.)

Table 6.13: Measured quantities including their systematic uncertainties used for the cross section calculation.

Fiducial cross section

Within the acceptance region defined in Sec. 6.6 this translates into the following measured fiducial cross section of the $W \to \tau_{\text{had}}\nu_\tau$ decay:

$$\sigma^{\text{fid}}_{W\to\tau_{\text{had}}\nu_\tau} = \sigma^{\text{fid}}_{W} \times \text{BR}(W \to \tau\nu_\tau) \times \text{BR}(\tau \to (\text{had})\nu_\tau) = (0.70 \pm 0.02\,(\text{stat.}) \pm 0.11\,(\text{syst.}) \pm 0.02\,(\text{lumi.}))\,\text{nb}$$

Total cross section

Including the acceptance factor this yields a total $W \to \tau_{\text{had}}\nu_\tau$ cross section of:

$$\sigma^{\text{tot}}_{W\to\tau_{\text{had}}\nu_\tau} = \sigma^{\text{tot}}_{W} \times \text{BR}(W \to \tau\nu_\tau) \times \text{BR}(\tau \to (\text{had})\nu_\tau) = (7.2 \pm 0.2\,(\text{stat.}) \pm 1.1\,(\text{syst.}) \pm 0.2\,(\text{lumi.}))\,\text{nb}$$

After correcting the cross section for branching ratio of a hadronically decaying τ lepton $\text{BR}(\tau \to \text{had}\nu_\tau)$, 0.6479 ± 0.0007 [2], this yields the following *inclusive* cross section of the $W \to \tau\nu_\tau$ decay:

$$\sigma^{\text{tot}}_{W\to\tau\nu_\tau} = \sigma^{\text{tot}}_{W} \times \text{BR}(W \to \tau\nu_\tau) = (11.1 \pm 0.3\,(\text{stat.}) \pm 1.7\,(\text{syst.}) \pm 0.4\,(\text{lumi.}))\,\text{nb}$$

Interpretation of Results

The measured inclusive cross section is in good agreement with the theoretical prediction at NNLO, $\sigma^{\text{NNLO}}_{W\to\tau\nu_\tau}(10.46 \pm 0.52)$ nb [72, 118, 119] and the ATLAS measurements of the $W \to e\nu_e$ and $W \to \mu\nu_\mu$ cross sections, $\sigma^{\text{tot}}_{W\to e\nu_e} = (10.26 \pm 0.03\,(\text{stat.}) \pm 0.19\,(\text{syst.}) \pm 0.35\,(\text{lumi.}) \pm 0.16\,(\text{acc.}))\,\text{nb}$ and $\sigma^{\text{tot}}_{W\to\mu\nu_\mu} = (10.21 \pm 0.03\,(\text{stat.}) \pm 0.18\,(\text{syst.}) \pm 0.35\,(\text{lumi.}) \pm 0.15\,(\text{acc.}))\,\text{nb}$ [73]. The comparison of the cross section measurements for the different lepton final states with ATLAS and the theoretical expectation is shown in Fig. 6.15.

After the here presented analysis was published, the same measurement has also been performed by the CMS collaboration at $\sqrt{s} = 7$ TeV with a data sample of 32 pb^{-1} [131]. The resulting cross section of $\sigma^{\text{tot}}_{W\to\tau\nu_\tau} = (8.96 \pm 0.51\,(\text{stat.})\,^{+2.32}_{-2.26}\,(\text{syst.}) \pm 0.36\,(\text{lumi.}))\,\text{nb}$ is also in good agreement with the here described ATLAS measurement.

This analysis is the first $W \to \tau\nu_\tau$ cross section measurement performed at the LHC and is therefore an important milestone in the starting phase of the LHC physics program in understanding and measuring the Standard Model processes with its detectors. This process is a significant source of background in

searches for new physics involving τ_{had} leptons, in particular the $H \to \tau\tau$ decay which is topic of the next chapter.

Moreover, it is also the first measurement of a physics process with τ_{had} candidates performed in ATLAS. The developed methods and the results obtained during this analysis successfully tested the τ_{had} reconstruction and identification algorithms and also the measurement of $E_{\text{T}}^{\text{miss}}$, which are the fundamental ingredients to many physics processes at the LHC. In particular, they also constitute the final state of the $H \to \tau_{\text{lep}}\tau_{\text{had}}$ decay. The study of the τ_{had} and $E_{\text{T}}^{\text{miss}}$ performance in the framework of the $W \to \tau\nu_\tau$ cross section measurement therefore form an important basis to develop a sensitive analysis to search for $H \to \tau_{\text{lep}}\tau_{\text{had}}$ decays in ATLAS data.

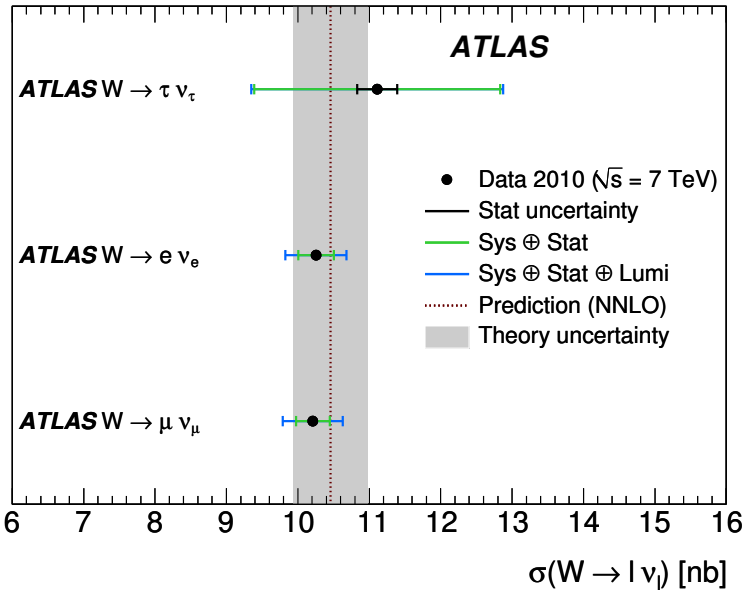

Figure 6.15: Cross sections for the different $W \to \ell\nu_\ell$ channels measured in ATLAS with 2010 data (points). Systematic, luminosity and statistical uncertainties are added in quadrature. The theoretical NNLO expectation is also shown (dashed line) together with its uncertainty (filled area).

CHAPTER 7

Search for the Standard Model Higgs Boson in the $\tau_{\text{lep}}\,\tau_{\text{had}}$ Final State

In this chapter a search for the $H \to \tau\tau$ decay in the $\tau_{\text{had}}\,\tau_{\text{lep}}$ final state in 2012 ATLAS data corresponding to a total integrated luminosity of 20.3 fb^{-1} is presented. This analysis has the goal to contribute to a first observation of $H \to \tau\tau$ decays in ATLAS in order to establish evidence for the direct Yukawa coupling to fermions of the Higgs boson (Sec. 4.1.3).

Section 7.1 outlines the strategy and main goals of the analysis and puts it in context with previous and complementary searches for $H \to \tau\tau$. Next, an overview of the characteristics and kinematics of the $H \to \tau_{\text{lep}}\tau_{\text{had}}$ decay and the background processes, which form the basis for the development of the analysis methods, is provided in Sec. 7.2. In Sec. 7.3 the preselection applied to data events and the reconstruction of event kinematics and the invariant $m_{\tau\tau}$ mass are explained. Section 7.4 motivates and describes the choice of analysis categories and corresponding selection criteria. In Sec. 7.5 the methods to estimate the contribution of the different sources of background and their validation are explained. The final composition of the signal region and mass distributions are investigated in 7.6. Section 7.7 lists the relevant sources of systematic uncertainties. Finally, the test of the signal hypothesis in data with a profile likelihood fit is described in Sec. 7.8. In Sec. 7.9 the fit results are presented and interpreted.

7.1 Outline of the Analysis Strategy

The search for the $H \to \tau\tau$ decay with the ATLAS detector divides into the different possible final states resulting from the τ decays: $H \to \tau_{\text{lep}}\tau_{\text{lep}}$, where both τ leptons decay leptonically to a light charged lepton (e or μ) accompanied by four neutrinos; $H \to \tau_{\text{lep}}\tau_{\text{had}}$, where one τ lepton decays leptonically and the other one hadronically and three additional neutrinos occur; $H \to \tau_{\text{had}}\tau_{\text{had}}$, where both τ leptons decay to hadrons with only two accompanying neutrinos.

The $H \to \tau_{\text{lep}}\tau_{\text{had}}$ channel is studied in this thesis. It has the largest branching ratio of all τ pair decays (46%). The lepton has a very clear signature in the detector, which allows to efficiently trigger possible signal events and to achieve a good suppression of background processes like multi-jet production. The hadronically decaying τ on the other hand has a large branching ratio, which increases the acceptance of signal events (Sec. 5.2). Moreover, it is accompanied by only one neutrino. With three neutrinos in total in the final state, a better mass reconstruction is possible than in the fully leptonic decay. This decay channel is therefore expected to yield the highest sensitivity on a Higgs signal among the three $H \to \tau\tau$

decay channels.

The final goal is to combine the $H \to \tau_{\text{lep}}\tau_{\text{had}}$ analysis with the other two analysis channels, to profit from the accumulated sensitivities of all three decay channels (Chap. 8).

The low cross section times branching ratio of the $H \to \tau\tau$ decay and the complex topology of the leptonically and hadronically decaying τ leptons with a large amount of missing transverse energy arising from the three neutrinos lead to the following challenges for the $H \to \tau_{\text{lep}}\tau_{\text{had}}$ analysis:

- A low signal-to-background ratio is expected with large contributions of background processes with $j \to \tau_{\text{had}}$ and $\ell \to \tau_{\text{had}}$ misidentifications and of the irreducible $Z \to \tau\tau$ background. The latter is hardly distinguishable from the signal since it features the same final state of two τ leptons coming from a heavy particle with a similar mass.

- A poor resolution of the invariant $m_{\tau\tau}$ mass due to the multiple neutrinos, the limited energy resolution of $E_{\text{T}}^{\text{miss}}$ and the τ_{had} momentum.

The main challenges of an analysis to search for a $H \to \tau_{\text{lep}}\tau_{\text{had}}$ signal are thus to increase the signal-to-background ratio, estimate the different sources of background and to measure the $\tau\tau$ mass as precisely as possible. The analysis is designed as follows:

Preselection Events are selected with the exact set of well-reconstructed objects that is expected for the Higgs signal events. In particular, τ_{had} identification and lepton veto algorithms are applied to reduce the large background of jets and leptons misreconstructed as τ_{had} candidates.

Categorisation The data events are grouped into different categories. These make use of different kinematic properties of the Higgs production mechanisms, in order to select specific types of signal events with a high signal-to-background ratio or a high mass resolution. For example, a category with the signature of VBF signal events is defined, or another one that contains events with a high Higgs transverse momentum. This concept increases the overall sensitivity to a possible Higgs signal of this analysis compared to a fully inclusive analysis [132].

Event selection For each category a set of quantities is used to discriminate between signal and background. They are based on of the kinematic properties of the Higgs decay products and production mechanisms in the respective category. Selection criteria based on these quantities are applied with the goal to maximise the signal-to-background ratio in each category.

Most sensitive observable The invariant $m_{\tau\tau}$ mass distribution is the key observable of this analysis. It provides the highest separation power of signal and background, in particular of the irreducible $Z \to \tau\tau$ background. A signal of a Higgs boson would manifest as an excess in this distribution over the total background. A good modelling and precise reconstruction are therefore crucial. Although it cannot be directly measured in data, an approximate value is obtained by the missing mass calculator. It recovers the missing kinematic information from the neutrinos. This distribution is the basis for the final hypothesis test to evaluate the compatibility of data with a Higgs signal.

Background estimation In order to minimise systematic uncertainties due to inaccurate modelling of processes in simulation, the contributions of the major sources of background are estimated from data (*data-driven* analysis method). For $Z \to \tau\tau$ an embedding technique is used (Sec. 4.3). For other sources of background, such as multi-jets, W+jets, top decays and $Z \to \ell\ell$, control regions in data are defined from which the shape and/or normalisation of the background is derived.

Signal extraction Finally, a profile likelihood fit based on the mass distributions of the selected data events in each category (Sec. 4.2.2) is performed. It tests the compatibility of the measurement with a $H \to \tau_{\text{lep}}\tau_{\text{had}}$ signal and gives an estimate of the observed significance and signal strength. All sources of statistical and systematic uncertainties of the analysis are taken into account in the form of nuisance parameters in the fit.

The analysis presented in the following is based on previous $H \to \tau\tau$ searches with ATLAS. The first effort to search for a generic Higgs boson decaying to τ leptons was made based on the first data collected with ATLAS in 2010 (36 pb^{-1}) and 2011 (1.06 fb^{-1}) at $\sqrt{s} = 7$ TeV in the context of the minimal supersymmetric SM [133, 134]. The 2011 analysis also established upper limits on the cross section times branching ratio of a SM $H \to \tau\tau$ decay. The first dedicated search for SM $H \to \tau\tau$ decays in data was published in [132] based on the full data set recorded in 2011 at $\sqrt{s} = 7$ TeV (4.6 fb^{-1}). Individual categories were formed to select signal events in a specific phase space. In addition, the object-based $E_{\text{T}}^{\text{miss}}$ calibration was used based on studies described in Sec. 5.3.1 which increased the resolution of the invariant mass significantly. This led, together with the larger data sample, to significantly improved upper limits on the SM $H \to \tau\tau$ cross section times branching ratio.

The first $H \to \tau_{\text{lep}}\tau_{\text{had}}$ search that has been performed in this thesis includes a re-analysis of the ATLAS data taken in 2011 of 4.6 fb^{-1} at $\sqrt{s} = 7$ TeV and an analysis of the first 13.0 fb^{-1} of 2012 data at $\sqrt{s} = 8$ TeV [97]. Major improvements of the categorisation, event selection and the background estimation methods are introduced, which led together with the larger size of the data sample to a much improved upper limit of the cross section times branching ratio in comparison to the previous results, bringing the analysis very close to an observation or exclusion of $H \to \tau\tau$ decays in data. These results are summarised in Appendix C.

Two different concepts are developed in parallel for the subsequent analysis of the *full* 2012 data set corresponding to an integrated luminosity of 20.3 fb^{-1} with the goal to provide evidence for the direct Higgs coupling to fermions already in Run 1: The first analysis is the topic of this thesis and described in detail in this chapter[1]. It has the purpose to continue the already established methods as described above and transfer them on the full data sample. It uses the $m_{\tau\tau}$ mass distribution to test the compatibility of data with a potential signal and thus can directly compare different Higgs mass hypotheses. The second analysis uses a multivariate approach to improve the sensitivity on a Higgs signal in data with the help of statistical learning algorithms [135]. The statistical analysis of data is based on the multivariate discriminant, which does not contain a direct mass information. These two conceptually different and complementary analysis methods provide an independent cross check and thus additional confirmation of the search results. The analysis concepts and results obtained with both methods are compared in Chap. 8, also for the combination of all $H \to \tau\tau$ decays channels. These results are published in [136].

Although it is intended to keep the $H \to \tau_{\text{lep}}\tau_{\text{had}}$ analysis concept presented in this chapter close to the one developed for first part of the 2012 data set (13.0 fb^{-1}), it is important to re-investigate the analysis methods on the full data sample: Besides a larger data sample, also simulated W+jets, $Z \to \ell\ell$ and embedded $Z \to \tau\tau$ samples with significantly more events are available. Under these conditions of reduced statistical uncertainties, categorisation, event selection and background estimation methods are validated and it is tested if there is further potential for optimisation. Moreover, the effects of improved τ_{had} identification algorithms and $E_{\text{T}}^{\text{miss}}$ reconstruction (Chap. 5, [105, 113]) are studied, which should contribute to an improved resolution of the $m_{\tau\tau}$ mass and a reduction of systematic uncertainties.

[1] Since the contribution of the 2011 data set to the sensitivity on a $H \to \tau_{\text{lep}}\tau_{\text{had}}$ signal in data is expected to be small compared to the full 2012 data sample, it is not included in this final analysis presented here.

7.2 Signal and Background Processes

Higgs Signal

In this thesis the Higgs boson decay to a pair of leptonically and hadronically decaying τ leptons is investigated. It features a reconstructed τ_{had} [2], one isolated electron or muon and a significant $E_{\text{T}}^{\text{miss}}$ resulting from the three neutrinos in the final state. The Feynman graph of this decay can be seen in Fig. 7.1. The energies of the τ decay products are expected to be relatively high due to the large mass difference m_τ/m_H. Moreover, they are all expected to be produced centrally in the detector.

In case no additional particles are produced apart from the Higgs boson in the event, its transverse momentum is very small. The two τ leptons are emitted in opposite direction in the transverse plane. Since the τ decay products are usually emitted almost collinear with the τ leptons, this leads to a small missing transverse energy, since the neutrino momenta cancel each other. If additional high-p_{T} jets occur, the Higgs boson can gain a high transverse momentum, i.e. it is *boosted* in the transverse plane of the detector. This increases the p_{T} of the τ leptons and in particular $E_{\text{T}}^{\text{miss}}$, since the neutrino momenta add up in this case. Since the resolution of high momentum objects is much better, this improves also the resolution of the invariant $m_{\tau\tau}$ mass. The two different scenarios of a low and high Higgs transverse momentum are illustrated in Fig. 7.2.

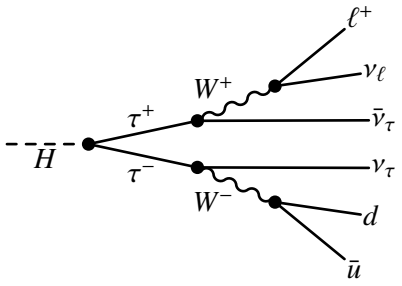

Figure 7.1: Feynman diagram of the $H \to \tau\tau$ decay to a leptonically and hadronically decaying pair of τ leptons.

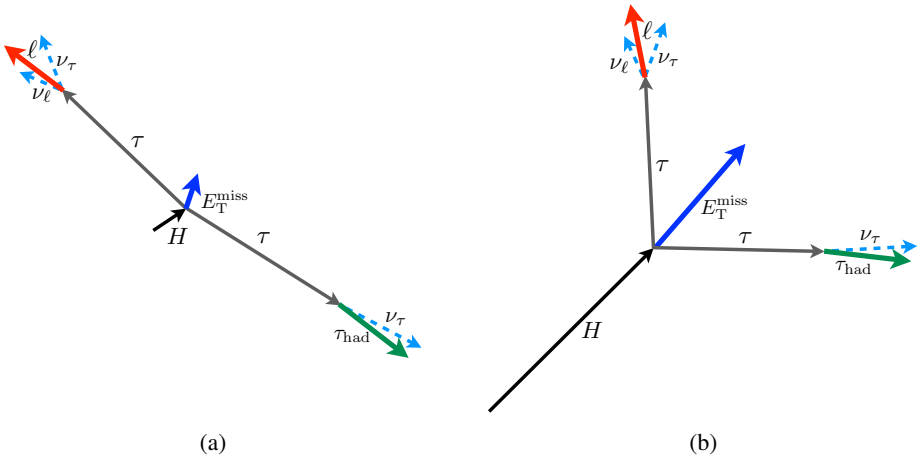

(a) (b)

Figure 7.2: Sketch of the kinematics in the $H \to \tau_{\text{lep}}\tau_{\text{had}}$ decay in the transverse plane with (a) a low Higgs transverse momentum (b) a significant boost of the Higgs boson.

[2] As explained in Sec. 5.1 this is built from the visible decay products of the hadronically decaying τ lepton, i.e. the hadrons.

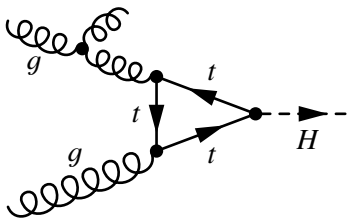

Figure 7.3: Example Feynman graph of NLO gluon fusion with a radiated gluon.

In the Standard Model four different mechanisms are predicted for the production of the Higgs boson (Sec. 4.1.2). The three with the largest cross section can be exploited in the search for $H \to \tau\tau$ with the ATLAS detector, gluon fusion, vector-boson fusion and the associated production with a vector boson, W or Z. They determine the kinematics of the Higgs boson and its decay products and their characteristic topologies can be exploited for a further separation from background processes. The corresponding Feynman diagrams are shown in Fig. 4.4. The cross section of the fourth production process (ttH) is too small to contribute significantly in comparison to the other production mechanisms.

The cross sections times branching ratio of these signal processes are summarised as an example for $m_H = 125$ GeV for $\sqrt{s} = 8$ TeV in Tab. 7.1. To obtain the cross section for the $H \to \tau_{\text{lep}}\tau_{\text{had}}$ decay mode, these numbers must be multiplied by the branching ratio $\text{BR}(\tau\tau \to \ell\text{had}3\nu) = 0.456 \pm 0.001$ [2].

	$\sigma_{\text{ggF}} \times \text{BR}$ [fb]	$\sigma_{\text{VBF}} \times \text{BR}$ [fb]	$\sigma_{\text{WH}} \times \text{BR}$ [fb]	$\sigma_{\text{ZH}} \times \text{BR}$ [fb]
$\sqrt{s} = 8$ TeV	$1218\,^{+144.4}_{-144.4}$	$99.73\,^{+6.26}_{-6.31}$	$44.53\,^{+2.78}_{-2.76}$	$26.25\,^{+1.83}_{-1.82}$

Table 7.1: SM Higgs boson cross sections times branching ratio calculated at NNLO for $H \to \tau\tau$ at a mass hypothesis of $m_H = 125$ GeV for the relevant Higgs production mechanisms ggF, VBF, WH and ZH in pp collisions at $\sqrt{s} = 8$ TeV [79].

The characteristics of these processes relevant for the $H \to \tau_{\text{lep}}\tau_{\text{had}}$ search are outlined in the following:

Gluon fusion The gluon fusion process has the largest cross section. At leading order, no additional particles from the production process occur thus $E_{\text{T}}^{\text{miss}}$ is expected to be relatively small as explained above. This makes a distinction from background processes difficult. At NLO however, radiated gluons or quarks result in additional jets, which cause the Higgs boson to have a significant transverse momentum and thus enhance the $E_{\text{T}}^{\text{miss}}$. An example is shown in Fig. 7.3. Since the ISR probability is higher for gluon initiated processes than for quark initiated ones, the jet multiplicity for this process is on average larger than for the main background process $q\bar{q} \to Z$ [4].

Vector-boson fusion The VBF production process has a cross section which is about one order of magnitude smaller than ggF. But the two additional jets (*tagging jets*) resulting from the two associated quarks provide a clear signature for an identification of this signal process and rejection of background. These quarks have usually a very high energy, since the vector bosons only carry a small fraction of the initial quark momentum (around $1/2m_H$). Their *transverse* momentum of the quarks is compared to their total momentum very small ($p_{\text{T}} \sim m_V$). As a consequence the tagging jets are typically found at a high pseudorapidities in opposite hemispheres of the detector and have a high invariant dijet mass. The $H \to \tau_{\text{lep}}\tau_{\text{had}}$ decay products usually lie in between the two tagging jets. Additional jets in the central region are usually not present: Additional gluons are mostly emitted at small angles in the forward/backward detector region, since the two VBF quarks do not exchange colour [4].

Associated production The VH production process has an even lower cross section, but in this case the decay products of the W, Z bosons occur as additional particles in the detector. These can be one or two additional leptons ($\ell\nu$ or $\ell\ell$), or two additional quarks. The leptonic decay is not exploited in the $H \to \tau_{\text{lep}}\tau_{\text{had}}$ analysis presented here, due to the very different signal topology, but is further investigated in Sec. 9.1. Due to these additional particles the Higgs boson and thus the τ decay products often have very high transverse momenta. This fact, together with the large jet multiplicity in case of the W/Z to quarks, are additional criteria to separate this signal process from background.

The p_{T} spectrum of all reconstructed $H \to \tau_{\text{lep}}\tau_{\text{had}}$ final state particles/objects, lepton (here electron), τ_{had} and $E_{\text{T}}^{\text{miss}}$, are shown in Fig. 7.4 for all investigated Higgs production processess. The shift of the spectra towards higher momenta for VBF and VH production processes is clearly visible. An event display of the characteristic appearance in the ATLAS detector of a candidate signal event is shown in Fig. 7.5.

In order to exploit the different characteristics of these production processes different categories are defined for the $H \to \tau_{\text{lep}}\tau_{\text{had}}$ search, based on their distinct signatures. This is explained in detail in Sec. 7.4.

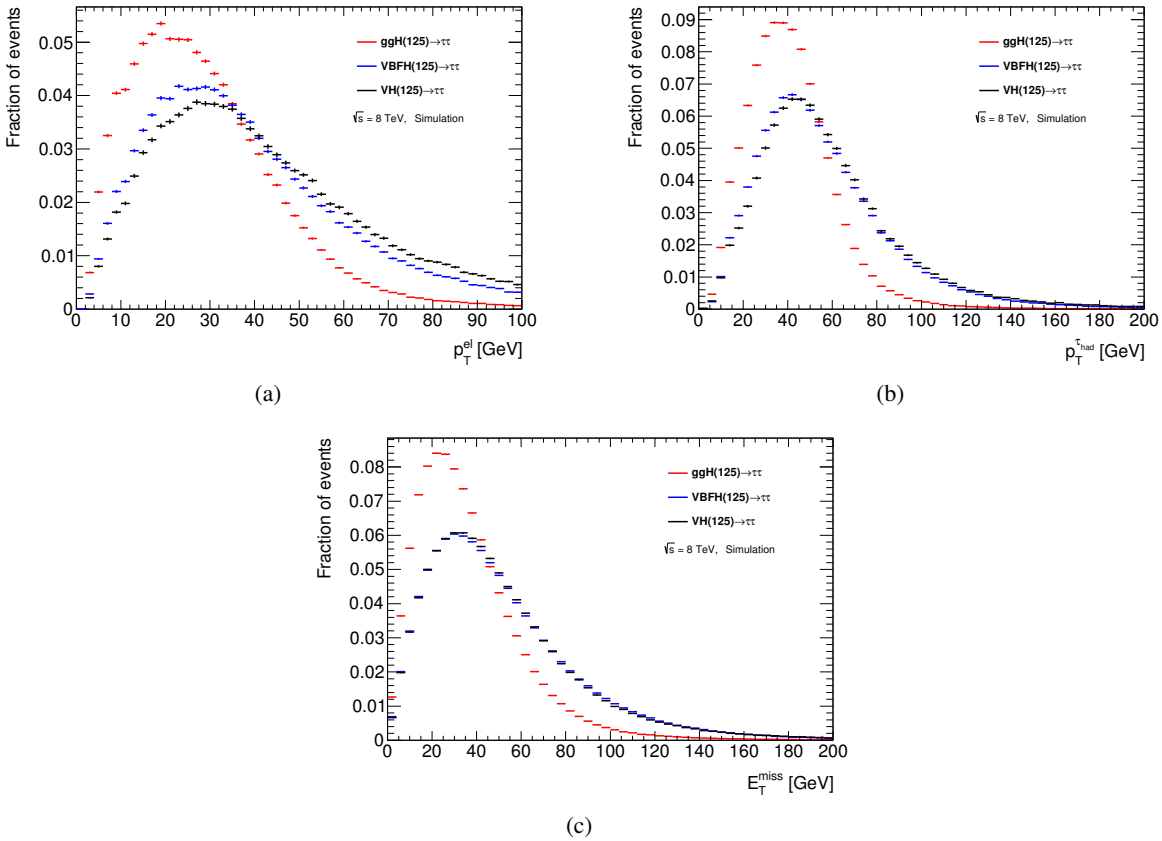

Figure 7.4: Kinematic distributions of the final $H \to \tau_{\text{lep}}\tau_{\text{had}}$ decay products after reconstruction: (a) Transverse momentum of the lepton (electron), (b) the τ_{had} and (c) $E_{\text{T}}^{\text{miss}}$ resulting from the three neutrinos. Shown are the three investigated processes of Higgs production: gluon-gluon fusion (red), vector-boson fusion (blue) and associated production with an electroweak boson (black) for a Higgs mass of 125 GeV, based on simulations at $\sqrt{s} = 8$ TeV.

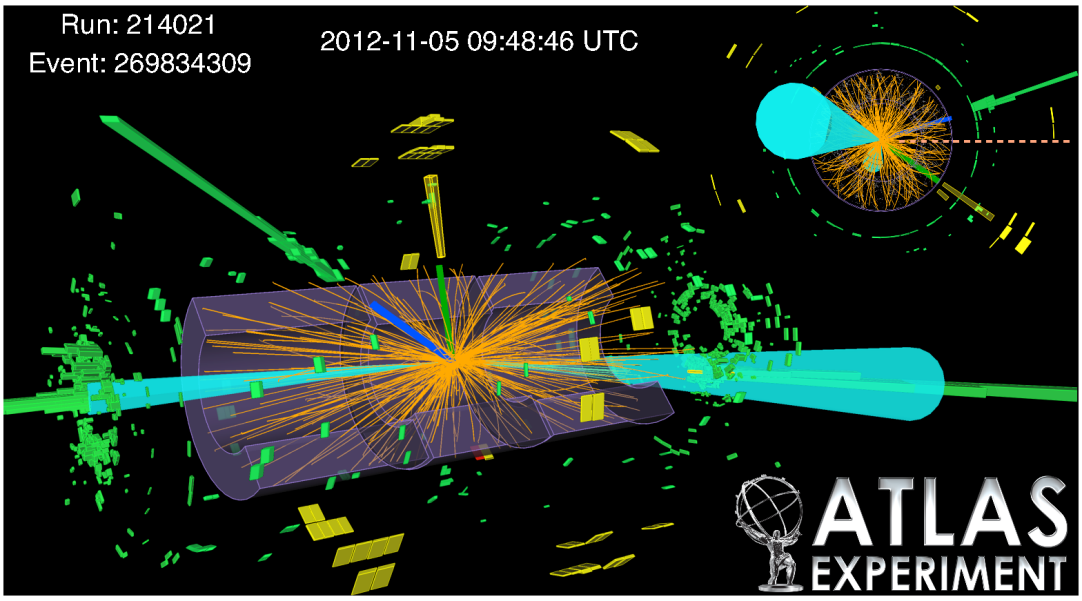

Figure 7.5: Event display of a $H \to \tau_{\text{lep}}\tau_{\text{had}}$ candidate produced via vector-boson fusion [137]. One τ decays to an electron (blue track matched to a green calorimeter cluster). The other hadronically decaying τ lepton has one track (green track and yellow calorimeter cluster). The two tagging jets are visualised as turquoise cones. The $E_{\text{T}}^{\text{miss}}$ direction is indicated by a pink dashed line in the transverse plane view (top right).

Background Processes

Several background processes can mimic the $H \to \tau_{\text{lep}}\tau_{\text{had}}$ signal. They can be grouped into different categories: An irreducible background is $Z \to \tau\tau$, since it has exactly the same final state. In addition, there are different reducible background processes. They contain either genuine hadronically decaying τ leptons and electrons or muons in the final state or misidentified ones. In the latter case QCD jets or a different lepton type are misidentified as the τ_{had} candidate or the light lepton. In general, due to the similar characteristics of jets and τ_{had} candidates the $j \to \tau_{\text{had}}$ and $e \to \tau_{\text{had}}$ misidentification cases are the dominating ones[3].

The main characteristics and challenges of each background process relevant to the $H \to \tau_{\text{lep}}\tau_{\text{had}}$ search are outlined in the following:

$Z \to \tau\tau$ This process has the identical final state and very similar kinematics as the $H \to \tau\tau$ signal. Therefore it is the dominant source of background and very difficult to reject. Two example Feynman graphs can be seen in Fig. 7.6, for a final state with no jets and two additional jets. In the first case the Z boson is produced from QCD interaction of two quarks, while in the second case it is produced from two vector bosons (EW interaction). The EW production is very similar to the VBF signal production process, and also results in almost the same jet properties, e.g. the dijet mass and their pseudorapidity distribution.

The most important criterion that can be used to distinguish between the $H \to \tau\tau$ and $Z \to \tau\tau$ decays is the different mass of the two bosons. The reconstructed invariant $\tau\tau$ mass (see Sec. 7.3) is therefore the most sensitive variable for a separation of this background (and all others) from the $H \to \tau_{\text{lep}}\tau_{\text{had}}$ signal. Consequently, a good reconstruction and resolution of the invariant

[3] The probability for a light lepton to be misidentified as a jet $\ell \to j$ after reconstruction and identification is roughly two orders of magnitude smaller than the $j \to \tau_{\text{had}}$ misidentification probability (Secs. 3.4 and 5.2).

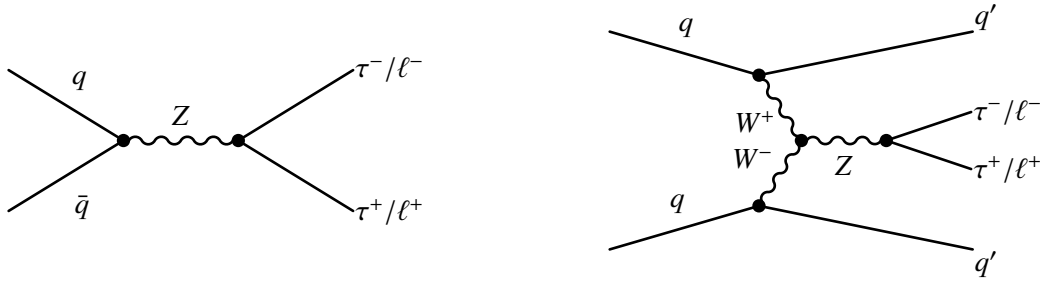

Figure 7.6: Example Feynman diagrams of Z boson production and decay to a pair of light leptons (e or μ) or τ leptons. (a) Leading order process from QCD interaction. (b) Z production from EW interaction with two associated quarks (jets).

mass is crucial for a good separation of these two processes, which implies in particular a good resolution of $E_{\mathrm{T}}^{\mathrm{miss}}$. In addition a good modelling of the $Z \to \tau\tau$ background needs to be ensured, which is particularly challenging since no signal-free region can be defined as a control region for this background.

$Z \to \ell\ell$+jets The $Z \to ee$ and $Z \to \mu\mu$ decays can mimic the signal signature, when one of the leptons fails the lepton reconstruction[4]. Two scenarios can occur: Either the second lepton is misidentified as hadronic τ candidate (denoted as $Z \to \ell\ell(\ell \to \tau_{\mathrm{had}})$ in the following) or the event features an additional jet, which fakes the τ_{had} candidate ($Z \to \ell\ell(\mathrm{j} \to \tau_{\mathrm{had}})$), compare Fig. 7.6. The first case is more problematic for a distinction from the signal process, since the mass of lepton and τ_{had} is close to the Higgs mass. The fraction of $Z \to \ell\ell$ events belonging to these two different classes is roughly 40% $Z \to \ell\ell(\ell \to \tau_{\mathrm{had}})$ and 60% $Z \to \ell\ell(\mathrm{j} \to \tau_{\mathrm{had}})$ after a loose preselection of $H \to \tau_{\mathrm{lep}}\tau_{\mathrm{had}}$-like events is applied (Sec. 7.3).

Due to the complex τ_{had} identification algorithms the modelling of these misidentification probabilities in simulation is difficult (see Sec. 5.2). An important aspect in the $H \to \tau_{\mathrm{lep}}\tau_{\mathrm{had}}$ search is therefore to estimate the difference of selection efficiencies between data and simulation and correct for them.

In order to mimic the signal signature, a significant amount of $E_{\mathrm{T}}^{\mathrm{miss}}$ must be reconstructed in the event. Although no genuine $E_{\mathrm{T}}^{\mathrm{miss}}$ is expected for these Z decays, mismeasurement of the energies of final state particles and the finite $E_{\mathrm{T}}^{\mathrm{miss}}$ resolution can lead to this. Consequently, a good resolution of $E_{\mathrm{T}}^{\mathrm{miss}}$ helps to reduce this background.

W+jets W decays also constitute a major source of background to the $H \to \tau_{\mathrm{lep}}\tau_{\mathrm{had}}$ signal, since they have a similar signature with one light lepton (electron, muon) or a hadronically or leptonically decaying τ lepton and $E_{\mathrm{T}}^{\mathrm{miss}}$. In contrast to the $Z \to \ell\ell$ decay no second lepton is present and only an additionally emitted jet can be misidentified as the τ_{had} candidate or the light lepton. W+jets is nevertheless is one of the leading background processes, since the cross section of this process is one order of magnitude higher compared to $Z \to \ell\ell$. The important Feynman graphs for the W production can be seen in Fig. 4.2. The $W \to \tau_{\mathrm{had}}\nu_\tau$ decay discussed in the previous chapter (Chap. 6) is one of the contributing final states to the W+jets background, although it plays a smaller role, since here the less likely case occurs that a jet is misidentified as the light lepton.

[4] The notation ℓ always refers to the decay to light leptons, i.e. electrons or muons, since τ leptons are usually treated separately.

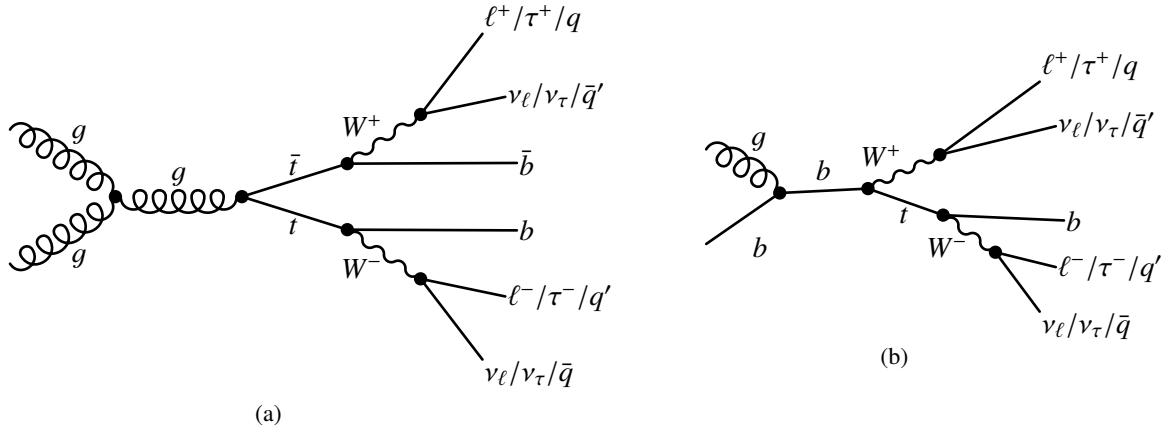

Figure 7.7: Example Feynman diagrams of (a) top-pair production and decay and (b) single top production and decay in association with a W boson.

Also for the W+jets background the good knowledge of misidentification probabilities and correction of the modelling in simulation is crucial for a precise estimation of the contribution of this background in the $H \to \tau_{\text{lep}}\tau_{\text{had}}$ search.

Top quark production Another non-negligible background is the production of two top quarks ($t\bar{t}$) or a single top quark, since genuine leptons (including τ leptons) and $E_{\text{T}}^{\text{miss}}$ often occur in the final state of the decay $t \to Wb$. Two examples for the Feynman graphs of these processes are shown in Fig. 7.7. In case of the $t\bar{t}$ process (Fig. 7.7a), the $H \to \tau_{\text{lep}}\tau_{\text{had}}$ final state is mimicked when one top quark decays to a hadronically decaying τ lepton and the other one to a light lepton and the accompanying neutrinos lead to significant $E_{\text{T}}^{\text{miss}}$. The two b-jets can in particular fulfil the criteria of the two high-p_{T} tagging jets characteristic for the signal VBF production process. If one lepton is lost or if one or both top quarks decay to light quarks, a jet is misidentified as the τ_{had} and/or the light lepton. Due to the small branching ratio of the $t\bar{t}$ decay to a genuine pair of τ and light lepton, the cases with genuine and misidentified particles contribute both with a similar probability as background to $H \to \tau_{\text{lep}}\tau_{\text{had}}$.

In single top production process also different scenarios can occur. If the top quark is produced in association with a W boson (Fig. 7.7b), the light lepton and τ_{had} lepton can be produced from the decay of the two W bosons. In the other cases, jets are misidentified as τ_{had} candidates and in rare cases also the light leptons.

Since in practically all top decays the characteristic b-jets occur, this background can be efficiently brought under control by applying a veto of b-jets found by the b-tagging algorithm (compare Sec. 3.4). For the decays with misidentified leptons and τ_{had} candidates, the measurement and correction of the misidentification probability in simulation play also an important role for the quantification of this background.

Diboson production Under this background all processes are summarised where a pair of electroweak bosons is produced (WW, WZ, ZZ). There is a large variety of topologies, genuine and misidentified τ_{had} candidates and leptons as well as $E_{\text{T}}^{\text{miss}}$ can occur. The WW decay is similar to the above explained $t\bar{t}$ decay, but the characteristic b-jets do not occur here. An example of a Feynman graph is shown in Fig. 7.8a. For ZZ decays the largest contribution as a background to $H \to \tau_{\text{lep}}\tau_{\text{had}}$ is the decay of one of the Z bosons to a lepton, which is then similar to the single Z production

explained above. The WZ process is also similar to single Z or W decays, depending on which of them decays to a light lepton. Decays to genuine τ and light leptons of both dibosons in ZZ and WZ are unlikely to contribute as background to the $H \to \tau_{\text{lep}}\tau_{\text{had}}$ signal, since more than two leptons occur in the final state.

The additional jets from the decays of Z and W often have different kinematics compared to the ones from the signal process. For instance the invariant mass of two jets from a vector boson is roughly $m_{jj} \approx m_V$, which is much smaller than in the VBF $H \to \tau_{\text{lep}}\tau_{\text{had}}$ signal process. Overall, the cross section times branching ratio of the diboson decay channels contributing as a background is not too large, therefore it constitutes one of the smaller background processes in the $H \to \tau_{\text{lep}}\tau_{\text{had}}$ search.

QCD production This background definition summarises all processes where only quarks and gluons are produced via QCD interactions. An example is shown in Fig. 7.8b. The signature of a $H \to \tau_{\text{lep}}\tau_{\text{had}}$ decay can only be mimicked, if two QCD jets are misidentified as the τ_{had} and light lepton. In addition, since no neutrinos occur in these processes, a significant amount of $E_{\text{T}}^{\text{miss}}$ can only be measured due to finite resolution and misreconstruction in the event. Although the probability for this is quite small, the total cross section of QCD processes is several order of magnitude higher compared to the signal production, which means that these cases contribute significantly as a source of background.

As explained for the $W \to \tau\nu_\tau$ analysis (Chap. 6), it is very difficult to model this background accurately in simulation. Therefore a reliable estimation of this background can only be based on a data control sample.

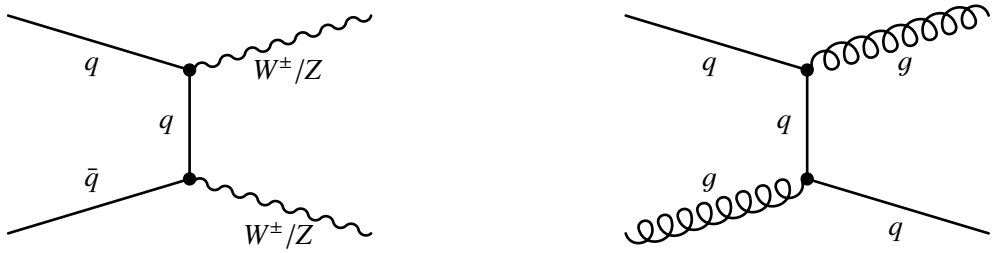

Figure 7.8: Example Feynman diagrams for (a) the production of a boson pair and (b) a process with pure QCD interaction.

Data and Simulated Samples

The search for the $H \to \tau_{\text{lep}}\tau_{\text{had}}$ decay presented in this chapter is based on proton-proton collisions collected with the ATLAS detector at a centre-of-mass energy of $\sqrt{s} = 8$ TeV in 2012. The integrated luminosity of the data set for which all subsystems of the ATLAS detector relevant for this analysis were fully operational is 20.3 fb^{-1} (Tab. 3.1).

The simulated samples used to investigate the signal and background processes in the $H \to \tau_{\text{lep}}\tau_{\text{had}}$ search are listed in the following. For a general description of generator types and the phenomenology of pp collisions see Secs. 3.5 and 2.2, respectively.

The simulation of signal events produced via ggF and VBF is provided by the Powheg [138, 139] event generator interfaced with Pythia and the CT10 [67] PDF set. The VH production is simulated

with Pythia and the CTEQ6L1 [66] PDF set. In the gluon fusion process, the Higgs boson transverse momentum spectrum is reweighted to the one provided by the HqT program [140], to ensure an accurate treatment of quark mass effects.

The SM cross sections times branching ratio for all Higgs production processes are calculated at NNLO (Tab. 7.1). Signal samples with masses in steps of 5 GeV in the mass range 100–150 GeV are investigated in this analysis to test different mass hypotheses.

The $Z \to \tau\tau$ process is simulated with an embedding technique, as explained in Secs. 4.3 and 7.5.

The background of all other W/Z+jets samples are simulated with the Alpgen generator interfaced with Pythia[5]. Since higher order electroweak corrections are not included by these generators, the production of $Z \to \ell\ell$ +jets via the EW interaction is simulated with Sherpa [141]. To compensate for high statistical uncertainties in the $Z \to \ell\ell$ data set as a background to Higgs signal events produced via VBF, samples with a filter condition are added. A filter to select events with the typical VBF signature is applied on generator level to gain a sample enriched with these events. The loose (tight) filter conditions applied are: $\Delta\eta_{jj} > 2.0$ (4.0) and $m_{jj} > 200$ (400) GeV for the leading pair of jets after hadronisation. These filtered samples are obtained with the Alpgen generator combined with Herwig/Jimmy. Finally, a hybrid of events from the loosely and tightly filtered samples and the unfiltered samples is used to model the $Z \to \ell\ell$ background. Corrections are applied to account for the different simulation of parton shower, hadronisation and underlying event in filtered and unfiltered samples, as explained in Sec. 7.5.

Top pair samples are produced with the Mc@nlo generator interfaced with Herwig/Jimmy, while single top events are generated with AcerMC [142] interfaced with Pythia. For the simulation of diboson production, Herwig is used as a generator for WZ and ZZ and Alpgen interfaced with Herwig/Jimmy for WW. Also loop-induced $gg \to WW$ processes are included, generated with the dedicated generator gg2WW [143].

The PDF set used with AcerMC, Alpgen and Herwig event generators is CTEQ6L1, while CT10 is used for the generation of events with Mc@nlo, Sherpa and gg2WW.

To fully match the simulated samples with the sample of data being studied, they are reweighted to adjust the distribution of the average number of interactions per bunch crossing to the one in data [144].

The normalisation of these background processes is either estimated from data control regions as described in 7.5, to correct for differences in modelling of e.g. misidentification probabilities, or calculated from their NLO cross sections. The order of magnitude of these cross sections can be seen in Fig. 4.1.

7.3 Preselection of Physics Objects and $\tau\tau$ Mass Reconstruction

Reconstruction of the Invariant $\tau\tau$ Mass

An accurate reconstruction of the $\tau\tau$ mass with a good resolution is crucial for the $H \to \tau_{\text{lep}}\tau_{\text{had}}$ search, as explained before: This observable is used in the profile likelihood fit to test the compatibility of data with a Higgs signal (Sec. 4.2.2), since it provides a very good separation of the signal from all other background processes, in particular $Z \to \tau\tau$. A complete reconstruction of four-momenta is only possible for the visible τ decay products, while for neutrinos only the sum of their transverse momenta is measured through $E_{\text{T}}^{\text{miss}}$. This makes a direct measurement of the invariant $m_{\tau\tau}$ mass in the event impossible. A complete reconstruction of the event kinematics and the original resonance is provided by the so called missing mass calculator (MMC) [145].

In the $H \to \tau_{\text{lep}}\tau_{\text{had}}$ decay channel, three additional neutrinos occur in the τ lepton decay. Consequently an equation system with seven unknown quantities has to be solved: Two sets of momentum

[5] For the low mass range $m_{\ell\ell}$ (10–60 GeV) they are generated with Alpgen combined with Herwig/Jimmy.

components (x, y, z) of the neutrinos, one from each τ decay, here the two neutrinos of the leptonically decaying τ lepton are combined; and the invariant mass of the two neutrinos from the leptonic τ decay. Four-momentum conservation and the assumption that $E_{\mathrm{T}}^{\mathrm{miss}}$ only results from the τ decay yields the following equations for the kinematics of the decay particles:

$$\begin{aligned} m_{\tau,i}^2 &= (p_{\mathrm{vis},i} + p_{\mathrm{miss},i})^2 \\ \vec{p}_{\mathrm{miss},i}^{\,2} &= E_{\mathrm{miss},i}^2 - m_{\mathrm{miss},i}^2 \\ \vec{E}_{\mathrm{T}}^{\mathrm{miss}} &= \vec{p}_{\mathrm{T,miss},1} + \vec{p}_{\mathrm{T,miss},2} \end{aligned} \tag{7.1}$$

Here the variable $p_{\mathrm{vis},i}$ denotes the four-momentum of the visible decay products of one of the two τ leptons ($i = 1, 2$) and $p_{\mathrm{mis},i}$ the four-momentum carried by the invisible neutrinos associated to either τ. $m_{\tau_i} = 1.777$ GeV is the τ lepton mass and $\vec{E}_{\mathrm{T}}^{\mathrm{miss}}$ the measured total missing transverse energy. $\vec{p}_{\mathrm{miss},i}$, $E_{\mathrm{miss},i}$ and $m_{\mathrm{miss},i}$ denote the three-momentum, the energy and the invariant mass of the neutrinos associated to either of the τ leptons. In the case of the hadronically decaying τ lepton, $m_{\mathrm{miss},i}$ is zero, since it is only accompanied by one neutrino.

Solving these equations leaves three free parameters (for example the azimuthal angles $\phi_{\mathrm{miss},1}$, $\phi_{\mathrm{miss},2}$ and the invariant neutrino mass from the leptonic τ decay $m_{\mathrm{miss},1}$). The MMC algorithm performs a scan of all possible values for the three free parameters in the full parameter space and for each point calculates the invariant $m_{\tau\tau}$ mass based on Eqs. 7.1. Constraints on these parameters are included based on the knowledge of τ decay kinematics to find the most likely solutions. In the current MMC implementation [97] the three-dimensional angle θ_{3D} between the visible and invisible decay products of each τ lepton is used for that purpose. Probability distribution functions are derived from simulated $Z \to \tau\tau$ decays as a function of the original τ transverse momentum for leptonic and hadronic τ decays. This information is included as an additional constraint in form of a global event weight:

$$P_{\mathrm{event}} = P(\Delta\theta_{3D,1}, p_{\tau,1}) \times P(\Delta\theta_{3D,2}, p_{\tau,2}) \tag{7.2}$$

Here $P(\Delta\theta_{3D,i}, p_{\tau,i})$ denotes the parametrised PDFs specific to the decay type. Each scan point is then weighted by this probability and the most likely $m_{\tau\tau}$ mass obtained from these scans is then taken as the final estimator of $m_{\tau\tau}$.

The performance of the MMC algorithm is highly correlated to the resolution of $E_{\mathrm{T}}^{\mathrm{miss}}$. To compensate for this effect, the possibility of a $E_{\mathrm{T}}^{\mathrm{miss}}$ mismeasurement is included in the invariant mass estimation. For this purpose the dimensionality of the scanned parameter space is increased to include the two components of $E_{\mathrm{T}}^{\mathrm{miss}}$ and probability functions $P(\Delta E_x^{\mathrm{miss}})$ and $P(\Delta E_x^{\mathrm{miss}})$ are added to the event weight. These PDFs are defined as:

$$P(\Delta E_{x,y}^{\mathrm{miss}}) = \exp\left(-\frac{(\Delta E_{x,y}^{\mathrm{miss}})^2}{2\sigma^2}\right) \tag{7.3}$$

σ is the $E_{\mathrm{T}}^{\mathrm{miss}}$ resolution measured with ATLAS (Sec. 5.3) and $\Delta E_{x,y}^{\mathrm{miss}}$ denotes the differences between the measured values of the $E_{\mathrm{T}}^{\mathrm{miss}}$ components and the values in the parameter space which are scanned. This increases significantly the efficiency of the algorithm in finding the correct mass.

In general, the efficiency of the MMC in finding a solution for $m_{\tau\tau}$ is very high ($> 99\%$) for signal and Z decays, while a lower efficiency is found for the background[6]. This provides an additional criterion to suppress the latter in the preselection of events.

[6] The efficiency is defined as the number of events, where an invariant mass can be calculated, to the total number of events subjected to the algorithm. The calculation fails, when the true values of the parameters are outside the scanned range.

The distributions of the invariant mass $m_{\tau\tau}$ calculated with the MMC algorithm are compared in Fig. 7.9 for different analysis categories for the VBF $H \to \tau_{\text{lep}}\tau_{\text{had}}$ signal process at different masses and the $Z \to \tau\tau$ background (The analysis categories are defined in Sec. 7.4). The resulting resolution for the VBF signal sample with $m_H = 125$ GeV is listed in Tab. 7.2.

It is clearly visible, that different mass hypothesis for a Higgs boson can be distinguished from each other with this mass algorithm, as well as from the irreducible $Z \to \tau\tau$ background. The best resolution can be observed in the Boosted Category (which contains events with high transverse momenta and $E_{\text{T}}^{\text{miss}}$).

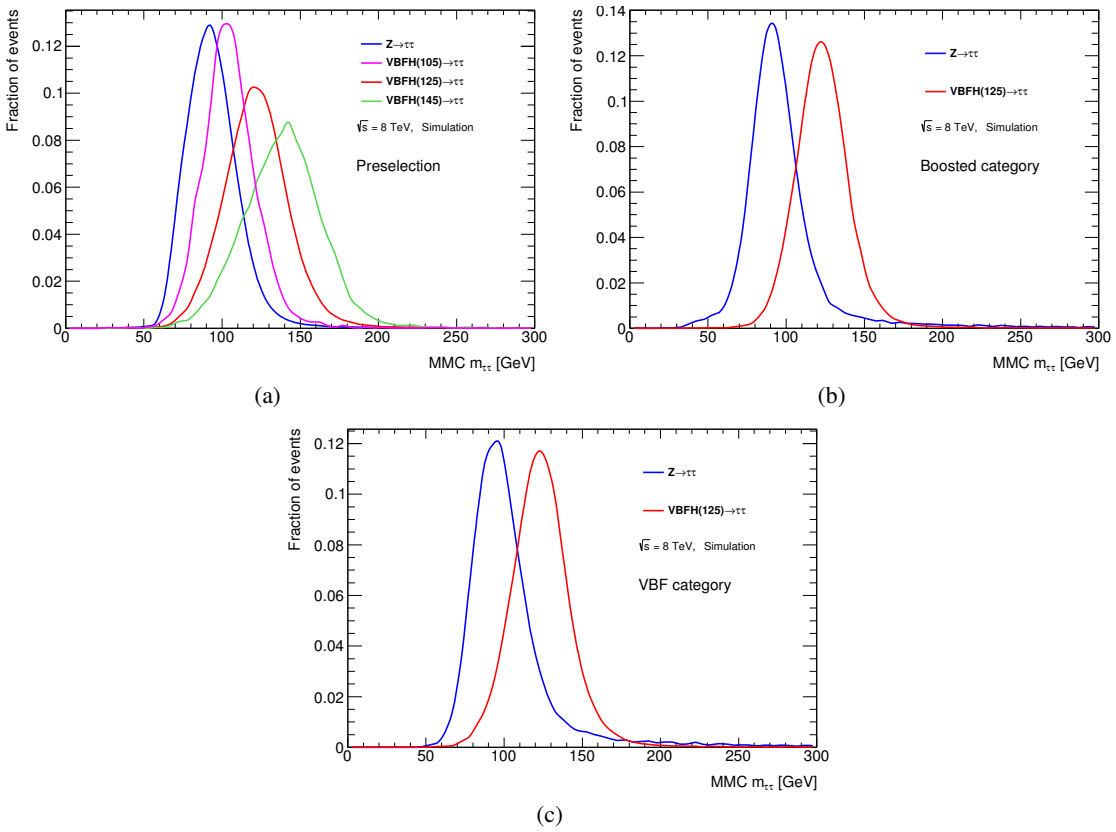

Figure 7.9: Shape of the invariant $m_{\tau\tau}$ mass reconstructed with the MMC algorithm in the $Z \to \tau\tau$ (blue), and the VBF Higgs signal samples at $m_H = 125$ GeV (20.3 fb^{-1}, $\sqrt{s} = 8$ TeV). (a) Preselection level. The shapes of signal samples with masses $m_H = 105$ GeV (pink) and $m_H = 145$ GeV (green) are also shown. (b) Loose Boosted selection ($p_{\text{T}}^{\text{H}} > 100$ GeV). (c) Loose VBF selection ($N_{\text{jets}} \geq 2$). The categories are described in Sec. 7.4.

Category	$< m_{\tau\tau} > \pm \Delta m_{\tau\tau}$ [GeV]
Preselection	121.4 ± 19.9
Boosted	122.7 ± 16.1
VBF	122.8 ± 17.7

Table 7.2: Mean value and resolution of the invariant $m_{\tau\tau}$ mass calculated by the MMC algorithm for different categories. The results are obtained with the VBF signal sample with $m_H = 125$ GeV (20.3 fb^{-1}, $\sqrt{s} = 8$ TeV). The values are derived from a Gauss fit to the distributions. The categories are described in Sec. 7.4.

Preselection

As a starting point for the analysis, events with the topology of the $H \rightarrow \tau_{\text{lep}}\tau_{\text{had}}$ signal are selected, which means they are required to contain:

- Exactly one good-quality τ_{had} candidate
- Exactly one good-quality lepton (e or μ) which is well isolated
- Significant missing transverse energy
- A certain number of jets depending on the Higgs production process, later used to define the analysis categories (Sec. 7.4)

In the following, the selection criteria applied to these physics objects on trigger and offline reconstruction level are described. The individual reconstruction and identification algorithms are explained in Sec. 3.4 and Chap. 5.

Trigger A mixture of triggers is used to select events in data. The event is accepted either if it was triggered by a single lepton trigger (SLT) or a combined τ_{had} and lepton trigger (LTT). The SLT has the advantage, that at trigger level only one simple object (e or μ) is selected. In contrast, for the LTT trigger the more complex τ_{had} reconstruction and selection criteria are applied at trigger level, which makes a modelling of the trigger decision more difficult and results in larger systematic uncertainties (compare Sec. 3.3). However, since two objects are included for the LTT trigger decision, the thresholds on the lepton p_{T} can be substantially lower compared to the SLT trigger and still fulfil the obliged band width limits in data.

As has been seen in Fig. 7.4 also relatively low-p_{T} leptons can be produced in the $H \rightarrow \tau_{\text{lep}}\tau_{\text{had}}$ decay, since a part of the τ momentum is carried away by the two neutrinos. The implementation of the LTT trigger in the analysis allows to include these leptons with lower offline reconstructed p_{T} in the analysis, and therefore increases the acceptance of signal events.

An overview of the selection criteria of the two triggers for the $e\tau_{\text{had}}$ and $\mu\tau_{\text{had}}$ final states in the 2012 data set is given in Tab. 7.3. The efficiency of the LTT τ trigger part and the SLT muon trigger is shown in Fig. 3.7.

Different kinematic ranges are defined, based on the offline transverse momenta of the lepton and τ_{had} candidate, so that one particular event is only required to pass one of the two trigger selections, SLT or LTT: For events with high p_{T} leptons ($p_{\text{T},e/\mu} > 26$ GeV) only the SLT trigger is considered, while for low p_{T} events ($17 < p_{\text{T},\mu} < 26$ GeV, $20 < p_{\text{T},e} < 26$ GeV) the LTT trigger decision is required to be passed. In LTT triggered events the offline p_{T} threshold of the τ_{had} candidate is in addition tightened to 25 GeV, to be well above the trigger p_{T} threshold[7].

The inclusion of the low-p_{T} events through the LTT trigger increases the number of $H \rightarrow \tau_{\text{lep}}\tau_{\text{had}}$ signal events that pass the preselection by about 23%.

Corrections are applied to the simulated events, to account for differences in the trigger efficiency between data and simulation for the individual triggers [36, 37, 146, 147].

[7] The offline p_{T} requirement is always chosen to be well above the corresponding trigger threshold, to avoid large systematic uncertainties arising from an inaccurate modelling on trigger turn-on curves (compare Sec. 6.3).

	SLT	LTT
$e\tau_{\text{had}}$ channel	isol. medium e, $p_{\text{T}} > 24$ GeV	medium e, $p_{\text{T}} > 18$ GeV
		BDT medium τ_{had}, $p_{\text{T}} > 20$ GeV
$\mu\tau_{\text{had}}$ channel	isol. μ, $p_{\text{T}} > 24$ GeV	μ, $p_{\text{T}} > 15$ GeV
		BDT medium τ_{had}, $p_{\text{T}} > 20$ GeV

Table 7.3: Overview over the trigger selections (single lepton and combined lepton τ_{had} trigger) used in the 2012 data sample at $\sqrt{s} = 8$ TeV for the $H \to \tau_{\text{lep}}\tau_{\text{had}}$ selection, separately for the $e\tau_{\text{had}}$ and $\mu\tau_{\text{had}}$ final states.

Event cleaning To ensure that only events with well-reconstructed physics objects and $E_{\text{T}}^{\text{miss}}$ are included in the analysis, several quality criteria are applied: At least one vertex with at least four associated tracks is required to ensure that the event is the result of a hard-scattering. In addition, further criteria based on calorimeter information are applied to reject non-collision events or mismeasured objects (Sec. 6.3 and [126, 148]).

Muon Muons are required to be reconstructed with the *combined* algorithm, have a transverse momentum larger than $p_{\text{T}} > 17$ GeV and a pseudorapidity within $|\eta| < 2.5$. Quality criteria to the inner detector track (number of hits in the ID sub-detectors) are applied to ensure a well measured momentum and a low fraction of misidentified muons. An isolation requirement both in the inner detector and calorimeters is applied to suppress $j \to \mu$ misidentification or muons from hadron decays within jets: In the ECal and the HCal it is required, that the additional energy deposition in a cone of radius $\Delta R = 0.2$ around the muon, corrected for additional depositions from pile-up interactions, is less than 6% of the muon transverse momentum. In the ID the sum of p_{T} of tracks (> 1 GeV) in a cone of $\Delta R = 0.4$ is required to be less than 6% of the muon track p_{T}. Additional correction factors are applied to simulated events to account for differences in the p_{T} resolution and efficiency of reconstruction and isolation criteria between data and simulation [46, 148].

Electron Electrons are required to follow *tight* identification criteria, have $p_{\text{T}} > 20$ GeV and be reconstructed within $|\eta| < 2.47$ and outside $1.37 < |\eta| < 1.52$, the transition region of ECal barrel and end-cap. The same isolation criteria in ID and calorimeters as for muons are applied. To account for mismodelling of reconstruction and identification efficiencies, energy scale, resolution and calorimeter isolation, correction factors are applied to simulated events [41, 43, 148].

Hadronically decaying τ lepton The τ_{had} candidates, reconstructed and calibrated as described in Sec. 5.2, are required to have $p_{\text{T}} > 20$ GeV and $|\eta| < 2.5$ [8]. Only candidates with exactly one or three associated tracks and unit charge (± 1) are considered for the analysis, to ensure the selected τ_{had} candidate has been reconstructed with the correct τ properties. The candidate is required to pass the *medium* BDT τ identification together with a *medium* BDT electron veto and a muon veto to suppress $j \to \tau_{\text{had}}$ and $\ell \to \tau_{\text{had}}$ misidentification (Tab. 5.2 and 5.3). To account for differences in the τ_{had} identification and lepton vetoes between simulation and data, correction factors are applied to simulated τ_{had} objects [99].

[8] One-prong τ_{had} candidates are only considered if they are reconstructed within $|\eta| < 2.47$, since no correction factors for an electron veto are provided outside this region [99].

Jets Jets are reconstructed as described in Sec. 3.4 and required to have $p_{\mathrm{T}} > 30$ GeV and $|\eta| < 4.5$. In order to suppress jets that are reconstructed due to pile-up activity, a threshold on the JVF is applied (Sec. 3.4): Jets with $|\eta| < 2.4$ and $p_{\mathrm{T}} < 50$ GeV are required to have JVF > 0.5 [9]. The categorisation of events due to the different Higgs production mechanism is based on this definition of jets (explained in Sec. 7.4). In the pseudorapidity range $|\eta| < 2.4$ events with b-jets identified by the b-tagging algorithm are rejected to suppress b-jets from top quark interactions (compare Sec. 7.2). A working point with an efficiency of 70% is used in this analysis (Sec. 3.4). Simulated events are corrected for differences of the b-tagging efficiency with respect to data [53].

Missing transverse energy The object-based definition of $E_{\mathrm{T}}^{\mathrm{miss}}$ is used, taking into account muon tracks and calorimeter energy depositions (Sec. 5.3).In order to avoid a degradation of the $E_{\mathrm{T}}^{\mathrm{miss}}$ resolution due to pile-up, the STVF pile-up suppression method is applied in the $E_{\mathrm{T}}^{\mathrm{miss}}$ reconstruction. An $E_{\mathrm{T}}^{\mathrm{miss}}$ requirement is applied at a later point of the analysis individually for the defined categories, as explained in Sec. 7.4.

Overlap removal Muons, electrons, τ_{had} candidates and jets are selected consecutively in this order of priority. When particle candidates passing the above selection overlap geometrically ($\Delta R < 0.2$), the particle with the higher priority is associated to this object for the further analysis. In order to avoid an overlap also between the less well-reconstructed or low-p_{T} objects, the selection criteria are partially relaxed. The p_{T} threshold of muons is lowered to 10 GeV and for electrons to 15 GeV. Additionally, in order to improve the rejection of $\mu \to \tau_{\mathrm{had}}$ misidentification of low-p_{T} muons, the muon p_{T}-threshold is lowered to 4 GeV when checking for overlap between muons and τ_{had} candidates. Furthermore, the e and μ isolation requirements are dropped, muons are not required to be *combined* and electrons just need to pass the *loose* identification. To provide further rejection against $e \to \tau_{\mathrm{had}}$ misidentification *medium* electrons found in the transition region of the detector ($1.37 < |\eta| < 1.52$) are also required to not overlap with τ_{had} candidates.

Dilepton veto In order to suppress sources of background with multiple leptons, such as $Z \to \ell\ell$, diboson and top production processes, events are discarded, when more than one lepton is found in the event. The same looser electron and muon definitions as for the overlap removal are used in this dilepton veto.

Charge product In addition, it is required that lepton and τ_{had} candidate have an opposite charge, as expected for the τ pairs coming from a Higgs boson. This criterion reduces the contribution from background processes such as QCD and W+jets, where a jet is misidentified as a light lepton or τ_{had} candidate or both. In these events, the selected lepton and τ_{had} candidate have an arbitrary charge correlation.

Summary of Preselection

In summary the following preselection criteria are applied:

- LTT or SLT trigger
- Event cleaning
- Overlap removal
- Dilepton veto

[9] Jets with no associated tracks, for which JVF cannot be calculated (JVF $= -1$) are also included in the analysis.

- **Exactly one** isolated tight **electron** with $p_T > 20$ GeV ($p_T > 26$ GeV for SLT triggered events) within $1.37 < |\eta| < 1.52$ and $|\eta| < 2.47$, or **exactly one** isolated combined **muon** with $p_T > 17$ GeV ($p_T > 26$ GeV for SLT triggered events), within $|\eta| < 2.5$
- **Exactly one τ_{had} candidate** with $p_T > 20$ GeV ($p_T > 25$ GeV for LTT triggered events) passing the medium BDT τ_{had} ID criteria and the medium BDT electron veto and the muon veto, within $|\eta| < 2.5$, with one or three tracks and charge ± 1
- Opposite charge of lepton and τ_{had} candidate
- Successful $m_{\tau\tau}$ calculation with the MMC algorithm

Table 7.4 shows the number of events at preselection for the different samples split into $e\tau_{had}$ and $\mu\tau_{had}$ channel. Basic kinematic distributions are shown in Figs. 7.10 and 7.11. The estimation of the contribution from different background processes is mostly data-driven and explained in Sec. 7.5. The signal fraction is negligible at this stage of the selection. One can see that the irreducible background $Z \to \tau\tau$ has still the largest contribution after the preselection as expected. In general, good agreement with data and the predicted contributions of all background processes can be observed in all distributions, which gives confidence that the kinematics are correctly modelled. Observables relevant for the further event selection are studied at preselection level in the next section, where also good agreement can be observed in all cases.

A slight shift can be observed in the distribution of $m_{\tau\tau}$ between data and background expectation in the range 70–120 GeV (Figs. 7.10d and 7.11d). Investigations of the systematic uncertainties influencing the shape of this distribution show that these vanish for the downwards variation of the TES uncertainty (Appendix E). Apparently, data is more conform with a slightly lower τ energy scale. These shape variations are taken into account in the fit of the invariant mass. The fit finds the TES value within the given uncertainty that describes data best, simultaneously taking into account all other uncertainties (Sec. 7.8).

Process	$e\tau_{had}$ channel	$\mu\tau_{had}$ channel
ZH($H \to \tau_{lep}\tau_{had}$) ($m_H = 125$ GeV)	6.7 ± 0.1	8.2 ± 0.1
WH($H \to \tau_{lep}\tau_{had}$) ($m_H = 125$ GeV)	9.7 ± 0.1	11.5 ± 0.1
VBF($H \to \tau_{lep}\tau_{had}$) ($m_H = 125$ GeV)	33.8 ± 0.2	40.8 ± 0.2
ggF($H \to \tau_{lep}\tau_{had}$) ($m_H = 125$ GeV)	339 ± 2	433 ± 2
$Z \to \tau\tau$	$88\,141 \pm 161$	$137\,647 \pm 176$
$Z \to \ell\ell(\ell \to \tau_{had})$	7111 ± 171	8333 ± 161
$Z \to \ell\ell(\mathrm{j} \to \tau_{had})$	0 ± 0	-1108 ± 23
Diboson	2879 ± 39	3292 ± 43
Top	$11\,012 \pm 82$	$10\,790 \pm 85$
W+jets	$92\,695 \pm 1237$	$99\,407 \pm 1324$
Same-sign	$140\,680 \pm 375$	$137\,997 \pm 390$
Total background	$342\,518 \pm 1317$	$396\,357 \pm 1404$
Data	342 821	395 206

Table 7.4: Number of signal and background events (estimated according to Sec. 7.5) after the preselection in the $e\tau_{had}$ and $\mu\tau_{had}$ channel including the statistical uncertainties. The same-sign events contain misidentified $j \to \tau_{had}$ candidates mostly from the W+jets and QCD background (Sec. 7.5).

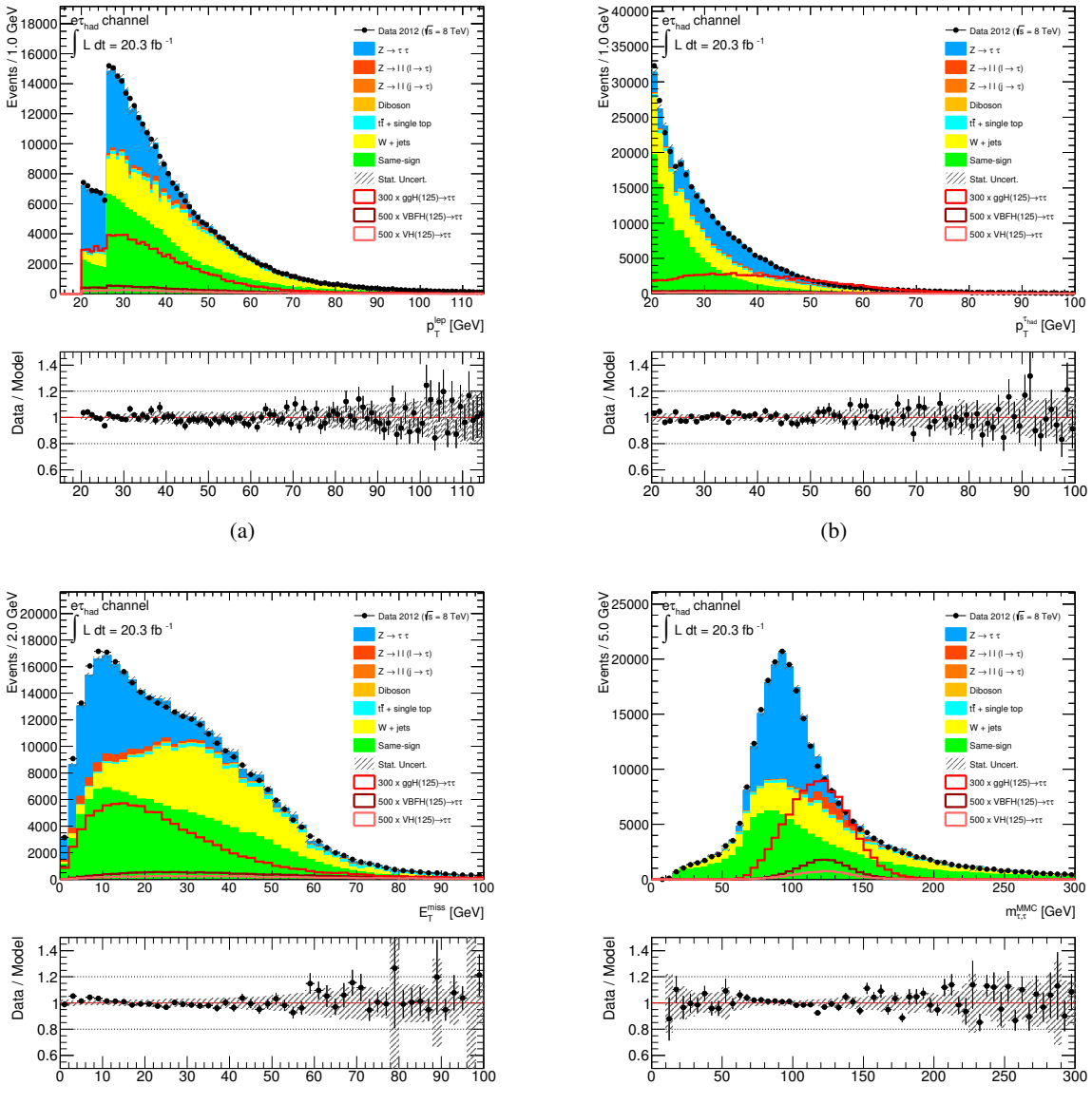

Figure 7.10: $e\tau_{\text{had}}$ **channel**: Kinematic distributions of (a) the lepton transverse momentum, (b) the τ_{had} transverse momentum, (c) the missing transverse energy and (d) the invariant $m_{\tau\tau}$ mass calculated with the MMC algorithm for data (black points), the stack of the expected distribution if all background processes (estimated according to Sec. 7.5) and the scaled signal processes after the preselection. The bottom plots show the ratio of data to the background model. Also the statistical uncertainties of both are shown.

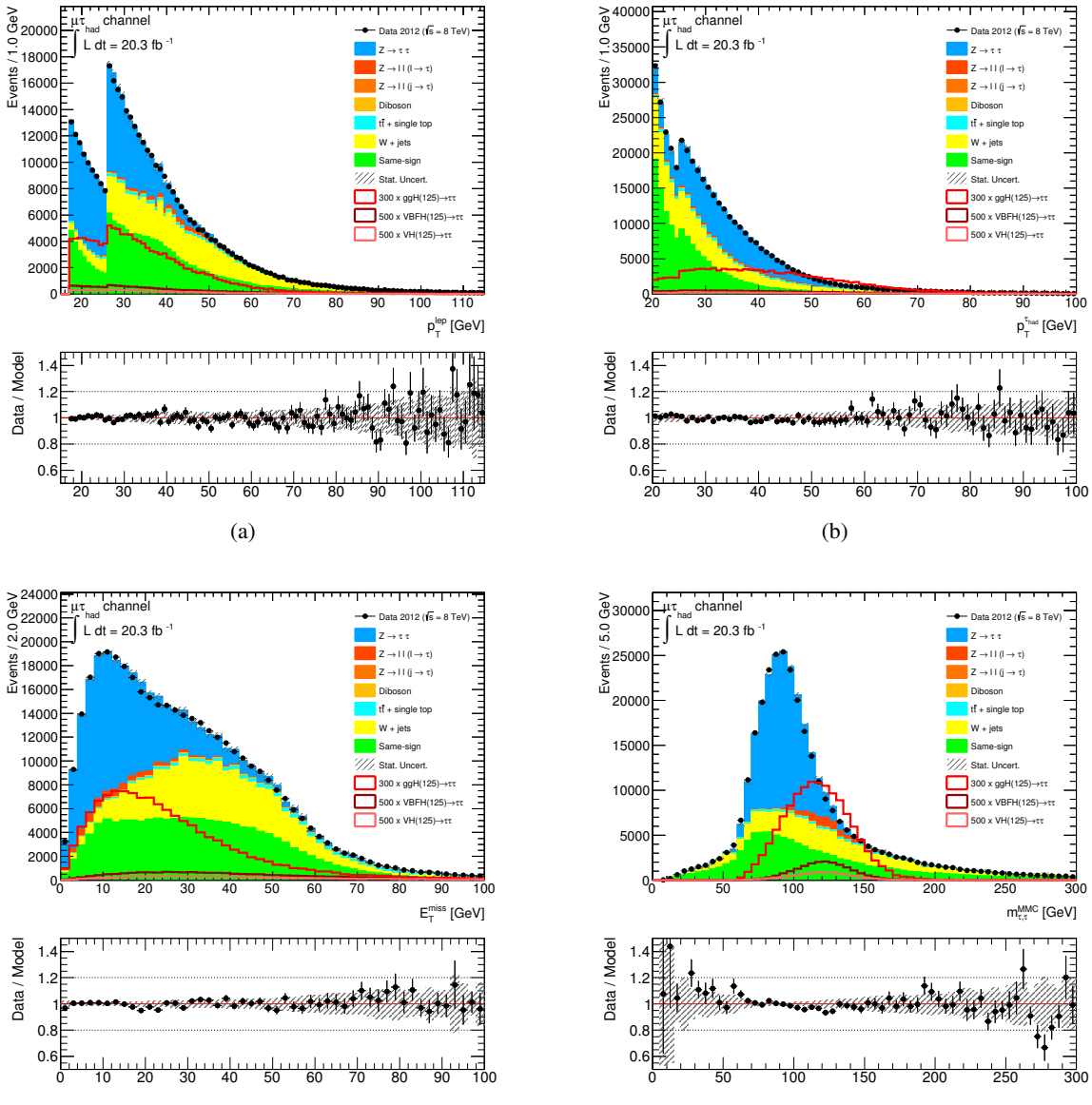

Figure 7.11: $\mu\tau_{\text{had}}$ **channel**: Kinematic distributions of (a) the lepton transverse momentum, (b) the τ_{had} transverse momentum, (c) the missing transverse energy and (d) the invariant $m_{\tau\tau}$ mass calculated with the MMC algorithm for data (black points), the stack of the expected distributions of all background processes (estimated according to Sec. 7.5) and the scaled signal processes after the preselection. The bottom plots show the ratio of data to the background model. Also the statistical uncertainties of both are shown.

7.4 Categorisation and Selection of Events

As explained in Sec. 7.2, the Higgs production processes differ in the number of associated jets which determine the kinematics of the Higgs boson and its decay products. These properties are used to define different analysis categories for the preselected events. This allows to individually develop and optimise the selection criteria in each category and to investigate events with a better mass resolutions separately.

Figure 7.12a shows the jet multiplicity for background and the three signal production mechanisms at preselection level, based on the jet selection criteria defined in Sec. 7.3. The multiplicity of jets is higher for the Higgs signal than for the background processes, especially for the VBF and VH production which feature the typical two additional jets from the accompanying quarks.

A variable quantifying the boost of the Higgs boson is the so called Higgs transverse momentum $p_{\mathrm{T}}^{\mathrm{H}}$, defined as the vectorial sum of the p_{T} of all its reconstructed decay products:

$$p_{\mathrm{T}}^{\mathrm{H}} = |\vec{p}_{\mathrm{T}}^{\,\ell} + \vec{p}_{\mathrm{T}}^{\,\tau_{\mathrm{had}}} + \vec{E}_{\mathrm{T}}^{\mathrm{miss}}| \tag{7.4}$$

Figure 7.12b shows the distribution of the $p_{\mathrm{T}}^{\mathrm{H}}$ for signal and background. A large fraction of signal events features a high $p_{\mathrm{T}}^{\mathrm{H}}$, while most of the background processes do not have such a large tail towards high values. Since the resolution of the transverse momenta and $E_{\mathrm{T}}^{\mathrm{miss}}$ is much higher for such boosted events, the resolution of the invariant $\tau\tau$ mass is significantly better for this class of events (as shown in Fig. 7.9).

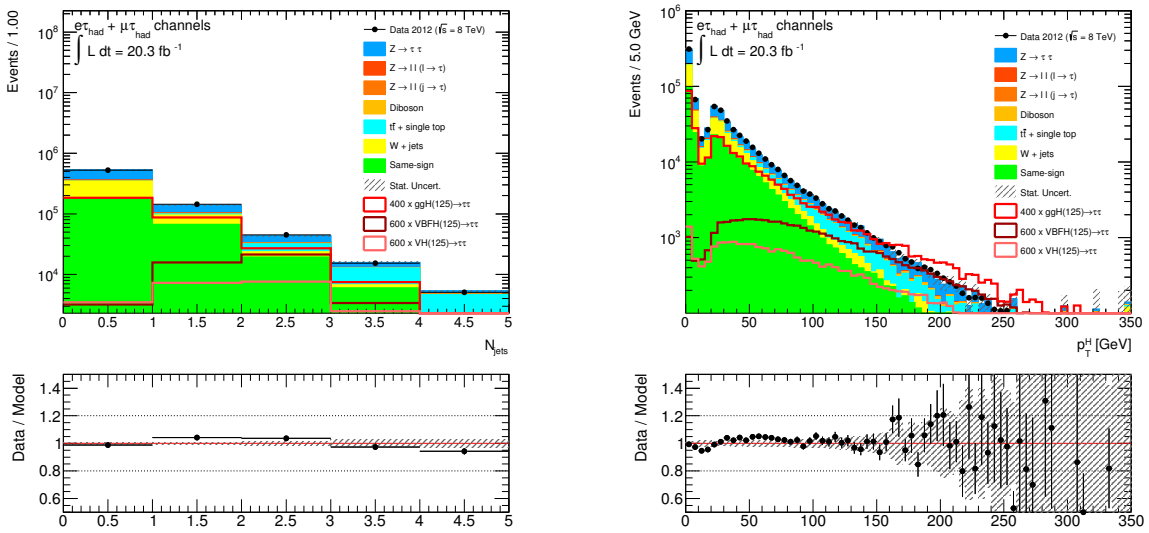

(a) (b)

Figure 7.12: Logarithmic distributions of (a) the number of jets ($p_{\mathrm{T}} > 30$ GeV) [10] and (b) $p_{\mathrm{T}}^{\mathrm{H}}$ (Eq. 7.4) shown for data, the expected background processes (estimated according to Sec. 7.5) and the scaled signal processes after the preselection for the combined $e\tau_{\mathrm{had}}$ and $\mu\tau_{\mathrm{had}}$ channel. The bottom plots show the ratio of data to the background model. Also the statistical uncertainties of both are shown.

[10] For simplicity an average correction of the simulated $j \to \tau_{\mathrm{had}}$ misidentification probability is applied to the full N_{jets} distribution in this histogram. In fact it depends on the fraction of quark- to gluon-initiated jets in a process. Therefore, correction factors are determined individually for each category to more accurately determine the background contribution in the final selected data samples. This also results in a better agreement between data and simulation in each jet bin than observed here (details are explained in Sec. 7.5).

Based on these observables the analysis categories are formed. The first category aims at the selection of signal events from VBF production (*VBF Category*). It includes events with at least two jets that have the characteristics of the typical VBF tagging jets. Due to this clear and unique signature a very high signal-to-background ratio can be achieved.

The second category (*Boosted Category*) selects boosted events through the requirement of a significant $p_{\mathrm{T}}^{\mathrm{H}}$ to only collect events with a high mass resolution. The signal events are expected to result mainly from gluon fusion with additional jets (compare Fig. 7.3). This also leads to a better separation from the irreducible $Z \to \tau\tau$ background (Sec. 7.3).

Two additional categories are formed of events with one or no jets (*Zero-* and *One-Jet Categories*). As can be seen in Fig. 7.12a, they contain a large number of ggF signal and the signal-to-background ratio is relatively low.

These last two categories do not add much to the final sensitivity on the Higgs boson in data due to this low signal-to-background ratio. But since a much higher number of events is contained in these categories compared to the Boosted and VBF ones, they help to gain confidence in the background modelling. For the first analysis of 2011 and 2012 data (Appendix C) they have been included in the profile likelihood fit on $m_{\tau\tau}$ to constrain the systematic uncertainties on the background modelling [97]. For the analysis based on the full 2012 data sample presented in this chapter, a good fit result is obtained based on the VBF and Boosted Categories alone, which is why the Zero- and One-Jet Categories are not included in the final fit. Nevertheless, also in this analysis they are important for a validation of the background estimation as an input to the fit.

In order to clearly assign events to only one category and to collect as many signal events as possible, the categories are built mutually exclusive in a subsequent order starting with the one with the highest signal-to-background ratio (the VBF Category). Events failing the criteria for one category are reconsidered for the subsequent ones. These category definitions also form the basis for the definition of background control regions (Sec. 7.5).

In addition to this category definition, further selection criteria in each category are applied with the purpose to further reduce the background. The events that fail these criteria are not reconsidered for another category.

The starting point for the development of the event selection and categorisation criteria applied to the here investigated 20.3 fb^{-1} data sample is the previous analysis performed with the first 13.0 fb^{-1} of the 2012 data set at $\sqrt{s} = 8$ TeV (Appendix C). Since the full 2012 data sample (20.3 fb^{-1}) is much larger and also the embedded and simulated samples contain significantly more events, it is important to re-investigate the selection criteria. The smaller statistical uncertainties offer the possibility to test the inclusion of additional selection criteria or to tighten the selection criteria.

The optimisation of the categorisation is done *blindly*, i.e. without comparing the sensitive invariant $m_{\tau\tau}$ mass region of 100–150 GeV in data with the expectation from the signal and background model, in order to prevent a bias in the optimisation towards an enhanced signal in data. To find an optimal selection leading to the highest expected significance (Sec. 4.2.2) poses a multidimensional problem due to the many variables for which the optimal selection threshold has to be found. A calculation of the exact significance with the binned profile likelihood fit for each selected phase space region is technically not possible. Therefore, the sum of the expected signal events relative to the number of background events in the sensitive mass range 100–150 GeV is maximised according to Eq. 4.15 as a first approximation. For that purpose the thresholds on multiple important observables are scanned simultaneously. For the best results the full profile likelihood fit is performed and the expected significance is calculated. The fit takes into account all statistical and systematic uncertainties and is thus able to find the optimal phase space selection that does not suffer from too low statistics or too high systematic uncertainties. It is found, that the event selection developed for the previous analysis of the 13.0 fb^{-1} sample is also

optimal for the full 2012 data set and yields the highest expected significance.

The final selection criteria for the event selection in each category are discussed in detail in the following. To illustrate the distribution and the separation power of the important discriminating variables, they are shown for the combined background and the individual signal processes (VH, VBF and ggF) after the preselection. For variables used to define the VBF Category an additional requirement of $N_{\text{jets}} \geq 2$ is applied for clarity. For the variables used in the Boosted Category $p_{\text{T}}^{\text{H}} > 100$ GeV is required.

VBF Category

The purpose of this category is to select signal events resulting from vector-boson fusion by using the special topology of the typical tagging jets and the kinematics of the Higgs decay products. The decay channels $e\tau_{\text{had}}$ and $\mu\tau_{\text{had}}$ are combined in this category to increase the total number of events. The selection criteria are based on the following observables:

Number of jets Only events with at least two additional jets are considered[11]. The jet multiplicity is shown in Fig. 7.12a.

Transverse momentum of jets The two jets with the highest p_{T} in the event are chosen to be the tagging jets. Figures 7.13a and 7.13b show the distribution of the transverse momentum of the leading and sub-leading jet (for events with at least two jets). As expected for VBF signal events their p_{T} is usually of the order of magnitude of the vector bosons from which the Higgs boson is produced. In order to suppress background with lower jet momenta, the p_{T} threshold of the leading jet is tightened to 40 GeV.

Dijet mass m_{jj} The invariant mass of the two jets is shown in Fig. 7.13c. VBF signal events are expected to have a very high dijet mass due to the high energy of the additional jets. In most other processes the additional jets result from ISR or FSR of gluons or other QCD interactions. They tend to have much lower energies and thus much lower dijet masses, in contrast to the VBF quarks which result from an EW interaction. By selecting events with a high dijet mass the number of background events can be reduced significantly. The dijet mass of the VH process peaks around the mass of the vector boson from which they are produced, a high threshold on this variable obviously reduces the contribution of this signal process to the VBF Category[12]. The selection criterion found to be optimal to define the VBF Category is $m_{jj} > 500$ GeV.

Pseudorapidity difference of jets $\Delta\eta_{jj}$ Directly correlated to the dijet mass is the pseudorapidity gap between the tagging jets, which also provides a very good separation of the VBF signal from background. Due to the kinematics of the VBF production process, the quarks in the final state are expected to be found in forward direction, close to the incoming direction of the quarks and in opposite hemispheres of the detector. The $\Delta\eta_{jj}$ is thus expected to be large, as can be seen in Fig. 7.13d. For the majority of background processes $\Delta\eta_{jj}$ is usually much smaller. Events with $\Delta\eta_{jj} > 3$ are selected for the VBF Category. Figure 7.14a shows the correlation of m_{jj} and $\Delta\eta_{jj}$ for signal and background events. A very clean sample of events is already obtained after these two selection criteria are applied.

[11] The maximum number of jets is not limited to avoid additional theoretical systematic uncertainties arising in case higher order quark/gluon emission corrections are excluded.

[12] An effort has been made to define a separate two-jet category with the purpose to enhance the VH signature, e.g. by requiring a dijet mass corresponding to the W or Z mass. However, since this sample is much more dominated by different sources of background with jets, it could not add much to the overall sensitivity of the analysis and was therefore not considered further.

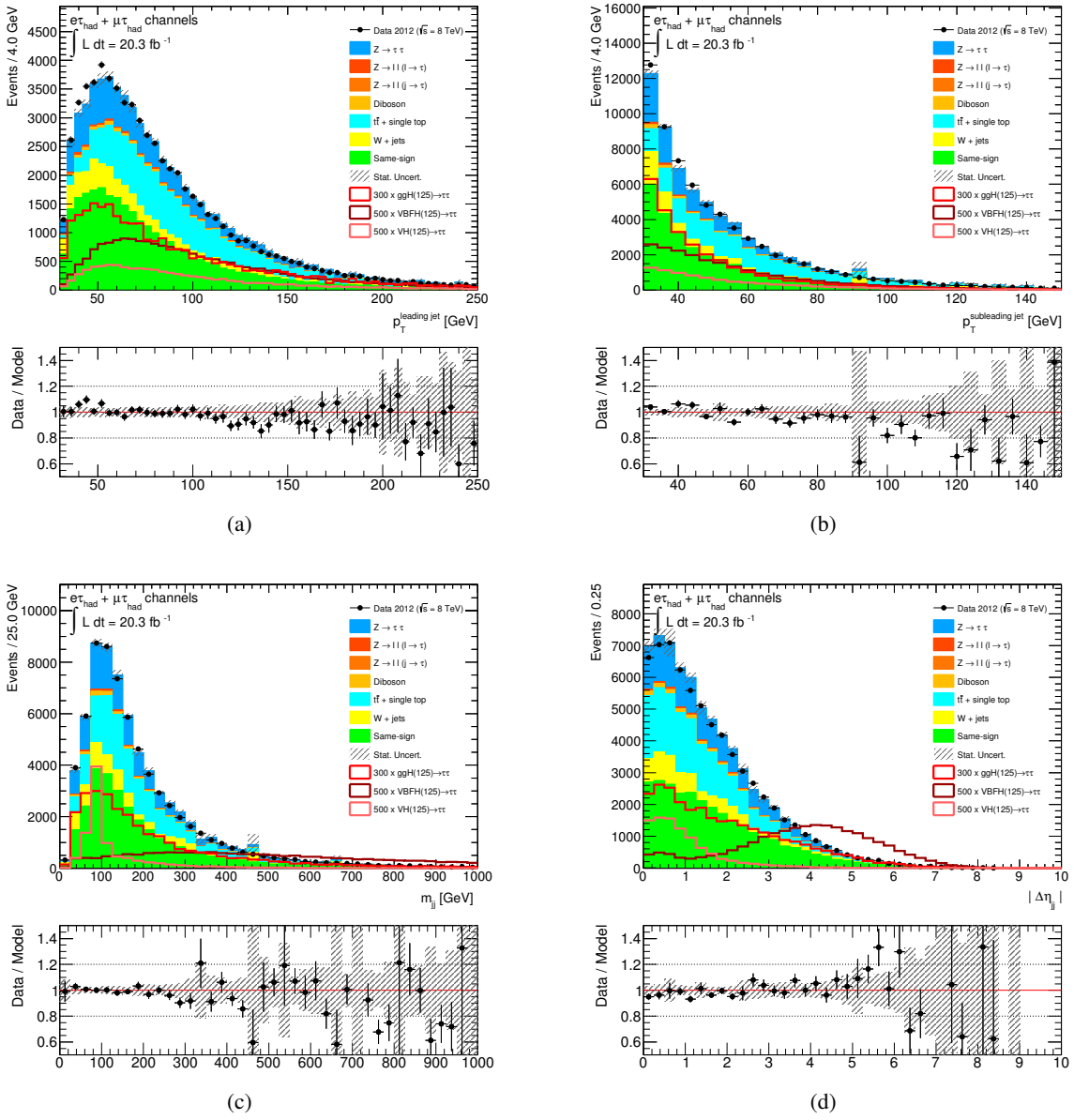

Figure 7.13: Variables used for the selection of events in the VBF Category: Distributions of (a) the p_{T} of the leading jet, (b) the p_{T} of the sub-leading jet, (c) the dijet mass (d) the pseudorapidity separation of the two leading jets $\Delta\eta_{jj}$. This is shown for data, the expected background processes (estimated according to Sec. 7.5) and the scaled signal processes after the preselection and requiring $n_{\mathrm{jets}} \geq 2$. The bottom plots show the ratio of data to the background model. Also the statistical uncertainties of both are shown.

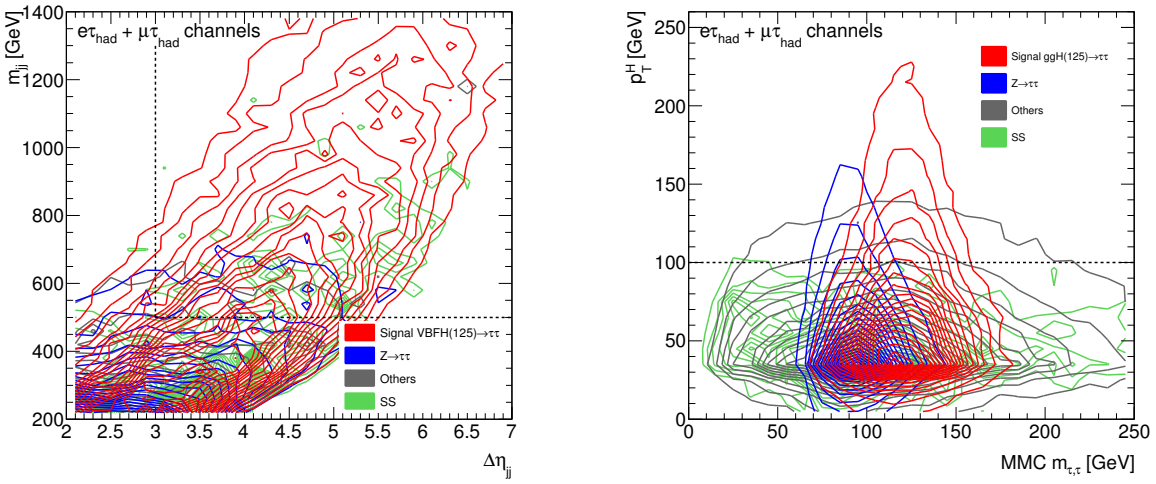

(a) (b)

Figure 7.14: Correlation of variables: (a) Mass and pseudorapidity separation of the two tagging jets in the VBF Category for signal and background events with at least two jets. (b) $p_{\mathrm{T}}^{\mathrm{H}}$ (Eq. 7.4) and $m_{\tau\tau}$ mass for signal and background events with at least one jet. The event selection criteria used in the analysis are indicated by the dashed lines.

Pseudorapidity product of jets $\eta_{j_1} \times \eta_{j_2}$ Since the jets are expected to lie in opposite hemispheres of the detector for the VBF signal, a negative product of the jet pseudorapidity is expected as shown in Fig. 7.15a. The background processes have no preferred correlation between the location of the jets in the detector halves. To select the VBF signal event with this specific characteristics, a requirement of $\eta_{j_1} \times \eta_{j_2} < 0$ is applied to the events. This provides an even better background rejection than the requirement of a large pseudorapidity separation $\Delta\eta_{jj}$ alone.

Centrality of τ decay products For VBF signal events it is expected that the decay products of the τ leptons lie inside the pseudorapidity gap spanned by the two tagging jets, as can be seen in Fig. 7.15b. This criterion is added as a criterion for the VBF selection.

τ_{had} transverse momentum Since in the Higgs signal process the τ_{had} candidate originates from a heavy particle, its transverse momentum is expected to be higher compared to processes with misidentified $j \to \tau_{\mathrm{had}}$ candidates (mainly in W+jets and QCD processes). The τ_{had} p_{T} distribution for events with at least two jets is shown in Fig. 7.15c. These sources of background can be reduced when the τ_{had} p_{T} threshold is tightened to 30 GeV.

Total transverse momentum $p_{\mathrm{T}}^{\mathrm{tot}}$ Another observable that reflects the typical kinematics of a VBF Higgs production process is $p_{\mathrm{T}}^{\mathrm{tot}}$, which is defined as the vectorial sum of the transverse momenta of the Higgs decay products and the two tagging jets:

$$p_{\mathrm{T}}^{\mathrm{tot}} = |\vec{p}_{\mathrm{T}}^{\,\ell} + \vec{p}_{\mathrm{T}}^{\,\tau_{\mathrm{had}}} + \vec{p}_{\mathrm{T}}^{\,\mathrm{j1}} + \vec{p}_{\mathrm{T}}^{\,\mathrm{j2}} + \vec{E}_{\mathrm{T}}^{\mathrm{miss}}| \tag{7.5}$$

This quantity is expected to be exactly zero if no additional jets are present in the event. Values slightly different from zero can occur due to the limited resolution of momenta, in particular $E_{\mathrm{T}}^{\mathrm{miss}}$. If an additional jet is found in the event, the $p_{\mathrm{T}}^{\mathrm{tot}}$ value is significantly larger. The $p_{\mathrm{T}}^{\mathrm{tot}}$ distribution is shown in Fig. 7.15d.

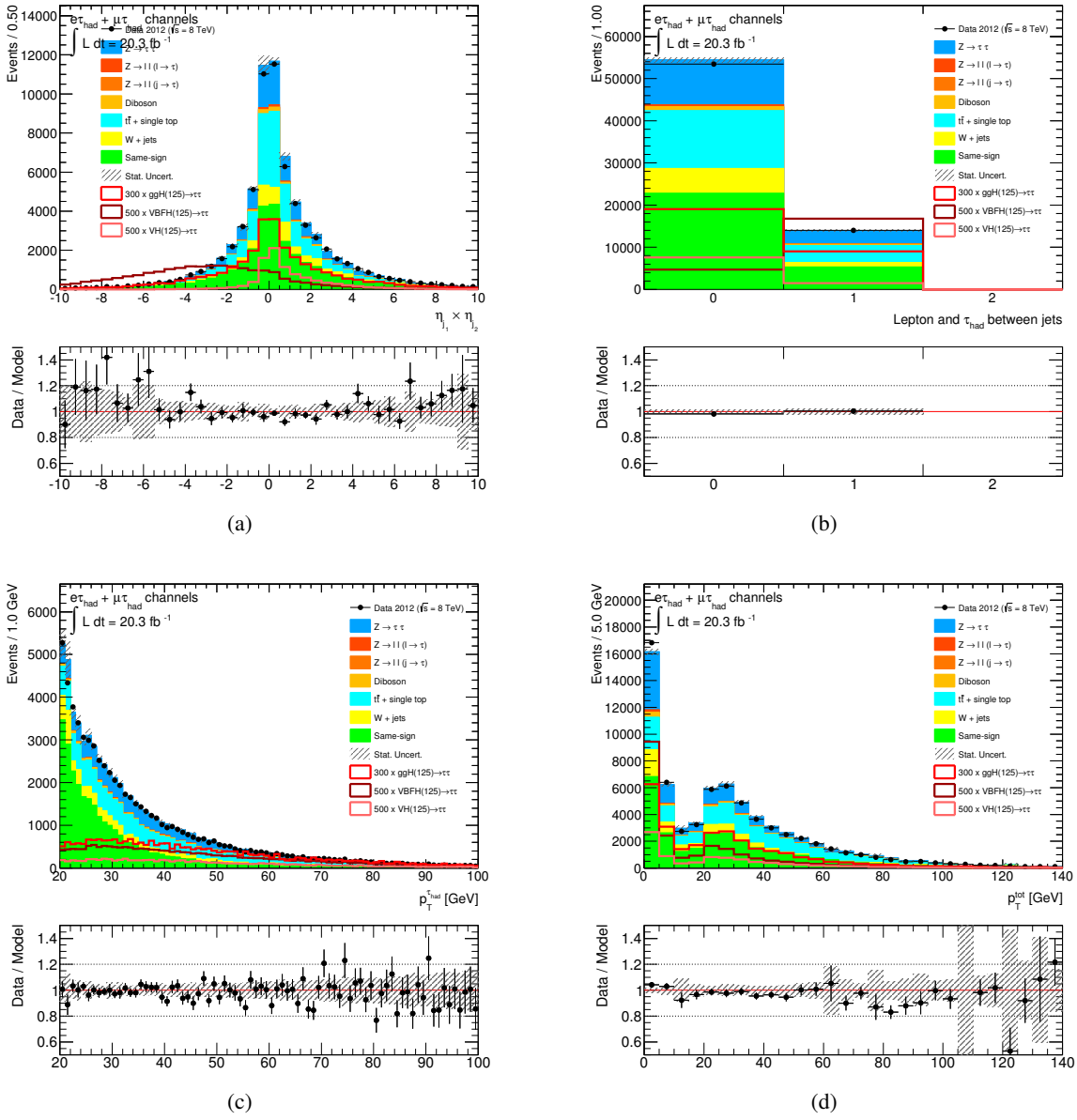

Figure 7.15: Variables used for the selection of events in the VBF Category: Distributions of (a) the product of the leading jet pseudorapidities and (b) the centrality of τ_{had} and lepton (1: they are between the tagging jets, 0: they are not), (c) the τ_{had} transverse momentum and (d) the total transverse momentum $p_{\text{T}}^{\text{tot}}$. This is shown for data, the expected background processes (estimated according to Sec. 7.5) and the scaled signal processes after the preselection and requiring $n_{\text{jets}} \geq 2$. The bottom plots show the ratio of data to the background model. Also the statistical uncertainties of both are shown.

Due to the fact that the radiation of additional quarks or gluons is suppressed for the VBF signal process, the fraction of events with a low $p_{\mathrm{T}}^{\mathrm{tot}}$ for this process is much higher than for the different background processes. In order to enhance the signal-to-background ratio in the data sample, $p_{\mathrm{T}}^{\mathrm{tot}} < 30$ GeV is required in this category. This variable is directly correlated with the veto of any central jet in the event. The $p_{\mathrm{T}}^{\mathrm{tot}}$ variable has the advantage that it is less sensitive to pile-up jets, which are not taken into account when calculating the p_{T} sum. Its only disadvantage is that in contrast to a central jet veto it is affected by the $E_{\mathrm{T}}^{\mathrm{miss}}$ resolution.

Missing transverse energy A significant measured $E_{\mathrm{T}}^{\mathrm{miss}}$ is expected for the VBF signal (Figs. 7.10c and 7.11c). Therefore an $E_{\mathrm{T}}^{\mathrm{miss}}$ of at least 20 GeV is required. This reduces background processes like QCD and $Z \to \ell\ell$, where no real $E_{\mathrm{T}}^{\mathrm{miss}}$ is expected. In addition, the resolution of $E_{\mathrm{T}}^{\mathrm{miss}}$ improves for larger values (compare Sec. 5.3), which directly impacts the resolution of the invariant mass reconstruction.

Boosted Category

In order to be selected for this category, the collision events are required to result from a boosted Higgs boson. As explained before this leads to a significantly improved invariant mass reconstruction. All events that are not selected for the VBF Category are reconsidered for this Boosted Category. The decay channels $e\tau_{\mathrm{had}}$ and $\mu\tau_{\mathrm{had}}$ are also combined in this category. No restriction on the number of jets is applied, although usually at least one jet is expected in the event, causing the boost of the Higgs boson (Fig. 7.3). These are the selection criteria for this category:

Higgs transverse momentum $p_{\mathrm{T}}^{\mathrm{H}}$ As explained before the most important variable that quantifies the boost of the Higgs boson is the $p_{\mathrm{T}}^{\mathrm{H}}$ which is defined by the transverse momenta of the decay products (Eq. 7.4). Alternatively, the boost can also be measured by the p_{T} of an additional jet in the event, from which the Higgs boson gets the recoil. The $p_{\mathrm{T}}^{\mathrm{H}}$ definition has the advantage that it does not directly depend on the jet energy scale or the jet modelling. Moreover, it provides a better separation of signal from *non-resonant* background processes like $t\bar{t}$ or QCD production, where the final state particles do not result from one heavy particle (compare Figs. 7.12b and 7.13a). The selection criterion for boosted events is $p_{\mathrm{T}}^{\mathrm{H}} > 100$ GeV. Figure 7.14b shows the correlation of this variable and the $m_{\tau\tau}$ mass. It can be clearly seen that the signal-to-background ratio and the mass resolution improve with higher $p_{\mathrm{T}}^{\mathrm{H}}$ values.

Visible p_{T} fraction of lepton and τ_{had}, x_ℓ and x_τ These variables denote the visible p_{T} fraction of the lepton and τ_{had}. They can be calculated under the assumption that all decay products of the two τ leptons have the same direction [149]. Given the high boost in this category, where all decay products are very close together, this is a reasonable assumption[13]. The definition of the variables is:

$$x_\ell = \frac{E^\ell}{E^{\tau_1}} = \frac{p_{\mathrm{x}}^{\tau_{\mathrm{had}}} \cdot p_{\mathrm{y}}^{\ell} - p_{\mathrm{y}}^{\tau_{\mathrm{had}}} \cdot p_{\mathrm{x}}^{\ell}}{p_{\mathrm{x}}^{\tau_{\mathrm{had}}} \cdot E_{\mathrm{y}}^{\mathrm{miss}} - p_{\mathrm{y}}^{\tau_{\mathrm{had}}} \cdot E_{\mathrm{x}}^{\mathrm{miss}} + p_{\mathrm{x}}^{\tau_{\mathrm{had}}} \cdot p_{\mathrm{y}}^{\ell} - p_{\mathrm{y}}^{\tau_{\mathrm{had}}} \cdot p_{\mathrm{x}}^{\ell}} \tag{7.6}$$

$$x_\tau = \frac{E^{\tau_{\mathrm{had}}}}{E^{\tau_2}} = \frac{p_{\mathrm{x}}^{\tau_{\mathrm{had}}} \cdot p_{\mathrm{y}}^{\ell} - p_{\mathrm{y}}^{\tau_{\mathrm{had}}} \cdot p_{\mathrm{x}}^{\ell}}{p_{\mathrm{y}}^{\ell} \cdot E_{\mathrm{x}}^{\mathrm{miss}} - p_{\mathrm{x}}^{\ell} \cdot E_{\mathrm{y}}^{\mathrm{miss}} + p_{\mathrm{x}}^{\tau_{\mathrm{had}}} \cdot p_{\mathrm{y}}^{\ell} - p_{\mathrm{y}}^{\tau_{\mathrm{had}}} \cdot p_{\mathrm{x}}^{\ell}} \tag{7.7}$$

[13] This approach is based on the *collinear approximation*, which was also used for a reconstruction of the $m_{\tau\tau}$ mass in early $H \to \tau\tau$ analyses. However, better results on the reconstructed mass are obtained with the here implemented MMC algorithm (Sec. 7.3 and [145]).

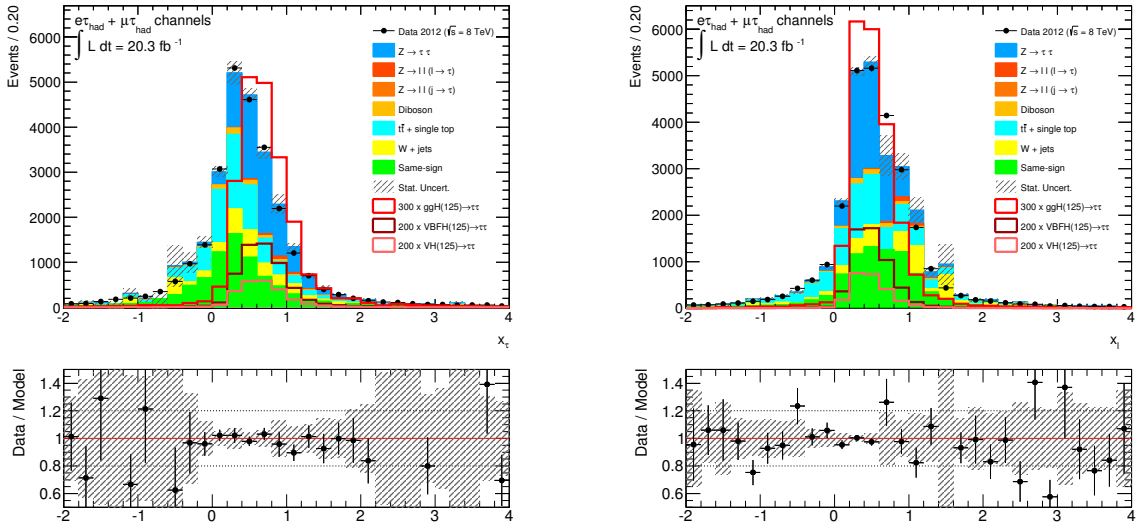

(a) (b)

Figure 7.16: Variables used for the selection of events in the Boosted Category: Distributions of visible momentum fraction of (a) the τ_{had} and (b) the lepton from the τ decay. This is shown for data, the expected background processes (estimated according to Sec. 7.5) and the scaled signal processes after the preselection in addition requiring $p_{\text{T}}^{\text{H}} > 100$ GeV. The bottom plots show the ratio of data to the background model. Also the statistical uncertainties of both are shown.

The variables $E^{\ell,\,\tau_{\text{had}}}$ and $p_{\text{x,y}}^{\ell,\,\tau_{\text{had}}}$ denote the energy and momentum components of the reconstructed visible τ decay products, τ_{had} and lepton. $E_{\text{x,y}}^{\text{miss}}$ are the two reconstructed $E_{\text{T}}^{\text{miss}}$ components. E^{τ_1} and E^{τ_2} are the total energies of the two initial τ leptons. For the signal process where $E_{\text{T}}^{\text{miss}}$ only results from the τ decay product values between 0 and 1 are expected. For background processes with no genuine $E_{\text{T}}^{\text{miss}}$ or where the neutrinos result from different particle decays this is not the case. Figures 7.16a and 7.16b show the distribution of these variables for boosted events with $p_{\text{T}}^{\text{H}} > 100$ GeV. A small fraction of signal events outside the interval 0 to 1 is observed as well, which is due to the limited $E_{\text{T}}^{\text{miss}}$ resolution. The x_τ variable is shifted to slightly larger values. This results from the fact that the τ_{had} reconstruction is more sensitive to pile-up and picks up additional energy during reconstruction. A good suppression of background without much loss of signal is achieved by requiring $0 < x_\ell < 1$ and $0.2 < x_\tau < 1.2$.

τ_{had} transverse momentum $p_{\text{T}}^{\tau_{\text{had}}}$ Also in this category the τ_{had} transverse momentum of signal processes is expected to be higher due to the boost and therefore it is required to lie above 30 GeV.

Missing transverse energy A significant missing transverse energy of at least 20 GeV is also required in this category.

One-Jet and Zero-Jet Category

Events failing the VBF and Boosted Categories are reconsidered for these categories. They are defined by requiring at least one jet or no jet, respectively. A minimum missing transverse energy of 20 GeV is required consistently in both categories. For the Zero-Jet Category this helps in particular to suppress the larger contamination of $Z \to \ell\ell$. The Zero- and One-Jet Categories are further split into the $e\tau_{\text{had}}$ and $\mu\tau_{\text{had}}$ decay channels to exploit and investigate the characteristics of the light leptons individually.

Further Background Suppression

In the above defined categories a large number events from various background processes is still included. The dominant background in all categories is the irreducible $Z \to \tau\tau$ background. QCD and W+jets also contribute significantly in all categories. The $Z \to \ell\ell$ background mainly contributes to the categories with lower jet multiplicities($n_{\text{jets}} < 2$), while top quark production plays a significant role for the categories with high jet multiplicity ($n_{\text{jets}} \geq 2$) and high transverse momenta.

Further selection criteria are applied to suppress all reducible sources of background in the different categories. They are explained in the following. Moreover, with the help of some of these observables also regions of the phase space can be defined which are dominated by one particular background, e.g. by the inversion of a selection criterion. These serve as a control region to estimate the contribution of this background from data.

Transverse mass m_{T} The transverse mass provides a good separation of signal from background processes where the final state particles are produced in a W decay, i.e. W+jets and top production. It is defined in a similar way as in the $W \to \tau_{\text{had}}\nu_\tau$ analysis (Eq. 6.2). In the $H \to \tau_{\text{lep}}\tau_{\text{had}}$ analysis the dominant source of background are events where the light leptons result from the W boson. Therefore, the transverse mass is defined instead from $E_{\text{T}}^{\text{miss}}$ and lepton transverse momentum p_{T}^{ℓ} and their angular separation $\Delta\phi$ in the plane perpendicular to the beam axis:

$$m_{\text{T}} = \sqrt{2 p_{\text{T}}^{\ell} E_{\text{T}}^{\text{miss}} (1 - \cos\Delta\phi(\ell, E_{\text{T}}^{\text{miss}}))} \tag{7.8}$$

$\Delta\phi(\ell, E_{\text{T}}^{\text{miss}})$ denotes the azimuthal angle between the lepton and $E_{\text{T}}^{\text{miss}}$. Figure 7.17a shows the m_{T} distribution of the expected signal and background processes. For the W background a maximum around the W mass is observed as expected, while all signal processes have much lower m_{T} values. Events in the different categories are therefore selected if $m_{\text{T}} < 50$ GeV ($m_{\text{T}} < 30$ GeV in the Zero-Jet Category). A better rejection of background could be achieved with a much lower m_{T} threshold, but at the cost of a significant loss of signal events. For this reason this relatively loose selection criterion is applied. A further rejection of the W background is provided by the $\sum\Delta\phi$ observable (as explained in the next paragraph). The high m_{T} region is clearly dominated by W+jets events, therefore the region with $m_{\text{T}} > 70$ GeV is used as a control region to estimate the W+jets background (see Sec. 7.5).

Sum of $\Delta\phi$ Additional suppression of the W background is provided by the following observable: The sum of the difference in the azimuthal angle ϕ between $E_{\text{T}}^{\text{miss}}$ and lepton, and $E_{\text{T}}^{\text{miss}}$ and the reconstructed τ_{had}:

$$\sum\Delta\phi = |\phi_{\ell} - \phi_{E_{\text{T}}^{\text{miss}}}| + |\phi_{\tau_{\text{had}}} - \phi_{E_{\text{T}}^{\text{miss}}}| \tag{7.9}$$

In the $H \to \tau_{\text{lep}}\tau_{\text{had}}$ processes the $E_{\text{T}}^{\text{miss}}$ vector usually points between the visible decay products, therefore $\sum\Delta\phi$ is smaller than π (compare Fig. 7.2). For W+jets and background processes with $E_{\text{T}}^{\text{miss}}$ resulting from energy mismeasurements, this is not necessarily the case. The distribution of this variable for signal and background can be seen in Fig. 7.17b. By accepting only events with a low $\sum\Delta\phi$ value this type of background processes is significantly reduced. Compared to a tight threshold on m_{T}, a much higher signal fraction can be maintained with the same background rejection using this criterion.

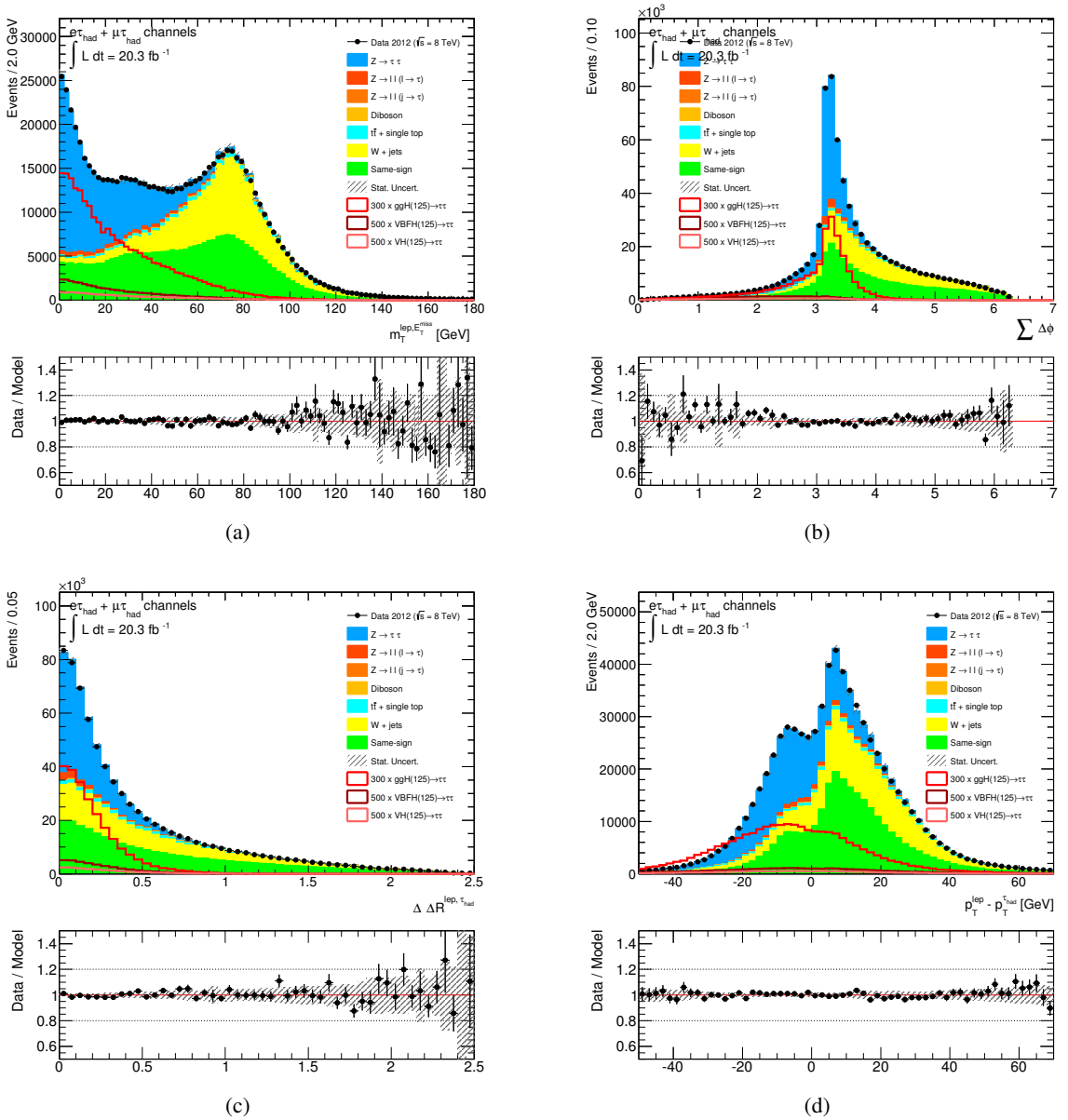

Figure 7.17: Variables used for the further suppression of background in the different categories: Distributions of (a) the transverse mass m_{T}, (b) the sum of $\Delta\phi$ between visible τ decay products and $E_{\mathrm{T}}^{\mathrm{miss}}$, (c) the difference between expected and measured $\Delta R^{\ell,\tau_{\mathrm{had}}}$ and (d) the transverse momentum difference $p_{\mathrm{T}}^{\ell} - p_{\mathrm{T}}^{\tau}$. This is shown for data, the expected background processes (estimated according to Sec. 7.5) and the scaled signal processes after the preselection (combined for the $e\tau_{\mathrm{had}}$ and $\mu\tau_{\mathrm{had}}$ channel). The bottom plots show the ratio of data to the background model. Also the statistical uncertainties of both are shown.

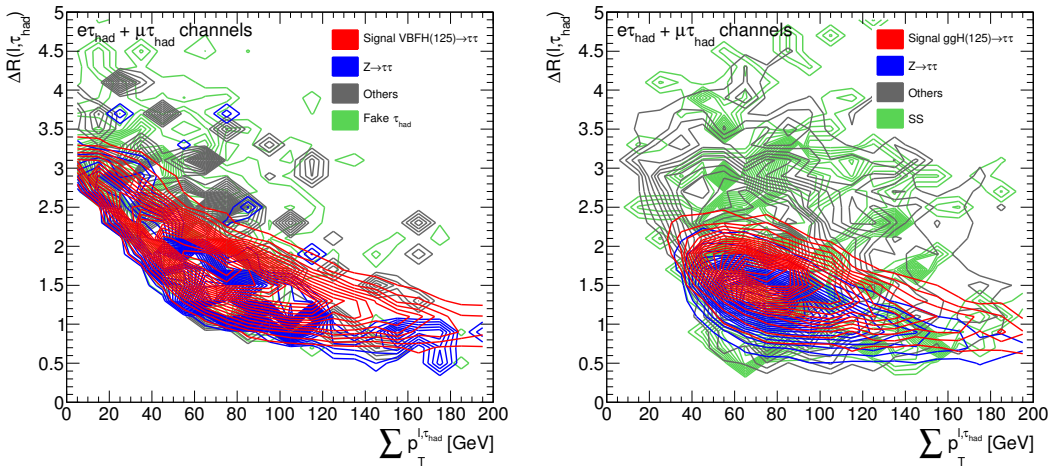

(a) (b)

Figure 7.18: Correlation of the distance between τ_{had} and lepton, $\Delta R^{\ell,\tau_{\text{had}}}$, and their vectorial sum of p_{T} for the VBF (ggF) signal and various background processes at $m_H = 125$ GeV after the (a) VBF and (b) Boosted Category selection.

Expected angular separation between lepton and τ_{had}, $\Delta\Delta R^{\ell,\tau_{\text{had}}}$ The angular separation $\Delta R^{\ell,\tau_{\text{had}}}$ of lepton and τ_{had} depends on the boost of the Higgs boson and is therefore directly correlated with the lepton and τ_{had} p_{T} for the signal process. This correlation is shown for the VBF and ggF signal processes in comparison with background in Fig. 7.18. For non-resonant background processes, in particular W+jets and QCD production, the lepton-τ_{had} pair does not show this behaviour. This observed correlation can be transferred to the definition of a selection criterion: The dependence of an average $\Delta R^{\ell,\tau_{\text{had}}}$ on the vectorial sum of the lepton and τ_{had} p_{T} for the $H \to \tau_{\text{lep}}\tau_{\text{had}}$ signal processes is parametrised by a Landau function individually for each category. As a result of this fit, the expected $\Delta R^{\ell,\tau_{\text{had}}}_{\text{pred}}(p_{\text{T}}^{\ell\tau_{\text{had}}})$ can be obtained as a function of the p_{T} value. Finally, the difference of this expected angular separation to the actual measured value in an event is defined:

$$\Delta\Delta R^{\ell,\tau_{\text{had}}} = |\Delta R^{\ell,\tau_{\text{had}}} - \Delta R^{\ell,\tau_{\text{had}}}_{\text{pred}}(p_{\text{T}}^{\ell\tau_{\text{had}}})| \tag{7.10}$$

The distribution of this variable at preselection is shown in Fig. 7.17c. For signal processes it is expected to be small, while for non-resonant background processes large deviations from $\Delta R^{\ell,\tau_{\text{had}}}_{\text{pred}}(p_{\text{T}}^{\ell\tau_{\text{had}}})$ occur. Compared to a direct threshold on $\Delta R^{\ell,\tau_{\text{had}}}$, this definition has the advantage that no particular phase space region in $\Delta R^{\ell,\tau_{\text{had}}}$ is rejected. This allows for an efficient rejection of background and a larger acceptance of signal events at the same time. The $\Delta\Delta R^{\ell,\tau_{\text{had}}}$ variable is calculated individually for each category.

p_{T} difference of lepton and τ_{had}, $p_{\text{T}}^{\ell} - p_{\text{T}}^{\tau}$ In the Zero-Jet Category background processes with misidentified τ_{had} candidates can be further suppressed by making use of the transverse momentum asymmetry of lepton and τ_{had}: For the Higgs signal the p_{T} of the lepton is expected to be smaller compared to the τ_{had} p_{T} since together with the lepton two neutrinos are produced in the τ decay, while the τ_{had} candidate is only accompanied by one neutrino. For the $j \to \tau_{\text{had}}$ background this asymmetry is not expected. The distribution of $p_{\text{T}}^{\ell} - p_{\text{T}}^{\tau}$ can be seen in Fig. 7.17d. This difference is most enhanced if no additional jet is present in the event.

Veto of b-tagged jets Due to the relatively large background of top quark processes in the VBF and Boosted Categories, events that contain jets identified as b-jets by the b-tagging algorithm are rejected (Sec. 7.3). This efficiently reduces this source of background. With the *requirement* of an identified b-jet in the event a control region dominated by top-quark processes can be defined, which is used to estimate the contribution of this background.

Rejection of $Z \to \ell\ell(\ell \to \tau_{\text{had}})$ background The $Z \to \ell\ell(\ell \to \tau_{\text{had}})$ decay is a problematic background since it peaks close to the expected signal in the invariant mass distribution. Most misidentified muons deposit only a very small fraction of their total energy in the ECal. This background can be suppressed efficiently if $f_{\text{EM}} > 0.1$ is required (Sec. 5.2 and Appendix A). This criterion is applied in the Zero-Jet Category to all one-prong τ_{had} candidates with an invariant mass of muon and τ_{had} track momentum within $80 < m_{\mu,\,\text{trk}} < 100$ GeV. The background of a $e \to \tau_{\text{had}}$ misidentifications is substantially reduced if one-prong τ_{had} candidates within $|\eta| < 0.05$ are rejected in the Zero- and One-Jet Categories[14].

In addition, two more selection criteria are applied in the VBF Category: Since no dedicated control region to estimate the contribution of the background of $j \to \tau_{\text{had}}$ can be defined for the LTT trigger (see Sec. 7.5), only SLT triggered events are considered in this category, i.e. only leptons with $p_{\text{T}} > 26$ GeV. Furthermore, the visible mass of the τ_{had} and lepton is required to be more than 40 GeV[15].

Summary of Categorisation

Table 7.5 summarises the final selection for all categories.

The good agreement between data and the background prediction observed in Figs. 7.12–7.17 gives confidence that all observables used for the definition of the categories are well modelled.

Figure 7.19 illustrates the fractional contribution of the different Higgs production mechanisms to each category and the expected signal-to-background ratio after the full selection. The VBF Category is clearly dominated by VBF signal events, a small fraction of ggF events is also selected. The signal-to-background ratio of 10% is the largest of all categories. All other categories are dominated by ggF and the signal-to-background ratio is smaller. In the Boosted and One-Jet Category also the VBF and VH production processes contribute with a non-negligible fraction to the total Higgs signal.

The categorisation and selection presented in this section has been first developed for the analysis of the 2011 and 2012 data sets at $\sqrt{s} = 7$ TeV and $\sqrt{s} = 8$ TeV (4.6 fb^{-1} and 13.0 fb^{-1}, Appendix C). It included major improvements compared to a first search for the Higgs boson in 2011 data [132]: A re-optimised tighter VBF Category (e.g. $m_{jj} > 300$ GeV tightened to $m_{jj} > 500$ GeV, addition of $p_{\text{T}}^{\text{tot}}$ selection), the implementation of the Boosted Category, the further background rejection in the categories ($\Delta\Delta R^{\ell,\tau_{\text{had}}}$, $\sum \Delta\phi$), and the inclusion of low p_{T} leptons by using the LTT trigger[16].

As explained at the beginning of this section, this event selection used for this previous analysis of 2012 data (13.0 fb^{-1}) has been re-investigated for the analysis of the full 2012 data sample (20.3 fb^{-1}) presented in this chapter. It is found to be also the optimal choice for this data sample. The only difference with respect to the previous analysis is that the Zero- and One-Jet Categories are not included in the fit of the full 2012 data, but are used for the validation of the background modelling before the fit.

[14] In this region the TRT and calorimeter information is missing, so the $e \to \tau_{\text{had}}$ misidentification probability is relatively high [23, 99].

[15] A slight discrepancy between data and simulation is observed at a very low visible mass. Detailed investigation has been done, but the cause of this problem could not be found. Since the fraction of signal in this region is negligible, this region is not considered for the fit of the $m_{\tau\tau}$ distribution.

[16] Together with an optimisation of the background estimation (Sec. 7.5), this let to an improvement of the expected sensitivity by about 45% in the $\sqrt{s} = 7$ TeV data set.

VBF Category	Boosted Category	One-Jet Category	Zero-Jet Category
$\star \geq 2$ jets	$\star\ p_{\mathrm{T}}^{\mathrm{H}} > 100$ GeV	$\star \geq 1$ jet	$\star$ 0 jets
$\star\ E_{\mathrm{T}}^{\mathrm{miss}} > 20$ GeV	$\star\ E_{\mathrm{T}}^{\mathrm{miss}} > 20$ GeV	$\star\ E_{\mathrm{T}}^{\mathrm{miss}} > 20$ GeV	$\star\ E_{\mathrm{T}}^{\mathrm{miss}} > 20$ GeV
$\star\ p_{\mathrm{T}}^{\tau_{\mathrm{had}}} > 30$ GeV	$\star\ p_{\mathrm{T}}^{\tau_{\mathrm{had}}} > 30$ GeV	$\star$ Fails VBF, Boosted Cat.	$\star$ Fails Boosted Cat.
$\star\ p_{\mathrm{T}}^{j1} > 40$ GeV, $p_{\mathrm{T}}^{j2} > 30$ GeV	$\star\ 0 < x_\ell < 1$		
$\star\ m_{jj} > 500$ GeV	$\star\ 0.2 < x_\tau < 1.2$		
$\star\ \Delta\eta_{jj} > 3.0$	$\star$ Fails VBF Cat.		
$\star$ Centrality of ℓ,τ_{had}			
$\star\ \eta_{j_1} \times \eta_{j_2} < 0$			
$\star\ p_{\mathrm{T}}^{\mathrm{tot}} < 30$ GeV			
$m_{\mathrm{T}} < 50$ GeV	$m_{\mathrm{T}} < 50$ GeV	$m_{\mathrm{T}} < 50$ GeV	$m_{\mathrm{T}} < 30$ GeV
$\Delta\Delta R^{\ell,\tau_{\mathrm{had}}} < 0.8$	$\Delta\Delta R^{\ell,\tau_{\mathrm{had}}} < 0.8$	$\Delta\Delta R^{\ell,\tau_{\mathrm{had}}} < 0.6$	$\Delta\Delta R^{\ell,\tau_{\mathrm{had}}} < 0.5$
$\sum \Delta\phi < 2.8$	b-tagged jet veto	$\sum \Delta\phi < 3.5$	$\sum \Delta\phi < 3.5$
b-tagged jet veto		$\lvert\eta_{\tau\ \mathrm{trk}}\rvert > 0.05$ ($e\tau_{\mathrm{had}}$)	$\lvert\eta_{\tau\ \mathrm{trk}}\rvert > 0.05$ ($e\tau_{\mathrm{had}}$)
SLT trigger ($p_{\mathrm{T}}^{\ell} > 26$ GeV)			$f_{\mathrm{EM}} > 0.1$ ($\mu\tau_{\mathrm{had}}$)
$m_{\mathrm{vis}} > 40$ GeV			$p_{\mathrm{T}}^{\ell} - p_{\mathrm{T}}^{\tau} < 0$

Table 7.5: Event selection of the analysis categories. Selection criteria marked with a ($\star$) are used in the definition of the mutually exclusive categories. Events failing these criteria are reconsidered for the subsequent categories. The not-marked criteria are applied in the individual categories for a further background suppression. Events failing these criteria are discarded.

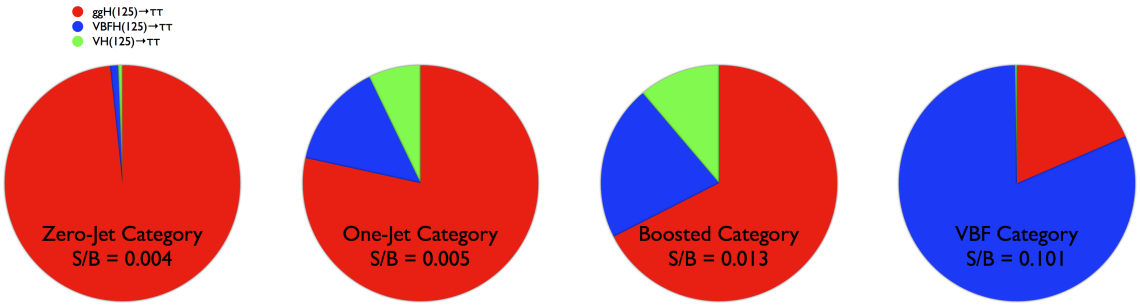

(a) (b) (c) (d)

Figure 7.19: Pie charts showing the contributions of all considered Higgs production processes (m_H = 125 GeV) in each category after the full event selection described in this section (combined for the $e\tau_{\text{had}}$ and $\mu\tau_{\text{had}}$ channel). Also stated are the resulting ratios of the total expected signal-to-background events.

7.5 Background Estimation

As explained in Sec. 7.2 there are several sources of background that can mimic the $H \to \tau_{\text{lep}}\tau_{\text{had}}$ signal. In order to be able to avoid large systematic uncertainties associated to the simulation, they are estimated from data where possible. Three main types of data-driven background estimation are used for this analysis:

- The dominant $Z \to \tau\tau$ background cannot be separated well from the $H \to \tau_{\text{lep}}\tau_{\text{had}}$ signal, therefore an *embedding* technique based on $Z \to \mu\mu$ data is used for a reliable modelling of this background.
- As explained before the QCD background is completely estimated from data. A region enriched with QCD and other $j \to \tau_{\text{had}}$ background is defined by requiring that lepton and τ_{had} candidate have the same charge. These same-sign events (SS) in data are used to model this background in the signal region, assuming the corresponding opposite-sign pairs (OS) are distributed in the same way. To model the QCD and W+jets (*fake* τ_{had}) background in the VBF Category a control region is defined by inverting the τ ID requirement. By applying a *fake factor*, denoting the ratio of successfully identified τ_{had} candidates to the number of failed identifications, the shape and normalisation of this background in the signal region is derived from this control region.
- For all other major background processes (W+jets in the Boosted Category, $Z \to \ell\ell$ and top) data control regions are defined by inversion of the relevant selection criteria. By comparing simulation to data, a correction of the normalisation is derived. Therefore, the normalisation of these background processes is derived from data, while the shapes of the kinematic distributions are based on simulations.

Figure 7.20 illustrates the fraction of different background processes in the categories as estimated by these methods. The dominance of the $Z \to \tau\tau$ background is clearly visible in all categories. The top background contributes with a significant fraction in the categories with higher jet multiplicity, while $Z \to \ell\ell$ is largest in the Zero-Jet Category, in particular in the $e\tau_{\text{had}}$ channel. The W+jets and QCD background contribute significantly in all categories[17].

The background estimation methods were already implemented for the previous $H \to \tau_{\text{lep}}\tau_{\text{had}}$ search with $\sqrt{s}$ = 7 TeV and $\sqrt{s}$ = 8 TeV data (Appendix C). The analysis of the full 2012 data set presented

[17] The exact composition of the fake τ_{had} and SS samples are discussed later in this section.

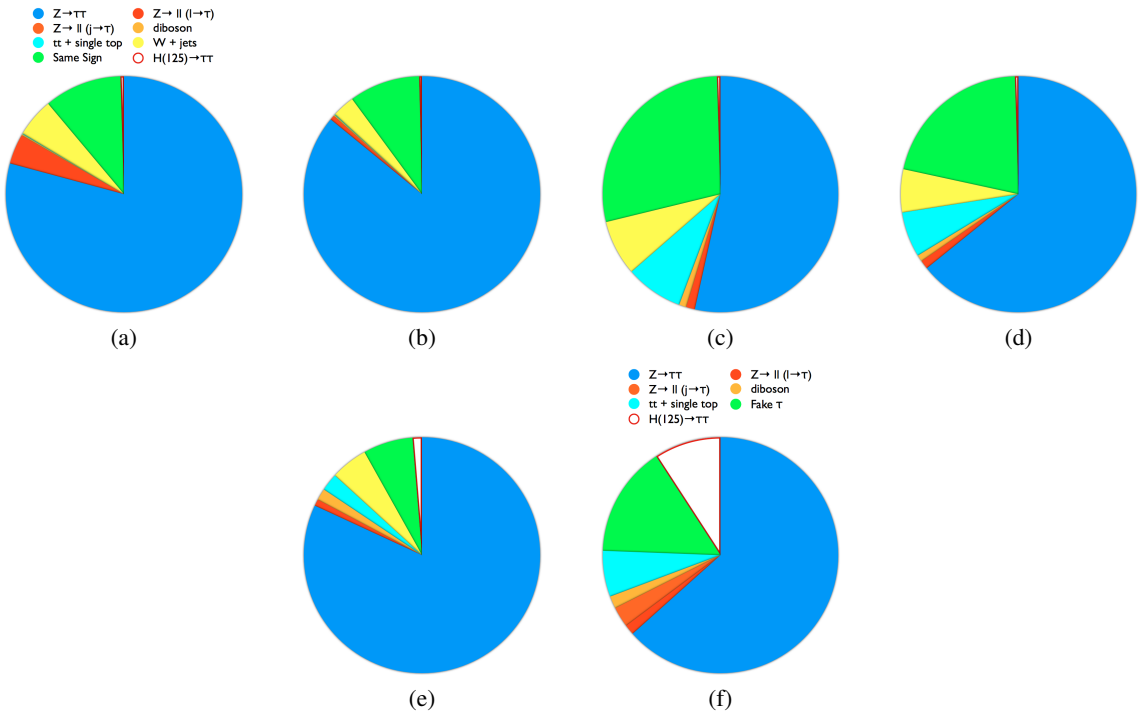

Figure 7.20: Pie charts showing the contributions of different background processes to each category after the full event selection. Also the signal fraction of the combined Higgs production processes (m_H = 125 GeV) is shown. (a) Zero-Jet $e\tau_{\text{had}}$, (b) Zero-Jet $\mu\tau_{\text{had}}$, (c) One-Jet $e\tau_{\text{had}}$, (d) One-Jet $\mu\tau_{\text{had}}$, (e) Boosted and (f) VBF Category. The methods that were used to estimate these background processes are explained in the text.

here is based on a much a larger data sample. Moreover, in this new analysis different generators are used for the simulation and the simulated W+jets and $Z \to \ell\ell$ and embedded $Z \to \tau\tau$ samples contain much more events (Sec. 7.2 and [97]). Therefore, it is important to validate if the background estimation methods can still be applied and if the smaller statistical uncertainties allow for a further improvement of the methods.

In the following the background estimation methods applied for the 20.3 fb^{-1} data sample and their validation are explained in detail. The different control regions enriched by a particular background are used to investigate if the important kinematic quantities agree well between prediction and data for this background. This either confirms the correct modelling of this background or reveals if additional systematic uncertainties have to be taken into account.

Embedding technique to model the $Z \to \tau\tau$ background

The embedding technique is used to model the dominant $Z \to \tau\tau$ background. Muons in a $Z \to \mu\mu$ data sample are replaced by τ leptons from simulated $Z \to \tau\tau$ decays, while the rest of the event including contributions from pile-up processes are taken directly from measured data, as explained in Sec. 4.3. This method allows to circumvent large systematic uncertainties on $E_{\text{T}}^{\text{miss}}$ and jet energy scale since everything apart from the signal decay is directly taken from data.

The embedding technique is used to model the $Z \to \tau\tau$ background in all categories. In the VBF Category it is used for the first time. For the previous $H \to \tau_{\text{lep}}\tau_{\text{had}}$ search (Appendix C) it was modelled by a simulated VBF-filtered $Z \to \tau\tau$ sample (Sec. 7.2) since the statistics of the embedded sample were not large enough in this category. The use of the embedded samples significantly reduces the systematic

uncertainties on jets and $E_{\mathrm{T}}^{\mathrm{miss}}$ in the VBF Categories because jets and pile-up effects are directly taken from data. A careful validation is performed to verify the consistency of both samples for the modelling of the $Z \to \tau\tau$ background.

The normalisation of the embedded $Z \to \tau\tau$ sample is derived in a data control region. The region is defined by the requirement that the visible mass is in the range of $40 < m_{\mathrm{vis}} < 70$ GeV for all events passing the preselection criteria. In this mass window the signal fraction is $< 0.1\%$. The normalisation of the embedded sample is calculated separately in the $e\tau_{\mathrm{had}}$ and $\mu\tau_{\mathrm{had}}$ channel, and for the SLT and LTT triggered events. The corresponding distributions are shown in Fig. 7.21. The obtained normalisation factors $k_{Z\to\tau\tau}$ are listed in Tab. 7.6. These normalisation factors obtained at preselection level are used commonly in all signal categories since no dependence on the investigated phase space regions is expected.

A validation to ensure a correct background modelling in the kinematic distributions relevant for this analysis is performed by defining a data control region which enhances the $Z \to \tau\tau$ background compared to the preselection samples. It is defined by the criteria $m_{\mathrm{T}} < 40$ GeV and $\sum \Delta\phi < 3.5$ applied in addition to the preselection, which reduces significantly the contribution of W+jets and QCD background processes (Sec. 7.4). A selection of kinematic observables is shown in Figs. 7.22 and 7.23 for this control sample. The other background processes are estimated according to the methods described in the following. A good agreement for all variables is visible.

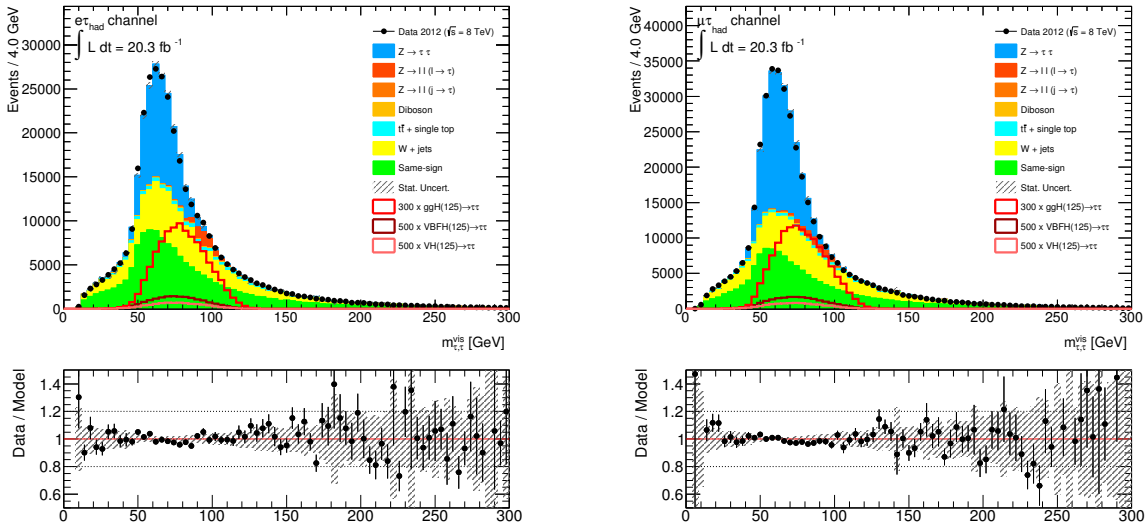

(a) (b)

Figure 7.21: Distribution of the visible $m_{\tau\tau}$ mass at preselection in the (a) $e\tau_{\mathrm{had}}$ and (b) $\mu\tau_{\mathrm{had}}$ channel. The region between $40 < m_{\mathrm{vis}} < 70$ GeV is used for the normalisation of the $Z \to \tau\tau$ background. The derived normalisation is already applied to these distributions. The data and the expected background including their statistical uncertainties are shown.

	$e\tau_{\mathrm{had}}$	$\mu\tau_{\mathrm{had}}$
$k_{Z\to\tau\tau}$ (SLT)	1.04 ± 0.07	0.90 ± 0.02
$k_{Z\to\tau\tau}$ (LTT)	1.16 ± 0.04	0.95 ± 0.02

Table 7.6: Normalisation factors applied to the embedded sample derived in a visible mass window $40 < m_{\mathrm{vis}} < 70$ GeV at preselection. They are listed separately for the two triggers used in the analysis (SLT and LTT). The uncertainty results from the statistical uncertainties of data and embedded sample.

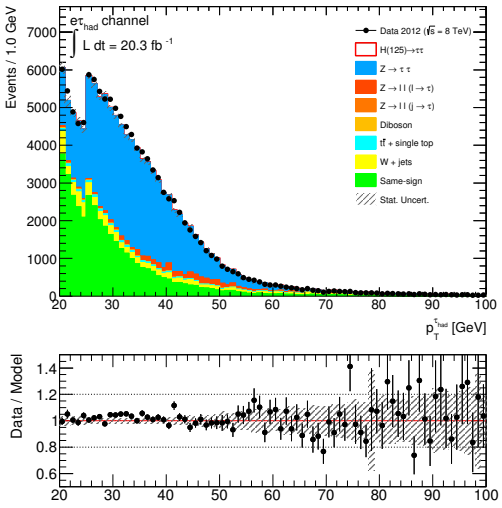

(a)

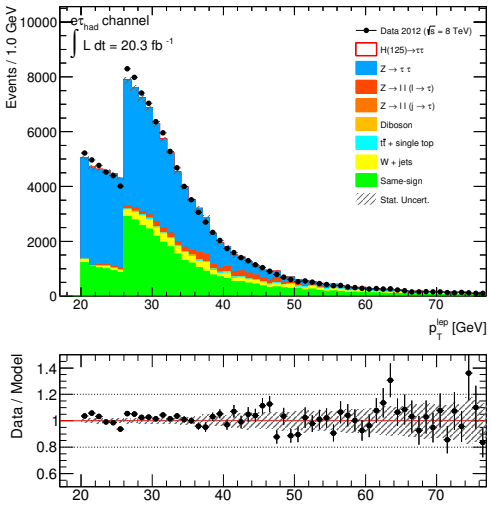

(b)

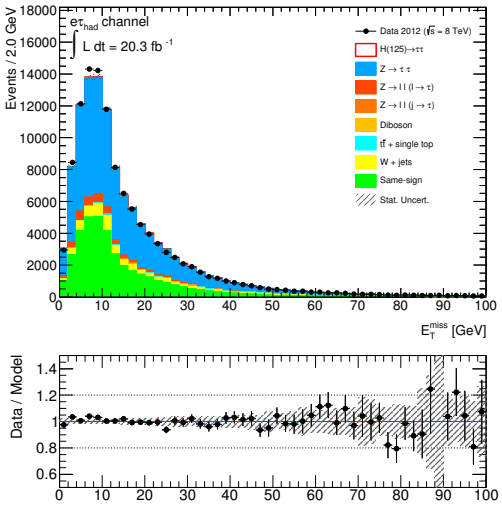

(c)

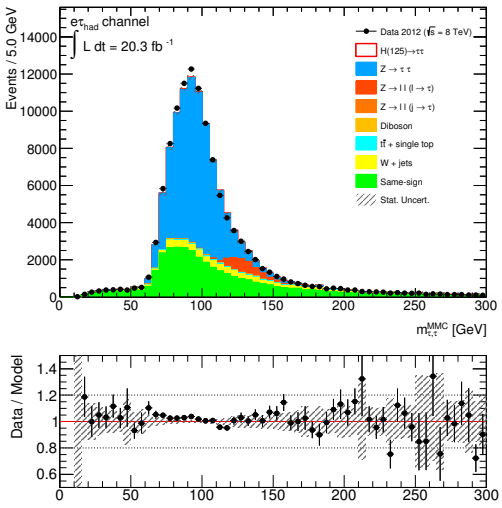

(d)

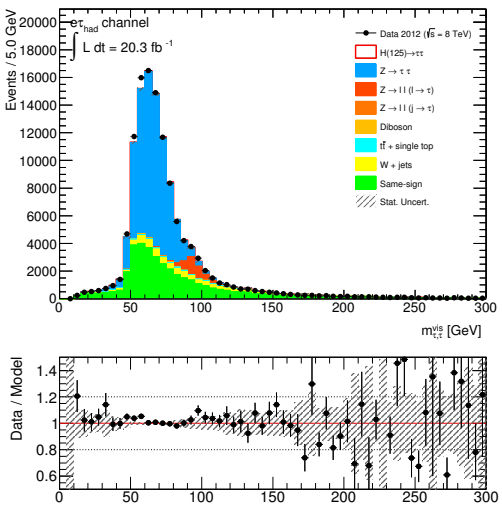

(e)

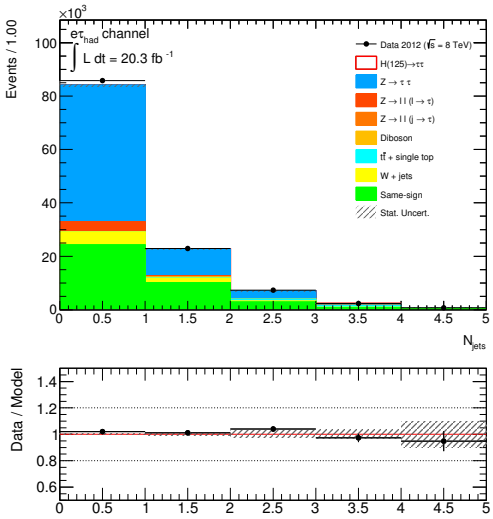

(f)

Figure 7.22: $e\tau_{\text{had}}$ **channel**: Distribution of important kinematic quantities in the $Z \to \tau\tau$ background-enriched region. (a) τ_{had} transverse momentum, (b) lepton transverse momentum, (c) missing transverse energy, (d) invariant $m_{\tau\tau}$ mass, (e) visible $m_{\tau\tau}$ mass and (f) number of jets. Data and the expected background including their statistical uncertainties are shown.

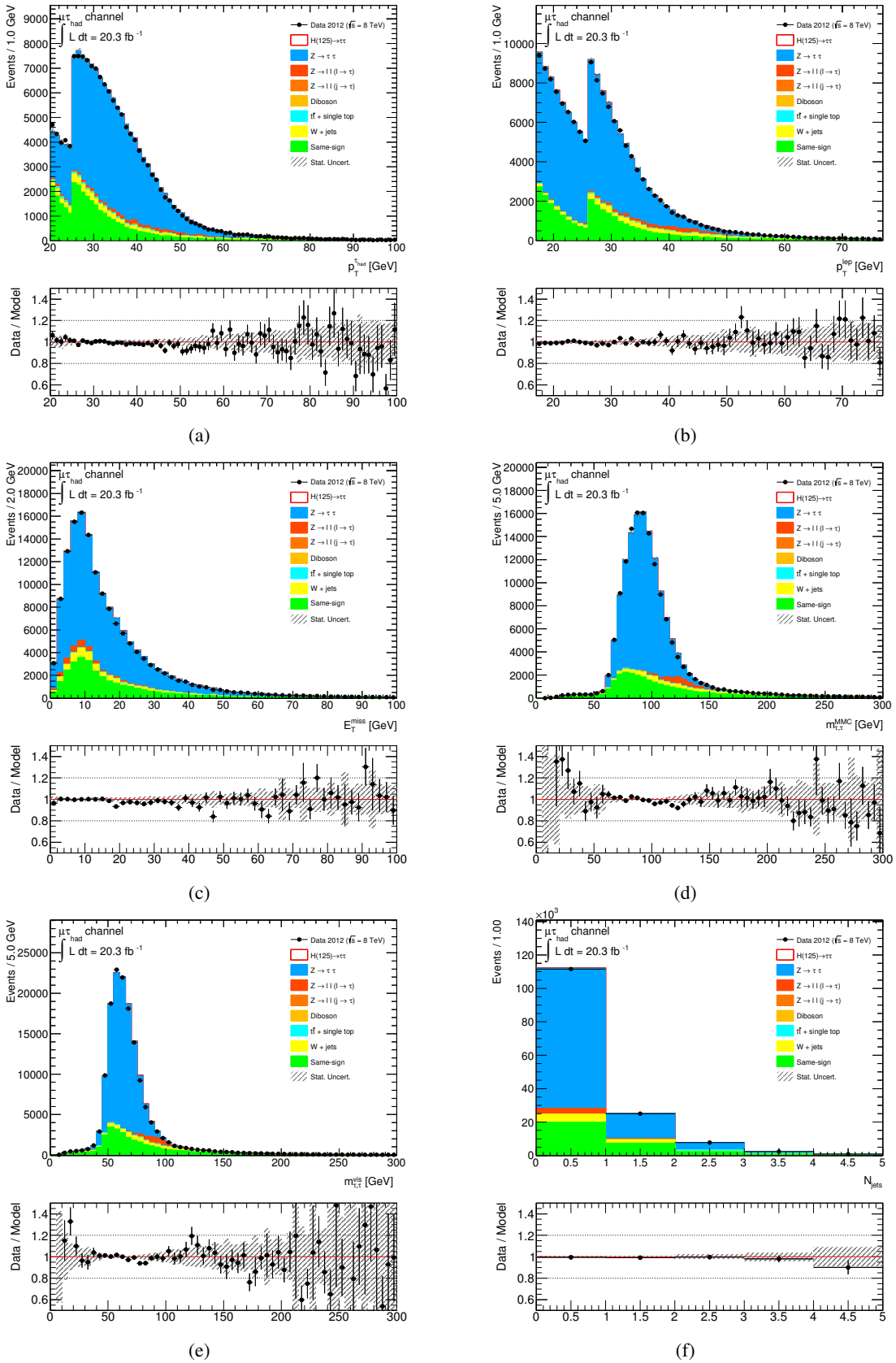

Figure 7.23: $\mu\tau_{\text{had}}$ **channel**: Distribution of important kinematic quantities in the $Z \to \tau\tau$ background-enriched region. (a) τ_{had} transverse momentum, (b) lepton transverse momentum, (c) missing transverse energy, (d) invariant $m_{\tau\tau}$ mass, (e) visible $m_{\tau\tau}$ mass and (f) number of jets. Data and the expected background including their statistical uncertainties are shown.

Background Estimation with a Same-Sign Sample

In order to estimate the QCD background, a data sample is selected by inverting the requirement of opposite charge of the τ_{had} and lepton $q_{\text{lep}} \times q_{\text{had}} < 0$ (OS) to the same charge $q_{\text{lep}} \times q_{\text{had}} > 0$ (SS) in the event selection (compare Sec. 7.3). Signal and other processes with genuine leptons and τ_{had} candidates in the final state ($Z \to \tau\tau$, several top and diboson processes), or leptons misidentified as τ_{had} candidates ($Z \to \ell\ell(\ell \to \tau_{\text{had}})$) are expected to have mainly pairs with opposite charges, as required for the signal region. For sources of background where the τ_{had} candidate is a misidentified jet (mainly QCD, W+jets, $Z \to \ell\ell(\text{j} \to \tau_{\text{had}})$ and several top processes), no strong charge correlation is expected and pairs with the same charge occur likewise.

Therefore, the SS sample in data is free of signal and contains a significant amount of QCD events. The shapes of the basic kinematic distributions, in particular the $m_{\tau\tau}$ mass, should not depend on the charge product of the particles for $j \to \tau_{\text{had}}$ background processes. Therefore, it can be assumed that the distribution of SS pairs is the same as the one of the OS pairs in the signal region for this kind of background. Consequently, the SS events can be used to model the contribution of these background processes including QCD in the signal region.

For the QCD background the ratio of the number of OS to the number of SS events, N_{OS} and N_{SS}, is expected to be almost equal. For other background processes contributing to the SS sample, like W+jets, a certain asymmetry ($N_{\text{OS}} > N_{\text{SS}}$) is expected due to the contribution of production processes where the misidentified jet results from an associated quark, like in Fig. 4.2d. The total number of background events $N_{\text{OS}}^{\text{bkg}}$ in the signal region of each category is calculated as:

$$N_{\text{OS}}^{\text{bkg}} = r_{\text{QCD}} \times N_{\text{SS}}^{\text{data}} + N_{\text{OS-SS}}^{Z\to\tau\tau} + N_{\text{OS-SS}}^{Z\to\ell\ell(\ell\to\tau_{\text{had}})} + N_{\text{OS-SS}}^{Z\to\ell\ell(\text{j}\to\tau_{\text{had}})} + N_{\text{OS-SS}}^{W\text{+jets}} + N_{\text{OS-SS}}^{\text{top}} + N_{\text{OS-SS}}^{\text{diboson}} \tag{7.11}$$

$N_{\text{SS}}^{\text{data}}$ is the number of data events measured in the SS control sample. It consists of QCD events and events of the other $j \to \tau_{\text{had}}$ background processes. The factor $r_{\text{QCD}} = N_{\text{OS}}^{\text{QCD}}/N_{\text{SS}}^{\text{QCD}}$ is the ratio of the number of OS to SS QCD events. Since the $j \to \tau_{\text{had}}$ misidentification probabilities are different for quark or gluon jets [106], the final number of QCD events depends on the fraction of gluon- to quark-jets in a sample. Since the composition of parton pairs in the QCD processes can be slightly different in the OS and SS sample, the r_{QCD} factor is determined to obtain the correct normalisation in the signal region. The factor is estimated in a QCD-dominated control region.

$N_{\text{OS-SS}}^{x}$ denotes the additional number of all other background processes in the OS sample. More exactly, it is the surplus of opposite-sign pairs resulting from the charge product asymmetry which is large or small depending on the sample, as explained before. For each background this number is calculated according to this formula (for each bin in the considered distribution):

$$N_{\text{OS-SS}}^{x} = k_x^{\text{OS}} N_{\text{OS}}^{x,\,\text{MC}} - r_{\text{QCD}} k_x^{\text{SS}} N_{\text{SS}}^{x,\,\text{MC}} \tag{7.12}$$

$N_{\text{OS}}^{x,\,\text{MC}}$ and $N_{\text{SS}}^{x,\,\text{MC}}$ are the expected event numbers from each background process in the OS and SS sample, predicted by simulation or the embedded $Z \to \tau\tau$ sample, respectively[18].

The number of OS and SS events is also corrected by the factors k_x^{OS} and k_x^{SS}, which take into account a possible mismodelling of selection efficiencies or misidentification probabilities. These correction factors are derived in separate data control regions for each background. How this estimation is done for the different sources of background is explained later in this section.

[18] Some of the $N_{\text{OS-SS}}^{x}$ terms can be negative, in particular for background processes with an approximately even number of OS and SS events, e.g. $Z \to \ell\ell(\text{j} \to \tau_{\text{had}})$. This results from the fact that the SS parts of this background contained in $N_{\text{SS}}^{\text{data}}$ are overestimated by the r_{QCD} factor. The negative values of $N_{\text{OS-SS}}^{x}$ are a correction of this effect.

To measure the QCD normalisation factor r_{QCD}, two QCD-dominated regions with opposite- and same-sign pairs are defined by these criteria: $E_{\text{T}}^{\text{miss}} < 15$ GeV, $m_{\text{T}} < 30$ GeV, requiring events to pass the BDT loose τ_{had} ID and omitting the lepton isolation criteria. The remaining fraction of background processes predicted by simulation is subtracted in the OS and SS control samples separately[19].

The missing isolation requirement can influence the r_{QCD} measurement. A larger amount of non-isolated leptons from hadron decays within jets is included, changing the probability for different charge configurations. The ratio of OS to SS QCD events is therefore evaluated as a function of the relative calorimeter isolation and extrapolated to the signal region to obtain the correct r_{QCD} [98].

Different kinematic variables in the QCD control samples with OS and SS pairs are compared to validate that the shapes of the two samples are consistent. An example is shown in Fig. 7.24, where the transverse mass distributions of the OS and SS samples are compared. The ratio of OS to SS events is constant within uncertainties. The assumption that the shapes of the distributions are the same for OS and SS QCD events is therefore reasonable.

The measured r_{QCD} values for the $e\tau_{\text{had}}$ and $\mu\tau_{\text{had}}$ samples are listed in Tab. 7.7.

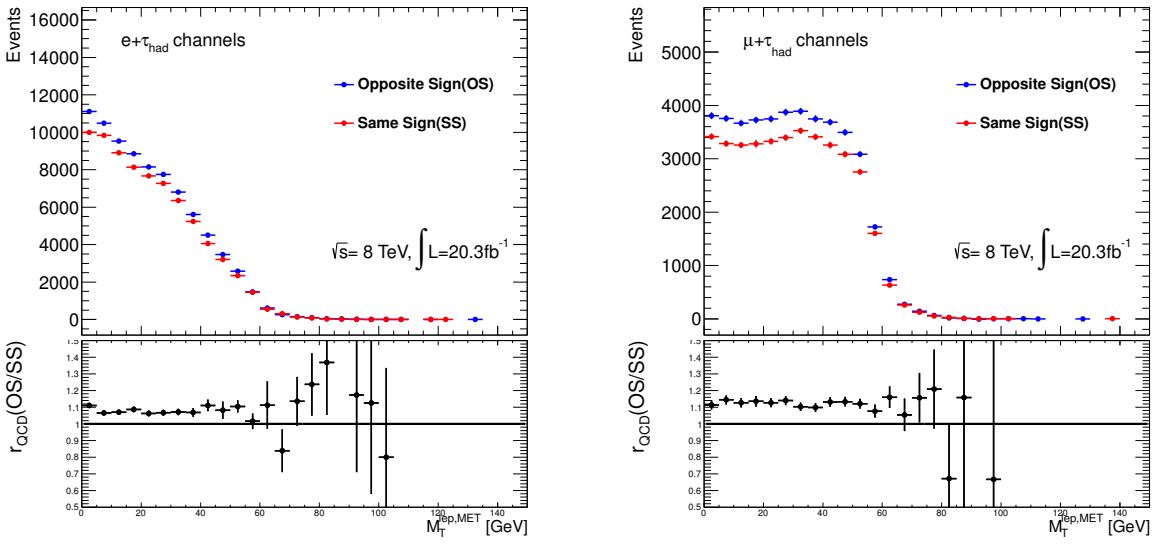

(a) (b)

Figure 7.24: Transverse mass distribution in the QCD control region (see text) of OS (red) and SS (blue) data events in (a) the $e\tau_{\text{had}}$ and (b) the $\mu\tau_{\text{had}}$ channel. The small contribution from other background processes (mainly W+jets and top) is subtracted from both data samples. The bottom distribution shows the ratio of OS to SS events in each bin [98].

	$e\tau_{\text{had}}$	$\mu\tau_{\text{had}}$
r_{QCD}	1.00 ± 0.12 (syst.)	1.10 ± 0.13 (syst.)

Table 7.7: Measured values and systematic uncertainties (explained in 7.7) of the ratio of OS to SS events r_{QCD} for the estimation of the QCD contribution in the signal region.

[19] The normalisation of W+jets is derived in a data control region defined by $m_{\text{T}} > 80$ GeV on top of the QCD control region selection.

This background estimation method is implemented for all categories apart from the VBF Category. Figures 7.25a–7.25c show the composition of background processes in the SS sample for the individual categories. While for the Zero- and One-Jet Category the SS sample is clearly dominated by QCD, the W+jets background has the largest contribution in the Boosted Category. Also $Z \to \tau\tau$, top, diboson and $Z \to \ell\ell$ background contribute to the SS samples[20].

By inverting the $\Delta\Delta R^{\ell,\tau_{\text{had}}}$ distribution in the event selection (see Sec. 7.4) a sample with an enlarged fraction of QCD and other $j \to \tau_{\text{had}}$ background processes is obtained. This can be used to validate the background estimation performed with this method. Figure 7.26 shows for instance the distribution of the $m_{\tau\tau}$ mass. A reasonable agreement between data and the prediction from the background modelling is observed within the statistical uncertainties.

A disadvantage of the SS estimation is that statistics in this control region are roughly the same as in the signal region, which can be a problem in the categories with low statistics. For this reason it is not used in the VBF Category.

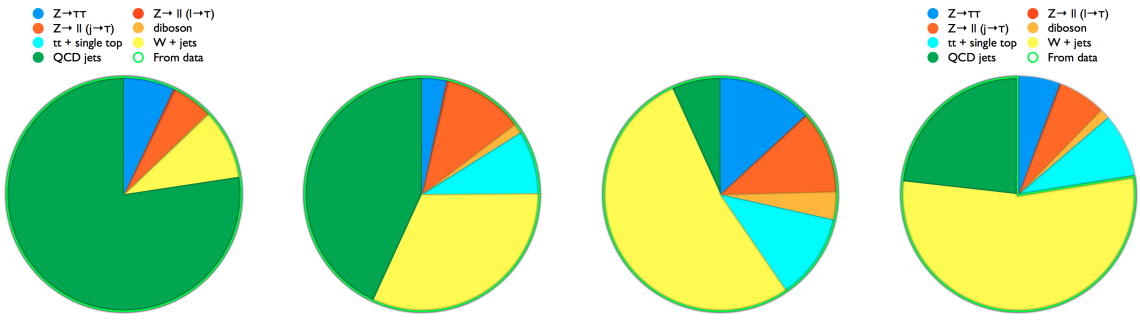

Figure 7.25: Pie charts showing the contributions of different background processes in the SS/ anti-ID τ_{had} sample of each category as expected from simulation for the combined $e\tau_{\text{had}}$ and $\mu\tau_{\text{had}}$ channels (QCD is calculated from the fraction of events that remain in the data sample after subtraction of all other background processes). SS sample of (a) Zero-Jet, (b) One-Jet and (c) Boosted Category. (d) Anti-ID τ_{had} sample of VBF Category. The part that is taken directly from data to estimate the contained background processes in the signal region is indicated by the light green line.

[20] It should therefore be noted, that in all figures and tables showing the expected background contributions in the selected samples estimated with the SS method, only the OS-SS surplus of W+jets, $Z \to \tau\tau$, $Z \to \ell\ell$ top and diboson is shown individually for each sample. The rest of background events is included in the SS sample.

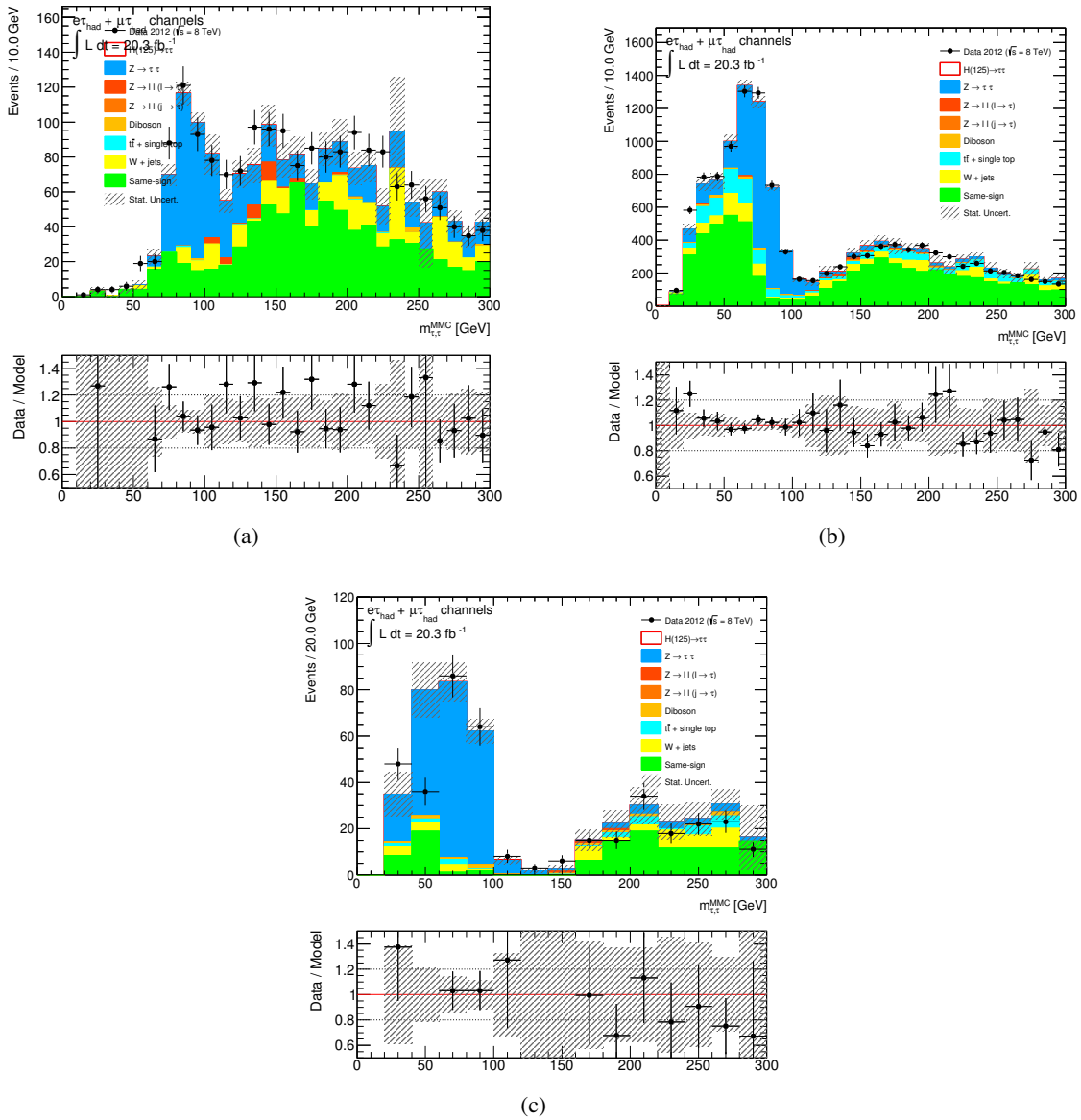

Figure 7.26: Distribution of the invariant $m_{\tau\tau}$ mass in the inverted $\Delta\Delta R^{\ell,\tau_{\text{had}}}$ control region enriched by QCD background of the combined $e\tau_{\text{had}}$ and $\mu\tau_{\text{had}}$ channel in (a) the Zero-Jet Category, (b) the One-Jet Category and (c) the Boosted Category. Data and the expected background including their statistical uncertainties are shown.

Background Estimation with a Fake-Factor Method

In the VBF region a different method is applied to estimate the contribution of the QCD background. The $j \to \tau_{\text{had}}$ background (QCD and W+jets) is estimated via a so-called *fake factor* method. For this purpose a control region in data is formed by applying all selection criteria, but inverting the BDT medium τ_{had} ID requirement, i.e. selecting candidates that fail the τ_{had} identification (*anti-ID* τ_{had} candidates).

The expected ratio of such anti-ID candidates to successfully identified τ_{had} candidates (*fake factor*) is defined as:

$$r_{\text{f}} = \frac{N_{\text{pass } \tau_{\text{had}} \text{ ID}}}{N_{\text{fail } \tau_{\text{had}} \text{ ID}}} \tag{7.13}$$

In contrast to r_{QCD} in the SS method, the fake factor is an event-by-event weight and is derived as a function of τ_{had} momentum and number of tracks. Applying this factor to the sample of *anti-ID* τ_{had} candidates in the anti-ID VBF control region yields the expected number of QCD and W+jets candidates in the signal region. A small fraction of events from other sources of background are also expected in this sample, which need to be taken into account.

The total background $N^{\text{bkg}}_{\tau_{\text{had}}\text{ ID}}$ in the signal region is thus estimated as follows:

$$\begin{aligned} N^{\text{bkg}}_{\tau_{\text{had}}\text{ ID}} = r_{\text{f}} \times (&N^{\text{data}}_{\text{anti }\tau_{\text{had}}\text{ ID}} - N^{Z\to\tau\tau}_{\text{anti }\tau_{\text{had}}\text{ ID}} - N^{Z\to\ell\ell(\ell\to\tau_{\text{had}})}_{\text{anti }\tau_{\text{had}}\text{ ID}} - N^{Z\to\ell\ell(\text{j}\to\tau_{\text{had}})}_{\text{anti }\tau_{\text{had}}\text{ ID}} - N^{\text{top}}_{\text{anti }\tau_{\text{had}}\text{ ID}} - N^{\text{diboson}}_{\text{anti }\tau_{\text{had}}\text{ ID}}) \\ &+ N^{Z\to\tau\tau}_{\tau_{\text{had}}\text{ ID}} + N^{Z\to\ell\ell(\ell\to\tau_{\text{had}})}_{\tau_{\text{had}}\text{ ID}} + N^{Z\to\ell\ell(\text{j}\to\tau_{\text{had}})}_{\tau_{\text{had}}\text{ ID}} + N^{\text{top}}_{\tau_{\text{had}}\text{ ID}} + N^{\text{diboson}}_{\tau_{\text{had}}\text{ ID}} \end{aligned} \tag{7.14}$$

$N^{\text{data}}_{\text{anti }\tau_{\text{had}}\text{ ID}}$ denotes the number of *anti-ID* τ_{had} candidates measured in the data control region which contains mainly the QCD and W+jets events. It is corrected for the expected contributions from other background samples $N^{\text{x}}_{\text{anti }\tau_{\text{had}}\text{ ID}}$, based on simulation[21]. $N^{\text{x}}_{\tau_{\text{had}}\text{ ID}}$ denotes the contributions from other background processes in the signal region. They are estimated from simulation or the embedded sample, respectively, and the correct normalisation is derived in control regions. The estimation of these correction factors is described later in this section.

The fake factor depends on the composition of partons in the anti-ID sample. This is due to the fact that the $j \to \tau_{\text{had}}$ misidentification probability differs for quark- and gluon-jets. Since the QCD background is dominated by misidentified quark-jets and the W+jets background is dominated by misidentified gluon-jets (Figs. 4.2 and 7.8b), two different fake factors are derived separately for the two background processes: r_{f}^{W} and $r_{\text{f}}^{\text{QCD}}$. By determining the fraction R_W of W events in the anti-ID control region, the final fake factor can be calculated:

$$r_{\text{f}} = R_W r_{\text{f}}^{W} + (1 - R_W) r_{\text{f}}^{\text{QCD}} \tag{7.15}$$

This is based on the assumption, that the composition of quark- and gluon-dominated processes in the signal region is the same as in the anti-ID control region.

The two fake-factors are measured in control regions enriched by either of these background processes. To measure r_{f}^{W}, the transverse mass requirement in the anti-ID control region is inverted to $m_{\text{T}} > 70$ GeV, while $r_{\text{f}}^{\text{QCD}}$ is measured in a region with no lepton isolation requirements and a *loose* identification requirement for muons and electrons [98]. To calculate R_W, a normalisation correction of the simulated sample is derived from data for events with a high m_{T} in the anti-ID control region. Then R_W is calculated from the fraction of the expected W events in the low-m_{T} anti-ID region.

[21] The normalisation of the $Z \to \ell\ell(\text{j} \to \tau_{\text{had}})$ background is derived in a dedicated control region to match the one in data as described later in this section.

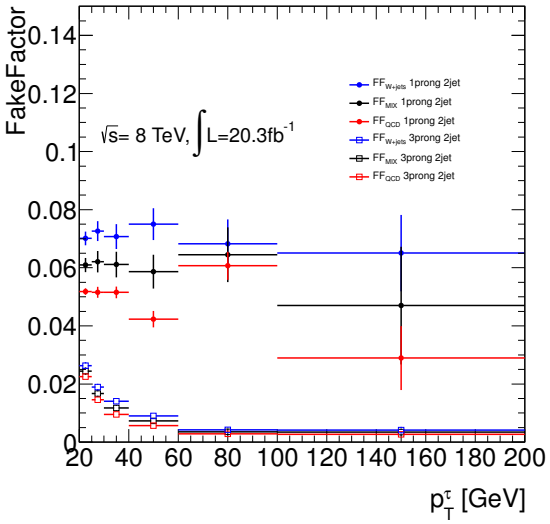

Figure 7.27: Estimated fake factors $r_{\mathrm{f}}^{\mathrm{QCD}}$ (red), r_{f}^{W} (blue) and the combined factor r_{f} (black) for one-prong (circles) and three-prong (squares) τ_{had} candidates [150].

The fake factors are derived as a function of p_{T} and the number of tracks of the τ_{had} candidate. The resulting factors for W+jets, QCD and the mixture of both in the anti-ID sample are shown in Fig. 7.27.

In general they are larger for low τ_{had} p_{T} and lie between 0.08 and 0.03 for one-prong candidates and between 0.03 and 0.005 for three-prong τ_{had} candidates[22].

Figure 7.25d illustrates the fractional contribution of different background processes to the anti-ID τ_{had} control region in the VBF Category.

The background prediction by the fake factor method can be validated in a sample of SS events fulfilling the VBF selection criteria, including the τ_{had} identification criteria. This sample has a negligible signal fraction and an enhanced contribution of the $j \rightarrow \tau_{\mathrm{had}}$ background processes. In order to increase the statistics of the SS sample, the VBF selection criteria on $p_{\mathrm{T}}^{\mathrm{tot}}$, $\Delta\Delta R^{\ell,\tau_{\mathrm{had}}}$, $\sum \Delta\phi$, the centrality and $\eta_{j_1} \times \eta_{j_2}$ are omitted.

Two example distributions are shown in Fig. 7.28. The predicted shape agrees reasonably well with data within the statistical uncertainties, but the overall contribution of the $j \rightarrow \tau_{\mathrm{had}}$ background is overestimated. This might result from the fact that the ratio of misidentified quark- to gluon-jets in the SS region, and thus also in the signal region, is different compared to the anti-ID regions. To account for these differences, a conservative systematic uncertainty of 50% is associated with the fake factor estimate, which covers the extreme cases of a pure quark-dominated ($R_W \approx 0$) and a pure gluon-dominated ($R_W \approx 1$) sample (Eq. 7.15).

In comparison to the SS background estimation method, the statistics in the anti-ID τ_{had} control region is usually one to two orders of magnitude larger than in the signal region. Therefore, the statistical uncertainty of this background estimation is much smaller and the background can be modelled more accurately in signal regions with only few events. The two largest sources of reducible background, W+jets and QCD, are entirely determined from data, while regarding the SS background estimation the surplus of OS W+jets events is still modelled by simulation. However, the fake factor estimate is afflicted with relatively large systematic uncertainties due to the uncertainty on the exact ratio of gluon- to quark-jets in the signal region.

[22] An estimate for the LTT triggered events can not be made with this method, since due to the BDT medium τ_{had} ID requirement on trigger level (Tab. 7.3) no unbiased anti-ID control region can be defined, and an accurate estimation of the fake factor cannot be done.

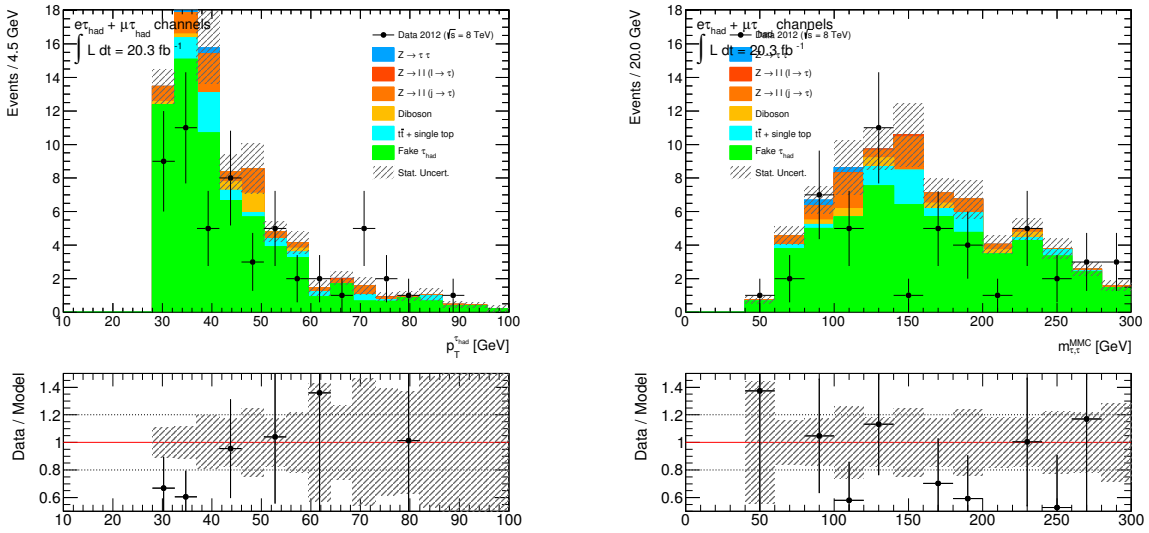

(a) (b)

Figure 7.28: Distribution of kinematic quantities in the SS control region enriched by $j \to \tau_{\text{had}}$ events of the combined $e\tau_{\text{had}}$ and $\mu\tau_{\text{had}}$ channel in the VBF Category. (a) τ_{had} transverse momentum and (b) invariant $m_{\tau\tau}$ mass. Data and the expected background including their statistical uncertainties are shown.

Normalisation of Background Processes in Data Control Regions

The estimation of all background processes apart from QCD and $Z \to \tau\tau$ (and W+jets in the VBF Category) is based on simulation[23].

The $\ell \to \tau_{\text{had}}$ and $j \to \tau_{\text{had}}$ misidentification probabilities are often not well modelled by simulation, which results in different selection efficiencies compared to data. By inverting event selection criteria, also in this case control regions enriched by a certain type of background are defined.

In these control regions the differences in the event yields are compared between data and simulation after a subtraction of the remaining small contribution of other background processes, and correction factors for the normalisation are derived. With this method the systematic uncertainties associated to the modelling of selection efficiencies by simulation can be significantly reduced (see Sec. 7.7). In the following, the definition of control regions and the resulting correction factors for the individual background processes are described.

W+jets background W+jets events are expected to have a high transverse mass, unlike other processes (Fig. 7.17a). As explained before, the misidentification probability $j \to \tau_{\text{had}}$ depends on the fraction of gluon- and quark-jets in the selected sample, which for W+jets varies in the different categories and in the OS and SS sample. Therefore individual scale factors are derived for each sample and category (compare Eq. 7.12).

For that purpose the category definition criteria are applied (Tab. 7.5) and in addition $m_{\text{T}} > 70$ GeV

[23] More precisely, in all categories where the SS method is applied only $N^{x}_{\text{OS-SS}}$, the surplus of OS events for each background process is estimated from simulation (Eq. 7.12).

is required to form the W control regions[24]. The obtained values for the scale factors $k^{\text{OS/SS}}_{W+\text{jets}}$ are listed in Tab. 7.8.

To validate the background estimation, distributions of important kinematic quantities are investigated in the W control regions. For instance, Figure 7.29 shows the distribution of the $m_{\tau\tau}$ mass for each category after the normalisation correction. A very good agreement of data and simulation is observed, which confirms the good modelling of the background also in the signal region.

$Z \to \ell\ell(\ell \to \tau_{\text{had}})$ background Also the $\ell \to \tau_{\text{had}}$ misidentification probability can be mismodelled in simulation. For the $e \to \tau_{\text{had}}$ case, correction factors dependent on the pseudo-rapidity are applied based on studies like the one presented in Sec. 5.2.1 [99].

A $Z \to ee$ ($e \to \tau_{\text{had}}$) enriched control region is defined to verify if this background is correctly predicted with these scale factors. On top of the analysis selection criteria, is required that no jets is in the event, $E_{\text{T}}^{\text{miss}} < 20$ GeV and $80 < m_{\text{vis}} < 100$ GeV. The τ_{had} candidate is required to originate from a true electron in simulation, to separate it from the $Z \to \ell\ell(\text{j} \to \tau_{\text{had}})$ part of this background. Figures 7.30a and 7.30b show the distribution of events in data compared to the background prediction, as an example for the τ_{had} pseudorapidity and $m_{\tau\tau}$. All distributions are well-modelled.

The $\mu \to \tau_{\text{had}}$ misidentification is much less likely and the fraction of background remaining after the event selection is small (Sec. 5.2). Therefore no normalisation correction factors are applied to the simulated samples. The investigation of this background in a control region with $80 < m_{\mu,\tau_{\text{had}}\text{trk}} < 100$ GeV (Sec. 7.4) and $E_{\text{T}}^{\text{miss}} < 20$ GeV reveals a slight discrepancy between data and simulation. Figures 7.30c and 7.30d show the $m_{\mu,\tau_{\text{had}}\text{trk}}$ and MMC mass distributions in this control region. A conservative uncertainty of ±15% is assumed as systematic uncertainty to account for these differences (Sec. 7.7).

	Zero-Jet		One-Jet		Boosted	VBF
	$e\tau_{\text{had}}$	$\mu\tau_{\text{had}}$	$e\tau_{\text{had}}$	$\mu\tau_{\text{had}}$		
$k^{\text{OS}}_{W+\text{jets}}$	0.82 ± 0.01	0.78 ± 0.01	0.94 ± 0.01	0.87 ± 0.02	0.90 ± 0.05	-
$k^{\text{SS}}_{W+\text{jets}}$	0.98 ± 0.02	0.94 ± 0.02	0.98 ± 0.03	0.88 ± 0.02	0.96 ± 0.08	-
$k^{\text{OS/SS/}\tau_{\text{had}}\text{ ID}}_{Z\to\ell\ell(\text{j}\to\tau_{\text{had}})}$	0.82 ± 0.01	0.82 ± 0.01	0.82 ± 0.01	0.82 ± 0.01	0.82 ± 0.01	0.82 ± 0.01
$k^{\tau_{\text{had}}\text{ anti-ID}}_{Z\to\ell\ell(\text{j}\to\tau_{\text{had}})}$	-	-	-	-	-	0.92 ± 0.02
$k^{\text{OS/}\tau_{\text{had}}\text{ ID}}_{\text{Top}}$	0.83 ± 0.01	0.83 ± 0.01	0.83 ± 0.01	0.83 ± 0.01	0.83 ± 0.01	0.83 ± 0.01
$k^{\text{SS}}_{\text{Top}}$	0.98 ± 0.03	0.98 ± 0.03	0.98 ± 0.03	0.98 ± 0.03	0.98 ± 0.03	-

Table 7.8: Normalisation correction factors k_x and their statistical uncertainties applied to the simulated samples of the W+jets, $Z \to \ell\ell(\text{j} \to \tau_{\text{had}})$ and top background in the OS/SS samples of the Zero-Jet, One-Jet and Boosted Category and the τ_{had} ID/anti-ID samples of the VBF Category, indicated by the superscript of k_x.

[24] Only for the Boosted Category the threshold on the p_{T}^{H} is lowered to 50 GeV to enlarge the statistics in the W control sample. A comparison with the normalisation factor obtained in the $p_{\text{T}}^{\text{H}} > 100$ GeV control region shows that the a looser threshold does not bias the correction factor.

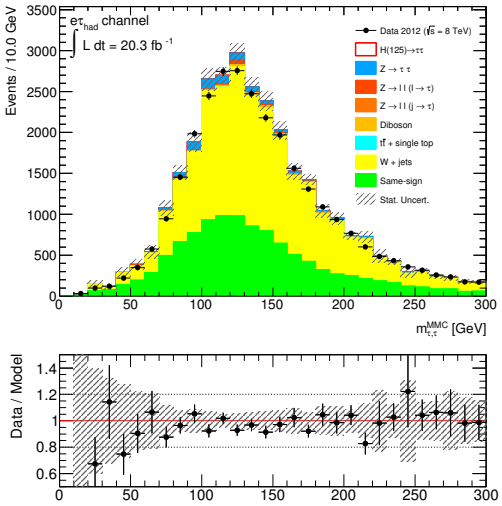

(a)

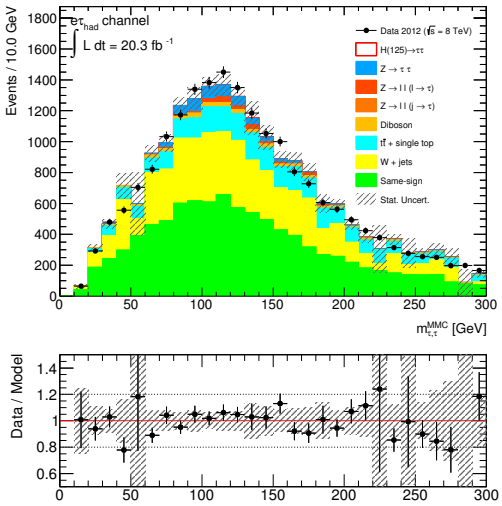

(b)

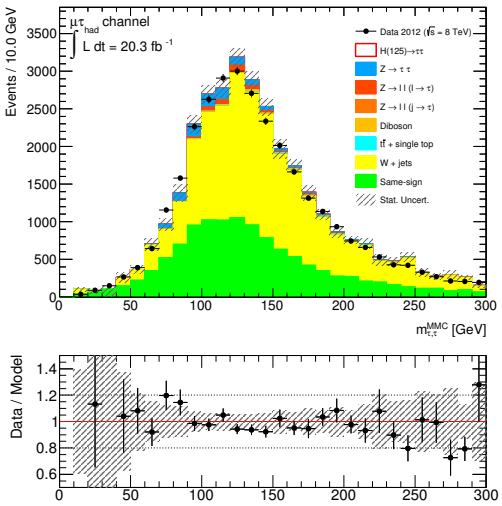

(c)

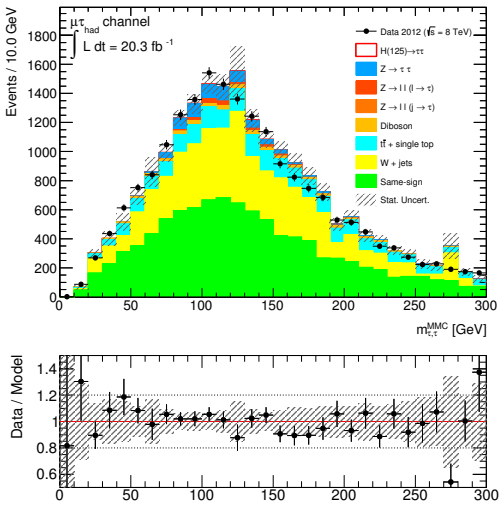

(d)

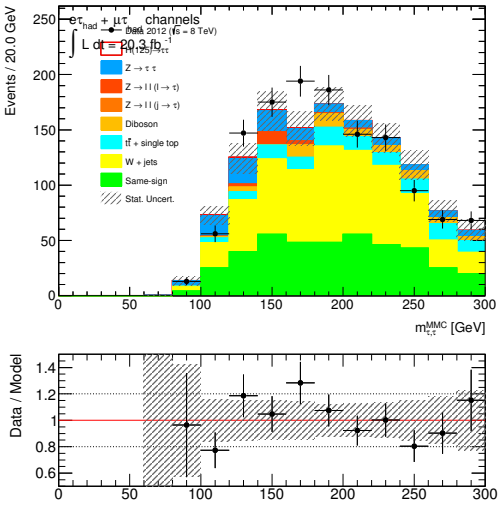

(e)

Figure 7.29: Distribution of the invariant $m_{\tau\tau}$ mass in the W control region in the Zero-Jet Category in the (a) $e\tau_{\text{had}}$ and (b) $\mu\tau_{\text{had}}$ channel, One-Jet Category in the (c) $e\tau_{\text{had}}$ and (d) $\mu\tau_{\text{had}}$ channel and (e) in the Boosted Category. Data and the expected background including their statistical uncertainties are shown.

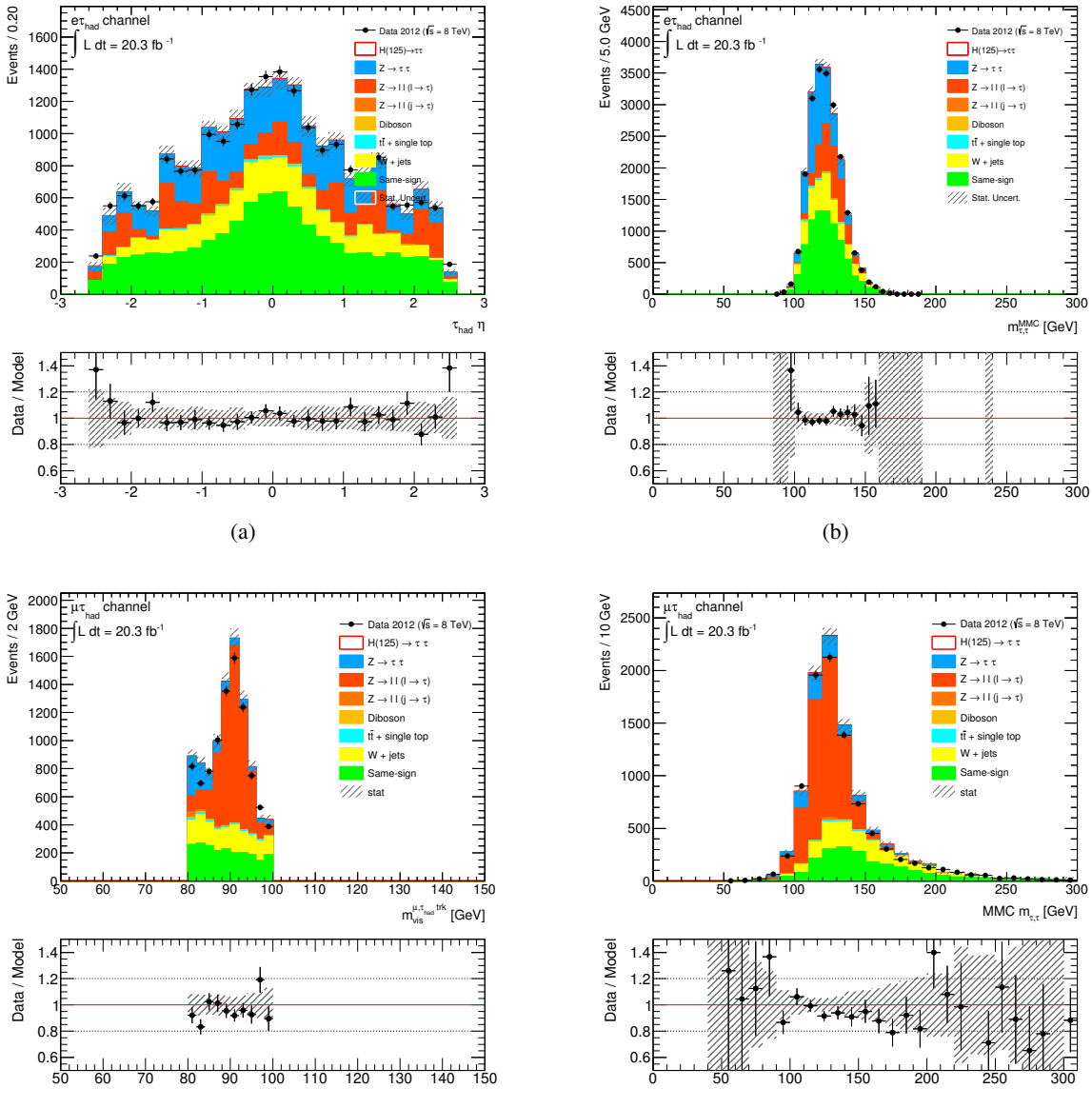

Figure 7.30: Distribution of important kinematic quantities in the $Z \to \ell\ell(\ell \to \tau_{\text{had}})$ background control region of the (top) $e\tau_{\text{had}}$ and (bottom) $\mu\tau_{\text{had}}$ channel. (a) τ_{had} pseudorapidity and (b) invariant $m_{\tau\tau}$ mass in the $Z \to ee(e \to \tau_{\text{had}})$ control region. (c) Invariant μ and τ_{had} track mass and (d) invariant $m_{\tau\tau}$ mass in the $Z \to \mu\mu(\mu \to \tau_{\text{had}})$ control region. Data and the expected background including their statistical uncertainties are shown.

$Z \to \ell\ell(\mathrm{j} \to \tau_{\mathrm{had}})$ background A control region to study the $Z \to \ell\ell(\mathrm{j} \to \tau_{\mathrm{had}})$ background is defined in the following way:

- Two leptons (ee or $\mu\mu$) with opposite charge
- Leptons pass the lepton selection and at least one of them the isolation criteria
- $61 < m_{\ell\ell} < 121$ GeV
- An additional τ_{had} candidate is found in the event passing the analysis selection criteria

No dependence of the $j \to \tau_{\mathrm{had}}$ misidentification probability on the charge correlation or lepton flavour is expected, which is why a common factor is used for all samples and channels. The factor is also found to be consistent for the different categories within statistics. For the VBF region a $Z \to \ell\ell(\mathrm{j} \to \tau_{\mathrm{had}})$ correction factor is derived for the anti-ID control region by inverting the τ_{had} ID requirement in the $Z \to \ell\ell$ control region.

The resulting normalisation factors $k^{\mathrm{OS}/\tau_{\mathrm{had}}\ \mathrm{ID/SS}}_{Z\to\ell\ell(\mathrm{j}\to\tau_{\mathrm{had}})}$ and $k^{\tau_{\mathrm{had}}\ \text{anti-ID}}_{Z\to\ell\ell(\mathrm{j}\to\tau_{\mathrm{had}})}$ are listed in Tab. 7.8. Figures 7.31a and 7.31b show several exemplary kinematic quantities that are investigated in this control region after the normalisation correction. Good agreement is observed between data and the prediction, which confirms a good modelling of this background.

Top background The top processes constitute an important background in the categories with higher jet multiplicity. Its properties of high $E_{\mathrm{T}}^{\mathrm{miss}}$ and high-p_{T} jets, some of them originating from b-jets, can be used to define a top-enriched control region. These criteria are applied in addition to the preselection:

- $E_{\mathrm{T}}^{\mathrm{miss}} > 20$ GeV
- $m_{\mathrm{T}} > 70$ GeV
- Number of jets ≥ 2
- At least one of the jets must originate from a b-jet (see Sec. 7.3)

After subtraction of the small fraction of other background processes, the correction factors $k^{\mathrm{OS}/\tau_{\mathrm{had}}\ \mathrm{ID}}_{\mathrm{Top}}$ and $k^{\mathrm{SS}}_{\mathrm{Top}}$ are derived[25]. For the $e\tau_{\mathrm{had}}$ and $\mu\tau_{\mathrm{had}}$ they are found to be consistent within uncertainties and a common factor is used.

The results are listed in Tab. 7.8. Figures 7.31c and 7.31d show the comparison of data and simulation for the missing transverse energy and invariant mass, which are investigated among other variables in this control region after the normalisation correction. Good agreement is observed confirming a good modelling of this background.

Diboson background The sum of WW, WZ and ZZ decays constitutes in all defined signal and control regions only a small fraction of the overall background ($< 2\%$). Moreover, these processes contribute mainly through final states with genuine τ_{had} and lepton candidates, which are well-modelled. Therefore the estimation of this background is completely based on simulation and the scaling factor k_{diboson} is assumed to be 1.

[25] For the W background a correction factor is derived for the normalisation of the simulated sample by applying the same selection as for the top control region, but rejecting events with a b-jet instead.

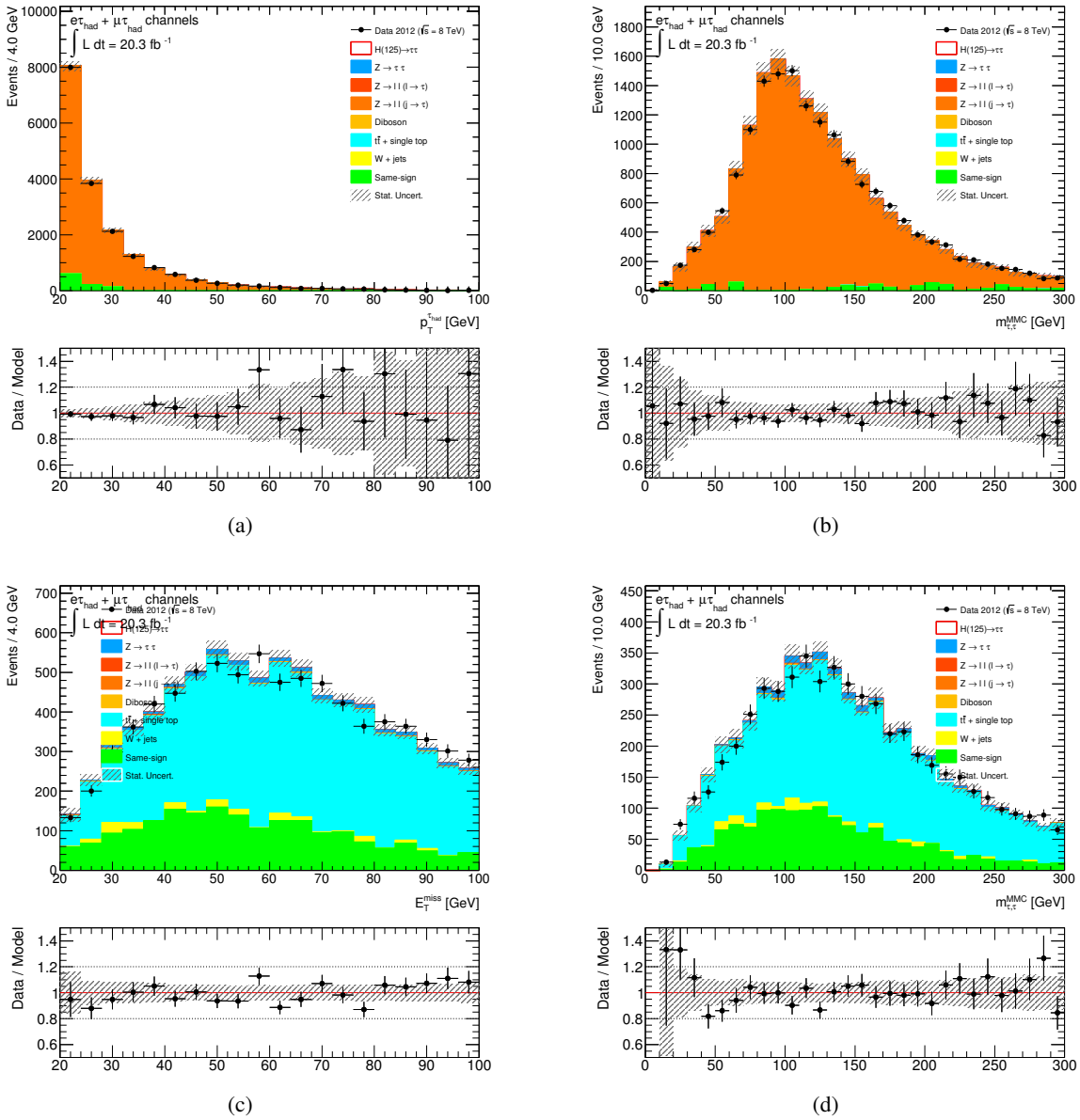

Figure 7.31: Distribution of important kinematic quantities in the (top) $Z \rightarrow \ell\ell(\mathrm{j} \rightarrow \tau_{\mathrm{had}})$ and (bottom) top background control region for the $e\tau_{\mathrm{had}}$ and $\mu\tau_{\mathrm{had}}$ channels. (a) τ_{had} transverse energy and (b) invariant $m_{\tau\tau}$ mass in the top control region. (c) missing transverse energy and (d) invariant $m_{\tau\tau}$ mass in the $Z \rightarrow \ell\ell(\mathrm{j} \rightarrow \tau_{\mathrm{had}})$ control region. Data and the expected background including their statistical uncertainties are shown.

Further Corrections of Simulated and Embedded Samples

Apart from the normalisation correction of the simulated and embedded samples, some further small mismodelling effects are found which are corrected, in order to provide an accurate prediction of the background contributions in this analysis[26].

The embedded sample is biased by the $Z \to \mu\mu$ selection applied to data which influences the muon transverse momentum spectrum and thus also the embedded τ_{had} objects (Sec. 7.2). For instance the muon trigger and reconstruction efficiencies change the acceptance of the embedded $Z \to \tau\tau$ events. A correction for these effects must be applied in order to accurately model the τ_{had} decay spectrum from a true $Z \to \tau\tau$ decay. Weights are obtained from the reciprocal efficiencies of these selection requirements as a function of p_{T}, η and ϕ, which are applied to the embedded sample to compensate for these effects [98]. In addition, the trigger efficiencies of the SLT and LTT triggers are emulated by reweighting the embedded τ_{had} and lepton p_{T} spectra.

A further shape correction is applied to the simulated W+jets samples to account for a shape disagreement of simulation and data initially observed in the W control region. For this purpose two shape dependent correction functions are applied, one parametrised as a function of $p_{\text{T}}^{\ell}/p_{\text{T}}^{\tau_{\text{had}}}$ and one as a function of $\Delta\eta(\ell, \tau_{\text{had}})$. Details of the procedure are described in [98].

Another issue in the VBF category is the merging of the VBF-filtered samples with non-filtered samples to model the $Z \to \ell\ell$ background (Sec. 7.2). Different generators are used for these samples in which the $j \to \tau_{\text{had}}$ misidentification probabilities differ. Therefore, the VFB-filtered samples (modelled with Alpgen+Herwig) are reweighted to the probability found in the Alpgen+Pythia sample and afterwards a common normalisation correction factor is derived as explained above.

The modelling of jet properties which form the basis for the event selection of the VBF Category have been investigated in the $Z \to \ell\ell$ control region for these samples. A reweighting function parametrised in $\Delta\eta_{jj}$ is applied to all kinematic distributions to correct for observed differences in data and simulation [98]. Still, a remaining disagreement of the VBF selection efficiency between data and the simulated samples of $\approx 10\%$ is found, which is taken into account as an additional systematic uncertainty for these samples (Sec. 7.7).

Summary of Background Estimation Methods

In all background control regions good agreement between data and the estimated background is observed. This gives confidence that the background processes are accurately modelled.

Most of the above presented background estimation methods have been used already for the previous $H \to \tau_{\text{lep}}\tau_{\text{had}}$ search results of the 4.6 fb^{-1} data set at $\sqrt{s} = 7$ TeV and 13.0 fb^{-1} at $\sqrt{s} = 8$ TeV (Appendix C). The data-driven normalisation of top and $Z \to \ell\ell$(j $\to \tau_{\text{had}}$) and $Z \to \tau\tau$ processes was implemented for the first time in this previous analysis, which significantly reduced the systematic uncertainties on the modelling of these background processes. The same-sign method was refined by the explicit measurement of the r_{QCD} factor, instead of assuming it to be one as it was done beforehand. For the VBF Category this method was replaced by the fake factor method providing a more accurate estimation of the $j \to \tau_{\text{had}}$ background due to a much larger number of events in the data control region.

As presented in this section, it is found that all methods provide an accurate estimation of the different background processes also for the full data set of 2012 (20.3 fb^{-1}). An additional improvement of the background estimation in the VBF Category has been introduced: The $Z \to \tau\tau$ background is modelled by the embedded sample for the first time. This significantly improves the accuracy of the background modelling, since jets and pile-up effects are directly taken from data.

[26] These corrections are applied in all distributions shown in this thesis.

7.6 Final Sample Decomposition

After the background estimation methods have been validated and all event selection criteria are found to be well modelled, the prediction of the sample composition and the kinematic distributions of the events in the signal regions in the defined categories can be investigated[27].

The following Figs 7.32–7.37 show the final distributions of τ_{had} and lepton momenta, missing transverse energy and the invariant $m_{\tau\tau}$ mass for all defined signal categories. Tables 7.9–7.10 show the event yields in the analysis categories after the event selection in the 2012 data sample.

It is clearly visible that a major part of all reducible background processes is rejected by the event selection, in particular in the VBF and Boosted Categories, compared to the preselected samples (Figs. 7.10 and 7.11). The irreducible $Z \to \tau\tau$ background is dominant in all categories. The Boosted and VBF Categories have as expected the lowest statistics, but the largest signal-to-background ratios. The expected distribution of a Higgs boson signal with $\mu = 1$ and $m_H = 125$ GeV is also shown in the distributions.

In the Zero- and One-Jet Categories a slight shift of the $m_{\tau\tau}$ distribution between data and the estimated combined background, as already seen in the preselection distributions in Figs. 7.10d and 7.11d a small overestimation of the combined background can be observed. It is found that a variation of the τ_{had} energy scale within its uncertainties influences these distributions and that shape and normalisation agree much better for the downwards 1σ TES variation. The distributions with the TES variation are shown in Appendix E. Therefore, the data is more compatible with a lower TES than with the nominal one. This does not pose a problem for the final hypothesis test in data, since the profile likelihood fit is allowed to vary within all uncertainties simultaneously in order to find the optimal parametrisation (Sec. 4.2.2). In the Boosted and VBF Categories the effects of the TES variations are not as strongly visible due to their different kinematics and lower statistics.

In the Boosted Category a slight underestimation of the background expectation is visible, judging from the low and high $m_{\tau\tau}$ region, where the signal is expected to be negligible. This results from the selection criterion on the $\Delta\Delta R^{\ell,\tau_{\text{had}}}$ variable, caused by a slight discrepancy between data and simulation in $\Delta R^{\ell,\tau_{\text{had}}}$ (see Appendix E). Due to the good agreement of $\Delta R^{\ell,\tau_{\text{had}}}$ between data and simulation in all background control regions it can be excluded that this results from a mismodelling of a particular source of background (see Appendix E). Moreover, since the ΔR discrepancy is within the statistical uncertainties, this is not considered to be a problem for an accurate hypothesis test in data.

After these considerations it can be concluded that the combination of all estimated background contributions gives a good description to all kinematic variables in the signal regions after the complex event selection has been applied. The distribution in data is consistent with the predictions both in shape and normalisation within the uncertainties. In particular, the good agreement observed in the high-statistics Zero- and One-Jet Categories provides further confidence in the good modelling of all kinematic variables after the event selection also for the Boosted and VBF Categories.

The spectra of the invariant mass distributions of the Boosted and VBF Categories as shown here are used as input to the profile likelihood fit to test the compatibility of the data with a Higgs signal.

[27] Before the hypothesis test on data was performed, these distributions have only been investigated outside the sensitive mass range $100 < m_{\tau\tau} < 150$ GeV.

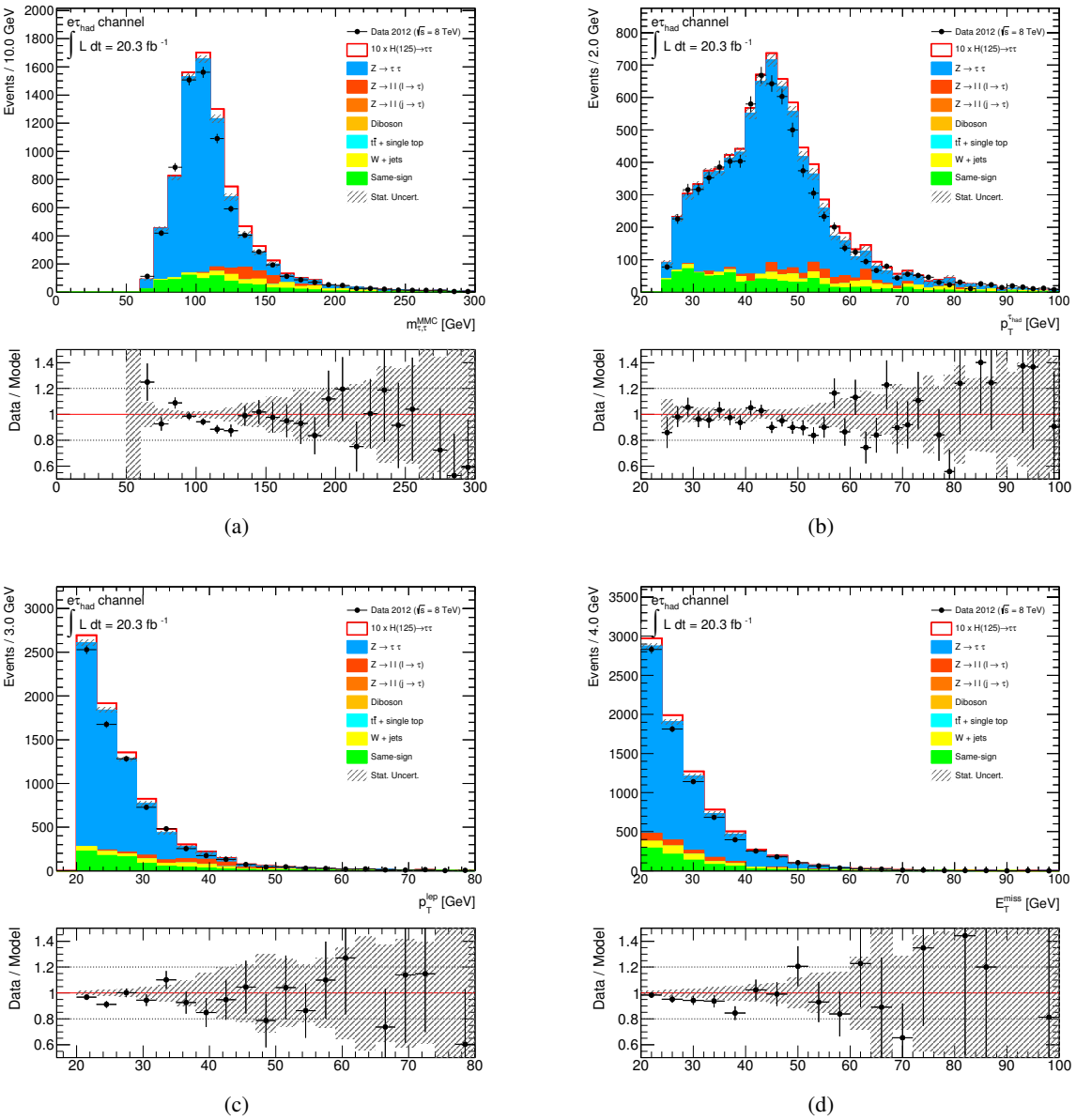

Figure 7.32: $e\tau_{\text{had}}$ **channel of the Zero-Jet Category**: Distribution of kinematic quanitities in the signal region for data and the (scaled) signal and background expectation after the full event selection summarised in Tab. 7.5. (a) Invariant $m_{\tau\tau}$ mass (calculated with the MMC algorithm), (b) transverse energy of the τ_{had} candidate, (c) transverse momentum of the lepton and (d) missing transverse energy. The bottom plots show the ratio of data to the background model. Also the statistical uncertainties of both are shown.

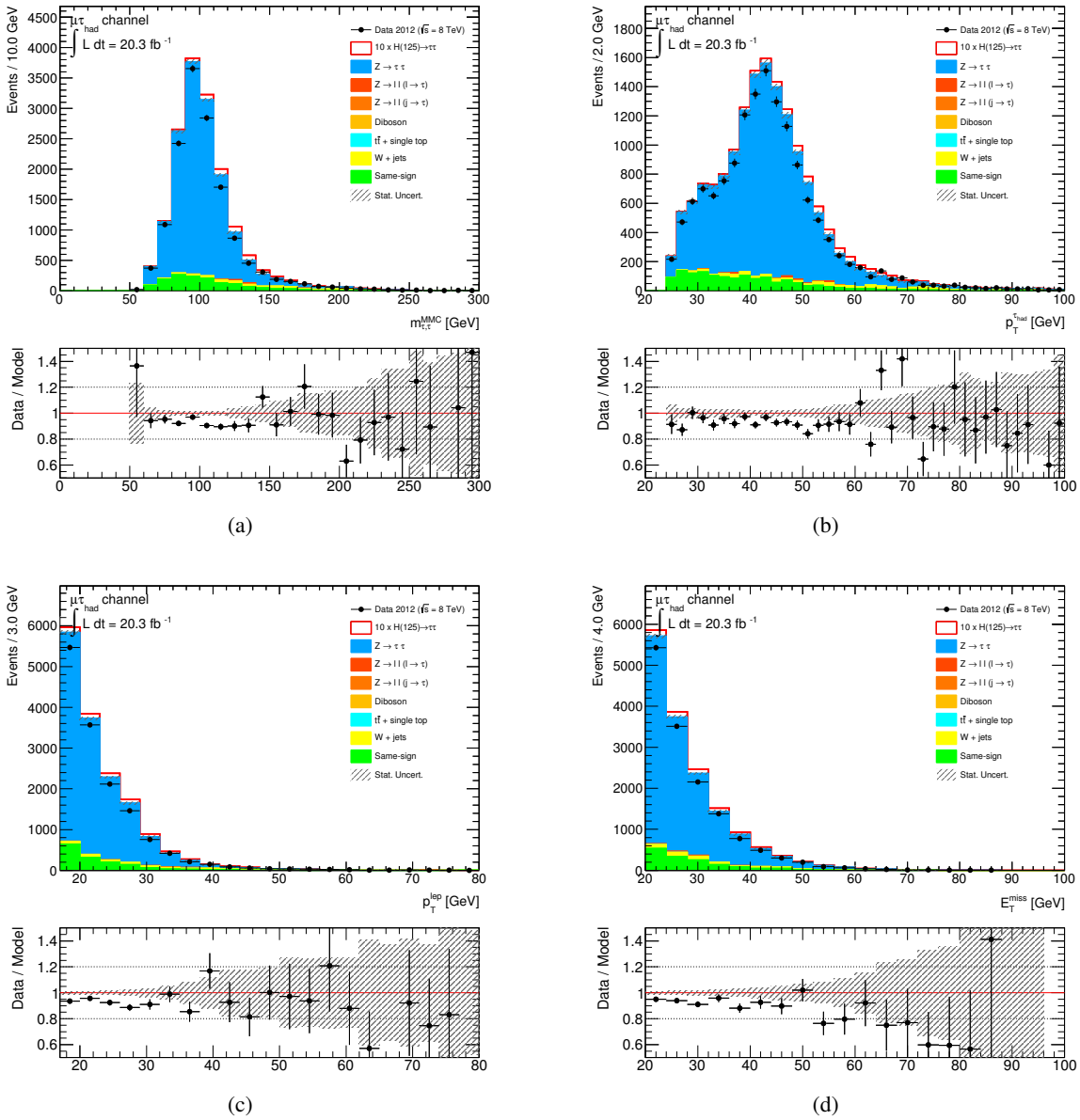

Figure 7.33: $\mu\tau_{\text{had}}$ **channel of the Zero-Jet Category**: Distribution of kinematic quantities in the signal region for data and the (scaled) signal and background expectation after the full event selection summarised in Tab. 7.5. (a) Invariant $m_{\tau\tau}$ mass (calculated with the MMC algorithm), (b) transverse energy of the τ_{had} candidate, (c) transverse momentum of the lepton and (d) missing transverse energy. The bottom plots show the ratio of data to the background model. Also the statistical uncertainties of both are shown.

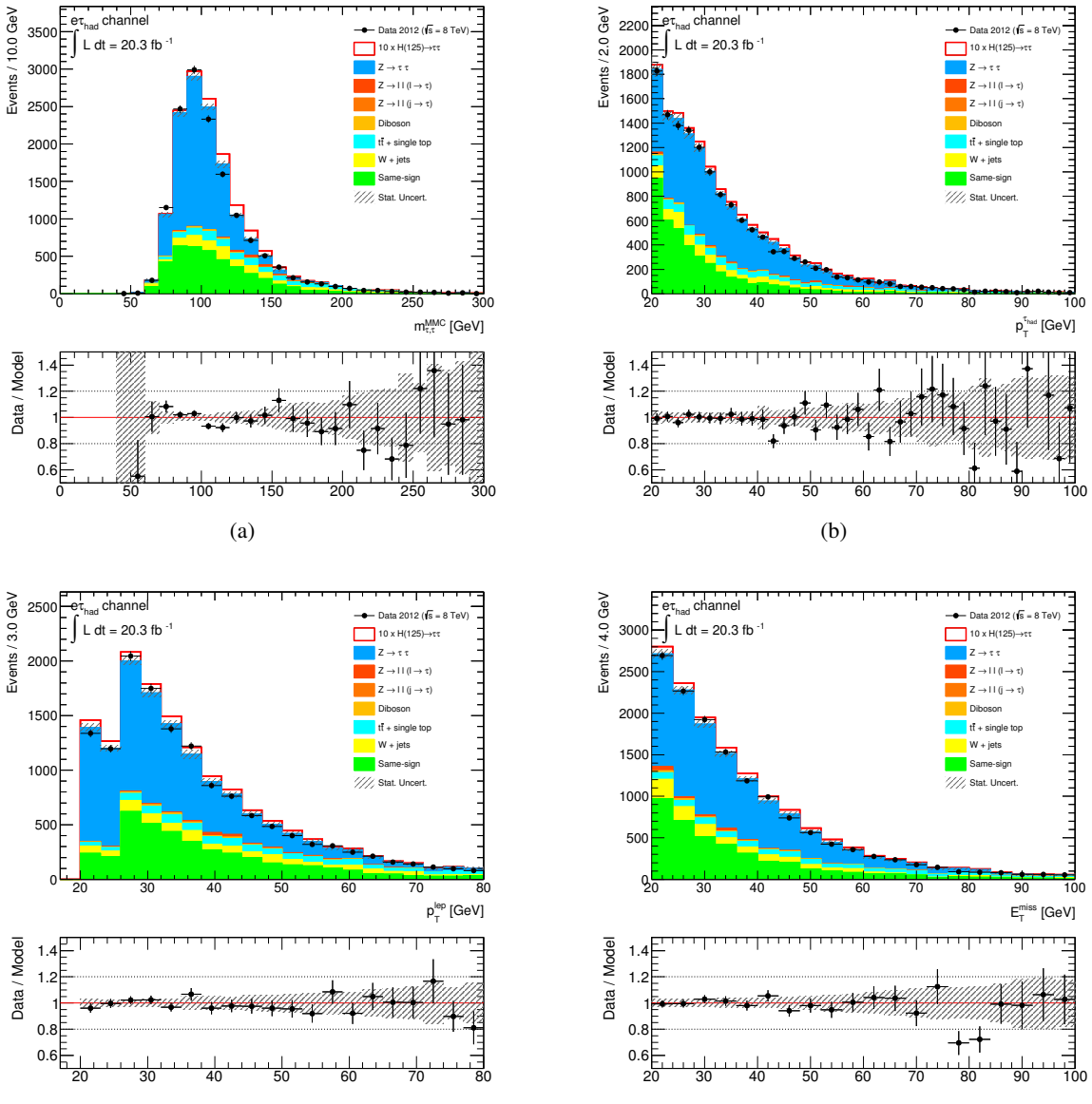

Figure 7.34: $e\tau_{\text{had}}$ **channel of the One-Jet Category**: Distribution of kinematic quantities in the signal region for data and the (scaled) signal and background expectation after the full event selection summarised in Tab. 7.5. (a) Invariant $m_{\tau\tau}$ mass (calculated with the MMC algorithm), (b) transverse energy of the τ_{had} candidate, (c) transverse momentum of the lepton and (d) missing transverse energy. The bottom plots show the ratio of data to the background model. Also the statistical uncertainties of both are shown.

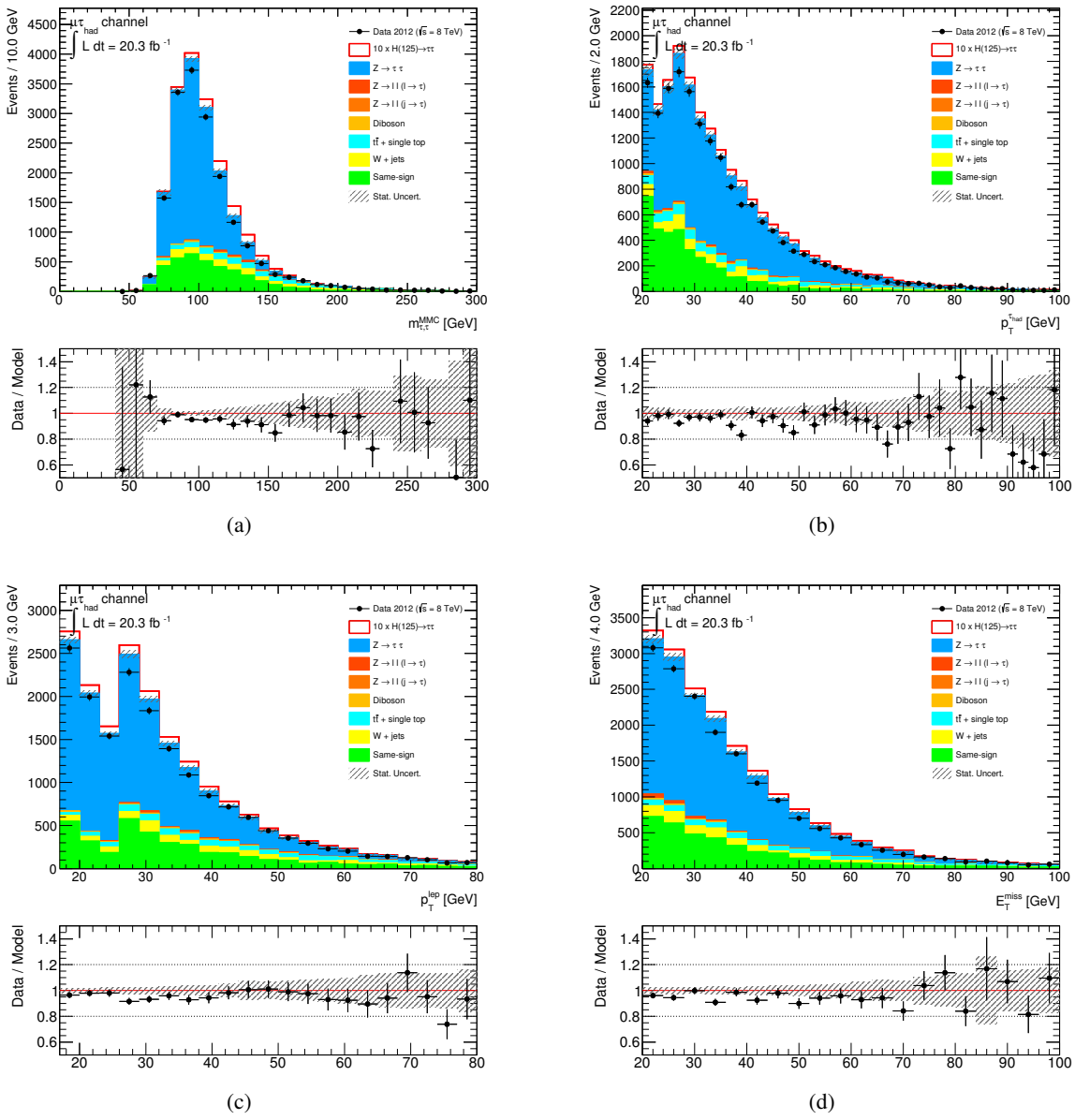

Figure 7.35: $\mu\tau_{\text{had}}$ **channel of the One-Jet Category**: Distribution of kinematic quantities in the signal region for data and the (scaled) signal and background expectation after the full event selection summarised in Tab. 7.5. (a) Invariant $m_{\tau\tau}$ mass (calculated with the MMC algorithm), (b) transverse energy of the τ_{had} candidate, (c) transverse momentum of the lepton and (d) missing transverse energy. The bottom plots show the ratio of data to the background model. Also the statistical uncertainties of both are shown.

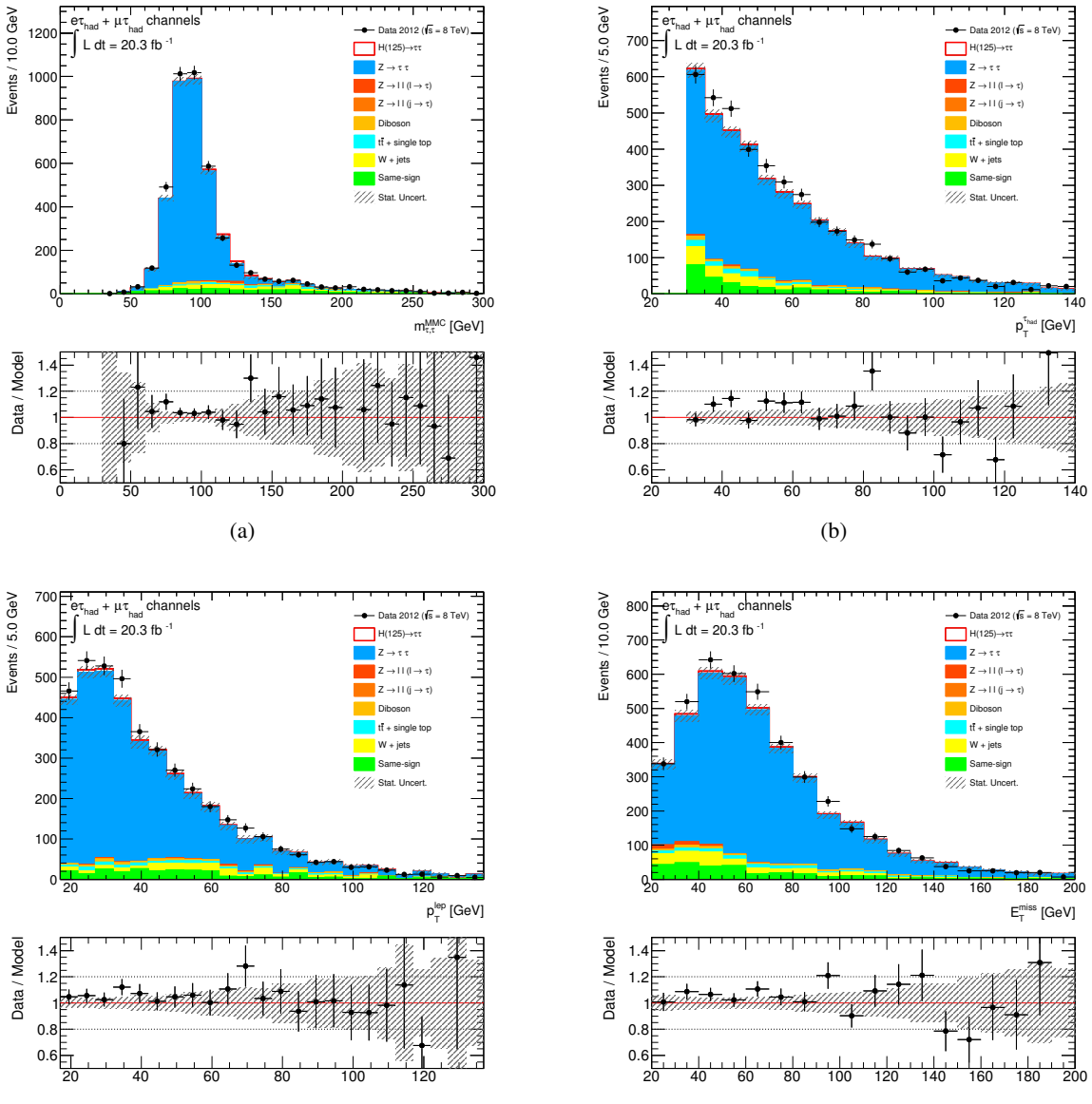

Figure 7.36: **Combined $e\tau_{\text{had}}$ and $\mu\tau_{\text{had}}$ channel of the Boosted Category**: Distribution of kinematic quantities in the signal region for data and the (scaled) signal and background expectation after the full event selection summarised in Tab. 7.5. (a) Invariant $m_{\tau\tau}$ mass (calculated with the MMC algorithm), (b) transverse energy of the τ_{had} candidate, (c) transverse momentum of the lepton and (d) missing transverse energy. The bottom plots show the ratio of data to the background model. Also the statistical uncertainties of both are shown.

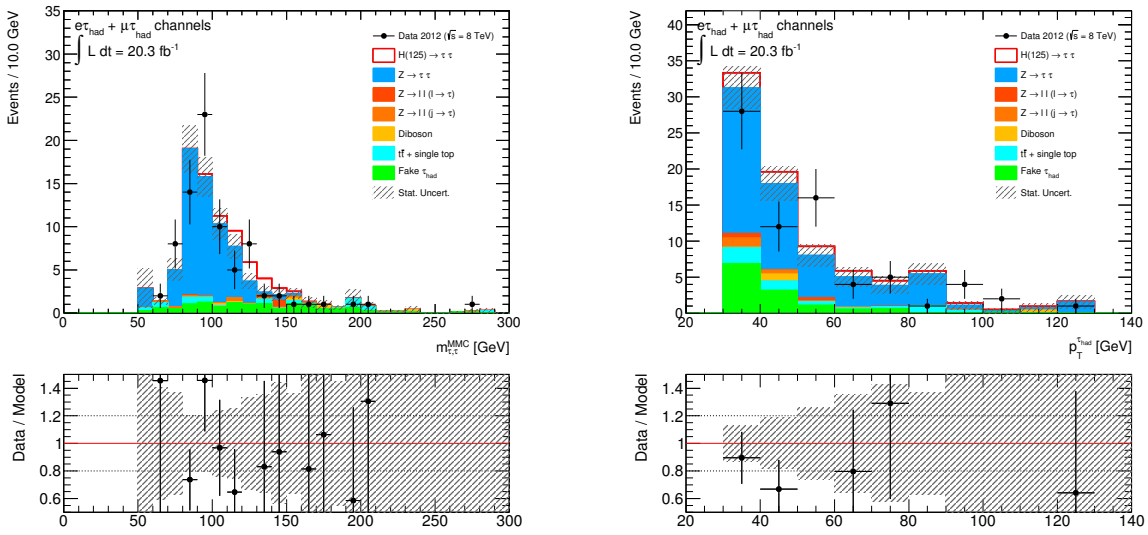

(a)

(b)

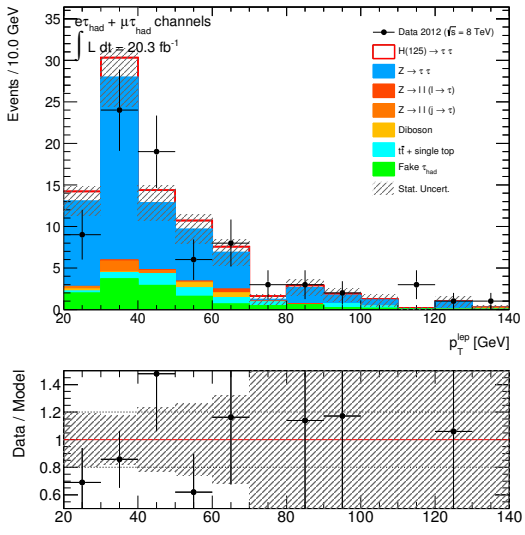

(c)

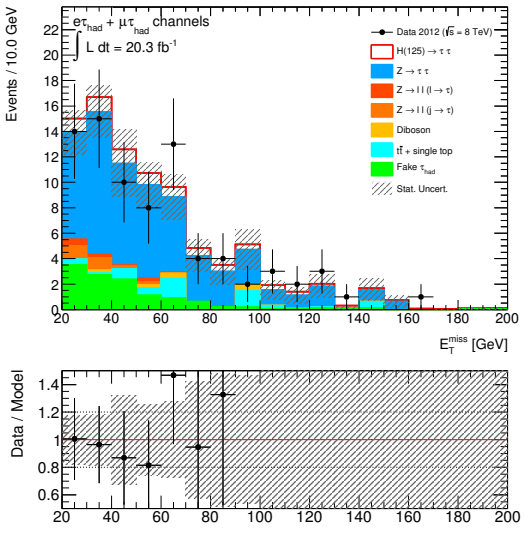

(d)

Figure 7.37: **Combined $e\tau_{\text{had}}$ and $\mu\tau_{\text{had}}$ channel of the VBF Category**: Distribution of kinematic quantities in the signal region for data and the (scaled) signal and background expectation after the full event selection summarised in Tab. 7.5. (a) Invariant $m_{\tau\tau}$ mass (calculated with the MMC algorithm), (b) transverse energy of the τ_{had} candidate, (c) transverse momentum of the lepton and (d) missing transverse energy. The bottom plots show the ratio of data to the background model. Also the statistical uncertainties of both are shown.

Process	Zero-Jet		One-Jet	
	$e\tau_{\text{had}}$ channel	$\mu\tau_{\text{had}}$ channel	$e\tau_{\text{had}}$ channel	$\mu\tau_{\text{had}}$ channel
ZH($H \to \tau_{\text{lep}}\tau_{\text{had}}$)	0.10 ± 0.01	0.17 ± 0.01	2.13 ± 0.04	2.60 ± 0.05
WH($H \to \tau_{\text{lep}}\tau_{\text{had}}$)	0.16 ± 0.02	0.16 ± 0.02	3.31 ± 0.07	4.04 ± 0.07
VBF($H \to \tau_{\text{lep}}\tau_{\text{had}}$)	0.42 ± 0.02	0.65 ± 0.02	10.92 ± 0.09	13.31 ± 0.10
ggF($H \to \tau_{\text{lep}}\tau_{\text{had}}$)	38.92 ± 0.56	57.93 ± 0.69	57.76 ± 0.70	74.72 ± 0.80
$Z \to \tau\tau$	6303 ± 40	13 412 ± 49	7814 ± 47	11 896 ± 49
$Z \to \ell\ell(\ell \to \tau_{\text{had}})$	326 ± 38	90 ± 17	177 ± 21	228 ± 20
$Z \to \ell\ell(\text{j} \to \tau_{\text{had}})$	0 ± 0	−8 ± 3	0 ± 0	−21 ± 2
Diboson	15 ± 2	26 ± 3	138 ± 9	169 ± 10
Top	5 ± 2	8 ± 2	1101 ± 27	1106 ± 27
W+jets	414 ± 28	481 ± 31	1095 ± 72	1073 ± 75
Same-sign	829 ± 29	1496 ± 41	4069 ± 64	3871 ± 65
Total background	7892 ± 68	15 506 ± 73	14 393 ± 112	18 322 ± 116
Data	7580	14 481	14 266	17 442

Table 7.9: Number of signal and background events in the signal region of the Zero- and One-Jet Categories in the $e\tau_{\text{had}}$ and $\mu\tau_{\text{had}}$ channel including the statistical uncertainties. The signal samples are generated with a mass of 125 GeV.

Process	Boosted	VBF
	$e\tau_{\text{had}} + \mu\tau_{\text{had}}$ channel	$e\tau_{\text{had}} + \mu\tau_{\text{had}}$ channel
ZH($H \to \tau_{\text{lep}}\tau_{\text{had}}$)	1.88 ± 0.04	0.004 ± 0.002
WH($H \to \tau_{\text{lep}}\tau_{\text{had}}$)	3.78 ± 0.07	0.014 ± 0.004
VBF($H \to \tau_{\text{lep}}\tau_{\text{had}}$)	10.69 ± 0.09	6.54 ± 0.07
ggF($H \to \tau_{\text{lep}}\tau_{\text{had}}$)	33.93 ± 0.54	1.49 ± 0.11
$Z \to \tau\tau$	3308 ± 35	56.3 ± 4.9
$Z \to \ell\ell(\ell \to \tau_{\text{had}})$	37.8 ± 4.4	1.2 ± 0.5
$Z \to \ell\ell(\text{j} \to \tau_{\text{had}})$	−1.4 ± 0.2	2.4 ± 0.4
Diboson	65.7 ± 5.1	1.4 ± 0.7
Top	91.4 ± 8.1	5.4 ± 1.6
W+jets	204 ± 20	-
Same-sign	271 ± 17	-
Fake τ_{had}	-	12.7 ± 0.9
Total background	3976 ± 45	79.5 ± 5.3
Data	4179	80

Table 7.10: Number of signal and background events in the signal region of the Boosted and VBF Categories in the combined $e\tau_{\text{had}}$ and $\mu\tau_{\text{had}}$ channel including the statistical uncertainties. The signal samples are generated with a mass of 125 GeV.

7.7 Systematic Uncertainties

Numerous sources of systematic uncertainties affect the $H \to \tau_{\text{lep}}\tau_{\text{had}}$ analysis presented here. Each systematic uncertainty is incorporated in form of nuisance parameters (NPs) in the profile likelihood fit of the $m_{\tau\tau}$ mass (Sec. 4.2.2). All sources of systematic uncertainties influence the event yield in the categories (referred to as *normalisation* uncertainty). Some of them, e.g. energy scale uncertainties, influence the kinematic properties of an event in addition, which has an effect on the $m_{\tau\tau}$ mass shape (*shape* uncertainty). Both types of uncertainty are incorporated in the fit for each nuisance parameter if a significant impact on normalisation or shape of the mass distribution is found.

In general the nuisance parameters are treated fully correlated in the fit, i.e. one parameter is used for all signal and background processes influenced by this uncertainty. For some parameters it is more reasonable to treat the systematic uncertainties uncorrelated for different groups of processes. An example is the jet energy scale uncertainty, which has a different effect on quark- or gluon-initiated processes. In this case the nuisance parameter is split into two uncorrelated parameters in the fit, which avoids artificial effects on the fit result due to false correlations.

A short discussion of each systematic uncertainty is given in this section, together with the names of the nuisance parameters that are introduced. Similar to the $W \to \tau_{\text{had}}\nu_\tau$ analysis (Sec. 6.7) the systematic uncertainties are grouped into three different types: Experimental uncertainties that affect the accuracy of the physics object measurements (τ_{had}, leptons, $E_{\text{T}}^{\text{miss}}$ and jets), background estimation uncertainties and theoretical uncertainties that affect the signal and background section for the calculation of expected events.

Experimental Uncertainties

The analysis is mostly affected by experimental uncertainties on the jet and τ_{had} energy scales since they strongly influence the $m_{\tau\tau}$ mass reconstruction. More uncertainties arise from the corrections applied to physics objects to account for differences between data and simulation (Sec. 7.3). Usually they only have a small effect on the event yield and mass distribution. The experimental uncertainties have mostly been investigated in generic studies for ATLAS and are directly transferred to this analysis. The effect on the event yields of all these experimental uncertainties for the individual signal and background processes is listed in Appendix D. The following sources of systematic uncertainties are taken into account:

Pile-up and luminosity measurement The uncertainty on the luminosity measurement in ATLAS affects the normalisation of signal and all background processes which are not normalised in data control regions (diboson and $Z \to \ell\ell(\ell \to \tau_{\text{had}})$). In 2012 data it is measured to be $\pm 2.8\%$ [28]. The modelling of pile-up activity in simulation, measured by the expected number of interactions in a collision event $< \mu >$, is adjusted to data (Sec. 7.2, [151]). The uncertainty on this procedure of $\pm 3\%$ is included as a source of systematic uncertainty in the analysis (Nuisance parameters: *LUMI_2012* and *PU_RESCALE_2012*).

Trigger efficiency As explained in Secs. 7.3 and 7.5, correction factors are applied to the simulated and embedded samples to adjust the trigger efficiencies to the ones in data individually for each trigger and trigger part. These correction factors are varied within the associated systematic uncertainties to obtain the effect on the final event yield in the categories [36, 37, 146, 147] (NP: *TAU_TRIG_2012*). The lepton trigger efficiencies are included in the nuisance parameters for the offline efficiency corrections (see next item). Uncorrelated parameters are used for the embedded sample (with the additional suffix *_Emb*) due to the different methods of efficiency correction with respect to the simulated samples.

Lepton reconstruction, identification and isolation Correction factors for reconstruction and identification efficiencies are applied to selected electrons and muons in simulated and embedded samples (Sec. 7.3, [41, 46]). These factors are varied within their uncertainty to obtain the effect of the associated systematic uncertainties within the analysis. Also the systematic uncertainty of the applied lepton isolation correction is taken into account [148]. These uncertainties, together with the lepton trigger uncertainties, are incorporated in one single nuisance parameter by adding the individual uncertainties in quadrature (NPs: *EL_EFF* and *MU_EFF*). Uncorrelated parameters for the embedded sample are used (suffix *_Emb*).

Lepton energy resolution The muon energy scale and the electron energy scale and resolution are corrected to match the one in data in the embedded and simulated samples. The precision of the corresponding measurement is incorporated by varying these corrections within the provided uncertainties (see Sec. 3.4 and [43, 46]). These uncertainties also influence the $m_{\tau\tau}$ distribution, but since the effect is found to be very small they are not considered as shape uncertainties in the fit (NPs: *EL_SCALE*, *EL_RES* and *MU_SCALE*).

***b*-tagging uncertainties** Due to the b-jet veto in the Boosted and VBF Categories, the b-tagging efficiency corrections are applied for simulated samples. Therefore, the respective systematic uncertainties are also taken into account (Sec. 3.4 and [53]) for the cases that a light jet, a c-jet or a b-jet are found by the algorithm (NPs: *ATLAS_BTag_LEFF*, *ATLAS_BTag_CEFF*, *ATLAS_BTag_BEFF*).

τ_{had} identification and lepton vetoes The systematic uncertainties associated to the correction of the τ_{had} BDT identification efficiency are applied to all processes where the τ_{had} candidates originate from a *true* hadronically decaying τ lepton in simulated and embedded samples. Furthermore, the uncertainties arising from the correction of $e \rightarrow \tau_{\text{had}}$ and $\mu \rightarrow \tau_{\text{had}}$ misidentification probabilities (for all τ_{had} candidates originating from a *true* electron or muon) are taken into account as nuisance parameters (Sec. 5.2 and [99]), (NPs: *TAU_ID_2012*, *TAU_EFAKE_2012* and *TAU_MUFAKE_2012*).

Jet energy scale and resolution The uncertainty on the jet resolution is investigated by folding the jet energy components with a Gaussian to model a resolution of $+1\sigma$ (Sec. 3.4 and [148, 152]), (NP: *JER_2012*).

To investigate the effect of the jet energy scale uncertainties, several uncorrelated components are considered (Sec. 3.4 and [49, 153]). Only the ones which were found to have a significant effect on the $m_{\tau\tau}$ normalisation and shape in this analysis are included in the fit to avoid artificial effects due to statistical fluctuations. These components can be grouped into different types: The *in-situ energy correction uncertainties* take into account uncertainties from different physical sources that affect the measurement of the energy scale. The *η intercalibration uncertainty* incorporates uncertainties resulting from differences in the calibration in different pseudorapidity regions of the detector. The *Flavour related uncertainties* refer to uncertainties on different calorimeter responses to quark- and gluon-initiated jets and the uncertainty on the quark-gluon composition of jets (only for light jets). To account for the individual compositions of the signal and background processes, the uncertainties are treated as uncorrelated for processes with mainly gluon-initiated jets (ggF, W+jets, Z+jets) and for processes with mainly quark-initiated jets (VBF, VH, top, diboson). The *b-jet uncertainty* is an uncertainty associated to the modelling of b-jets. The *PileUp uncertainties* summarise all uncertainties arising from the effects of in-time and out-of-time pile-up on the JES. They are evaluated as a function of μ, the average number of interaction per

bunch crossing, and *NPV*, the number of primary vertices. An uncertainty on the method used for pile-up correction is also included, separately for qq-initiated processes (VBF, VH and diboson), qg-initiated ones (W+jets, Z+jets), and gg-initiated ones (ggF, top). Table 7.11 summarises the groups of uncertainties and the associated nuisance parameters.

All JES nuisance parameters are included as shape uncertainties in the fit. The JES uncertainty with the largest influence on the shape and normalisation, *JES_Eta_Modelling* is shown as an example in Fig. 7.38 for the two dominating signal processes in Boosted and VBF Categories.

Finally, also the uncertainty on the efficiency of the jet vertex fraction selection is taken into account. The selection threshold of the JVF is varied up- and downwards within its uncertainty to assess the effect of this uncertainty on the analysis (Sec. 3.4 and [154]), (NP: *JVF_2012*).

Uncertainty type	Nuisance parameter	Splitting
In-situ corrections	*JES_2012_Detector1* *JES_2012_Modelling1* *JES_2012_Statistical1*	
η intercalibration	*JES_Eta_Modelling* *JES_2012_Eta_StatMethod*	
Flavour	*JES_2012_FlavComp* *JES_2012_FlavResp*	*_q* (quark-initiated) and *_g* (gluon-initiated)
b-jets	*JES_2012_Flavb*	
PileUp	*JES_Mu* *JES_NPV* *JES_2012_PileRho*	*_qq*, *_qg* and *_gg*

Table 7.11: Jet energy scale uncertainty groups considered in the analysis and the associated nuisance parameters.

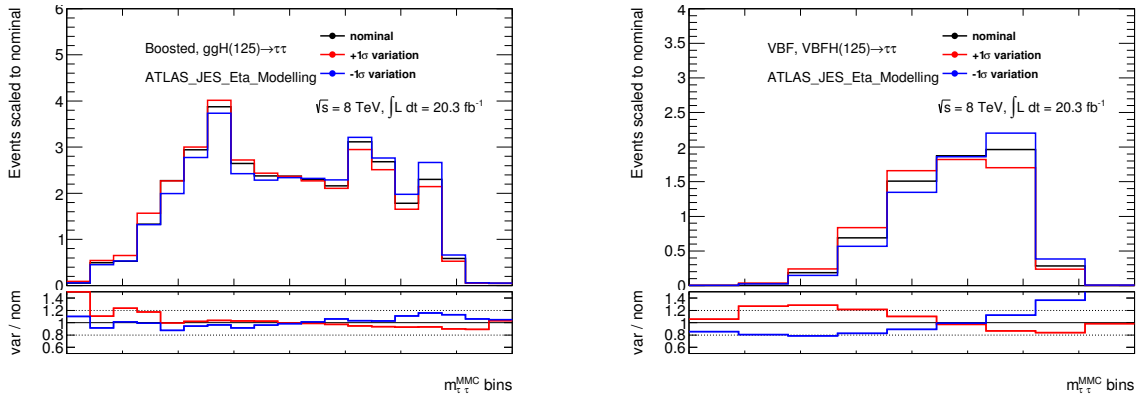

(a) (b)

Figure 7.38: Shape variations of the invariant mass under the systematic up- and downwards variation of one of the JES uncertainties (*JES_Eta_Modelling*), compared to the nominal distribution. Both variations are scaled to the nominal distribution. They are shown for the largest contributing signal processes, (a) ggF production in the Boosted and (b) VBF production in the VBF Category. The bin size in these distributions is the one used in profile likelihood fit, see Tab. 7.12. Uniform bin widths have been chosen for clarity.

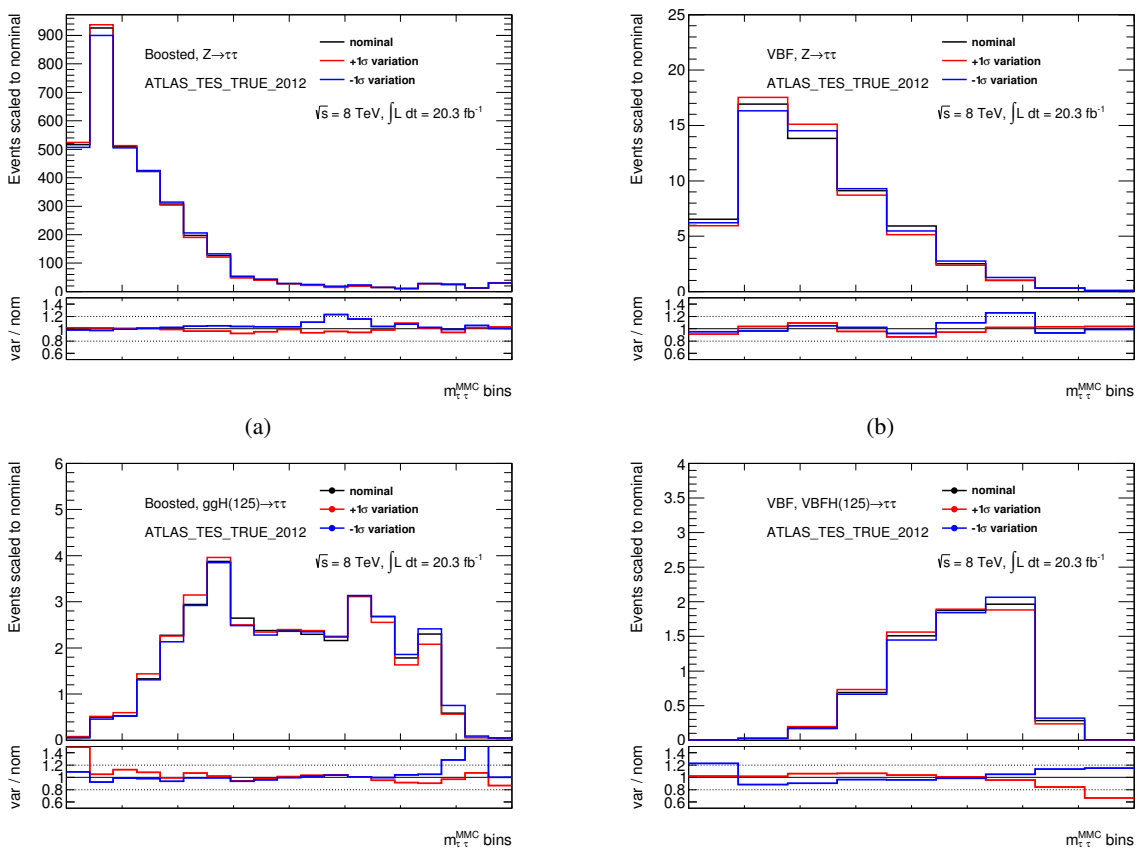

Figure 7.39: Shape variation of the invariant mass with the systematic up- and downwards variation of the τ_{had} energy scale (*TES_TRUE_2012*), compared to the nominal distribution. Both variations are scaled to the nominal distribution. They are shown for $Z \to \tau\tau$ in (a) the Boosted and (b) the VBF Category and the (c) ggF signal process in the Boosted and (d) VBF signal process in the VBF Category. The bin size in these distributions is the one used in profile likelihood fit, see Tab. 7.12. Uniform bin widths have been chosen for clarity.

τ_{had} energy scale Systematic uncertainties on the τ_{had} energy scale play an important role in the $H \to \tau_{\text{lep}}\tau_{\text{had}}$ analysis. Simultaneously to a variation of the τ_{had} energy itself (Sec. 5.2 and [100]), the systematic variations are propagated to $E_{\text{T}}^{\text{miss}}$ and the missing mass distribution is recalculated with these variations. It is found to be one of the largest systematic uncertainties affecting both normalisation and shape of the $m_{\tau\tau}$ distribution and is therefore also taken into account as shape uncertainty in the fit. Since the energy of real and misidentified τ_{had} candidates can be affected in different ways, independent nuisance parameters are chosen for τ_{had} candidates that originate from *true* hadronically decaying τ leptons and for $\ell \to \tau_{\text{had}}$ or $j \to \tau_{\text{had}}$ misidentified candidates. Figure 7.39 shows the effect of the up- and downwards variation of the TES uncertainty on the mass distribution in comparison with the nominal distribution for the signal and background processes in the Boosted and VBF Categories (NPs: *TES_TRUE_2012* and *TES_FAKE_2012*).

Missing transverse energy reconstruction All variations of lepton, τ_{had} and jet energy scale are directly propagated to $E_{\text{T}}^{\text{miss}}$. In addition, uncertainties on the energy scale and resolution of the $E_{x(y)}^{\text{miss,SoftTerm}}$ term are also taken into account (Sec. 5.3 and [113]). These uncertainties are also considered as shape uncertainties in the fit (NPs: *MET_RESOSOFT* and *MET_SCALESOFT*).

Background Estimation Uncertainties

The methods used to model the different background processes (Sec. 7.5) are also affected by several sources of systematic uncertainties:

Embedding procedure The following sources of systematic uncertainties are considered for the embedded sample used to model the $Z \to \tau\tau$ background: The preselection of $Z \to \mu\mu$ data, in particular the isolation requirement on the muons, can influence the final $Z \to \tau\tau$ distributions (Sec. 4.3). In order to address this uncertainty the isolation requirement is varied: No isolation and tighter isolation criteria are applied and the results are compared to the nominal selection (NP: *ANA_EMB_ISOL*).

An additional systematic uncertainty arises from the subtraction of energy deposited by the muon in the surrounding calorimeter cells when it is replaced by the τ lepton. These energy depositions are estimated from simulation (Sec. 4.3). The uncertainty from this procedure is estimated by varying the energy deposition in each cell by ±20% before subtraction (NP: *ANA_EMB_MFS*). Both uncertainties can affect the normalisation and shape of the $m_{\tau\tau}$ distribution. The effect of these variations on the $m_{\tau\tau}$ mass is shown in Fig. 7.40.

Moreover, the systematic uncertainties on the normalisation correction of the embedded sample in the visible mass window at preselection is taken into account (Sec. 7.5). For this purpose the correction factors are varied within their statistical uncertainties (Tab. 7.6) when calculating the expected number of events in the signal regions (NP: *ANA_LH12_Emb*).

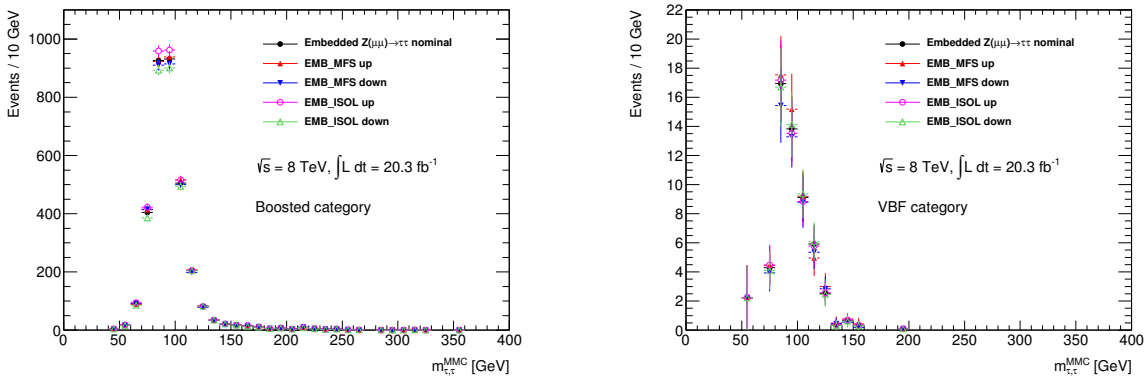

(a) (b)

Figure 7.40: Variation (normalisation and shape) of the mass distribution of the embedded $Z \to \tau\tau$ sample in (a) the Boosted and (b) the VBF Category under the up- and downwards variation of the embedding specific uncertainties: Nominal distribution (filled circles), cell energy deposition variation (*ANA_EMB_MFS*, filled triangles) and μ isolation criterion variation (*ANA_EMB_ISOL*, empty triangle and circle).

Background estimation To include the systematic uncertainties on the normalisation correction of the different background processes, the correction factors for W+jets, top and $Z \to \ell\ell(\mathrm{j} \to \tau_{\mathrm{had}})$ background are varied up- and downwards within their statistical uncertainties (Tab. 7.8), (NPs: *ANA_LH12_Wlnu_boost*, *ANA_LH12_Top* and *ANA_LH12_Zll*).

The systematic uncertainty on the estimation of the QCD normalisation factor r_{QCD} is calculated in the following way: The selection criteria (τ_{had} identification) for the definition of the QCD control region, the fit range, and the isolation variable (E_{T}- or p_{T}-based) are varied to obtain the dependence on the lepton isolation. Moreover, also the uncertainty resulting from the statistical uncertainty on the r_{QCD} estimation is included. The difference with respect to the nominal r_{QCD} resulting from these variations is combined and taken as systematic uncertainty [150]. The resulting uncertainties are listed in Tab. 7.7 (NP: *ANA_LH12_QCD*).

Finally, a systematic uncertainty for the estimation of the $j \to \tau_{\mathrm{had}}$ background (W+jets and QCD) via the fake-factor method in the VBF Category is included. As explained in Sec. 7.5, due to the fact that the exact quark-gluon composition of the $j \to \tau_{\mathrm{had}}$ background in the signal region is not precisely known, a conservative uncertainty of ±50% is assigned to the estimation of the $j \to \tau_{\mathrm{had}}$ background, covering the two extreme cases that only quark-jets or only gluon-jets are contained in the anti-ID sample (NP: *ANA_LH12_Fake_vbf*).

Shape correction of simulated samples The corrections applied to simulation (Sec. 7.5) are also associated with systematic uncertainties that influence the final sample composition: The reweighting functions of the simulated W+jets samples as a function of $p_{\mathrm{T}}^{\ell}/p_{\mathrm{T}}^{\tau_{\mathrm{had}}}$ and of $\Delta\eta(\ell, \tau_{\mathrm{had}})$ are varied within the uncertainties found for the reweighting parametrisation [150]. The corresponding nuisance parameters are considered both as normalisation and shape uncertainty (NPs: *ANA_LH12_WJetsPythiaPt* and *ANA_LH12_WJetsPythiaDEta*). The mismodelling of the VBF selection efficiency and the correction of the difference in misidentification probabilities in the VBF-filtered $Z \to \ell\ell$ samples (Sec. 7.5) are also included as systematic uncertainties in the fit (NPs: *ANA_LH12_Zjet* and *ANA_LH12_Zll_HERWIG*).

Statistical uncertainty of background estimation In addition, also the statistical uncertainties of the background estimation in each bin of the $m_{\tau\tau}$ distributions are taken into account (NPs: *stat_boost_MMC_bin_x* and *stat_vbf_MMC_bin_x*).

Theoretical Uncertainties

Uncertainties resulting from theory calculation affect the signal cross section and the cross section of background processes that are directly taken from simulation (diboson and $Z \to \ell\ell(\ell \to \tau_{\mathrm{had}})$). Therefore, they are included as normalisation uncertainties in the profile likelihood fit. The uncertainties are derived from generic studies for the LHC [79, 91]. The resulting effects of the theoretical uncertainties on the different signal and background processes are summarised in Appendix D.

Underlying event modelling The use of different tunes to adjust the underlying event modelling to ATLAS data (Sec. 6.2) influences the signal acceptance in the VBF Category since it changes the distributions of the two tagging jets, mainly the $\Delta\eta_{jj}$ distribution [150]. Effects on the ggF and VBF cross section are therefore taken into account. The systematic uncertainty is derived from the observed differences between the default tune AUET2B [155] and the PERUGIA 2011C tune [129]. The corresponding nuisance parameters are treated as uncorrelated for ggF and VBF production (NPs: *ATLAS_UE_gg* and *ATLAS_UE_gg*).

PDF sets Uncertainties also arise from the choice of proton PDF set for the calculation of signal and background cross sections. The inclusive cross sections obtained with different PDF sets (MSTW, CT10 and NNPDF [156], see Sec. 3.5) are compared to evaluate the uncertainties [150]. For the signal the uncertainties are split into gluon-initiated processes for ggF (NP: *pdf_Higgs_gg*) and quark-initiated processes for VBF and VH production (NP: *pdf_Higgs_qq*). For the diboson and $Z \to \ell\ell(\ell \to \tau_{\text{had}})$ background the PDF uncertainty is taken into account as a separate nuisance parameter (NP: *pdf_qq*).

$H \to \tau\tau$ branching ratio The uncertainty on the branching ratio of $H \to \tau\tau$ for all considered signal masses is also included in the fit [157] (NPs: *BR_tautau*).

QCD scale uncertainties An important source of systematic uncertainty is the missing inclusion of higher order pertubative QCD corrections. The corrections depend on the choice of the renormalisation and factorisation scales (Sec. 2.2). The nominal scales have the same order of magnitude as the hard interaction process ($\sim m_H$) and the systematic uncertainty is assessed by the variation of these scales by a factor two up- and downwards [157].

The influence of the QCD scale on the cross section is particularly large for gluon fusion since the higher-order terms contribute significantly to the cross section [4, 79]. As the analysis is divided into categories of different jet multiplicities, the signal yield in each of them is differently affected by the QCD scale variation. The uncertainty is therefore evaluated individually for the different jet multiplicities taking into account correlations between the jet bins[28] [158]. In total, three nuisance parameters denoting the uncertainties on the inclusive jet multiplicity cross sections are included to account for the QCD scale uncertainty in the categories (NPs: *QCDscale_ggH1in*, *QCDscale_ggH2in* and *QCDscale_ggH3in*).

Since for the VH and VBF production the dependence on the QCD scale is smaller, an overall systematic uncertainty from the variation of renormalisation and factorisation scales is derived for these samples (*QCDscale_VH* and *QCDscale_qqH*). Also for the background cross section directly estimated from simulation the influence of the QCD scale variation is taken into account (NPs: *QCDscale_V* for $Z \to \ell\ell(\ell \to \tau_{\text{had}})$ and *QCDscale_VV* for the diboson sample).

Modelling of Higgs transverse momentum The Higgs boson transverse momentum p_{T}^{H} (Eq. 7.4) is influenced by the masses of the heavy quarks in the loop of the $gg \to H$ production process (Fig 4.4a), mostly at high Higgs momenta [4, 79]. Since this variable is used for the event categorisation, the analysis is very sensitive to variations of the p_{T}^{H} spectrum. In order to assess the uncertainty associated to the modelling of these quark mass effects, the Powheg generator used in the analysis is compared to a Mc@nlo generator (Sec. 3.5). The difference in event yield after the final event selection observed with these two generators is taken as systematic uncertainty. The two generated samples have been adjusted to each other for this comparison such that effects due to the different underlying event and parton shower modelling and the different QCD scales are not double counted [150] (NP: *Gen_Qmass_ggH*).

[28] First the impact of the scale variation on the *inclusive* partial cross sections for different jet multiplicities ($\sigma_{\geq 2j}$, $\sigma_{\geq 1j}$) is calculated. In a second step, the corresponding *exclusive* cross sections $\sigma_N = \sigma_{\geq N} - \sigma_{\geq N+1}$, are derived.

7.8 Hypothesis Test

The goal of this analysis is to test if the measured data is compatible with a signal-plus-background or background-only hypotheses in order to find evidence or exclude a Higgs boson decaying to τ leptons. The observed signal strength μ is determined, i.e. the cross section times branching ratio of the $H \to \tau\tau$ decay relative to the Standard Model prediction. The compatibility of data with the signal and background expectation is evaluated with a profile likelihood fit following the description in Sec. 4.2.2.

In the following the construction of the likelihood function is explained. In addition, a set of tests is performed to confirm the stability and unambiguity of the maximum likelihood fit. All investigations are first performed in a blinded way, i.e. no information on the final observed significance or signal strength in data is included. This strategy ensures that no optimisation of the fit towards a certain signal strength is done.

Construction of the Likelihood Function

The statistical analysis of data is performed within the framework of the Histfactory tool [89] which is based on RooFit [159] and RooStats packages [160] incorporated in ROOT [161]. The $m_{\tau\tau}$ mass distributions in the VBF and Boosted Categories of all events passing the selection criteria (Figs. 7.37 and 7.36) form the basis for the binned profile likelihood fit. Provided to Histfactory are the templates of the expected mass distributions of signal and background obtained from simulation or the background estimation methods (Sec. 7.5). Different signal mass hypotheses are tested between 100 and 150 GeV in steps of 5 GeV [29]. For each Higgs mass the test of the compatibility with the data is performed separately.

As discussed in Sec. 7.7, the statistical and systematic uncertainties that affect the normalisation and shape of the $m_{\tau\tau}$ distribution are included as a set of nuisance parameters.

Due to the tight selection criteria the number of events in the categories is relatively small. As a consequence a systematic variation of the mass shape might be covered or falsified by a statistical fluctuation. This may cause problems in the fit stability, e.g. through broadening, shifts or discontinuities in the likelihood ratio or additional maxima. In addition, this might lead to double counting of statistical uncertainties and an overestimation of the uncertainty on the signal strength. To avoid these cases and obtain a reasonable fit result based on true systematic variations, all shape uncertainties are subjected to the following procedure:

Pruning In order to quantify the degree of difference between the nominal and the $\pm 1\sigma$ variations of the mass distributions for each potential shape uncertainty, a Kolgomorov-Smirnov-Test (KS) [162] is performed. This algorithm tests the compatibility of two histograms based on their largest deviation from each other. It returns values between 0 and 1, where 0 denotes a large difference of the shapes of the histograms and 1 reflects a good agreement. If it is found that both varied distributions are too similar with the nominal one (KS test > 0.95), the variation is most likely dominated by statistical fluctuations and the shape uncertainty of the corresponding NP is not included in the likelihood function. In addition, all mass histograms are scanned bin-by-bin and if no bin is found where the difference between the nominal histogram and the up- or downwards variation is larger than 0.5%, the shape uncertainty of the NP is not considered in the fit either.

Smoothing The remaining shape uncertainties are subjected to a smoothing algorithm [163] which has the purpose to dampen fluctuations between neighbouring bins. Since systematic variations

[29] This step size is dictated by the simulated signal samples that are available for the $H \to \tau\tau$ signal prediction (Sec. 7.2).

are expected to cause a more homogenous change bin-by-bin, while statistical fluctuations vary more strongly between individual bins, the smoothing also helps to reduce these statistical fluctuations[30].

Symmetrisation Shape uncertainties that are very asymmetric or only defined in one direction (jet energy resolution and isolation selection of embedded samples) are symmetrised: A symmetric up- or downwards variation in each bin is defined based on the largest deviation with respect to the nominal value. This allows to form a continuous probability distribution function for these NPs (Sec. 7.7), which also helps to increase the fit stability.

Since the likelihood function is formed from the binned mass distributions, an optimal binning must be chosen. To achieve the best possible sensitivity towards a Higgs signal in data, a balance must be found between a good separation of signal and background and not too large statistical uncertainties in each bin. In particular bins where due to statistical fluctuation no background event is found pose a potential problem: The fit assumes no background is present in this bin, and since also statistical and systematic uncertainties can not be taken into account correctly, this might lead to an overestimation of the significance of the result.

Consequently, the binning is chosen finest around the expected Higgs signal between 100 and 150 GeV while broad bins are chosen at the tails of the mass distribution where a negligible signal fraction and a low number of background events are expected. In addition, in order to avoid empty bins the background processes with a small contribution to the selected sample are combined in the fit: Diboson, $Z \to \ell\ell(\mathrm{j} \to \tau_{\mathrm{had}})$, $Z \to \ell\ell(\ell \to \tau_{\mathrm{had}})$ and $t\bar{t}$. The final binning choice for the two fitted categories that yields the best expected significance is given in Tab. 7.12.

Category	Bin boundaries of fitted $m_{\tau\tau}$ distribution
VBF	[0,80,90,100,110,120,130,150,180,400]
Boosted	[0,80,90,95,100,105,110,115,118,121,124,127,130,135,140,145,160,180,200,400]

Table 7.12: Bin boundaries of the $m_{\tau\tau}$ distribution used in the profile likelihood fit in the different categories.

Test of the Fit Stability

The maximum likelihood fit adjusts the signal and background templates and all nuisance parameters to best fit the data distributions. It is important to ensure that the fit result is stable and unambiguous, so that a Higgs boson signal can be correctly measured and is not falsified by a systematic effect in the fit. Therefore, the behaviour of the likelihood ratio as a function of the nuisance parameters and their influence on the fit result must be understood.

These investigations are done with the help of an Asimov data set (Sec. 4.2.2) with signal strength $\mu = 1$ and $\mu = 0$. Moreover, the investigations are performed with the selected data sample. In this case the templates of the signal mass distributions are scaled to a high unknown signal strength. With this procedure the fit performance can directly be tested on data without revealing the resulting signal strength relative to the SM prediction. Only after the fit stability is ensured, the full data set is investigated using the signal samples at the SM signal strength.

[30] The smoothing is applied to the ratio of the respective variation and the nominal distribution. The smoothened $+1\sigma$ and -1σ distributions are obtained by multiplying the nominal histogram with the smoothened ratio.

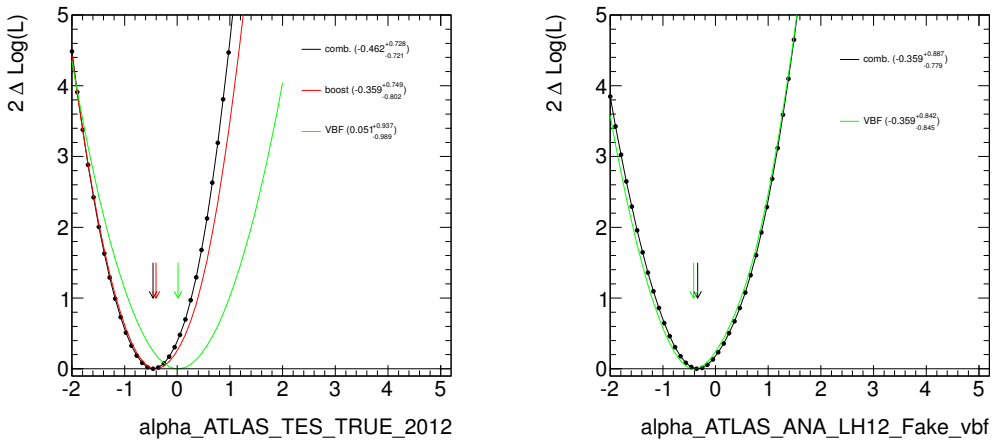

(a) (b)

Figure 7.41: Difference of the negative logarithmic likelihood ratio (Eq. 4.8) with respect to its minimum as a function of the nuisance parameter values (a) *TES_TRUE_2012* and (b) *ANA_LH12_Fake_vbf* in units of its initial uncertainty before the fit. The scans are shown for a fit of Boosted (red) and VBF (green) Categories only and for the combined fit of both (black).

Within these tests each nuisance parameter is investigated with respect to the following aspects:

- At which value does the nuisance parameter maximise the likelihood ratio?
- Are there constraints of nuisance parameters introduced by the fit?
- Is the nuisance parameter function smooth (no kinks or additional maxima)?
- Are there correlations between nuisance parameters and the fitted signal strength (μ)?
- What is the impact of each NP on the uncertainty on the signal strength μ?

A few of these studies are explained in more detail:

The likelihood ratio is derived as a function of each nuisance parameter in the following way: The value of the nuisance parameter is varied around the value which maximises the likelihood ratio. For each value of the nuisance parameter the likelihood ratio is maximised again by leaving all other nuisance parameters except for the considered one free in the fit.

Fig 7.41 shows two example distributions for the resulting nuisance parameter functions (*profiles*). The difference of the nuisance parameter value that maximises the likelihood (*post-fit value*) to its initial value (*pre-fit value*) divided by its uncertainty, $(\hat{\theta} - \theta_0)/\Delta\theta$, is called *pull*[31]. If the uncertainty obtained from the fit is smaller than the input uncertainty, a *constraint* on the parameter is introduced by the fit. In the two example distributions one can see that both uncertainties are slightly constrained and pulled towards a negative value, but both profiles are smooth.

Figure 7.42 shows the pulls and constraints of the most important nuisance parameters after the combined fit on ATLAS data for a test of the Higgs mass $m_H = 125$ GeV, while Figs. 7.43 and 7.44 show the same distributions for a fit performed in the individual Boosted and VBF Categories. The nuisance parameters representing systematic shape and/or normalisation uncertainties are included, as well as the statistical uncertainties on the background expectation in each bin. The nuisance parameters are ranked according to their effect on the relative uncertainty of the measured signal strength $\Delta\hat{\mu}/\hat{\mu}$.

[31] As explained in Sec. 4.2.2 the nuisance parameter function is approximated by a normalised Gaussian function, thus its initial value is 0 and the uncertainty is ±1.

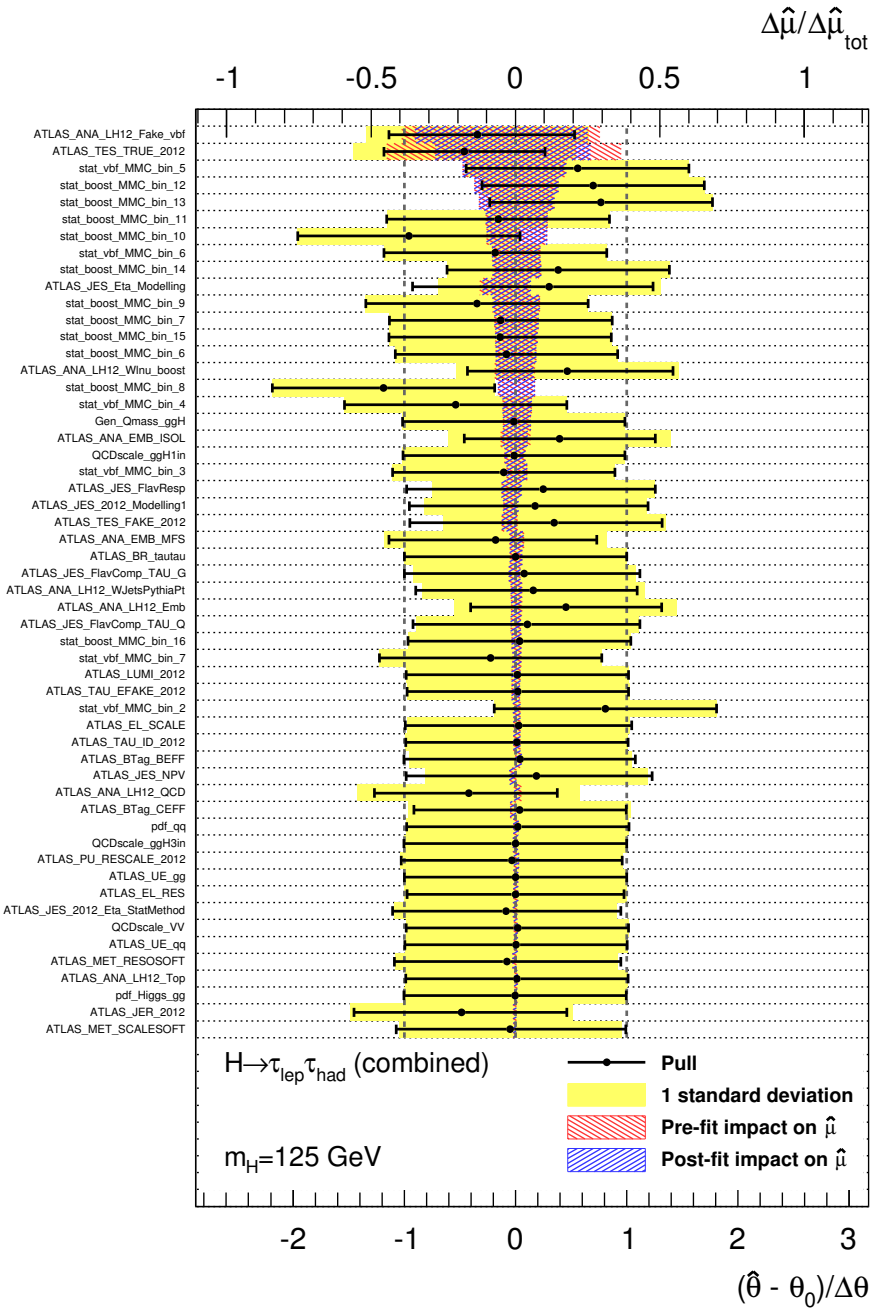

Figure 7.42: **Combination of all analysis categories**: Pulls of all significant nuisance parameters (systematic and statistical) entering the maximum likelihood fit. The units of the pulls are shown on the bottom x-axis. The black dots and error bars show the fit result for each parameter with respect to its initial value (at zero). The yellow bars show the pre-fit uncertainty on the parameter relative to the post-fit central value. The dashed vertical lines indicate the pre-fit error centred around zero. The parameters are ranked with respect to their effect on the relative uncertainty of the measured signal strength μ based on the post-fit uncertainty (blue hashed bars). The units are shown on the top x-axis. Also shown is the relative uncertainty based on the pre-fit uncertainty of each nuisance parameter (red hashed bars).

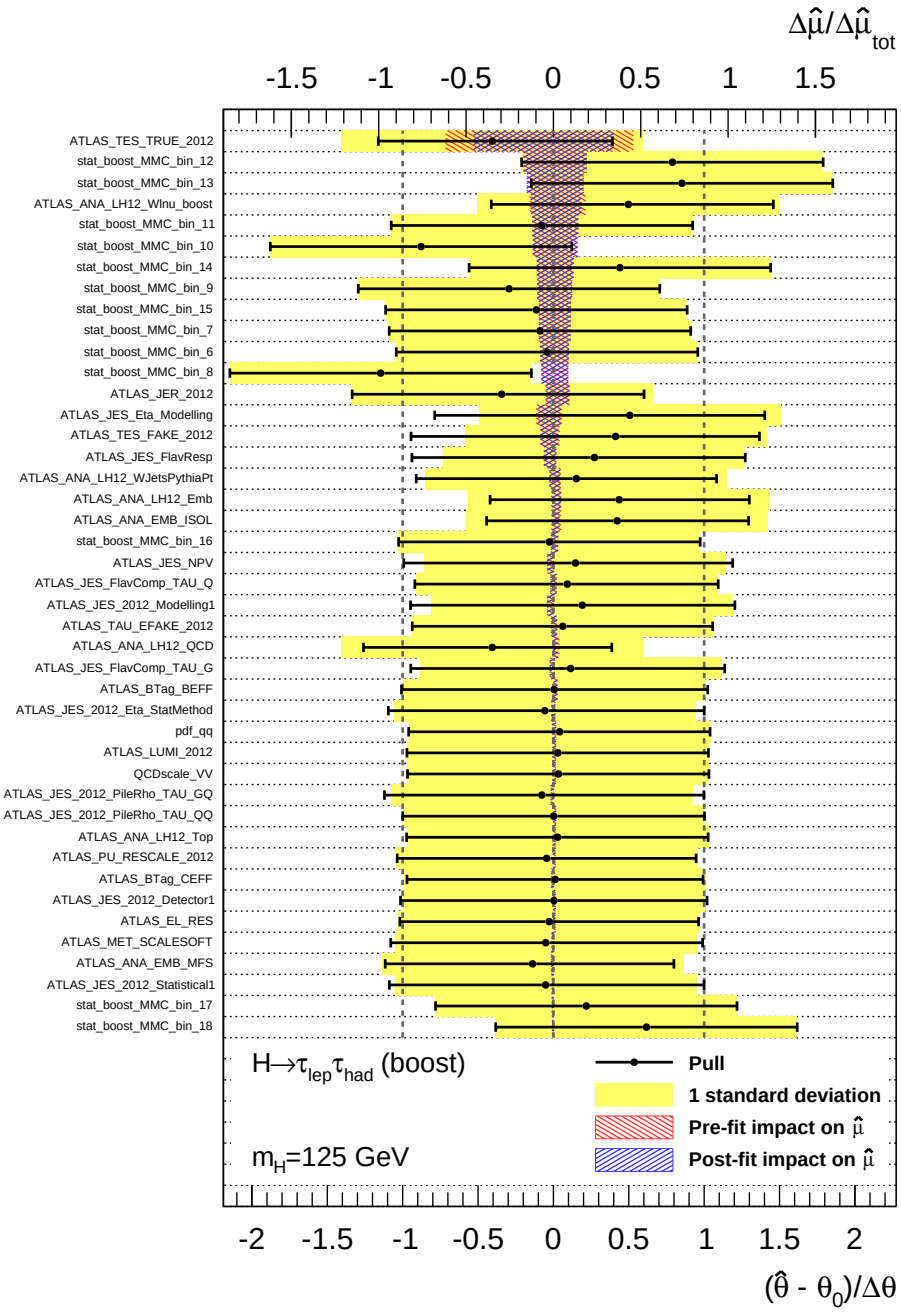

Figure 7.43: **Boosted Category**: Pulls of all significant nuisance parameters (systematic and statistical) entering the maximum likelihood fit. The units of the pulls are shown on the bottom x-axis. The black dots and error bars show the fit result for each parameter with respect to its initial value (at zero). The yellow bars show the pre-fit uncertainty on the parameter relative to the post-fit central value. The dashed vertical lines indicate the pre-fit error centred around zero. The parameters are ranked with respect to their effect on the relative uncertainty of the measured signal strength μ based on the post-fit uncertainty (blue hashed bars). The units are shown on the top x-axis. Also shown is the relative uncertainty based on the pre-fit uncertainty of each nuisance parameter (red hashed bars).

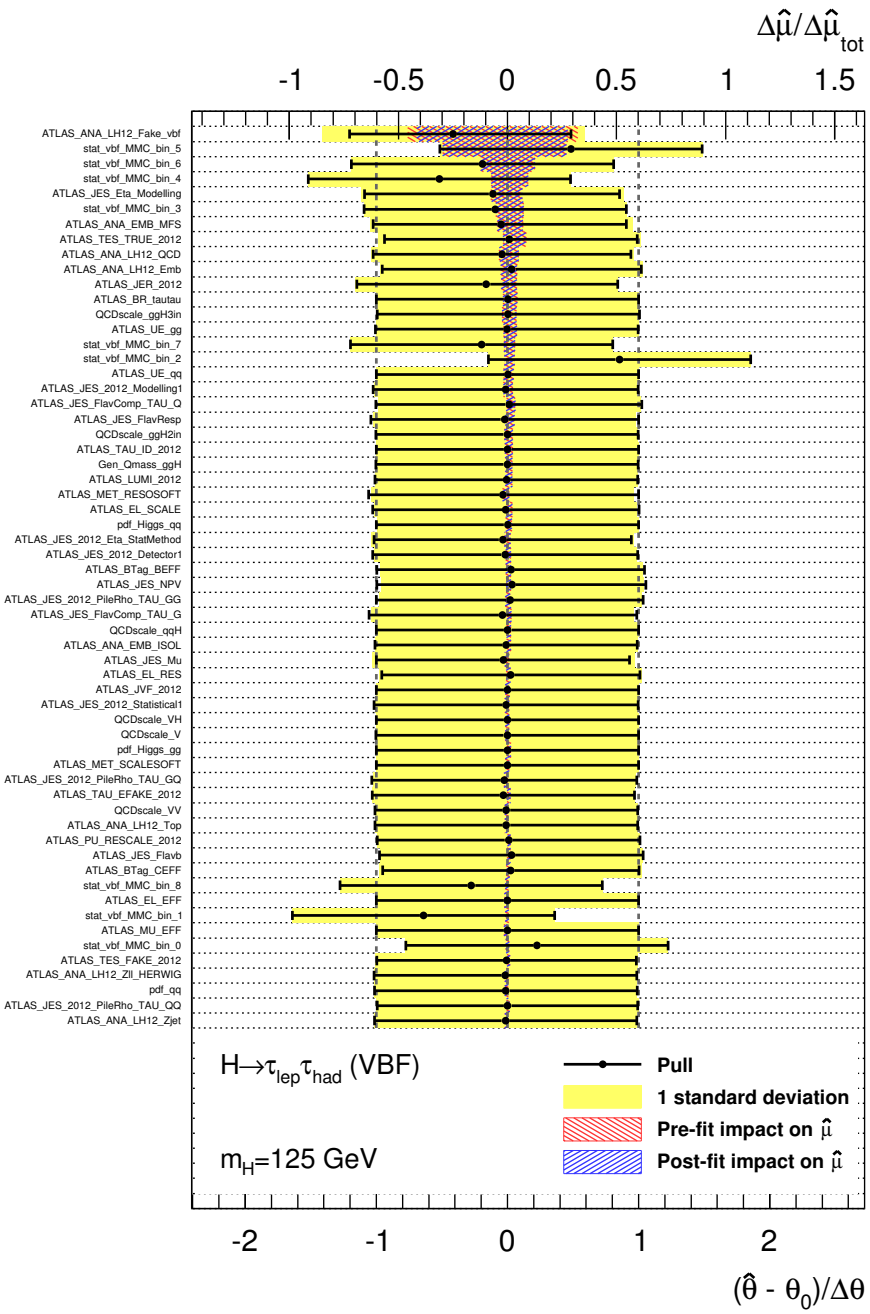

Figure 7.44: **VBF Category**: Pulls of all significant nuisance parameters (systematic and statistical) entering the maximum likelihood fit. The units of the pulls are shown on the bottom x-axis. The black dots and error bars show the fit result for each parameter with respect to its initial value (at zero). The yellow bars show the pre-fit uncertainty on the parameter relative to the post-fit central value. The dashed vertical lines indicate the pre-fit error centred around zero. The parameters are ranked with respect to their effect on the relative uncertainty of the measured signal strength μ based on the post-fit uncertainty (blue hashed bars). The units are shown on the top x-axis. Also shown is the relative uncertainty based on the pre-fit uncertainty of each nuisance parameter (red hashed bars).

No strong pulls or constraints of systematic uncertainties are visible in these distributions. The systematic uncertainties that have the largest impact on the measurement of μ are the TES uncertainties, several JES uncertainties and the normalisation uncertainties of the $j \to \tau_{\text{had}}$ background processes. This is expected, since it was found that they have the largest effect on the $m_{\tau\tau}$ distribution (Sec. 7.7). In addition, several statistical uncertainties of both categories (*stat_boost* and *stat_vbf*) have a high impact on the μ uncertainty. These bins are the ones closest to the expected signal, $100 < m_{\tau\tau} < 130$ GeV for the VBF Category and $121 < m_{\tau\tau} < 135$ GeV for the Boosted Category (Tab. 7.12). Therefore, their strong influence on the precision of the μ estimation is reasonable. Their high ranking also shows that the statistical uncertainty of the background expectation is one of the dominating uncertainties in the search for $H \to \tau_{\text{lep}}\tau_{\text{had}}$ decays with the investigated data set.

For a few important nuisance parameters the deviation from their initial values and uncertainties seen in these figures is explained in more detail in the following:

TES_TRUE_2012 This parameter is slightly pulled downwards and constrained. In the investigation of the kinematic distributions of the selected data events it was already found that data is more conform with a downwards variation of the τ energy scale in simulation (Sec. 7.6). The pull of this NP is consistent with this observation. Detailed studies have been done on the constraint resulting from the fit [150]. It is found that since the likelihood fit uses the full information from the $m_{\tau\tau}$ distributions to determine which TES variation is compatible with data, it can measure the TES value with a smaller uncertainty compared to the generic measurement, from which the initial TES value is derived (Sec. 5.2).

ANA_LH12_Fake_vbf A conservative uncertainty on the QCD and W+jets background estimate for the VBF Category has been defined (Sec. 7.7) which is most likely an overestimation of the true uncertainty. The fit takes into account all uncertainties simultaneously and thus can constrain the uncertainty on this background better than the initial estimate. A slight overestimation of the central value of this background normalisation parameter has already been seen in the studies of the SS control region (Fig. 7.28), which explains also the pull of this parameter.

ANA_LH12_Wlnu_boost This parameter also has a large initial uncertainty resulting from relatively low statistics in the W control region of the Boosted Category (Fig. 7.29e). Also in this case, the simultaneous evaluation of all parameters by the fit can constrain this parameter better.

ANA_EMB_ISOL* and *ANA_LH12_Emb The pull of these two parameters determining the normalisation of the $Z \to \tau\tau$ background (Sec. 7.7) mainly results from the Boosted Category. This is reasonable, since due to the small statistics of the VBF Category they can not gain much information on the correct estimation of this parameter from this category. This behaviour is also consistent with the small global difference between data and the background expectation seen for the Boosted Category (Fig. 7.36). A test of the maximum likelihood fit with the $Z \to \tau\tau$ normalisation as a free parameter is performed as a cross check[32]. Very similar fit results are obtained and also a slightly higher value of the $Z \to \tau\tau$ normalisation parameter is found by the fit compared to the pre-fit normalisation. The fact that both methods yield a similar result confirms the stability and reasonability of the fit, including the pulls of these nuisance parameters.

[32] The normalisation of the $Z \to \tau\tau$ background was initially intended to be a free parameter in the fit (as it is done in the multivariate analysis, Sec. 8.2 and [137]). However, the Boosted Category in this analysis contains no high statistics region with negligible contribution from a Higgs signal from which a reliable estimate can be done. Therefore, the normalisation method described in Sec. 7.5 is used instead and the uncertainty on the normalisation is included as nuisance parameter in the fit as a constraint for determining the optimal $Z \to \tau\tau$ normalisation.

In conclusion, no problematic issues are found from the investigations of the nuisance parameters. The results in the individual categories are also consistent with the combined result. This gives further confidence in the performance of the maximum likelihood fit in order to correctly extract a possible Higgs boson signal in data.

7.9 Results and Interpretation

The profile likelihood fit defined in the previous section is performed on the selected data sample to test if it is compatible with a background-only model or a deviation can be observed resulting from $H \to \tau_{\text{lep}}\tau_{\text{had}}$ decays. It is quantified at which significance the background-only model can be excluded and which signal strength with respect to the SM prediction can be measured (Sec. 4.2.2).

The maximisation of the likelihood ratio is performed without assuming a fixed mass of the Higgs boson. Instead, different mass hypotheses between 100 and 150 GeV are tested independently, as explained before. Another important information to gain from this analysis is therefore if an excess seen in data is compatible with a certain Higgs mass, most importantly if it is compatible with the discovery of the Higgs boson at $m_H = 125$ GeV (Sec. 4.1.3).

The final goal is to combine the results of this thesis with the analyses of the other $H \to \tau\tau$ decay channels, the fully hadronic and fully leptonic $\tau\tau$ decays. With the statistical combination of these independent results a much higher significance can be achieved than with the single channels. This will be discussed in Chap. 8.

Statistical Significance

The *observed* and *expected* p_0 values and the corresponding significances for the combined fit of the $H \to \tau_{\text{lep}}\tau_{\text{had}}$ VBF and Boosted Categories are shown as a function of the Higgs mass in Fig. 7.45. Also p_0 values for the individual fit of Boosted and VBF Categories are shown for comparison. Table 7.13 states the obtained values for expected and observed signal significance for a mass of $m_H = 125$ GeV.

At m_H =125 GeV the observed significance for the combined data samples is 1.0σ. This corresponds to a small excess of data over the expected background. The probability that this or a larger observed deviation results from the background alone is 15%. The maximum of the significance curve is observed at $m_H = 125$ GeV.

The expected significance at this mass is 1.7σ. It is also the largest one in the considered mass range. This results mainly from the fact that for high masses the branching ratio of the $H \to \tau\tau$ decay gets smaller, reducing the total number of events expected from a Higgs signal in the data sample. At very low masses, it gets more difficult to disentangle a possible Higgs signal from the $Z \to \tau\tau$ background in the $m_{\tau\tau}$ distribution (Fig 7.9). The VBF Category provides the highest significance as expected, since it has the highest signal-to-background ratio.

The observed excess over the expected background is compatible with a SM Higgs signal, which is expected at $m_H = 125$ GeV based on the discovery of its decay to bosons (see Sec. 4.1.3)[33]. The excess is not significant enough to claim the observation of a $H \to \tau\tau$ signal in data based on this channel alone. However, this interpretation is confirmed by the statistical combination of this $H \to \tau_{\text{lep}}\tau_{\text{had}}$ analysis with the other $H \to \tau\tau$ decay channels (Chap. 8).

	p_0 [σ]
Observed Combined	1.0
Expected Combined	1.7
Expected Boosted	1.0
Expected VBF	1.3

Table 7.13: Expected and observed signal significance in units of the standard deviation for a Higgs mass of $m_H = 125$ GeV ($\sqrt{s} = 8$ TeV, 20.3 fb^{-1}). The expected limits are also given for a fit of the individual categories.

[33] The compatibility of this observation with different mass hypotheses is investigated further at the end of this section.

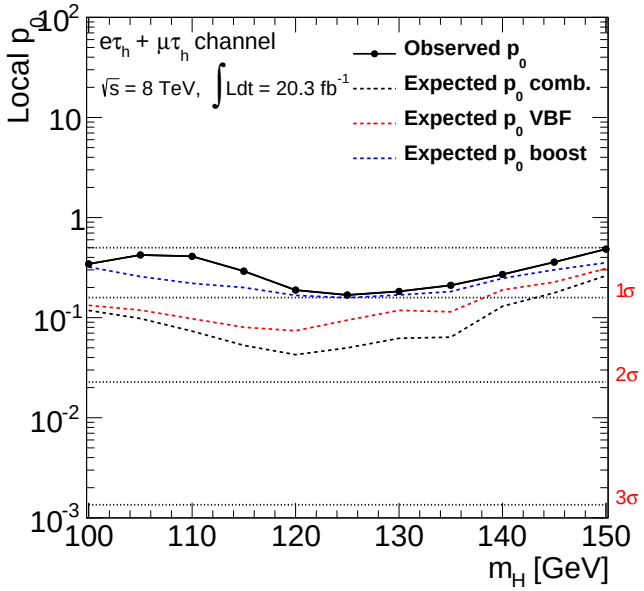

Figure 7.45: Observed (solid line) and expected (dashed line) p_0 values and the corresponding signal significance in units of standard deviation (right axis) as a function of different mass hypotheses m_H for the combined fit of the categories of the $H \to \tau_{\text{lep}}\tau_{\text{had}}$ analysis with 20.3 fb^{-1} at $\sqrt{s} = 8$ TeV. The expected p_0 value obtained from a fit of the individual Boosted (blue line) and VBF (red line) categories are also shown.

Exclusion Limits

It is also tested which cross section times branching ratio relative to the Standard Model expectation can be excluded at 95% confidence level with this analysis (Sec. 4.2.2). The observed and expected *upper limits* on the cross section times branching ratio obtained from the selected data set as a function of m_H can be seen in Fig. 7.46. The expected and observed limits for $m_H = 125$ GeV are listed in Tab 7.14.

The expected upper limit lies above 1 in the entire mass range, thus the predicted signal strength of the Standard Model (CL_S at 1) is not expected to be excluded for any mass of the Higgs boson with this analysis. The observed limit lies for almost the full mass range (>115 GeV) above the expected one within 1 standard deviation. At $m_H = 125$ GeV the expected limit on the cross section times branching ratio is $1.2 \times \sigma_{\text{SM}}$, while the observed one is $1.5 \times \sigma_{\text{SM}}$. The small excess of the observed limit in this mass range is equivalent to the small excess observed in data over the expected background.

	Observed μ limit	Expected μ limit	-2σ	-1σ	$+1\sigma$	$+2\sigma$
Combined fit	1.5	1.2	0.9	0.7	1.8	2.7

Table 7.14: Expected and observed 95% CL_S limit on the signal cross section times branching ratio relative to the Standard Model expectation and the $\pm 1/2\sigma$ error bands of the expected limits at $m_H = 125$ GeV with 20.3 fb^{-1} at $\sqrt{s} = 8$ TeV.

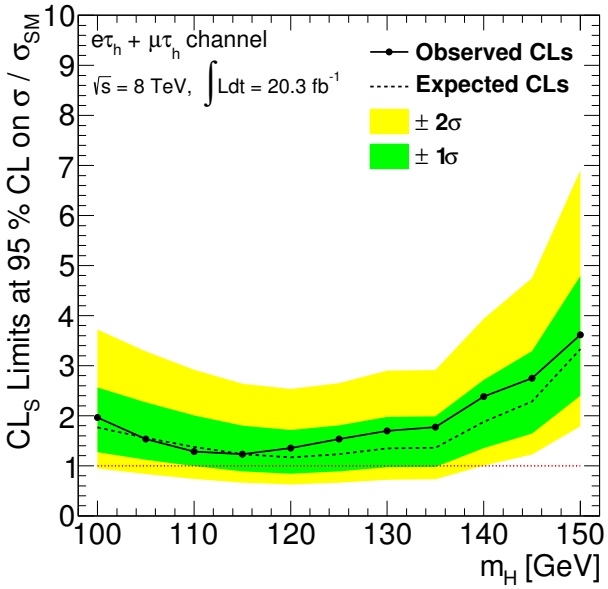

Figure 7.46: Observed (solid line) and expected (dashed line) upper limits on the signal cross section times branching ratio relative to the Standard Model expectation at 95% confidence level as a function of different m_H hypotheses. The green and yellow bands indicate the $\pm 1\sigma$ and $\pm 2\sigma$ uncertainty on the expected upper limit. The results are based on 20.3 fb^{-1} at $\sqrt{s} = 8$ TeV of ATLAS data, combing the Boosted and VBF Categories of the $H \to \tau_{\text{lep}}\tau_{\text{had}}$ analysis.

Signal Strength and Post Fit Distributions

The excess of data over the expected background is measured in units of the *signal strength* μ relative to the SM Higgs boson cross section times branching ratio. For the Higgs boson with mass $m_H = 125$ GeV decaying to a pair of τ leptons the signal strength in this data set relative to the SM expectation is measured to be:

$$\mu = 0.4^{+0.6}_{-0.6}$$

In Tab. 7.15 also the signal strength measurements resulting from the fit of the individual analysis categories are given. All values are consistent with the expectation for a Standard Model Higgs boson ($\mu = 1$).

In Tab. 7.16 the total uncertainty on the signal strength is split into its constituents. The uncertainty is clearly dominated by the statistical uncertainties of the data (*statistical* uncertainty) and the statistical uncertainty on the background prediction from simulation or the data-driven methods (*background prediction statistical* uncertainty). This results from the low number of events in the investigated categories, in particular the VBF Category, due to the tight event selection needed to obtain a high signal-to-background ratio in the sample. These statistical uncertainties are therefore a large limiting factor for the sensitivity that can be achieved with this analysis.

The predictions for the signal and background composition in each category based on the fit results are shown in Fig. 7.47. Good agreement of the signal and background contributions with data is seen in both categories.

Category	μ
VBF	$0.5^{+0.8}_{-0.7}$
Boosted	$0.1^{+1.0}_{-0.9}$
Combined	$0.4^{+0.6}_{-0.6}$

Table 7.15: Observed signal strength μ and total uncertainty from the combined and individual fit of the categories at $m_H = 125$ GeV with 20.3 fb^{-1} at $\sqrt{s} = 8$ TeV.

Components	$\Delta\mu$
Total	±0.6
Statistical	±0.4
Systematic	±0.4
Background pred. statistical	±0.3
Theoretical	±0.1
Experimental	±0.3

Table 7.16: Decomposition of the uncertainties on the measured signal strength μ at $m_H = 125$ GeV with 20.3 fb^{-1} at $\sqrt{s} = 8$ TeV.

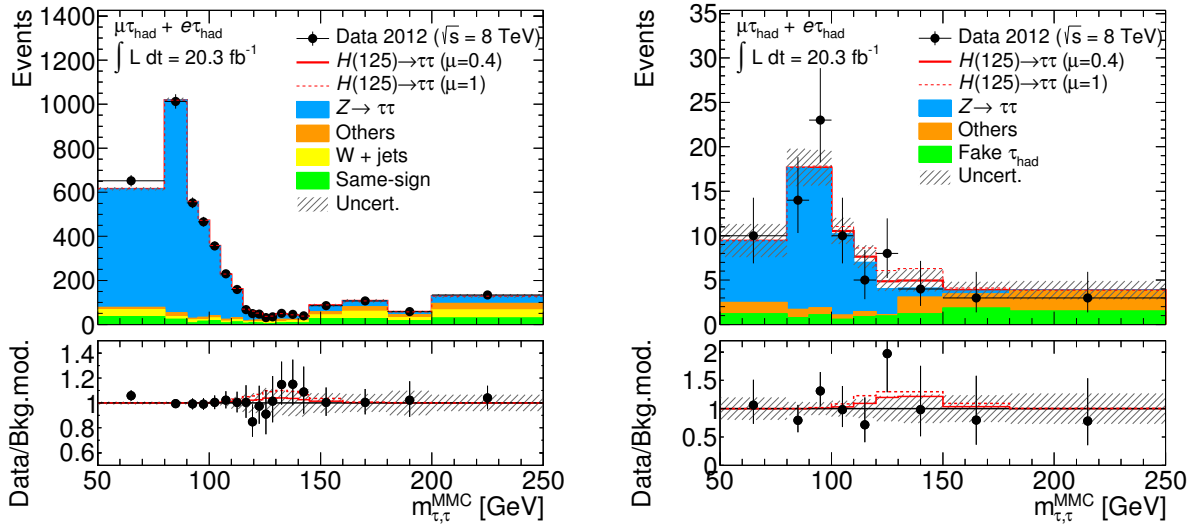

(a) (b)

Figure 7.47: $m_{\tau\tau}$ distribution (binning according to Tab. 7.12) in (a) the Boosted and (b) the VBF Category. The signal (red solid line) and background expectation are estimated by the combined fit of both categories. The dashed red line indicates the SM signal expectation ($\mu = 1$). The bottom panel shows the ratio of data to the background-only model. Also shown is the change in the model when including a Higgs signal with $\mu = 0.4$ ($\mu = 1$) indicated by the red solid (dashed) line. Statistical and systematic normalisation uncertainties are indicated by the hashed band. The first and the last bins also contain the events outside the displayed range (< 50 and > 250 GeV).

Sensitivity on the Higgs Boson Mass

A small excess of data over the expected background has been observed in Fig. 7.45. The highest significance in data is observed around a mass of $m_H = 125$ GeV. In the following it is investigated, how well different mass hypotheses can be distinguished with this analysis and how compatible the observed significance and signal strength are with different Higgs masses.

For this purpose, the observed significance in data at each mass point between 100–150 GeV is compared to the significance that is expected if the presence of a SM Higgs boson with signal strength $\mu = 1$ and a *fixed* Higgs mass of 105, 125 or 145 GeV is assumed. The results can be seen in Fig. 7.48.

The curves of the expected significance values clearly differ for the three mass samples. The maximum of each of the three significance curves (i.e. the minimum p_0 value) is reached where the tested mass hypothesis is equal to the assumed mass in the sample, e.g. it reaches its maximum at $m_H = 125$ GeV for the sample including a 125 GeV Higgs boson.

The maximum significance in data is observed at $m_H = 125$ GeV and also the form of the observed p_0 curve as a function of m_H is most compatible with the one expected for a 125 GeV Higgs boson.

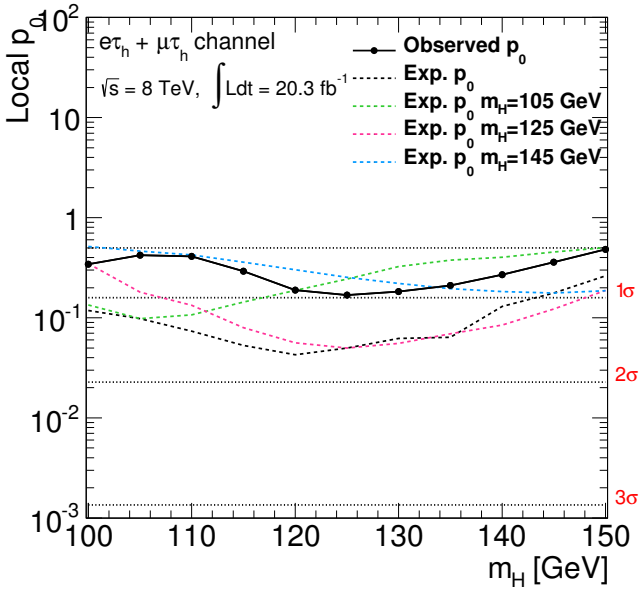

Figure 7.48: Observed and expected p_0 values and the corresponding signal significance in units of the standard deviation (right axis) as a function of m_H (black solid and dashed line) from the combined fit of both categories with 20.3 fb^{-1} at $\sqrt{s} = 8$ TeV. For comparison the p_0 expectation is shown when a Higgs boson with a *fixed* mass and $\mu = 1$ is assumed to be present in the data sample: $m_H = 105$ GeV (green), $m_H = 125$ GeV (pink) and $m_H = 145$ GeV (blue).

Furthermore, the observed signal strength values as a function of m_H are compared with the expectation assuming a SM Higgs signal with a fixed mass. Figure 7.49 shows the observed signal strength values in data compared to the expected values assuming a Higgs boson with a mass of 105, 125 or 145 GeV and $\mu = 1$.

The expected signal strength curves for these three masses are very different. For the 105 GeV sample it is expected to measure a falling signal strength curve with a signal strength 1 at 105 GeV. For the 145 GeV sample it is expected to measure a rising curve with a signal strength of 1 at m_H =145 GeV. For the 125 GeV sample also a rising curve is expected, but with a signal strength of 1 at m_H =125 GeV.

Due to the large uncertainties none of the mass hypotheses can be excluded yet with the observed signal strength curve when comparing it to these three expected curves. Nevertheless it can be concluded that the observed curve is compatible with the expected signal strength measurements for a SM Higgs boson mass of 125 GeV.

These studies form an important basis for the combination of this $H \rightarrow \tau_{\text{lep}}\tau_{\text{had}}$ channel with the other two decay channels, with which a stronger confirmation of the mass compatibility can be obtained. This will be presented in the next chapter.

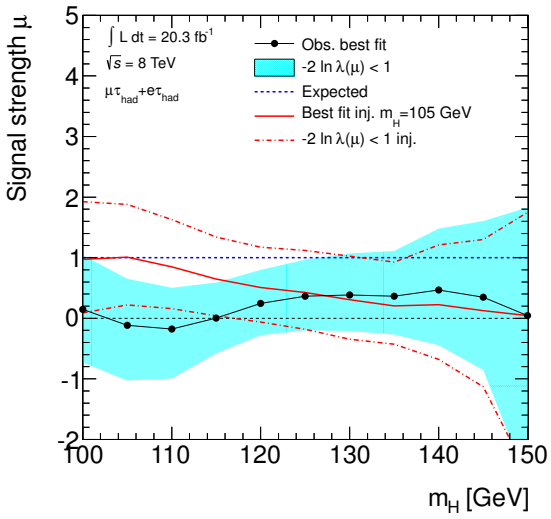

(a)

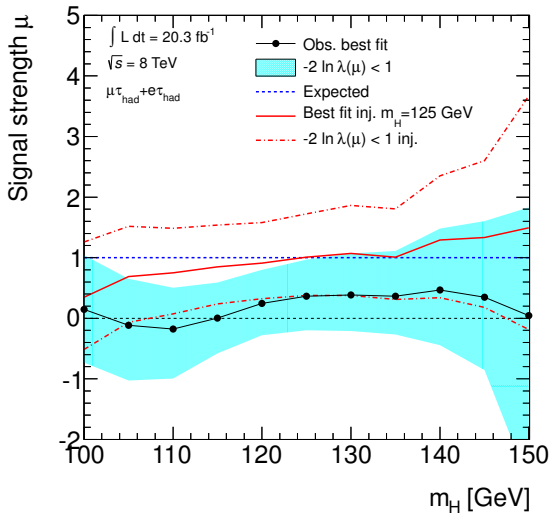

(b)

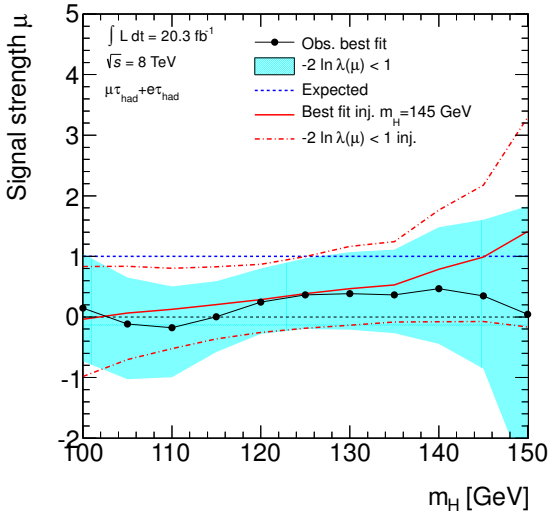

(c)

Figure 7.49: Observed (black line) and expected (blue line) μ values as a function of the Higgs boson mass hypothesis obtained from the combined fit of both categories with 20.3 fb^{-1} at $\sqrt{s} = 8$ TeV. The turquoise contours show the total uncertainty on the resulting μ values. For comparison the expected signal strength (solid red line) and uncertainty (dashed red line) for an included Higgs boson with a fixed mass are shown: (a) $m_H = 105$ GeV, (b) $m_H = 125$ GeV and (c) $m_H = 145$ GeV.

Comparison to Previous Results

The results of this $H \to \tau_{\text{lep}}\tau_{\text{had}}$ search can be compared to the ones obtained from the smaller data set of 13.0 fb^{-1} at $\sqrt{s}$ = 8 TeV combined with 4.6 fb^{-1} at $\sqrt{s}$ = 7 TeV (details see Appendix C and [97]). With this previous analysis the observed (expected) significance at m_H = 125 GeV was 0.1 (1.2)σ. For the previous analysis of the 8 TeV data set (13.0 fb^{-1}) only, a significance of -0.2 (0.9)σ was observed (expected) at this mass point. The results obtained from the analysis of the full 2012 data set with 20.3 fb^{-1} discussed here show an improvement of 40% compared to these earlier results of $\sqrt{s}$ = 7 TeV and $\sqrt{s}$ = 8 TeV data, and of 85% in comparison to the analysis of the 13.0 fb^{-1} $\sqrt{s}$ = 8 TeV data set alone.

This can be attributed to the increased statistics of the full 2012 data set and the embedded $Z \to \tau\tau$ sample, and the use of simulated W+jets and $Z \to \ell\ell$ samples with three times more simulated events in the new analysis (Sec. 7.2). In addition to the resulting reduced statistical uncertainties, this also allows a finer binning for the fit of the $m_{\tau\tau}$ distribution and thus a significant improvement of the analysis sensitivity. Moreover, also the inclusion of the latest improvements on the τ_{had} identification and $E_{\text{T}}^{\text{miss}}$ reconstruction (Chap. 5 and [105, 113]) play a role for this large improvement of the analysis results: The τ_{had} identification provides a better rejection of the $j \to \tau_{\text{had}}$ background and at the same time a higher signal efficiency. Thus the signal-to-background ratio with respect to this type of background (W+jets and QCD) is increased by a factor of 1.5 and leads to a reduction of the systematic uncertainties associated to the modelling of these background processes. The additional rejection of three-prong $e \to \tau_{\text{had}}$ candidates (Sec. 5.2) reduces the contribution of the $Z \to \ell\ell(\ell \to \tau_{\text{had}})$ background further. The improved $E_{\text{T}}^{\text{miss}}$ resolution increases the signal and background separation of variables depending on $E_{\text{T}}^{\text{miss}}$, e.g. $p_{\text{T}}^{\text{tot}}$, and most importantly also the $m_{\tau\tau}$ resolution by about 10–15% [34].

Summary

In this chapter the search for a SM Higgs boson decaying to τ leptons in the $H \to \tau_{\text{lep}}\tau_{\text{had}}$ decay channel is presented. It is based on the 2012 ATLAS data sample at $\sqrt{s}$ = 8 TeV corresponding to a luminosity of 20.3 fb^{-1}. A major improvement of the analysis sensitivity with respect to the previous search results based on the first 2012 data is achieved.

An excess of data over the expected background can be observed in the investigated data sample of 20.3 fb^{-1}, which is in good agreement with a Standard Model Higgs boson decaying to τ leptons with a mass of m_H = 125 GeV.

These results of the $H \to \tau_{\text{lep}}\tau_{\text{had}}$ analysis provide an important basis for the combination of all $H \to \tau\tau$ analysis channels in the full 2012 data sample, where the $H \to \tau_{\text{lep}}\tau_{\text{had}}$ decay channel provides the highest sensitivity on a $H \to \tau\tau$ signal. The results of the combination of all $H \to \tau\tau$ channels based on 20.3 fb^{-1} data are presented in the next chapter.

[34] The replacement of the simulated $Z \to \tau\tau$ sample by the embedded sample in the VBF Category (Sec. 7.5) improves the modelling of the $Z \to \tau\tau$ background significantly and reduces the systematic uncertainties. However, the statistical uncertainties of the embedded $Z \to \tau\tau$ sample are larger compared to the simulated sample. Therefore, no large improvement of the expected significance in data is observed due to this change alone.

CHAPTER 8

Combination of Results and Comparison to Other $H \to \tau\tau$ Analysis Methods

As explained in the previous chapter, two analyses have been performed in parallel to search for a $H \to \tau\tau$ signal in the full data set of 20.3 fb^{-1} collected in 2012 at a centre-of-mass energy of $\sqrt{s}$ = 8 TeV: One analysis applies a sequence of selection criteria (*cuts*) to define the signal regions in the different categories and a fit of $m_{\tau\tau}$ distributions is performed testing different mass hypotheses. The investigation of the $H \to \tau_{\text{lep}}\tau_{\text{had}}$ decay channel with this analysis method, referred to as *cut-based analysis* (CBA), is the topic of this thesis and is explained in Chap. 7. The other *multivariate analysis* (MVA) uses boosted decision trees (BDTs) to classify signal and background and the fit is performed on the resulting BDT discriminant [135]. Therefore, these two methods provide an independent and complementary cross check of the $H \to \tau\tau$ search results: Both methods constitute evidence of the direct Yukawa coupling of the recently discovered Higgs boson to τ leptons in ATLAS data. These results are published in [136].

In Sec. 8.1 of this chapter the statistical combination of the $H \to \tau_{\text{lep}}\tau_{\text{had}}$ channel investigated in this thesis and the other $H \to \tau\tau$ decay channels is discussed. Several minor changes are also explained that have been applied to the $H \to \tau_{\text{lep}}\tau_{\text{had}}$ analysis for this combination. Section 8.2 outlines the main concept and results of the multivariate approach. Section 8.3 highlights several conceptual differences of MVA and CBA and the role of both analyses for the obtained results.

8.1 Combination of Cut-Based $H \to \tau\tau$ Analyses

A combined fit of all $H \to \tau\tau$ decay channels is performed based on the full $\sqrt{s}$ = 8 TeV data set corresponding to an integrated luminosity of 20.3 fb^{-1}.

The combination is based on a slightly different version of the $H \to \tau_{\text{lep}}\tau_{\text{had}}$ analysis compared to the one presented in Chap. 7. Several small changes are implemented to mainly improve the pre-fit modelling of the expected background and to harmonise this channel with the other channels and the MVA[1].

[1] These changes have only been developed after a finalisation of the $H \to \tau_{\text{lep}}\tau_{\text{had}}$ analysis as presented in Chap. 7. Although a few first studies have been performed (see Appendix F), an inclusion of these changes in the analysis was beyond the scope of this thesis. For this reason the results of these changes are not documented in detail here, except in the combination with the other $H \to \tau\tau$ decay channels. More details on the effects of these changes on the $H \to \tau_{\text{lep}}\tau_{\text{had}}$ analysis can be found in [136].

The following alterations are included in the $H \to \tau_{\text{lep}}\tau_{\text{had}}$ analysis to combine it with the other decay channels:

Improved TES measurement Based on generic studies of the differences observed between simulation and data in the $Z \to \tau\tau$ visible mass distribution, a correction of the TES in data is applied [164]. This improves the agreement of data and simulation (Sec. 7.6). Also several uncorrelated nuisance parameters for the TES uncertainties are introduced in order to better separate the effects of different systematic uncertainties in the profile likelihood fit.

Improved treatment of τ spin correlations in the embedded sample Due to the missing information of the initial quark configuration in the embedded $Z \to \tau\tau$ sample, the correct Z polarisation cannot be determined and is not taken into account for the determination of polarisation and spin correlations of τ leptons. An additional correction is therefore applied to the embedded sample to account for the average Z polarisation of $p \approx -0.15$ [165]. These corrections result in a small improvement of the modelling of the $Z \to \tau\tau$ decay kinematics.

Improved fake factor estimation In addition to the W+jets and QCD background, also the estimation of the $j \to \tau_{\text{had}}$ background contribution from $Z \to \ell\ell$ and top processes is derived with the help of the fake factor method (Sec. 7.5) for the VBF Category. Moreover, to define the anti-ID control region, only τ_{had} candidates passing a loose threshold of the τ_{had} ID BDT discriminant (Sec. 5.2) are included. This excludes the region of very low τ_{had} BDT values, where the quark-gluon composition is very different from the signal region, and improves the accuracy of the background prediction.

Splitting of the VBF Category The previous VBF Category (Sec. 7.4) is split into two categories with a looser and a tighter selection. For the tighter category an additional requirement of $p_{\text{T}}^{\text{H}} > 100$ GeV is applied. For the looser category no p_{T}^{H} requirement, a looser m_{jj} (> 300 GeV) and a looser τ_{had} p_{T} requirement (> 20 GeV) are applied. This results in one signal region with a very high signal-to-background ratio and a very good mass resolution and another signal region which still contains a large number of signal events but is less pure. Combining these two separate categories yields a better expected significance than with a single VBF Category. This new concept of category splitting is further is investigated in Appendix F.

The fit results obtained before and after these changes are very similar. A small increase of the expected significance of about 2% is observed, mainly resulting from this re-categorisation of events [136].

Figure 8.1a shows the $m_{\tau\tau}$ distribution combined for all channels in data and the expected background. The events are weighted by a factor ln(1+S/B) based on the ratio of signal (S) to background (B) events in the categories of all analysis channels. For comparison the expected distributions of a Higgs signal at different masses are shown. A clear excess of data over the expected background is visible, which is most compatible with a Higgs boson mass of $m_H = 125$ GeV.

Figure 8.1b shows the observed and expected p_0 values as a function of m_H obtained from this combination of $H \to \tau\tau$ analysis channels. For comparison also the observed and expected significances obtained with the MVA at $m_H = 125$ GeV are shown. These are further explained in the next section. A clear excess of data over the expected background is visible with a minimum at $m_H = 125$ GeV in this combination of all $H \to \tau\tau$ analyses: The background-only hypothesis for a Higgs mass of $m_H = 125$ GeV can be excluded with an observed significance of 3.2σ. The expected significance at this mass is 2.5σ [2].

[2] The expected significances in the single $H \to \tau\tau$ analysis channels are: 0.8σ in $H \to \tau_{\text{lep}}\tau_{\text{lep}}$, 1.7σ in $H \to \tau_{\text{lep}}\tau_{\text{had}}$ and 1.6σ in $H \to \tau_{\text{had}}\tau_{\text{had}}$ [136].

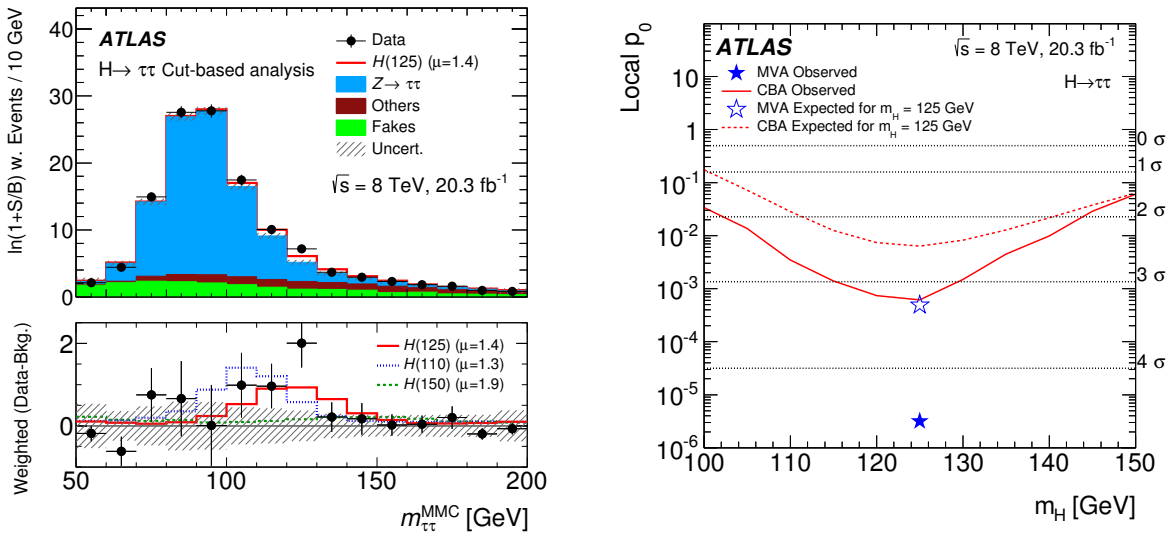

(a) (b)

Figure 8.1: (a) Distribution of the $m_{\tau\tau}$ mass combined for all $H \to \tau\tau$ channels in the full $\sqrt{s} = 8$ TeV data sets, obtained from the CBA. The observed data is compared to signal ($\mu = 1.4$) and background expectation as obtained from the fit. All events are weighted by a factor ln(1+S/B), based on the signal (S) to background (B) ratio in each category. The statistical and systematic normalisation uncertainties are indicated as hashed bands. In the lower panel the ratio between weighted data events and weighted background events is shown. Different signal hypotheses with masses 110 GeV (blue), 125 GeV (red) and 150 GeV (green) with the respective signal strengths obtained from the fit are shown for comparison.
(b) Observed (solid line) and expected (dashed line) p_0 values and the corresponding signal significances in units of the standard deviation (right axis) as a function of m_H for the combination of all channels in the CBA for the full $\sqrt{s} = 8$ TeV data set. The observed and expected p_0 values resulting from the MVA of this data set are also included for $m_H = 125$ GeV (full and open star) [136].

The signal strength of a $m_H = 125$ GeV boson observed for the combination of all channels is:

$$\mu = 1.4\,^{+0.6}_{-0.5} = 1.4 \pm 0.4\,(\text{stat.})\,^{+0.4}_{-0.3}\,(\text{syst.}) \pm 0.1\,(\text{theo.})$$

This value is in good agreement with the expectation for a SM Higgs boson ($\mu = 1$) [3].

A two-dimensional likelihood fit with both the signal strength μ and m_H as free parameters is performed to test the compatibility of the observed excess with different mass hypotheses. The mass points are tested in steps of 5 GeV in the range 100–150 GeV. The best fit value is found at $\mu = 1.4$ and $m_H = 125$ GeV. The results are shown in Fig. 8.2. This confirms that the observation is most compatible with a Higgs boson mass of 125 GeV.

These results thus provide evidence that the recently discovered Higgs boson (Sec. 4.1.3) with a mass of $m_H = 125$ GeV couples directly to fermions.

The conclusions drawn from the $H \to \tau_{\text{lep}}\tau_{\text{had}}$ channel alone, based on a small observed excess of data with 1σ with a minimum p_0 value at $m_H = 125$ GeV corresponding to a signal strength of $\mu = 0.4\,^{+0.6}_{-0.6} = (0.4 \pm 0.4\,(\text{stat.}) \pm 0.4\,(\text{syst.}) \pm 0.1\,(\text{theo.}))$ (Sec. 7.9), are thus strongly confirmed by this combination of all cut-based $H \to \tau\tau$ analyses. As expected the $H \to \tau_{\text{lep}}\tau_{\text{had}}$ analysis is the most sensitive of all channels, an thus provides the largest contribution to this result.

[3] The measured signal strengths in the single $H \to \tau\tau$ analysis channels are: $\mu = 3.2\,^{+1.4}_{-1.3}$ in $H \to \tau_{\text{lep}}\tau_{\text{lep}}$, $\mu = 0.7\,^{+0.7}_{-0.6}$ in the updated $H \to \tau_{\text{lep}}\tau_{\text{had}}$ and $\mu = 1.6\,^{+0.9}_{-0.7}$ in $H \to \tau_{\text{had}}\tau_{\text{had}}$ [136].

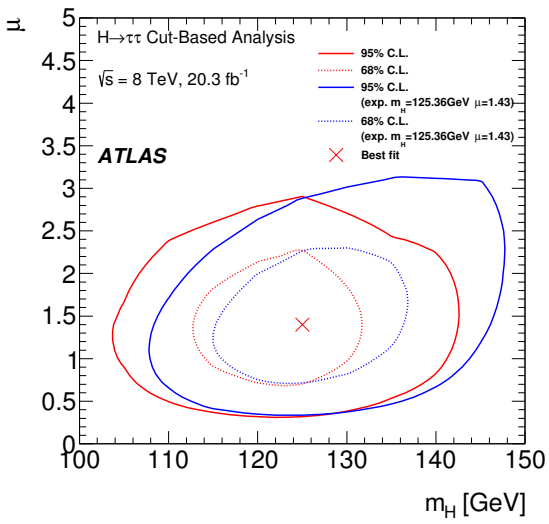

Figure 8.2: Two-dimensional likelihood fit in the m_H and μ plane for the combination of all channels in the CBA for the full $\sqrt{s} = 8$ TeV data set. The 68% and 95% CL contours are also shown (red dashed and solid lines). The best-fit value is indicated as a red cross. The expected 68% and 95% CL contours for $m_H = 125.36$ GeV and $\mu = 1.43$ are shown for comparison (blue dashed and solid lines) [136].

8.2 Summary of the Multivariate $H \to \tau\tau$ Analysis

In the multivariate analysis a set of characteristic observables is combined to a discriminant with a BDT algorithm, which classifies the events as signal (high output value) or background (low output value) in loosely defined VBF and Boosted Categories. Also the reconstructed $m_{\tau\tau}$ mass is added to the set of discriminating variables in the BDT. The data sample (20.3 fb^{-1} at $\sqrt{s} = 8$ TeV) and preselection of events is identical to the CBA. The main background contributions are also estimated in a data-driven way in the MVA, using in principal the same methods as explained in Sec. 7.5. The profile likelihood fit for a statistical analysis of data is performed on the distribution of the BDT discriminant.

First preliminary results of the MVA are documented in [135, 137]. The latest results including several improvements as mentioned in the previous section are published in [136] and are briefly presented here. The resulting distribution of the BDT discriminant in the VBF Category of the MVA in the $H \to \tau_{\text{lep}}\tau_{\text{had}}$ channel in data compared to the signal and background expectation is shown in Fig. 8.3a. An accumulation of the signal events is seen at high BDT output values and a clear excess over the expected background is observed in data which is compatible with the signal of a Standard Model Higgs boson.

For the combination of the MVA results in all $H \to \tau\tau$ decay channels, the observed (expected) significance at $m_H = 125$ GeV is found to be 4.5 (3.3) σ as shown in Fig. 8.1b, the measured signal strength is $\mu = 1.5^{+0.5}_{-0.4}$. The MVA results obtained with the 2012 data set are also combined with 4.5 fb^{-1} of the 2011 data set at $\sqrt{s} = 7$ TeV. The final resulting signal strength for the combined fit of both data sets is $\mu = 1.4^{+0.4}_{-0.4}$ for a Higgs mass of 125 GeV.

Figure 8.3b shows the weighted invariant MMC $m_{\tau\tau}$ distribution of the combination of all multivariate $H \to \tau\tau$ analyses and the $\sqrt{s} = 7$ TeV and $\sqrt{s} = 8$ TeV data sets. Also here a clear excess in data over the expected background is observed which is compatible with a Higgs boson mass of 125 GeV.

In agreement with the previously presented CBA results also these MVA results provide evidence for the direct coupling of the discovered Higgs boson to fermions as predicted by the SM.

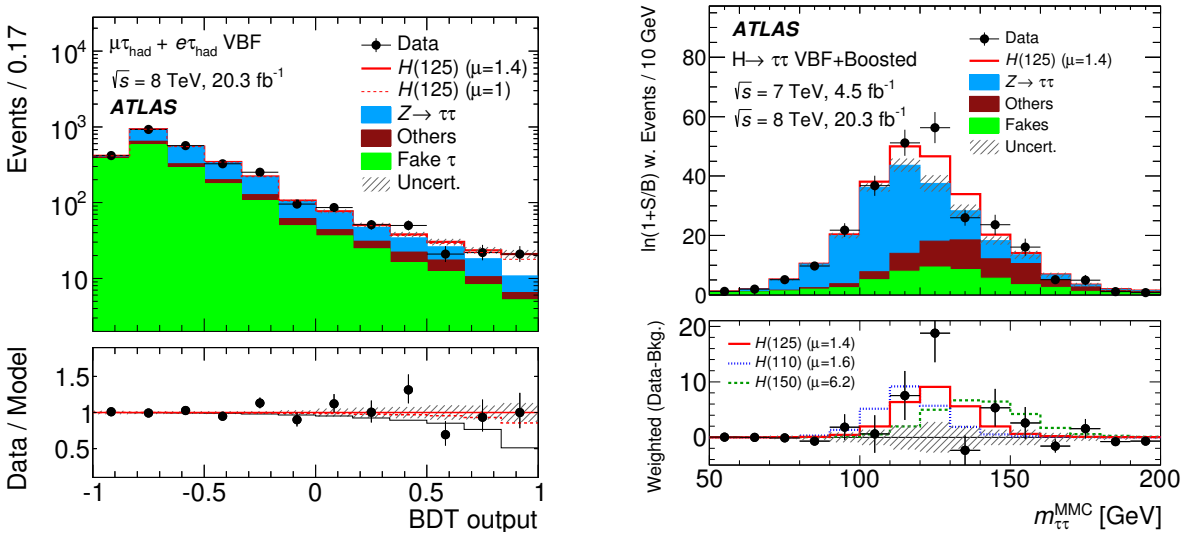

(a) (b)

Figure 8.3: Results of the MVA: (a) Distributions of the BDT discriminant for the VBF Category signal region in the $H \to \tau_{\text{lep}}\tau_{\text{had}}$ channel for data and the expected background based on the fit result in the $\sqrt{s} = 8$ TeV data set. The Higgs boson signal for a mass of $m_H = 125$ GeV is also shown with the SM signal strength ($\mu = 1$, dashed line) and the fit result ($\mu = 1.4$, solid line). The lower panel shows the ratio between data and the signal and background expectation with $\mu = 1.4$. Also the model with $\mu = 1$ (dashed line) and the background-only model are shown (black line).
(b) Distribution of the $m_{\tau\tau}$ mass combined for all $H \to \tau\tau$ channels and the $\sqrt{s} = 7$ TeV and $\sqrt{s} = 8$ TeV data sets. The observed data is compared to signal ($\mu = 1.4$) and background expectation obtained from the fit. All events are weighted by a factor ln(1+S/B), based on the signal (S) to background (B) ratio in each BDT bin. In the lower panel the difference between weighted data events and weighted background events is shown. Different signal hypotheses with masses 110 GeV (blue), 125 GeV (red) and 150 GeV (green), with the respective signal strengths obtained from the fit are shown. In both distributions the statistical and systematic normalisation uncertainties are indicated by the hashed band [136].

8.3 Comparison of Multivariate and Cut-Based Approaches

The cut-based and multivariate analyses constitute two conceptually different and partially complementary methods to search for a $H \to \tau\tau$ boson.

In the MVA new and more complex methods are implemented to search for a $H \to \tau\tau$ signal in data, while the CBA aims at the continuation of already established analysis methods in order to repeat the previous analysis of the first 13.0 fb^{-1} of 2012 data (Appendix C) on the full data sample.

Through the statistical learning algorithm the multivariate analysis takes into account the correlation of all selection variables simultaneously. This allows to optimise the selection in a way that multiple phase space regions with an accumulation of signal events can be included. Due to the sequential application of the selection criteria in the cut-based analysis, it is more limited in an inclusion of these multidimensional correlations and it rather focusses on the selection of the phase space region in each category where the highest signal-to-background ratio is expected.

Consequently, the multivariate analysis manages to achieve a higher sensitivity on the Higgs boson signal in data: The CBA expected significance is 2.5σ at $m_H = 125$ GeV, while the MVA expects a significance of 3.3σ at this mass in the combination of all $H \to \tau\tau$ decay channels in the $\sqrt{s} = 8$ TeV

data set (Fig. 8.1b).
Due to these different selection methods, also the resulting signal regions differ in both analyses. The cut-based analysis defines clear fiducial signal regions with a small number of events (Figs. 7.36 and 7.37). In contrast to that, the MVA signal regions include a much higher number of events, but a clear physical phase space region with a high number of signal events is not as well defined (Fig. 8.3a). The CBA is therefore also an important basis for future measurements of the fiducial or differential Higgs cross section in the $\tau\tau$ channel, where a clearly defined signal region is needed for which efficiencies and fiducial acceptance can be measured (as described in Chap. 6).

Another aspect in which the two analyses differ significantly, is the inclusion of the information on the mass of the Higgs boson. In the multivariate analysis the invariant $m_{\tau\tau}$ distribution is included in the set of observables of the BDT discriminant. The fit to data is based on the BDT discriminant, where the signal accumulates in a few bins with a high BDT output value which are not clearly associated with the information of the signal mass (Fig. 8.3a). Hence, the profile likelihood fit can not differentiate well between different mass hypotheses.

The cut-based analysis uses the $m_{\tau\tau}$ mass distribution as a basis for the fit and thus has a direct sensitivity to the Higgs mass: A deviation in data from the background model can be clearly assigned to a certain mass. As it has been shown in Figs. 8.1 and 8.2 the curve of measured p_0 and signal strength values as a function of m_H differs clearly for different masses and can be used to test the compatibility with different mass hypotheses.
This conceptual difference between the analyses is also visible in the weighted $m_{\tau\tau}$ distributions of the combined CBA and MVA results (Figs. 8.1a and 8.3b): The expected signals of different Higgs masses are more clearly separated from each other in the CBA distribution compared to the MVA one. Based on the results obtained with the CBA it can therefore be confirmed that the observed excess in data is most compatible with a Higgs boson with $m_H = 125$ GeV.

As it has been shown, both analyses play an important role in investigation of $H \to \tau\tau$ events in data. They provide an independent and complementary cross check of the obtained results, since they are two conceptually different measurements focussing on different phase spaces and with different dominating systematic uncertainties.

Figure 8.4 shows the resulting signal strength values obtained from the fit for $m_H = 125$ GeV for the MVA and CBA combination of all $H \to \tau\tau$ channels for the full $\sqrt{s} = 8$ TeV data set of 20.3 fb^{-1}. The result of the CBA in the $H \to \tau_{\text{lep}}\tau_{\text{had}}$ channel which has been investigated in this thesis (Chap. 7) is also included and for comparison also the MVA result in this channel is shown. In addition, the results for the individual fit of the respective VBF and Boosted Categories are included. The measured signal strengths are consistent between the different analyses, channels and categories and are all compatible with a Standard Model Higgs boson at $m_H = 125$ GeV. This adds further confidence in the obtained results[4].

In conclusion, both analysis methods find an excess in data with a compatible signal strength in 20.3 fb^{-1} data at $\sqrt{s} = 8$ TeV. This excess is compatible with a signal resulting from $H \to \tau\tau$ decays at a mass of $m_H = 125$ GeV. The observed signal strength is compatible with the prediction from the Standard Model.

This observation of $H \to \tau\tau$ decays provides the first evidence in ATLAS of a direct coupling of the recently discovered Higgs boson to fermions. The independent consistent results obtained with the

[4] Also a quantitative evaluation of the compatibility of CBA and MVA results is investigated [136]: By studying the correlations of both analyses depending on the overlap of the selected phase spaces with the help of the so-called Jackknife method [166], the uncertainty on the differences of the measured μ values, $\delta(\Delta\mu)$, can be derived. With the help of this method it is found that the results of both analyses are fully compatible, $\delta(\Delta\mu)$ is found to be smaller 1 for the individual $H \to \tau\tau$ channels and the combination of all.

MVA and CBA add further confidence in this observation. The analysis of the $H \to \tau_{\text{lep}}\tau_{\text{had}}$ channel presented in this thesis is the most sensitive channel of the combined CBA and thus provides an important contribution to this achievement.

The evidence for a direct coupling of a Higgs bosons to τ leptons at $m_H = 125$ GeV is also confirmed independently by CMS, where a signal strength of $\mu = 0.8 \pm 0.3$ is measured with a 3σ significance [167].

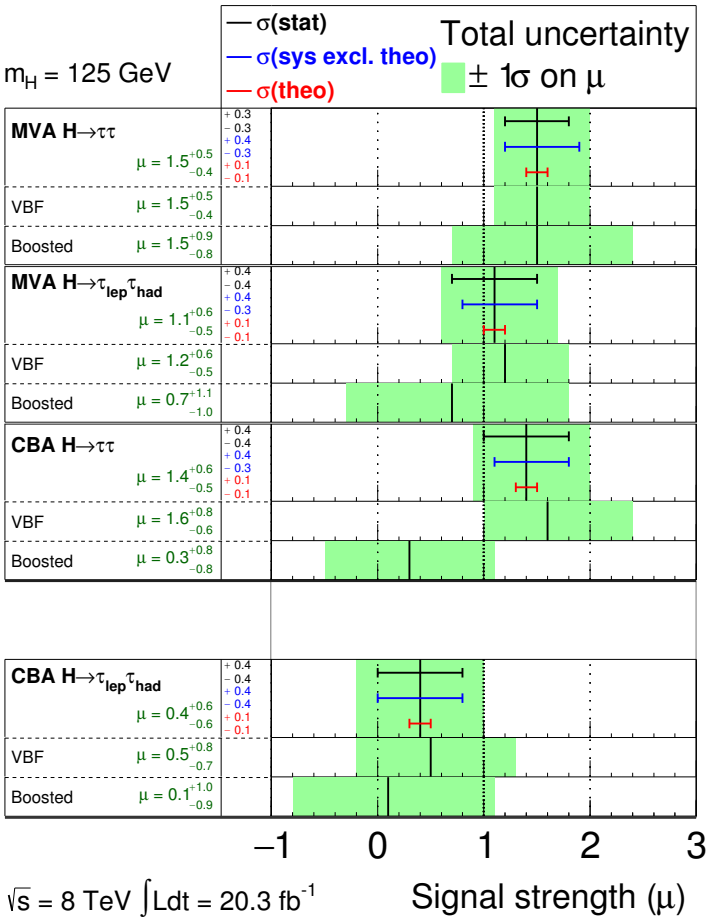

Figure 8.4: The best fit value of the signal strength μ for a Higgs boson with $m_H = 125$ GeV obtained for the combination of all $H \to \tau\tau$ channels with the MVA and CBA and the MVA $H \to \tau_{\text{lep}}\tau_{\text{had}}$ channel alone in the full $\sqrt{s} = 8$ TeV data for the Boosted and VBF Categories and combination of both [136]. These results are compared to the CBA results in the $H \to \tau_{\text{lep}}\tau_{\text{had}}$ channel investigated in this thesis. Shown are the total $\pm 1\sigma$ uncertainties (green band) on the signal strength and the error bars of the individual contributions from statistical (black), systematic (blue) and theory uncertainties (red).

CHAPTER 9

Improvements for Future $H \to \tau\tau$ Analyses

For future investigations of the $H \to \tau\tau$ decay the analysis concept presented in Chap. 7 provides an important basis. In the defined signal regions measurements of the total and differential cross section, the Higgs mass, spin or parity can be performed with the multiple times larger data sample planned to be collected in the next data taking periods of the LHC.

There are several possibilities for improvement in order to refine the $H \to \tau\tau$ analysis for future investigations with the same as well as with new data samples.

Improved background estimation For the combination of different $H \to \tau\tau$ analyses several improvements of the fake factor method have already been applied in the $H \to \tau_{\text{lep}}\tau_{\text{had}}$ analysis (Sec. 8.1). A further development in this direction could be the implementation of the fake factor method also for the Boosted Category to be able to estimate all $j \to \tau_{\text{had}}$ contributions directly from data. Moreover, a more realistic and less conservative estimation of the systematic uncertainty on the fake factor could be developed (compare Sec. 7.5) by evaluating the uncertainties on the fractional contribution of QCD, W, $Z \to \ell\ell$ and top events to the anti-ID sample and the effect on the final fake factor estimate. The fake factor method could also be extended to be able to include the low p_{T} leptons selected by the LTT trigger in the VBF Category to profit from the increase of signal acceptance (Sec. 7.3).

New categorisation The cut-based analysis is relatively limited in the selection of phase space regions due to the sequential application of selection criteria. In the future it could be adapted more to the concept of a multivariate event selection, which utilises correlations of variables to include as many signal-enriched phase space regions as possible with different purity. For this purpose the current categories of the cut-based analysis could be split further, in order to define tight signal regions with a very high signal-to-background ratio and looser ones which also contains a large number of signal events but are less pure. A first step in this direction, the splitting of the $H \to \tau_{\text{lep}}\tau_{\text{had}}$ VBF Category, has been introduced for the combination of all $H \to \tau\tau$ decay channels (Sec. 8.1). This analysis concept is discussed for a similar example in Appendix F.

Additional Higgs production topologies Another promising extension of $H \to \tau\tau$ analyses is the inclusion of another Higgs production topology: The Higgs production with an associated vector boson decaying to light leptons. The cross section times branching ratio of this process is much smaller compared to the other Higgs production mechanisms studied for $H \to \tau\tau$ decays. Moreover, the topology of this process is very different due to the additional leptons resulting

from the W or Z decay. Therefore it has not been explicitly investigated in the analysis of $H \to \tau\tau$ decays so far. The additional leptons in combination with the $H \to \tau\tau$ decay provide a very clean signature in the detector, which can be used to efficiently reject background and select a pure sample of these events. An inclusion of these VH($H \to \tau\tau$) signal processes could therefore contribute significantly to an improved sensitivity on the Higgs boson decaying to τ leptons. Moreover, it allows the definition of a signal region enriched with $H \to \tau\tau$ decays from the VH production mechanism. This is crucial for example for an analysis of the relative contributions of different Higgs production mechanisms to the total Higgs cross section and its coupling structure, i.e. the relative strength of the Higgs couplings to bosons and fermions.

In Sec. 9.1 a concept for the analysis of the Higgs production with an associated W or Z decay to leptons in the $H \to \tau_{\text{lep}}\tau_{\text{had}}$ decay mode is presented as a preparation for future analyses of this channel.

9.1 The $H \to \tau_{\text{lep}}\tau_{\text{had}}$ Decay in Association with a Leptonically Decaying Vector Boson

The studies of the VH($H \to \tau_{\text{lep}}\tau_{\text{had}}$) process are based on the investigated sample of 2012 data at $\sqrt{s} = 8$ TeV corresponding to an integrated luminosity of 20.3 fb^{-1}. The methods of the main $H \to \tau_{\text{lep}}\tau_{\text{had}}$ analysis (Chap. 7) are used as a starting point.

Since these studies are only a first approach without dedicated cross checks of all analysis methods, these studies are performed *blindly*, i.e. without comparing the expectation to data in the signal regions.

Signal and Background Processes

The Feynman graphs of the considered final states are shown in Fig. 9.1. In the associated production with a W boson (WH), one τ_{had}, two light leptons and $E_{\text{T}}^{\text{miss}}$ from the W and $H \to \tau_{\text{lep}}\tau_{\text{had}}$ decay are expected in the final state. For the production with an associated Z boson (ZH), the final state consists of three light leptons in addition to the τ_{had} and $E_{\text{T}}^{\text{miss}}$ only results from the neutrinos of the $H \to \tau_{\text{lep}}\tau_{\text{had}}$ decay. The momentum, invariant mass and charge correlations of the leptons can be used to associate them correctly to the Higgs or vector boson decay.

These final states with a τ_{had} and two or three leptons can be found in numerous sources of background: For the WH process, the WZ diboson decay is an irreducible background since it has exactly the same final state. Due to the large misidentification probability $j \to \tau_{\text{had}}$, the largest source of reducible background for WH are processes which have two genuine leptons and a misidentified τ_{had} candidate in the final state (Sec. 5.2). These final states occur in WW, $t\bar{t}$, single top with an associated W boson, $Z \to \ell\ell$ +jets and $Z \to \tau\tau$ +jets processes. The corresponding Feynman graphs can be found in Sec. 7.2. Less frequently the cases with one lost lepton (ZZ), or two or more misidentified τ_{had} candidates and light leptons (mainly W+jets, single top and $t\bar{t}$) contribute as sources of background. The ZH final state is identical to the one of a ZZ decay, except for the kinematic properties resulting from the H and Z mass differences. The WZ diboson decay contributes significantly if an additional jet is misidentified as the τ_{had} candidate. The prerequisite for other processes to contribute as background to ZH is the misidentification of at least two objects, usually one lepton and the τ_{had} candidate. These are mainly top processes, WW boson decays, $Z \to \ell\ell$ +jets and $Z \to \tau\tau$ +jets.

The background of QCD processes is not expected to contribute significantly as a background for WH and ZH, since three to four QCD jets would have to be misidentified as τ_{had} and light leptons, which is relatively unlikely.

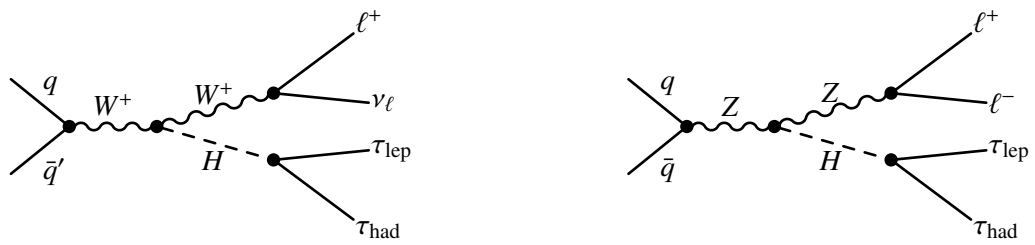

Figure 9.1: Schematic Feynman diagrams of the Higgs boson production in association with a leptonically decaying W (here W^+) and Z boson and the decay of the H boson to a hadronically and leptonically decaying pair of τ leptons. (a) Associated W boson decaying to a lepton and a neutrino, (b) associated Z boson decaying to a pair of leptons.

The samples used to investigate signal and background processes for this analysis are the same ones as in the main $H \to \tau_{\text{lep}}\tau_{\text{had}}$ analysis (Sec. 7.2) with one exception: A simulated sample is used for the estimation of the $Z \to \tau\tau$ background, since it includes also the $\tau_{\text{had}}\,\tau_{\text{had}}$ and $\tau_{\text{lep}}\,\tau_{\text{lep}}$ final states in contrast to the embedded sample (Sec. 4.3).

Object Selection and Mass Reconstruction

In order to select events with the WH and ZH signature, an adequate trigger selection and a preselection are applied which are basically the same as in the main $H \to \tau_{\text{lep}}\tau_{\text{had}}$ search (Sec. 7.3).

To trigger the events, the same mixture of a single lepton trigger (SLT) and a lepton and τ_{had} trigger (LTT) is applied. It is assumed that the lepton with the highest reconstructed p_{T} is the one that is subjected to the trigger requirements. Selecting only a single lepton on trigger level has the advantage, that the choice of offline p_{T} thresholds for the additional leptons are not restricted by the trigger thresholds. The LTT trigger allows to apply also a lower offline p_{T} threshold of the leading-p_{T} lepton.

The selection of physics objects (leptons and τ_{had} candidates), including an overlap removal between the objects, is also the same as in the main $H \to \tau_{\text{lep}}\tau_{\text{had}}$ analysis. The isolation requirement for the leptons is particularly important to suppress background processes with leptons within jets in W+jets, top and Z+jets processes. The following p_{T} thresholds are applied: The τ_{had} candidate is required to have $p_{\text{T}} > 25$ GeV to more strongly reduce the background of $j \to \tau_{\text{had}}$ misidentifications. The leading triggered electron (muon) is required to have a p_{T} between 20 (17) GeV and 26 GeV if the event was selected by the LTT trigger, and $p_{\text{T}} > 26$ GeV if it was selected by the SLT trigger. The sub-leading electrons (muons) are required to have $p_{\text{T}} > 15$ (10) GeV.

To define a sample of events with the WH signature, two leptons and a τ_{had} candidate passing these object requirements are selected. The lepton with the smaller p_{T} is associated to the Higgs boson decay (ℓ_H), since in general a smaller p_{T} is expected for the lepton resulting from the τ decay due to the additionally produced neutrino, in contrast to the lepton resulting from the W decay (ℓ_W)[1].

An event sample with the characteristics of ZH decays is defined by selecting three leptons and a τ_{had} candidate passing the object requirements (*ZH Category*). The pair of leptons that has the same flavour (ee or $\mu\mu$), opposite charge and an invariant mass closest to the Z boson mass is associated to the Z boson decay ($\ell_{Z,1}$, $\ell_{Z,2}$). The remaining lepton is assumed to result from the $H \to \tau_{\text{lep}}\tau_{\text{had}}$ decay (ℓ_H).

[1] This choice is correct in about 75% of the cases for the WH signal sample.

The calorimeter (track) isolation requirement on these two Z-decay leptons is loosened compared to Sec. 7.3: The additional energy deposition in a cone of radius $\Delta R = 0.2$ (0.4) around the lepton candidate is required to be less than 20%. This increases the acceptance of signal events and does not reduce the background rejection efficiency much.

The mass distributions of the $H \to \tau_{\text{lep}}\tau_{\text{had}}$ decay products provide the best separation from background, in particular the irreducible diboson decays. Therefore the mass distributions are used as a basis for the profile likelihood fit of data. For the ZH channel the invariant mass of the two τ leptons is reconstructed with the missing mass calculator from ℓ_H, τ_{had} and $E_{\text{T}}^{\text{miss}}$ (Sec. 7.3). This is not possible for the WH channel since the mass calculator assumes that $E_{\text{T}}^{\text{miss}}$ only results from the Higgs boson decay products, which is not the case for the WH production. Instead, the visible mass of the τ_{had} candidate and ℓ_H is used in the WH analysis channel. The resulting mass distributions in the signal samples and the irreducible diboson background in each of the two channels are shown in Fig. 9.2.

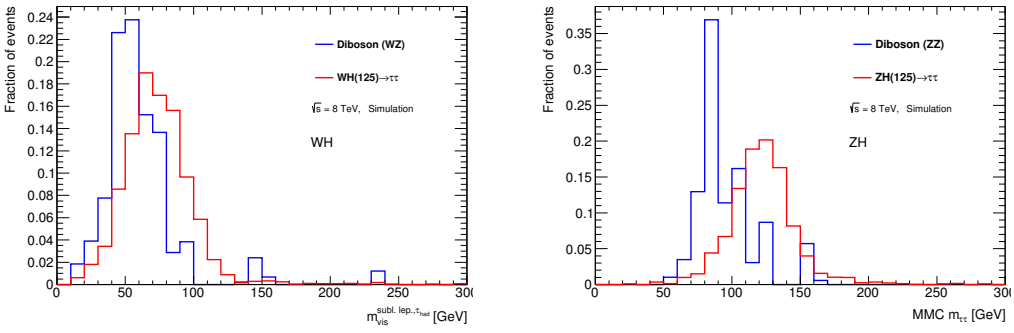

(a) (b)

Figure 9.2: (a) Shape of the visible mass of the τ_{had} candidate and the Higgs lepton ℓ_H in the WH channel for the signal and the irreducible WZ background. (b) Shape of the invariant $m_{\tau\tau}$ mass in the ZH channel for the signal and the ZZ background. The full event selection is applied.

Event Selection

After this preselection the samples are still dominated by background. Further criteria are applied to separate signal from background. The events with the WH signature are split further in two categories: The *WHsf Category* contains events with the same lepton flavour $ee\tau_{\text{had}}$ and $\mu\mu\tau_{\text{had}}$ while the *WHof Category* contains events with opposite flavour leptons ($e\mu\tau_{\text{had}}$). Since the $Z \to \ell\ell$ +jets background is only dominant in the first category, the selection can be adjusted individually in both categories.

In all categories (WHsf, WHof and ZH) a b-jet veto is applied to suppress the large background of top quark processes (Sec. 7.3). Furthermore, the pair of τ_{had} and ℓ_H associated to the $H \to \tau_{\text{lep}}\tau_{\text{had}}$ decay is required opposite charge (OS). Figures 9.3a and 9.3b show the charge correlations of leptons and τ_{had} in the WH Categories. It can be seen that opposite-sign ℓ_H and τ_{had} pairs are expected for signal, while for the $j \to \tau_{\text{had}}$ background processes no strong charge correlation is expected.

In the WHsf Category further selection criteria to suppress the large $Z \to \ell\ell$ background are applied: The missing transverse energy is required to be > 20 GeV and the visible mass of the two leptons ℓ_H and ℓ_W must lie outside the Z mass window ($80 > m_{\ell_H\ell_W} > 105$ GeV). As can be seen in Fig. 9.3b, an additional efficient rejection of $Z \to \ell\ell$ and top background can be achieved by making use of the charge correlation of the two leptons. For the WH signal it is expected that roughly half of the lepton pairs have the same charge ($\text{SS}_{\ell\ell}$), while for the $Z \to \ell\ell$ and top background processes the lepton pairs

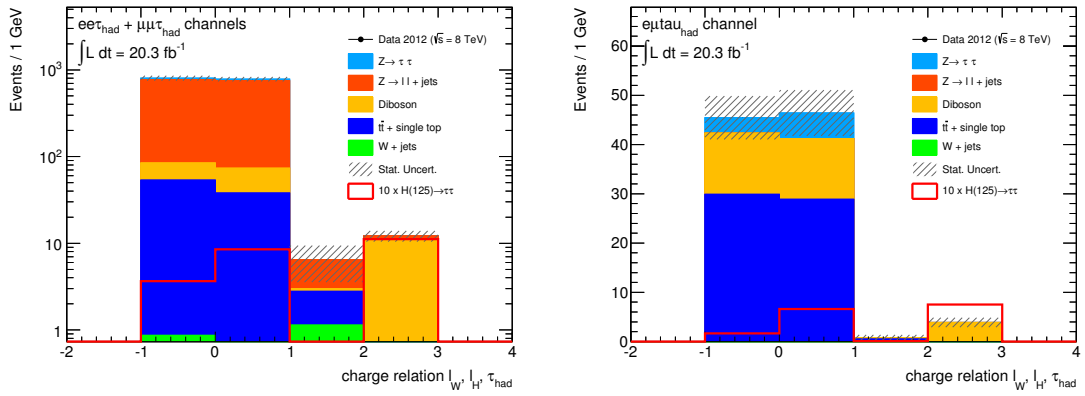

(a) (b)

Figure 9.3: The charge correlation of the objects expected for signal and background in (a) the WHsf Category in logarithmic scale and (b) the WHof Category in linear scale, after all selection criteria except for the charge correlation requirements are applied. The three objects are grouped into two pairs: τ_{had} and ℓ_H (OS or SS charge); ℓ_H and ℓ_W (OS$_{\ell\ell}$ or SS$_{\ell\ell}$ charge). The bins are filled in the following way: SS+OS$_{\ell\ell}$ (bin -1), OS+OS$_{\ell\ell}$ (bin 0), SS+SS$_{\ell\ell}$ (bin 1) and OS+SS$_{\ell\ell}$ (bin 2).

are expected to have mainly an opposite charge (OS$_{\ell\ell}$). Only events with the same charge of ℓ_H and ℓ_W are therefore selected in the WHsf Category.

In the WHof Category the dominating background processes are diboson, top and $Z \to \tau\tau$ after the previously described selection is applied. The τ_{had} p_{T} threshold is tightened to $p_{\text{T}} > 30$ GeV to reduce the $j \to \tau_{\text{had}}$ background. No requirement on the charge correlation of the two leptons is applied in this category. As can be seen in Fig. 9.3a, in this category the signal-to-background-ratio is relatively high for both SS$_{\ell\ell}$ and OS$_{\ell\ell}$ events, in contrast to the WHsf Category.

To increase the signal-to-background ratio in the ZH Category, the two leptons associated to the Z boson are required to have an invariant mass within $60 < m_{\ell_{Z,1}\ell_{Z,2}} < 120$ GeV. The requirement $E_{\text{T}}^{\text{miss}} > 20$ GeV reduces all background processes without neutrinos, i.e. all processes with Z bosons. Finally, it is required that the MMC algorithm successfully reconstructed a mass (Sec. 7.3).

Table 9.1 summarises the event selection for all categories. Figure 9.4 shows the expected mass distributions for signal and background after the event selection in the three analysis categories. Table 9.2 lists the numbers of signal and background events in each category expected in the 20.3 fb^{-1} sample at $\sqrt{s} = 8$ TeV after the full event selection. In all categories, in particular the WHsf and ZH Categories, a very high signal-to-background ratio is expected. However, only a small number of events is expected in total in the 20.3 fb^{-1} data sample. In addition, only a low number of simulated events used for the prediction of different background processes pass the full event selection. This results in relatively large statistical uncertainties and large background modelling uncertainties.

WHof Category	WHsf Category	ZH Category
b-jet veto	b-jet veto	b-jet veto
OS τ_{had}, ℓ_H	OS τ_{had}, ℓ_H	OS τ_{had}, ℓ_H
τ_{had} $p_{\text{T}} > 30$ GeV	$E_{\text{T}}^{\text{miss}} > 20$ GeV	$E_{\text{T}}^{\text{miss}} > 20$ GeV
$\sum p_{\text{T}}^{\ell_H,\ell_W} > 80$ GeV	$80 > m_{\ell_H\ell_W} > 105$ GeV	$60 < m_{\ell_{Z,1}\ell_{Z,2}} < 120$ GeV
	SS ℓ_H, ℓ_W	MMC $m_{\tau\tau}$ found

Table 9.1: Event selection for WHsf, WHof and ZH Categories in the analysis of the Higgs ($H \to \tau_{\text{lep}}\tau_{\text{had}}$) production in association with leptonically decaying vector bosons.

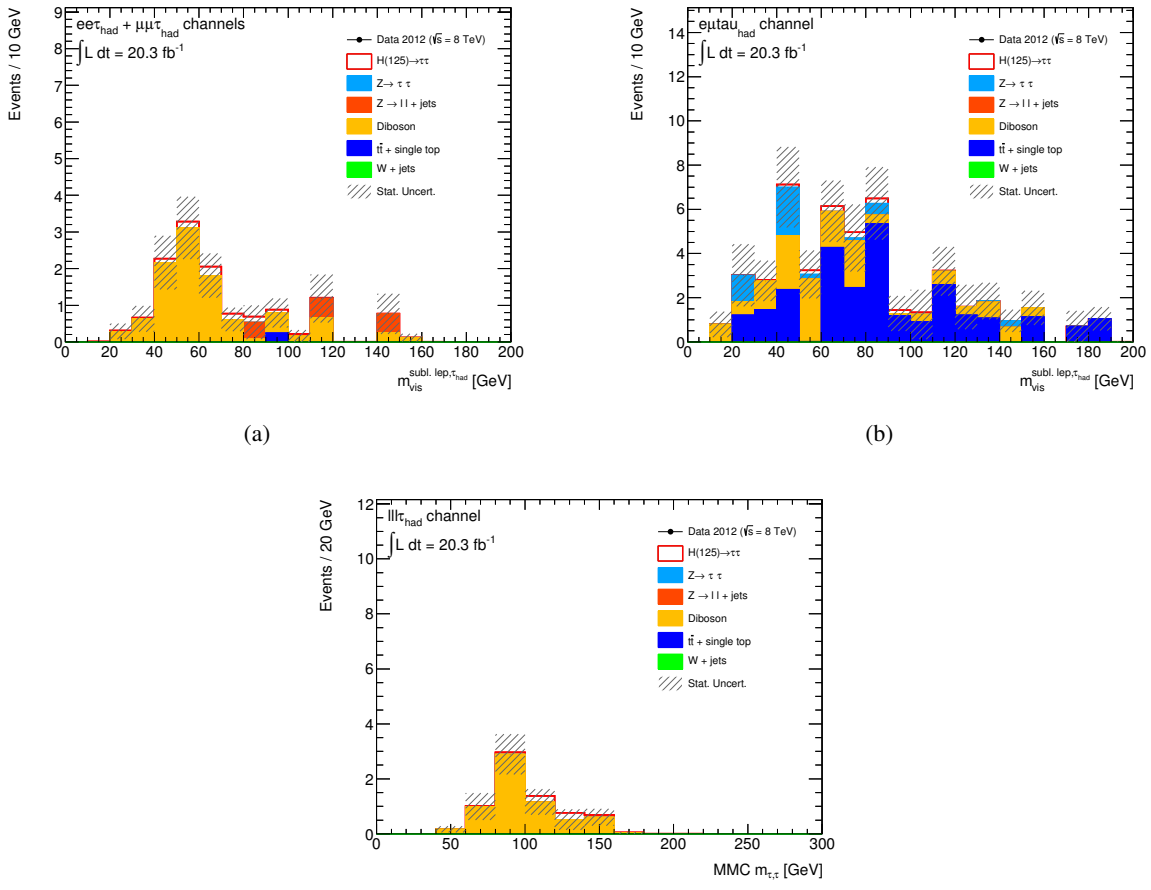

(a) (b)

(c)

Figure 9.4: Mass distributions of signal and background in the investigated VH($H \to \tau_{\text{lep}}\tau_{\text{had}}$) categories after the full event selection (Tab. 9.1) for an integrated luminosity of 20.3 fb^{-1} at $\sqrt{s} = 8$ TeV. Visible mass of τ_{had} and ℓ_H in (a) the WH same flavour Category and (b) the WH opposite flavour Category. (c) Invariant $m_{\tau\tau}$ mass calculated with the MMC algorithm in the ZH Category.

Process	Events		
	WHof	WHsf	ZH
WH($H \to \tau_{\text{lep}}\tau_{\text{had}}$)	1.30 ± 0.04	1.03 ± 0.04	0
ZH($H \to \tau_{\text{lep}}\tau_{\text{had}}$)	0.11 ± 0.01	0.08 ± 0.01	0.69 ± 0.02
other H($H \to \tau_{\text{lep}}\tau_{\text{had}}$)	0	0.01 ± 0.01	0
Diboson	16.45 ± 2.09	10.44 ± 1.50	6.57 ± 1.14
Top	28.62 ± 3.77	0.25 ± 0.24	0
$Z \to \tau\tau$	5.21 ± 1.97	0	0
$Z \to \ell\ell$ +jets	0	1.49 ± 0.86	0.02 ± 0.01
W+jets	0	0	0
Total background	50.28 ± 4.74	12.17 ± 1.75	6.59 ± 1.14

Table 9.2: Expected number of signal and background events including the statistical uncertainty after the full event selection (Tab. 9.1) for an integrated luminosity of 20.3 fb^{-1} at $\sqrt{s}$ = 8 TeV in the WHof, WHsf and ZH Categories. The signal samples are simulated with m_H = 125 GeV [2].

Background Estimation

In this first study of VH($H \to \tau_{\text{lep}}\tau_{\text{had}}$) processes, simulated samples are used for an estimation of the different background processes. A major part of the background processes includes a misidentified τ_{had} candidate. As has been outlined before (Sec. 7.5), these misidentification probabilities are often not well modelled by simulation. Therefore, control regions are defined in data which are dominated by these types of background.

A control region enriched by top processes is defined by inverting the b-tag veto in the two WH Categories. In addition, the charge correlation requirements are dropped to increase the number of events in this region. For the WHsf Category a $Z \to \ell\ell$ control region is defined in addition by requiring that both leptons have an invariant mass in the range $80 < m_{\ell_H\ell_W} < 105$ GeV and by dropping the charge correlation requirements.

The correction factors for the normalisation of the simulated samples found in these regions are: $k^{\text{top}}_{\text{WHsf}} = 1.11 \pm 0.13$, $k^{\text{top}}_{\text{WHof}} = 0.89 \pm 0.13$ and $k^{Z\to\ell\ell+\text{jets}}_{\text{WHsf}} = 0.74 \pm 0.01$. They are applied to the background samples in this analysis. Figure 9.5 shows two examples for distributions of two kinematic variables in these control regions in data, compared to simulation after the correction factors are applied. A reasonable agreement can be observed between data and simulation.

The contribution of QCD background to the selected WH and ZH samples is expected to be small, since at least three jets would have to be misidentified as τ_{had} and leptons. To test this a data control region can be defined for the WH Categories by requiring all objects to have the same charge (Fig. 9.3). The number of expected signal events is negligible in this region. If all objects are misidentified jets as it is the case for the QCD background, this charge correlation should occur as often as the other ones. The number of events expected by simulation in this control sample is compared to data. No significant excess in data can be observed, which verifies, that the contribution in the signal region of QCD background can be neglected.

The above described methods to correct the normalisation of the simulated samples do not solve the problem of the small number of simulated events in the studied signal regions. To reduce the large

[2] The remaining diboson background is constituted mainly of the irreducible background processes in each channel (WZ in the WHsf and WHof Categories and ZZ in the ZH Category).

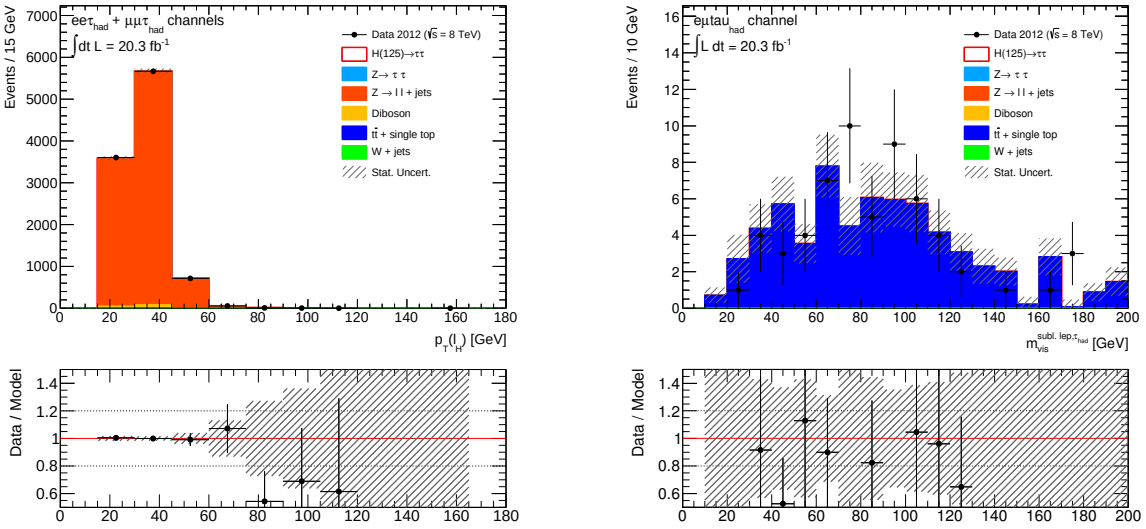

(a) (b)

Figure 9.5: Comparison of data and simulation in two background control regions of the WH Categories for 20.3 fb^{-1} data sample with $\sqrt{s}$ = 8 TeV. (a) ℓ_H transverse momentum distribution in the $Z \to \ell\ell$ +jets control region of the WHsf Category, (b) visible mass of τ_{had} and ℓ_H in the top control region of the WHof Category. The normalisation of simulation is adjusted to the one in data.

systematic uncertainties and get a more reliable estimate of these background processes, the background estimation for a more sophisticated analysis of the VH($H \to \tau_{\text{lep}}\tau_{\text{had}}$) processes should be based as completely as possible on data (see discussion at the end of this section).

Expected Sensitivity

Based on the mass distributions in Fig. 9.4, a first estimate of the expected sensitivity of this analysis to a Higgs signal is performed with the profile likelihood fit (Sec. 4.2.2).

The same experimental and theoretical uncertainties as in the main $H \to \tau_{\text{lep}}\tau_{\text{had}}$ analysis are included (Sec. 7.7). For the correction of top and $Z \to \ell\ell$ +jets background in the WH channel, the statistical uncertainties of the correction factors are taken as systematic uncertainty on the normalisation correction. In addition, a 30% uncertainty is assumed for all background predictions that are completely based on simulation and are not validated in a data control region[3].

The expected upper limits at 95% CL on the Higgs cross section times branching ratio with respect to the Standard Model prediction in a data sample corresponding to an integrated luminosity of 20.3 fb^{-1} at $\sqrt{s}$ = 8 TeV are shown in Fig. 9.6 as a function of m_H. Included are the results obtained from the combined fit of all categories and the individual fit of WH and ZH Categories.

At a Higgs mass of m_H = 125 GeV the combined expected upper limit is $3.87 \times \sigma_{\text{SM}}$. The fit of the ZH Category yields an expected limit of $5.80 \times \sigma_{\text{SM}}$, and for the WH Category the expected limit is $6.18 \times \sigma_{\text{SM}}$.

If only the statistical uncertainty of the number of events in the selected sample and the statistical uncertainty on the background prediction are included, the expected limit at m_H = 125 GeV is $3.39 \times \sigma_{\text{SM}}$

[3] The binning used for the mass distributions is essentially the one shown in Fig. 9.4, but the bins at the sides are merged to avoid empty bins.

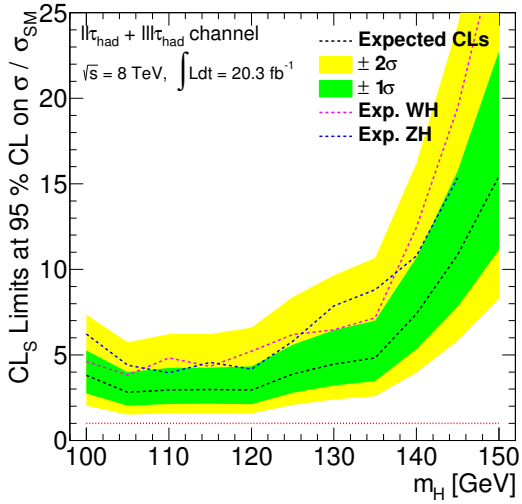

Figure 9.6: Expected upper CL_S limit on the $H \to \tau_{lep}\tau_{had}$ cross section time branching ratio at 95% CL for the analysis of the $H \to \tau_{lep}\tau_{had}$ decay in the production with an associated leptonically decaying vector boson (black line) as a function of m_H at 20.3 fb^{-1} with $\sqrt{s}$ = 8 TeV. The ± 1 (2)σ errors are shown as green (yellow) error bands. Also shown are the limits obtained for the individual analysis of the ZH (blue) and WH (pink) Categories.

($5.60 \times \sigma_{SM}$ for the ZH Category and $5.19 \times \sigma_{SM}$ for the WH Category). This shows that the resulting sensitivity on a $H \to \tau_{lep}\tau_{had}$ signal is mainly limited by the low number of events in the selected sample and the low number of simulated events used to estimate the background model in this analysis.

Summary

These studies of the $H \to \tau_{lep}\tau_{had}$ decay modes with an associated W or Z boson shows that very pure signal samples can be selected and a relatively high sensitivity to a $H \to \tau\tau$ signal in data can be achieved.

Several problems are also revealed by these studies for an analysis of this process in 20.3 fb^{-1} data: The number of selected events is very small, resulting in large statistical uncertainties. Moreover, due to the small statistics of the simulated samples the uncertainty on the background estimation is relatively large. Consequently, this first analysis concept has still room for improvement. Several aspects that can be investigated in more detail to obtain an improved result are summarised in the following.

Most importantly, to reduce the large uncertainties on the background estimation, a more accurate estimation of the $j \to \tau_{had}$ and $j \to \ell$ background processes should be developed which is fully based on data. A good approach is a fake factor method (Sec. 7.5) where the τ_{had} identification or lepton isolation requirements are inverted to define a control region and the number of misidentified τ_{had} or leptons in the signal region is estimated with a set of fake factors. This method is in particular well suited, since the statistics in these control regions are usually much higher compared to the signal region (Sec. 7.5). However, the fake factor method needed for this analysis is more complex compared to the main $H \to \tau_{lep}\tau_{had}$ analysis, since often multiple misidentified objects occur. Therefore, also a correct combination of these fake factors must be taken care of. First studies of a fake factor method for the VH($H \to \tau\tau$) are already ongoing [168].

With a better estimate of the $j \to \tau_{had}$ and $j \to \ell$ background, also the p_T thresholds of the considered objects that are not limited by the trigger thresholds can possibly be lowered in order to increase the

signal yield and statistics in the selected WH and ZH signal regions.

In addition, the choice of triggers could be investigated for this final state. For instance, the use of a dilepton trigger instead of a lepton-τ_{had} trigger allows low trigger p_{T} thresholds for both the leading and sub-leading lepton as well. At the same time systematic uncertainties arising from the modelling of the τ_{had} trigger component could be avoided.

In conclusion, the first studies presented in this chapter show that a dedicated analysis of $H \to \tau\tau$ decays in association with a leptonically decaying W or Z boson is worthwhile. The inclusion of VH enriched signal regions could be a promising addition for future $H \to \tau\tau$ analyses. In particular it can be used to investigate this production mechanism individually for a measurement of the relative Higgs coupling strengths and cross sections.

CHAPTER 10

Conclusion

A milestone in particle physics has been reached by the discovery of the Higgs boson at a mass of 125 GeV with the CMS and ATLAS experiments in 2012, which shows properties consistent with the predictions of the Standard Model. Since initially the Higgs boson was only observed through the decay to bosons, it was of prime importance to also provide evidence for a direct coupling of the Higgs boson to fermions and thus to confirm another important prediction of the Standard Model. The most prominent fermionic decay mode that can be investigated at the LHC is the Higgs decay to a pair of τ leptons.

In this thesis the decay of the Higgs boson to a hadronically and leptonically decaying pair of τ leptons in ATLAS has been investigated. This analysis provides the largest Higgs signal sensitivity of all $\tau\tau$ decay modes since it has the largest branching ratio and a clear signature in the detector. The analysis of this decay channel is challenging due to the significant missing transverse energy in the final state and the hadronically decaying τ lepton. This results in a relatively low invariant mass resolution and a large background of processes with quark-gluon jets in addition to the irreducible $Z \to \tau\tau$ background.

A second analysis performed in this thesis was the measurement of the W production cross section with the subsequent decay $W \to \tau\nu_\tau$. It was the first measurement of this process at the LHC and complemented the measurement of the W production cross section at ATLAS. Moreover, the $W \to \tau\nu_\tau$ decay has the same signature of $E_{\mathrm{T}}^{\mathrm{miss}}$ and τ leptons in the final state as the $H \to \tau\tau$ decay. Due to its large cross section it was one of the first physics processes in which the reconstruction and identification methods of $E_{\mathrm{T}}^{\mathrm{miss}}$ and hadronically decaying τ leptons could be investigated. This measurement therefore provided an important preparation for the $H \to \tau\tau$ search.

The precision of these two analyses strongly depends on the accuracy and efficiency of the missing transverse energy reconstruction and identification of hadronically decaying τ leptons. Several studies of these aspects have been performed in this thesis as a preparation for these physics measurements. The reconstruction of $E_{\mathrm{T}}^{\mathrm{miss}}$ in events with hadronically decaying τ leptons has been optimised, which allowed for an improved reconstruction of $E_{\mathrm{T}}^{\mathrm{miss}}$ and resulted in a better resolution of the invariant $m_{\tau\tau}$ mass. Furthermore, a method to measure the misidentification probability of electrons as hadronically decaying τ leptons in data was developed.

The measurement of the $W \to \tau\nu_\tau$ cross section was based on a data set collected in 2010 at a centre-of-mass energy of $\sqrt{s} = 7$ TeV corresponding to an integrated luminosity of 34 pb^{-1}. An efficient trigger and offline event selection has been developed to reject the large background of QCD processes and other W/Z decays, and to select a pure sample of $W \to \tau\nu_\tau$ events. Data-driven methods have been

implemented to estimate and validate the contribution of these background processes.

The product of the W production cross section and the $W \to \tau\nu_\tau$ branching ratio was measured to be $\sigma_W^{\text{tot}} \times \text{BR}(W \to \tau\nu_\tau) = (11.1 \pm 0.3\,(\text{stat.}) \pm 1.7\,(\text{syst.}) \pm 0.4\,(\text{lumi.}))\,\text{nb}$. The cross section is measured in a region of high detector acceptance and then extrapolated to the full phase space. This result is in good agreement with the theoretical prediction and the measurements performed in the $W \to e\nu_e$ and $W \to \mu\nu_\mu$ decay channels. As explained above this measurement constituted an important achievement in the starting phase of the LHC physics program.

The search for the $H \to \tau_{\text{lep}}\tau_{\text{had}}$ decay was performed with a data set taken in 2012 at $\sqrt{s} = 8$ TeV corresponding to an integrated luminosity of 20.3 fb^{-1}. The events were grouped into separate categories in order to exploit different kinematic and topological properties of the $H \to \tau_{\text{lep}}\tau_{\text{had}}$ signal. In one of the categories events with the typical properties of a $H \to \tau_{\text{lep}}\tau_{\text{had}}$ decay resulting from VBF production have been selected and a very high signal-to-background ratio was achieved. In another category events with a significant transverse momentum of the Higgs boson have been selected which resulted in a better resolution of $m_{\tau\tau}$. Mostly data-driven methods have been developed to estimate the background composition in these categories. The $m_{\tau\tau}$ distributions of the categories were compared to the signal and background predictions with a profile likelihood fit. A deviation from the predicted background-only hypothesis is observed in data with a maximum at $m_H = 125$ GeV of 1σ. The expected significance was found to be 1.7σ at this mass. The ratio of the measured signal yield to the Standard Model expectation at $m_H = 125$ GeV is determined as $\mu = 0.4 \pm 0.4\,(\text{stat.}) \pm 0.4\,(\text{syst.}) \pm 0.1\,(\text{theo.})$. These results are consistent with the expectation of the Standard Model for $H \to \tau\tau$ decays at this mass.

Also a combination of the results obtained in all three $H \to \tau\tau$ decay channels has been performed [136]. The $H \to \tau_{\text{lep}}\tau_{\text{had}}$ analysis is the major contributing channel, since it has the highest sensitivity of all $H \to \tau\tau$ decay modes. In the combination of all three $H \to \tau\tau$ analyses an excess in data with an observed (expected) significance of 3.2 (2.5) σ and a measured relative signal strength of $\mu = 1.4 \pm 0.4\,(\text{stat.})\,^{+0.4}_{-0.3}\,(\text{syst.}) \pm 0.1\,(\text{theo.})$ has been found. This is also consistent with the predicted coupling of the discovered Higgs boson to fermions in the Standard Model. An independent multivariate analysis of $H \to \tau\tau$ decays, which has been performed in parallel, has obtained a compatible result. This observation of $H \to \tau\tau$ decays provides evidence of a direct coupling of the discovered Higgs boson at $m_H = 125$ GeV to fermions in ATLAS and is another important verification of the predictions of the Standard Model. The $H \to \tau_{\text{lep}}\tau_{\text{had}}$ analysis performed in this thesis provides an important contribution to this achievement.

Finally, it was found in this thesis that a promising addition for future $H \to \tau\tau$ analyses could be the inclusion of signal processes resulting from a Higgs production in association with a vector boson decaying to one or two leptons. In particular, it could be used to investigate this production mechanism individually for a measurement of the relative Higgs coupling strengths and cross sections.

In the next data taking periods of the LHC, precision measurements of Higgs properties such as differential and fiducial cross sections, the Higgs mass, spin and parity can be performed using $H \to \tau\tau$ decays. The $H \to \tau_{\text{lep}}\tau_{\text{had}}$ analysis methods and defined signal region presented in this thesis provide an important basis for such measurements.

APPENDIX A

Variable Definitions for τ_{had} Identification Algorithms

This appendix gives a detailed overview of the variables defined for the τ_{had} identification algorithms to discriminate against QCD jets and light leptons.

Discrimination against QCD jets

The following variables are used in the τ_{had} identification algorithm to discriminate against the background of QCD jets [99, 101, 104, 105, 107]:

Cluster mass The invariant mass computed from associated topological clusters (m_{clusters}).

Track mass The invariant mass of the track system (m_{tracks}), where both core and isolation tracks are used for the invariant mass calculation (Sec. 5.2).

Track radius The p_{T}-weighted distance of track:

$$\text{R}_{\text{track}} = \frac{\sum_i^{\Delta R_i<0.4} p_{\text{T},i}\Delta R_i}{\sum_i^{\Delta R_i<0.4} p_{\text{T},i}} \tag{A.1}$$

where i runs over the core and isolation tracks associated to the τ_{had} candidate, ΔR_i is defined relative to the τ_{had} axis and $p_{T,i}$ is the track transverse momentum.

Leading track momentum fraction Defined as:

$$f_{\text{track}} = \frac{p_{\text{T,lead}}^{\text{track}}}{p_{\text{T}}^{\tau}} \tag{A.2}$$

where $p_{\text{T,lead}}^{\text{track}}$ is the transverse momentum of the leading core track of the τ_{had} candidate and p_{T}^{τ} is the transverse momentum of the τ_{had} candidate. For 2012 data the sum of the transverse energy calibrated at EM scale deposited in a cone of $\Delta R < 0.2$ around the τ_{had} axis is used instead in the denominator. In addition, a pile-up correction is applied in this case:

$$f_{\text{track}}^{\text{corr}} = f_{\text{track}} + 0.003 \cdot N_{\text{vtx}} \tag{A.3}$$

where N_{vtx} is the number of well-reconstructed vertices in the event.

Electromagnetic radius The transverse-energy-weighted shower width in the electromagnetic calorimeter:

$$R_{\text{EM}} = \frac{\sum_i^{\Delta R_i<0.4} E_{\text{T},i}^{\text{EM}} \Delta R_i}{\sum_i^{\Delta R_i<0.4} E_{\text{T},i}^{\text{EM}}} \tag{A.4}$$

where i runs over cells in the first three layers of the ECal associated to the τ_{had} candidate, ΔR_i is the distance of the cell relative to the τ_{had} axis and $E_{\text{T},i}^{\text{EM}}$ is the cell transverse energy at EM scale.

Calorimetric radius The transverse energy weighted shower width in the electromagnetic and hadronic calorimeter:

$$R_{\text{Cal}} = \frac{\sum_i^{\Delta R_i<0.4} E_{\text{T},i} \Delta R_i}{\sum_i^{\Delta R_i<0.4} E_{\text{T},i}} \tag{A.5}$$

where i runs over cells in the ECal and HCal associated to the τ_{had} candidate, ΔR_i is the distance of the cell relative to the τ_{had} axis and $E_{\text{T},i}$ is the cell transverse energy at EM scale.

Core energy fraction The fraction of transverse energy in the core ($\Delta R < 0.1$) of the τ_{had} candidate (also called *centrality fraction*) :

$$f_{\text{core}} = \frac{\sum_i^{\Delta R<0.1} E_{\text{T},i}}{\sum_i^{\Delta R<0.4(0.2)} E_{\text{T},i}} \tag{A.6}$$

where i runs over the energy at EM scale deposited in all cells associated to the τ_{had} candidate within ΔR_i of the τ_{had} axis. The cone size considered in the denominator is reduced to 0.2 in 2012 data. An additional pile-up correction for τ_{had} candidates with $p_{\text{T}} < 80$ GeV is applied:

$$f_{\text{core}}^{\text{corr}} = f_{\text{core}} + 0.003 \cdot N_{\text{vtx}} \tag{A.7}$$

where N_{vtx} is the number of well-reconstructed vertices in the event.

Electromagnetic fraction The fraction of transverse energy of the τ_{had} candidate deposited in the ECal:

$$f_{\text{EM}} = \frac{\sum_i^{\Delta R_i<0.4(0.2)} E_{\text{T},i}^{\text{EM}}}{\sum_j^{\Delta R_i<0.4(0.2)} E_{\text{T},j}} \tag{A.8}$$

where $E_{\text{T},i}$ ($E_{\text{T},j}$) is the transverse energy, calibrated at the EM scale, deposited in cell i (j), and i runs over the cells in the three layers of the ECal, while j runs over the cells in all layers of the calorimeter. From 2011 onwards the sum of the transverse energy calibrated at EM scale deposited in a smaller cone of $\Delta R < 0.2$ around the τ_{had} axis is used for the calculation.

Leading clusters energy fraction $f_{3\text{ lead clusters}}$, the fraction of transverse energy of the first three leading clusters with respect to the total energy of all clusters associated to the τ_{had} candidate.

Transverse flight path significance The decay length significance of the τ_{had} decay vertex for multi-prong τ_{had} candidates in the transverse plane:

$$S_{\text{T}}^{\text{flight}} = \frac{L_{\text{T}}^{\text{flight}}}{\delta L_{\text{T}}^{\text{flight}}} \tag{A.9}$$

where $L_{\mathrm{T}}^{\mathrm{flight}}$ is the reconstructed signed decay length, and $\delta L_{\mathrm{T}}^{\mathrm{flight}}$ is its estimated uncertainty.

Leading track impact parameter significance The impact parameter of the leading track of the τ_{had} candidate:

$$S_{\mathrm{leadtrk}} = \frac{d_0}{\delta d_0} \tag{A.10}$$

where d_0 is the distance of closest approach of the track to the τ_{had} vertex in the transverse plane, and δd_0 its estimated uncertainty.

Number of tracks in outer isolation cone $N_{\mathrm{track}^{\mathrm{iso}}}$, the number of tracks reconstructed within $0.2 < \Delta R < 0.4$ around the τ_{had} axis.

Maximum ΔR ΔR_{max} denotes the maximum distance between a track in the core-cone associated to the τ_{had} candidate and the τ_{had} axis.

Track and π^0 mass $m_{\pi^0+\mathrm{tracks}}$ denotes the invariant mass of all tracks and all reconstructed pi_0 mesons associated to the τ_{had} candidate within the core-cone.

Number of π^0 mesons N_{π^0}, the number of π^0 mesons in the core-cone.

Track and $\pi^0 p_{\mathrm{T}}$ fraction $p_{\mathrm{T}}^{\pi^0+\mathrm{tracks}}/p_{\mathrm{T}}^{\tau_{\mathrm{had}}}$ denotes ratio of the momentum of all tracks and all reconstructed π_0 mesons associated to the τ_{had} candidate within the core-cone to the total τ_{had} momentum.

A overview of the variables used for the BDT identification algorithm in the different data sets analysed in this thesis is shown in Tab. A.1.

Variable	Cut-based 2010	BDT 2010		BDT 2011		BDT 2012	
		1-prong	3-prong	1-prong	3-prong	1-prong	3-prong
$f_{\text{track}}^{\text{corr}}$						•	•
f_{track}		•	•	•	•		
$f_{\text{core}}^{\text{corr}}$						•	•
f_{core}	•	•	•	•	•		
R_{track}	•	•	•	•	•	•	•
S_{leadtrk}				•	•	•	
$N_{\text{track}^{\text{iso}}}$				•	•	•	
ΔR_{max}					•		•
$S_{\text{T}}^{\text{flight}}$			•		•		•
m_{tracks}			•		•		•
m_{clusters}		•	•	•	•		
R_{EM}	•	•	•				
R_{Cal}				•	•		
f_{EM}		•	•				
$f_{\text{3 lead clusters}}$				•	•		
$m_{\pi^0\text{+tracks}}$						(•)	(•)
N_{π^0}						(•)	(•)
$p_{\text{T}}^{\pi^0\text{+tracks}}/p_{\text{T}}^{\tau_{\text{had}}}$						(•)	(•)

Table A.1: Identification variables used for the BDT and cut-based identification method for the different investigated data sets of 2010, 2011 and 2012. The variables in brackets are only included in the $H \to \tau\tau$ analysis of the full 2012 data (20.3 fb^{-1}).

Discrimination against leptons

The following variables are defined to discriminate genuine τ_{had} candidates against electrons and muons [99, 104, 106, 107]:

TRT HT fraction f_{HT}, the ratio of high-threshold to low-threshold hits in the TRT for the leading p_{T} track in the core cone of the τ_{had} candidate. This variable can only be calculated within $|\eta| < 1.7$, the coverage of the TRT.

Secondary energy deposits $E_{\text{strip}}^{\text{max}}$, the maximum energy in three cells summed over ϕ in the strip layer of the ECal around the impact point of the leading τ_{had} track. The energy associated to the leading track is excluded. The variable is only calculated for $|\eta| \leq 1.7$, where the TRT provides discrimination power for electrons and hadrons.

ECal energy fraction The ratio between energy in the ECal and leading track momentum,

$$f_{\text{EM}}^{\text{track}} = \frac{\sum_{l}^{\Delta R<0.4(0.2)} E_{\text{T},l}^{\text{EM}}}{p_{\text{T}}^{\text{leadtrk}}} \tag{A.11}$$

where l runs over the cells associated to the τ_{had} candidate in the ECal and $p_{\text{T}}^{\text{leadtrk}}$ denotes the transverse momentum of the leading track of the τ_{had} candidate in the core region. Due to higher pile-up the cone size for the considered clusters was lowered to $\Delta R < 0.2$ in 2011.

Hadronic energy fraction The ratio between energy in the hadronic calorimeter and leading track momentum,

$$f_{\text{Had}}^{\text{track}} = \frac{\sum_{l}^{\Delta R<0.4(0.2)} E_{\text{T},l}^{\text{Had}}}{p_{\text{T}}^{\text{leadtrk}}} \tag{A.12}$$

where l runs over the cells associated to the τ_{had} candidate in the first layer of the hadronic calorimeter and $p_{\text{T}}^{\text{leadtrk}}$ denotes the transverse momentum of the leading track of the τ_{had} candidate in the core region. Due to higher pile-up the cone size for the considered clusters was lowered to $\Delta R < 0.2$ in 2011.

Presampler strip energy fraction The fraction of energy of the calorimetric clusters deposited in the presampler,

$$f_{\text{PS}} = \frac{\sum_{l=0}^{N_{\text{clus}}} E_{l}^{\text{PS}}}{\sum_{l=0}^{N_{\text{clus}}} E_{l}} \tag{A.13}$$

where l runs over the calorimeter clusters associated to the τ_{had} candidate, E_{l}^{PS} is the part of the cluster energy deposited in the presampler layer, and E is the total energy of a calorimeter cluster.

Charged pions fraction The ratio between the energy of charged pions in the ECal and the total ECal energy,

$$f_{\text{EM}}^{\pi^{\pm}} = \frac{\sum_{i}^{N_{\Delta R<0.2}} p_{i}^{\text{trk}} - \sum_{l=0}^{N_{\text{clus}}} E_{l}^{\text{Had}}}{\sum_{l=0}^{N_{\text{clus}}} E_{l}^{\text{EM}}} \tag{A.14}$$

where l runs over the calorimetric clusters associated to the τ_{had} candidate. E_{l}^{Had} denotes the energy deposited in the HCal for each cluster, while E_{l}^{EM} denotes the energy deposited in the ECal. i runs over the tracks associated to the τ_{had} candidate in the core region and p_{i}^{trk} denotes the track momentum.

Ring isolation The energy fraction of the τ_{had} candidate deposited in the inner cone around the τ_{had} axis,

$$f_{\text{iso}} = \frac{\sum_i^{N_{0.1<\Delta R_i<0.2}} E_{\text{T},i}}{\sum_j^{\Delta R_j<0.4(0.2)} E_{\text{T},j}} \tag{A.15}$$

Here E_{T} denotes the transverse energy calibrated at EM scale that is deposited in the calorimeter cells of the clusters associated to the τ_{had} candidate. In the numerator the sum runs over all cells of the clusters within $0.1 < \Delta R_i < 0.2$, while in the denominator the cells of the clusters within a cone of $\Delta R_j < 0.4$ are summed. Due to higher pile-up the cone size for the considered clusters was lowered to $\Delta R < 0.2$ in the denominator in 2011.

Hadronic radius The transverse-energy-weighted shower width in the hadronic calorimeter,

$$\text{R}_{\text{Had}} = \frac{\sum_i^{\Delta R_i<0.4(0.2)} E_{\text{T},i}^{\text{Had}} \Delta R_i}{\sum_i^{\Delta R_i<0.4(0.2)} E_{\text{T},i}^{\text{Had}}} \tag{A.16}$$

where i runs over cells in the hadronic calorimeter and the third layer of the ECal associated to the τ_{had} candidate, ΔR_i is the cell distance relative to the τ_{had} axis and $E_{\text{T},i}^{\text{Had}}$ is the cell transverse energy at EM scale. Due to higher pile-up the cone size for the considered clusters was lowered to $\Delta R < 0.2$ in 2011.

Table A.2 gives an overview over the variables used in the cut-based and BDT electron and muon veto.

Variable	BDT e-veto (1-prong)	cut-based e-veto (1-prong)	μ-veto
$f_{\text{track}}^{(\text{corr})}$	•		
f_{track}			•
$f_{\text{core}}^{(\text{corr})}$	•		
R_{track}	•		
f_{EM}	•		•
f_{HT}	•	•	
$E_{\text{strip}}^{\text{max}}$	•	•	
$f_{\text{Had}}^{\text{track}}$	•	•	
$f_{\text{EM}}^{\text{track}}$	(•)	•	
f_{PS}	(•)		
$f_{\text{EM}}^{\pi^{\pm}}$	(•)		
f_{iso}	•		
R_{Had}	•		

Table A.2: Variables used for the BDT and cut-based electron-veto and the muon veto. The variables in brackets and the pile-up correction for f_{track} and f_{core} were only added for 2012 data analyses.

APPENDIX B

Validation of the Background Estimation in the $W \to \tau\nu_\tau$ Analysis

In this appendix, further investigated distributions for a verification of the background modelling in the $W \to \tau\nu_\tau$ cross section measurement (Chap. 6) are included. Figure B.1 shows the distribution of the τ_{had} identification BDT discriminant for events in combined signal and background regions A and C. τ_{had} candidates in signal region A are identified by the medium BDT τ_{had} identification, while events in the control region C pass the looser BDT τ_{had} selection (see Secs. 6.3 and 6.4 for details).

Figure B.2 shows the distribution of several characteristic kinematic quantities in the selected signal region in data and the expected signal and background. The statistical and systematic uncertainties (Sec. 6.7) of the signal and background models are also included in the distributions.

Figure B.3 shows several kinematic quantities for the analysis performed using the cut-based τ_{had} identification instead of the BDT one for the definition of the signal and control regions.

Figure B.4 shows several kinematic quantities for the analysis performed using only events with one reconstructed primary vertex.

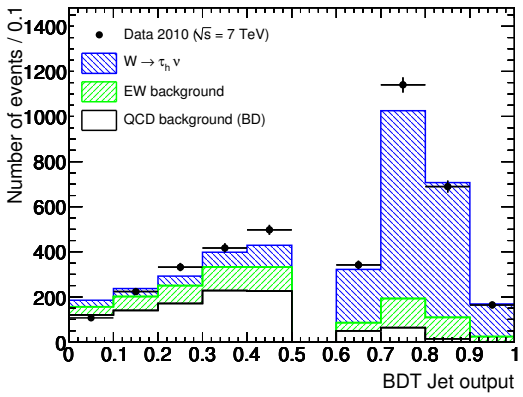

Figure B.1: Distribution of the τ_{had} identification BDT discriminant in the combined region AC. The QCD background shape has been extracted from regions BD. The expected signal and EW background contributions are also shown, normalised to the theoretical NNLO cross section.

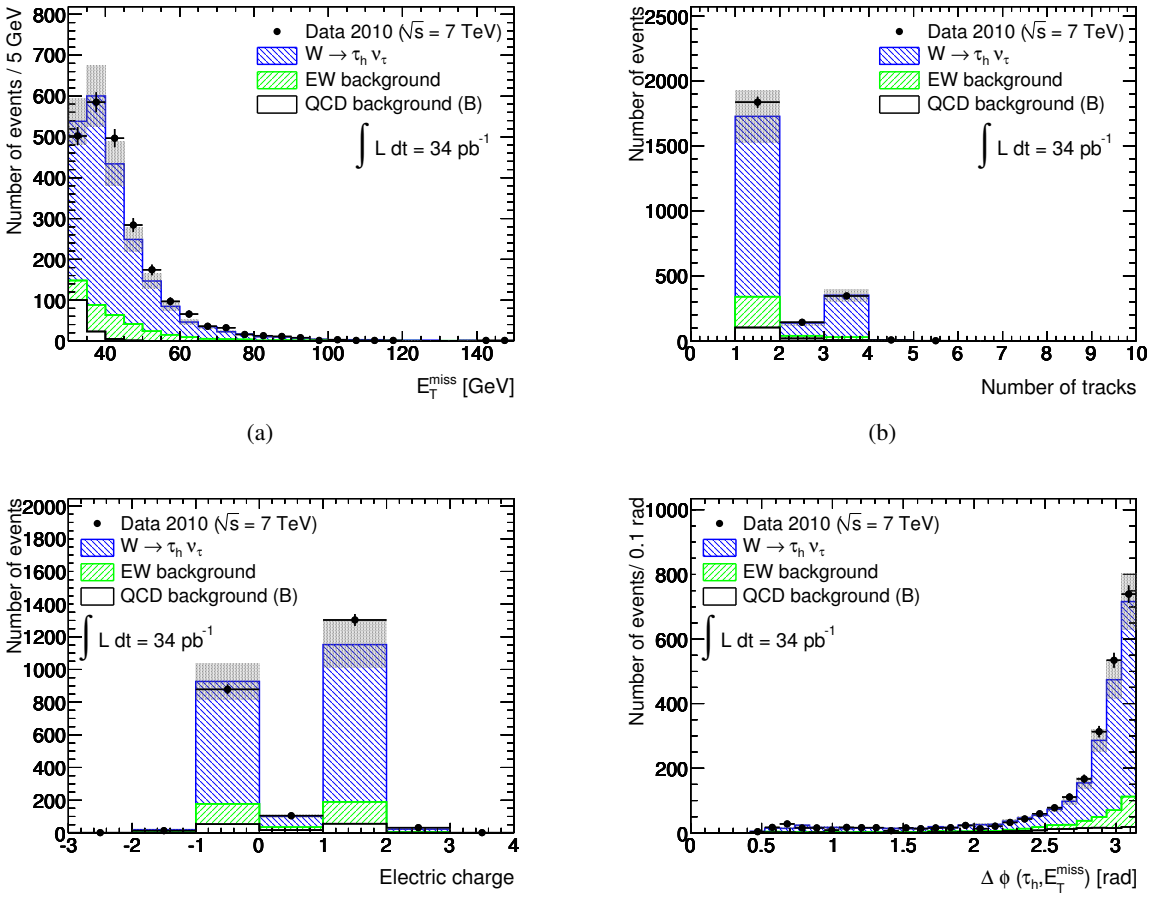

Figure B.2: Distribution of (a) missing transverse energy, (b) the number of tracks associated to the τ_{had} candidate, (c) the τ_{had} charge and (d) $\Delta\phi$ between $E_{\text{T}}^{\text{miss}}$ and the τ_{had} candidate in the signal region A after the full event selection. The QCD background shape has been extracted from region B. The expected signal and EW background contribution in region A are also shown, normalised to the theoretical NNLO cross section. The statistical and systematic uncertainties of the signal and background prediction are indicated by a grey hashed band.

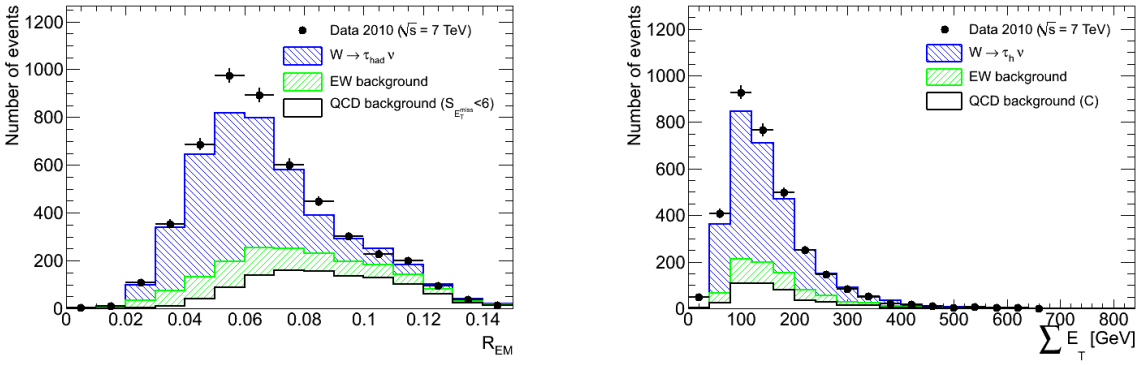

(a)

(b)

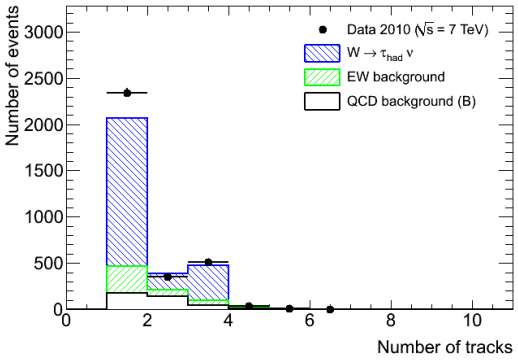

(c)

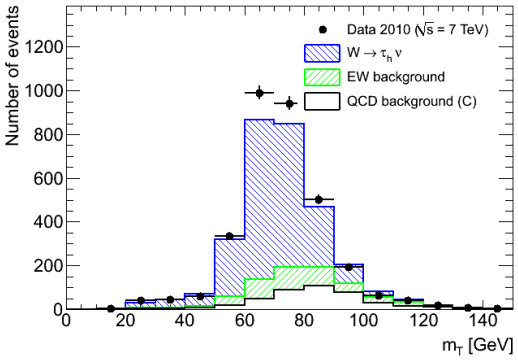

(d)

Figure B.3: Analysis using the cut-based τ_{had} identification for the selection of signal and control regions: (a) τ_{had} identification variable R_{EM} in the combined region AC. The QCD background shape has been extracted from the combined region BD. Distribution of (b) $\sum E_{\text{T}}$, (c) number of tracks associated to the τ_{had} candidate (d) the transverse mass in the signal region A after the full event selection. The QCD background shape has been extracted from region B or C. The expected signal and EW background is also shown, normalised to the theoretical cross section at NNLO.

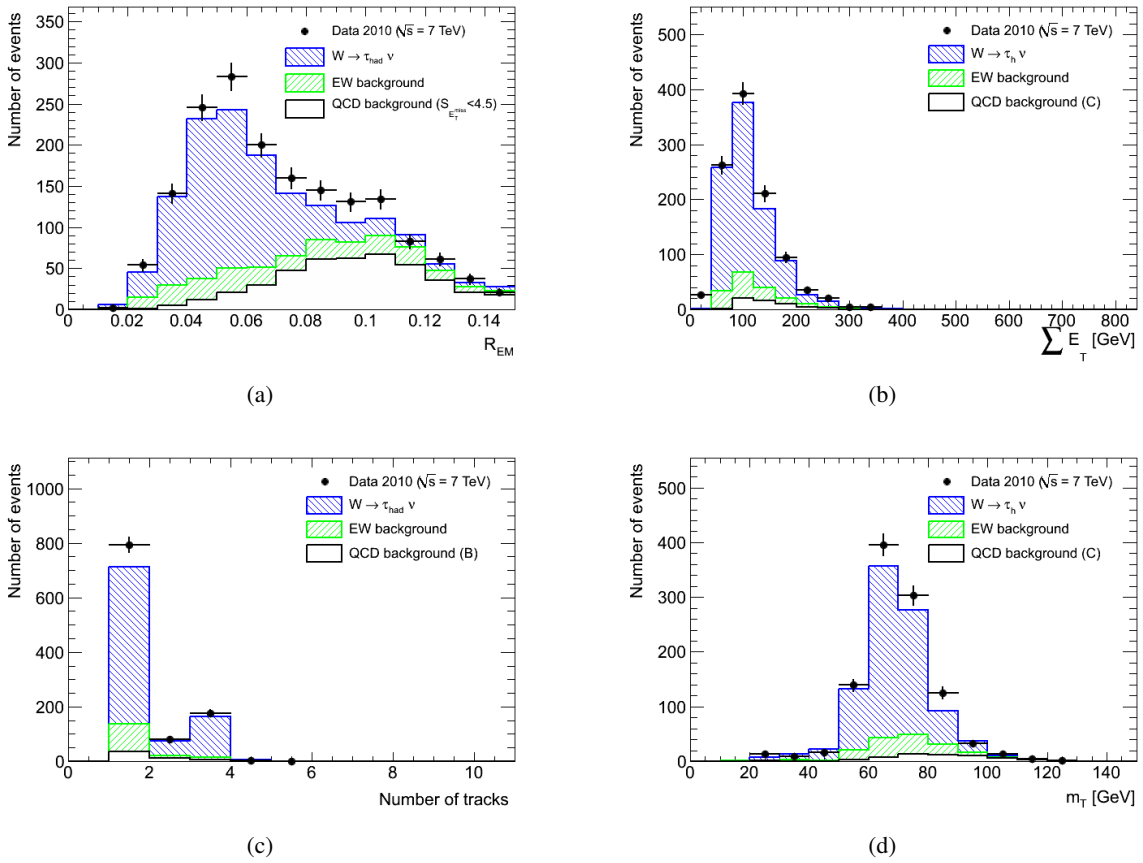

Figure B.4: Analysis of events with one primary vertex: (a) τ_{had} identification variable R_{EM} in the combined region AC. The QCD background shape has been extracted from the combined region BD. Distribution of (b) $\sum E_{\text{T}}$, (c) number of tracks associated to the τ_{had} candidate (d) the transverse mass in the signal region A after the full event selection. The QCD background shape has been extracted from region B or C. The expected signal and EW background is also shown, normalised to the theoretical cross section at NNLO.

APPENDIX C

$H \to \tau_{\text{lep}}\tau_{\text{had}}$ Search with 7 TeV and 8 TeV Data (4.6 + 13.0 fb^{-1})

In this appendix the results of the $H \to \tau_{\text{lep}}\tau_{\text{had}}$ search based on 2011 data at $\sqrt{s} = 7$ TeV corresponding to an integrated luminosity of 4.6 fb^{-1} and 2012 data at $\sqrt{s} = 8$ TeV corresponding to an integrated luminosity of 13.0 fb^{-1} are summarised [97].

The simulated samples used to investigate the signal and background processes are partially different to the ones used in the 20.3 fb^{-1} analysis (Sec. 7.2) with a much smaller number of generated events, for details see [97]. The preselection of objects and mass reconstruction is mainly the same as in the full 2012 data analysis (Sec. 7.3), with a few exceptions. The trigger p_{T} thresholds and thus also the selection thresholds on reconstruction level differ for the 2011 data sample, they are summarised in Tab. C.1. In addition, the object identification algorithms, in particular the τ_{had} one and the $E_{\text{T}}^{\text{miss}}$ reconstruction are slightly different compared to the full analysis, where more recent improvements based on generic studies have been included (Chap. 5).

The event selection and categorisation for both centre-of-mass energies is summarised in Tab. C.2. The background estimation methods are the same as described in Sec. 7.5. However, for the modelling of the $Z \to \tau\tau$ background a VBF-filtered $Z \to \tau\tau$ sample is used (Sec. 7.2), instead of the embedded sample. Details of the investigated sources of systematic uncertainties are described in [97].

Tables C.3 and C.4 show the event yields for all categories in the $\sqrt{s} = 7$ TeV and $\sqrt{s} = 8$ TeV analyses. Figures C.1 and C.2 depict the resulting mass distributions in both data samples. Unlike in the full 2012 analysis, the Zero- and One-Jet Categories are also included in the profile likelihood fit in this analysis.

In Fig. C.3 the expected and observed upper limit on the signal strength μ at 95% CL obtained with the $H \to \tau_{\text{lep}}\tau_{\text{had}}$ analysis is shown for the combined $\sqrt{s} = 7$ TeV and $\sqrt{s} = 8$ TeV data set. The observed (expected) upper limit on the SM Higgs cross section times branching ratio at 95% CL is 2.0 (1.7) $\times \sigma_{\text{SM}}$ at $m_H = 125$ GeV. This corresponds to a significance of 0.1 (1.2)σ. For the analysis of the 8 TeV data set (13.0 fb^{-1}) only, the observed (expected) limit is 2.3 (2.2) $\times \sigma_{\text{SM}}$, i.e. a significance of -0.2 (0.9)σ at this mass point.

Figure C.4 shows the expected and observed upper limit on the cross section, and the significance of the deviation from a background-only hypothesis for the combination of all three $H \to \tau\tau$ analysis channels based on the combined $\sqrt{s} = 7$ TeV and $\sqrt{s} = 8$ TeV data set. At $m_H = 125$ GeV the upper limit at 95% is observed (expected) to be 1.9 (1.2) $\times \sigma_{\text{SM}}$, and the corresponding p_0 value is 1.7 (1.1) σ.

Trigger	Trigger p_{T} threshold [GeV]	Offline p_{T} threshold [GeV]
single electron	$p_{\mathrm{T}}^{e} > 20$–22	$p_{\mathrm{T}}^{e} > 25$
	-	$p_{\mathrm{T}}^{\tau_{\mathrm{had}}} > 20$
single muon	$p_{\mathrm{T}}^{\mu} > 18$	$p_{\mathrm{T}}^{\mu} > 25$
	-	$p_{\mathrm{T}}^{\tau_{\mathrm{had}}} > 20$
combined $e + \tau_{\mathrm{had}}$	$p_{\mathrm{T}}^{e} > 15$	$17 < p_{\mathrm{T}}^{e} < 25$
	$p_{\mathrm{T}}^{\tau_{\mathrm{had}}} > 16$–$20$	$p_{\mathrm{T}}^{\tau_{\mathrm{had}}} > 25$

Table C.1: p_{T} thresholds for the considered objects on trigger level and reconstruction level (for SLT and LTT trigger) used in the 2011 data set (4.6 fb^{-1}, $\sqrt{s} = 7$ TeV).

7 TeV		8 TeV	
VBF Category	Boosted Category	VBF Category	Boosted Category
▹ $p_{\mathrm{T}}^{\tau_{\mathrm{had}}} > 30$ GeV	–	▹ $p_{\mathrm{T}}^{\tau_{\mathrm{had}}} > 30$ GeV	▹ $p_{\mathrm{T}}^{\tau_{\mathrm{had}}} > 30$ GeV
▹ $E_{\mathrm{T}}^{\mathrm{miss}} > 20$ GeV	▹ $E_{\mathrm{T}}^{\mathrm{miss}} > 20$ GeV	▹ $E_{\mathrm{T}}^{\mathrm{miss}} > 20$ GeV	▹ $E_{\mathrm{T}}^{\mathrm{miss}} > 20$ GeV
▹ ≥ 2 jets	▹ $p_{\mathrm{T}}^{\mathrm{H}} > 100$ GeV	▹ ≥ 2 jets	▹ $p_{\mathrm{T}}^{\mathrm{H}} > 100$ GeV
▹ $p_{\mathrm{T}}^{j1}, p_{\mathrm{T}}^{j2} > 30$ GeV	▹ $0 < x_{\ell} < 1$	▹ $p_{\mathrm{T}}^{j1} > 40, p_{\mathrm{T}}^{j2} > 30$ GeV	▹ $0 < x_{\ell} < 1$
▹ $\Delta\eta_{jj} > 3.0$	▹ $0.2 < x_{\tau} < 1.2$	▹ $\Delta\eta_{jj} > 3.0$	▹ $0.2 < x_{\tau} < 1.2$
▹ $m_{jj} > 500$ GeV	▹ Fails VBF	▹ $m_{jj} > 500$ GeV	▹ Fails VBF Cat.
▹ Centrality of ℓ, τ_{had}	–	▹ Centrality of ℓ, τ_{had}	–
▹ $\eta_{j1} \times \eta_{j2} < 0$	–	▹ $\eta_{j1} \times \eta_{j2} < 0$	–
▹ $p_{\mathrm{T}}^{\mathrm{tot}} < 40$ GeV	–	▹ $p_{\mathrm{T}}^{\mathrm{tot}} < 30$ GeV	–
–	–	▹ $p_{\mathrm{T}}^{\ell} > 26$ GeV	–
• $m_{\mathrm{T}} < 50$ GeV	• $m_{\mathrm{T}} < 50$ GeV	• $m_{\mathrm{T}} < 50$ GeV	• $m_{\mathrm{T}} < 50$ GeV
• $\Delta\Delta R^{\ell,\tau_{\mathrm{had}}} < 0.8$	• $\Delta\Delta R^{\ell,\tau_{\mathrm{had}}} < 0.8$	• $\Delta\Delta R^{\ell,\tau_{\mathrm{had}}} < 0.8$	• $\Delta\Delta R^{\ell,\tau_{\mathrm{had}}} < 0.8$
• $\sum \Delta\phi < 3.5$	• $\sum \Delta\phi < 1.6$	• $\sum \Delta\phi < 2.8$	–
–	–	• b-tagged jet veto	• b-tagged jet veto
One-Jet Category	Zero-Jet Category	One-Jet Category	Zero-Jet Category
▹ ≥ 1 jet, $p_{\mathrm{T}} > 25$ GeV	▹ 0 jets $p_{\mathrm{T}} > 25$ GeV	▹ ≥ 1 jet, $p_{\mathrm{T}} > 30$ GeV	▹ 0 jets $p_{\mathrm{T}} > 30$ GeV
▹ $E_{\mathrm{T}}^{\mathrm{miss}} > 20$ GeV	▹ $E_{\mathrm{T}}^{\mathrm{miss}} > 20$ GeV	▹ $E_{\mathrm{T}}^{\mathrm{miss}} > 20$ GeV	▹ $E_{\mathrm{T}}^{\mathrm{miss}} > 20$ GeV
▹ Fails VBF, Boosted Cat.	▹ Fails Boosted Cat.	▹ Fails VBF, Boosted Cat.	▹ Fails Boosted Cat.
• $m_{\mathrm{T}} < 50$ GeV	• $m_{\mathrm{T}} < 30$ GeV	• $m_{\mathrm{T}} < 50$ GeV	• $m_{\mathrm{T}} < 30$ GeV
• $\Delta\Delta R^{\ell,\tau_{\mathrm{had}}} < 0.6$	• $\Delta\Delta R^{\ell,\tau_{\mathrm{had}}} < 0.5$	• $\Delta\Delta R^{\ell,\tau_{\mathrm{had}}} < 0.6$	• $\Delta\Delta R^{\ell,\tau_{\mathrm{had}}} < 0.5$
• $\sum \Delta\phi < 3.5$	• $\sum \Delta\phi < 3.5$	• $\sum \Delta\phi < 3.5$	• $\sum \Delta\phi < 3.5$
–	• $p_{\mathrm{T}}^{\ell} - p_{\mathrm{T}}^{\tau} < 0$	–	• $p_{\mathrm{T}}^{\ell} - p_{\mathrm{T}}^{\tau} < 0$

Table C.2: Event selection criteria applied in the different categories of the $H \to \tau_{\mathrm{lep}}\tau_{\mathrm{had}}$ analysis of $\sqrt{s} = 7$ TeV and $\sqrt{s} = 8$ TeV data (4.6 fb^{-1} + 13.0 fb^{-1}). Requirements marked with a triangle (▹) are categorisation requirements, meaning that if an event fails that requirement it is still considered for the remaining categories. Requirements marked with a bullet (•) are only applied to events passing all categorisation requirements in a category; events failing such requirements are discarded.

Process	Zero-Jet $e\tau_{\text{had}}$	One-Jet $e\tau_{\text{had}}$	Zero-Jet $\mu\tau_{\text{had}}$	One-Jet $\mu\tau_{\text{had}}$
ggF($H \to \tau_{\text{lep}}\tau_{\text{had}}$) (125 GeV)	9.4 ± 0.3 ± 2.3	8.7 ± 0.2 ± 1.8	4.6 ± 0.2 ± 1.2	6.4 ± 0.2 ± 1.3
VBF($H \to \tau_{\text{lep}}\tau_{\text{had}}$) (125 GeV)	0.09 ± 0.01 ± 0.01	1.68 ± 0.03 ± 0.15	0.04 ± 0.00 ± 0.01	1.35 ± 0.03 ± 0.12
VH($H \to \tau_{\text{lep}}\tau_{\text{had}}$) (125 GeV)	0.05 ± 0.01 ± 0.01	0.73 ± 0.04 ± 0.07	0.03 ± 0.01 ± 0.00	0.67 ± 0.04 ± 0.06
$Z \to \tau\tau$	(2.57 ± 0.03 ± 0.44)×10^3	(1.63 ± 0.02 ± 0.24)×10^3	(0.88 ± 0.01 ± 0.17)×10^3	(1.20 ± 0.02 ± 0.17)×10^3
Diboson	2.1 ± 0.6 ± 0.3	12.2 ± 1.3 ± 1.1	2.3 ± 0.3 ± 0.4	9.1 ± 1.2 ± 0.8
$Z \to \ell\ell$	47 ± 5 ± 12	34 ± 5 ± 8	10 ± 3 ± 2	13 ± 3 ± 4
Top	0.7 ± 0.2 ± 0.2	121 ± 3 ± 19	0.5 ± 0.2 ± 0.1	92 ± 3 ± 14
W+jets	116 ± 15 ± 6	(0.24 ± 0.02 ± 0.03)×10^3	65 ± 11 ± 6	(0.15 ± 0.02 ± 0.02)×10^3
Same-sign	(0.40 ± 0.02 ± 0.06)×10^3	(0.82 ± 0.04 ± 0.04)×10^3	60 ± 8 ± 3	(0.31 ± 0.02 ± 0.02))×10^3
Total background	(3.13 ± 0.04 ± 0.44)×10^3	(2.85 ± 0.04 ± 0.25)×10^3	(1.01 ± 0.02 ± 0.17)×10^3	(1.78 ± 0.03 ± 0.18)×10^3
Observed data	3064	2828	958	1701

Process	Boosted	VBF
ggF($H \to \tau_{\text{lep}}\tau_{\text{had}}$) (125 GeV)	4.1 ± 0.1 ± 1.0	0.17 ± 0.03 ± 0.06
VBF($H \to \tau_{\text{lep}}\tau_{\text{had}}$) (125 GeV)	1.52 ± 0.03 ± 0.13	0.87 ± 0.02 ± 0.15
VH($H \to \tau_{\text{lep}}\tau_{\text{had}}$) (125 GeV)	0.86 ± 0.04 ± 0.08	<0.001
$Z \to \tau\tau$	(0.70 ± 0.02 ± 0.10)×10^3	6.5 ± 0.6 ± 1.5
Diboson	8.4 ± 0.7 ± 0.8	0.12 ± 0.06 ± 0.03
$Z \to \ell\ell$	3.7 ± 1.3 ± 1.0	0.8 ± 0.3 ± 1.0
Top	52 ± 2 ± 9	1.2 ± 0.3 ± 0.1
W+jets	41 ± 7 ± 8	–
Same-sign	90 ± 10 ± 5	–
Fake τ_{had}	–	0.8 ± 0.2 ± 0.4
Total background	(0.90 ± 0.02 ± 0.10)×10^3	9.5 ± 0.8 ± 1.9
Observed data	834	10

Table C.3: Number of events in the Zero-Jet, One-Jet, Boosted and VBF Categories for the $e\tau_{\text{had}}$ and $\mu\tau_{\text{had}}$ channels combined, for the 7 TeV analysis. The statistical and systematic uncertainties are also given, in this order [97].

Process	Zero-Jet $e\tau_{\text{had}}$	One-Jet $e\tau_{\text{had}}$	Zero-Jet $\mu\tau_{\text{had}}$	One-Jet $\mu\tau_{\text{had}}$
ggF($H \to \tau_{\text{lep}}\tau_{\text{had}}$) (125 GeV)	25.9 ± 0.8 ± 6.1	37.3 ± 0.9 ± 8.4	34.3 ± 0.9 ± 8.0	46 ± 1 ± 11
VBF($H \to \tau_{\text{lep}}\tau_{\text{had}}$) (125 GeV)	0.30 ± 0.05 ± 0.04	7.8 ± 0.3 ± 0.5	0.47 ± 0.06 ± 0.04	8.5 ± 0.3 ± 0.6
VH($H \to \tau_{\text{lep}}\tau_{\text{had}}$) (125 GeV)	0.27 ± 0.05 ± 0.03	3.5 ± 0.2 ± 0.2	0.20 ± 0.05 ± 0.02	3.7 ± 0.2 ± 0.3
$Z \to \tau\tau$	(3.59 ± 0.03 ± 0.278)×10^3	(4.50 ± 0.04 ± 0.37)×10^3	(7.13 ± 0.04 ± 0.48)×10^3	(6.14 ± 0.04 ± 0.45)×10^3
Diboson	9.9 ± 0.7 ± 0.9	27 ± 1 ± 2	10.5 ± 0.7 ± 0.9	30 ± 1 ± 3
$Z \to \ell\ell$	(0.41 ± 0.04 ± 0.13)×10^3	(0.28 ± 0.07 ± 0.14)×10^3	(0.10 ± 0.02 ± 0.02)×10^3	(0.12 ± 0.02 ± 0.03)×10^3
Top	8 ± 2 ± 1	(1.00 ± 0.02 ± 0.03)×10^3	10.4 ± 2.3 ± 0.6	(1.03 ± 0.03 ± 0.05)×10^3
W+jets	(0.48 ± 0.07 ± 0.04)×10^3	(1.32 ± 0.12 ± 0.12)×10^3	(0.51 ± 0.09 ± 0.04)×10^3	(1.0 ± 0.1 ± 0.14)×10^3
Same-sign	(0.66 ± 0.03 ± 0.03)×10^3	(3.68 ± 0.06 ± 0.18)×10^3	(1.03 ± 0.03 ± 0.07)×10^3	(3.27 ± 0.06 ± 0.24)×10^3
Total background	(5.16 ± 0.09 ± 0.31)×10^3	(10.8 ± 0.2 ± 0.5)×10^3	(8.8 ± 0.1 ± 0.5)×10^3	(11.6 ± 0.1 ± 0.5)×10^3
Observed data	5012	10409	8300	11373

Process	Boosted	VBF
ggF($H \to \tau_{\text{lep}}\tau_{\text{had}}$) (125 GeV)	20.3 ± 0.7 ± 5.1	0.5 ± 0.1 ± 0.3
VBF($H \to \tau_{\text{lep}}\tau_{\text{had}}$) (125 GeV)	5.3 ± 0.2 ± 0.3	2.5 ± 0.2 ± 0.4
VH($H \to \tau_{\text{lep}}\tau_{\text{had}}$) (125 GeV)	2.7 ± 0.2 ± 0.2	<0.001
$Z \to \tau\tau$	(1.78 ± 0.03 ± 0.11)×10^3	17 ± 2 ± 6
Diboson	12.2 ± 0.9 ± 1.0	0.6 ± 0.3 ± 0.4
$Z \to \ell\ell$	18 ± 9 ± 4	1.7 ± 0.5 ± 1.2
Top	111 ± 8 ± 33	2.0 ± 0.7 ± 1.0
W+jets	(0.27 ± 0.06 ± 0.04)×10^3	–
Same-sign	(0.34 ± 0.02 ± 0.01)×10^3	–
Fake τ_{had}	–	7.6 ± 0.7 ± 3.8
Total background	(2.53 ± 0.07 ± 0.13)×10^3	29 ± 2 ± 7
Observed data	2602	29

Table C.4: Number of events in the Zero-Jet, One-Jet, Boosted and VBF Categories for the $e\tau_{\text{had}}$ and $\mu\tau_{\text{had}}$ channels combined, for the 8 TeV analysis. The statistical and systematic uncertainties are also given, in this order [97].

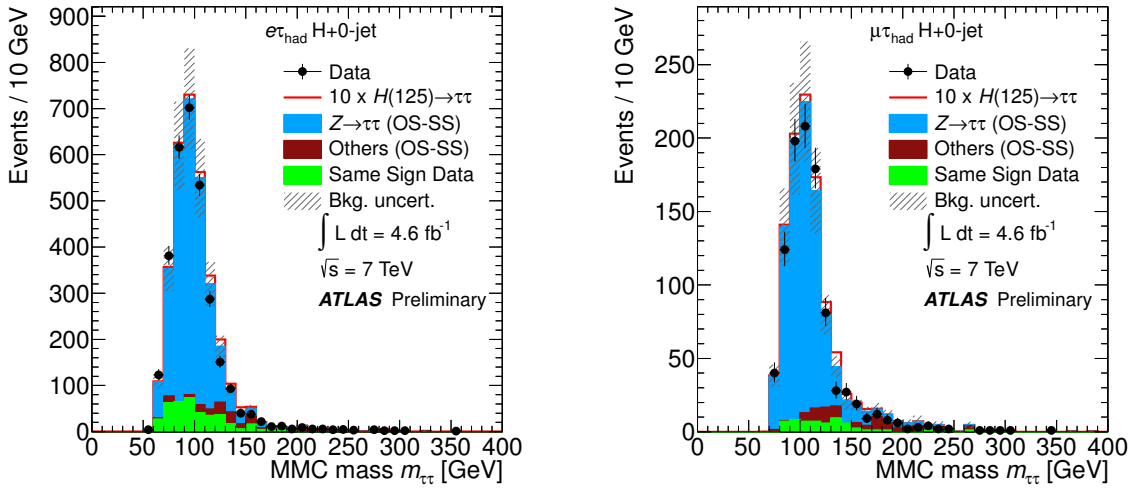

(a)

(b)

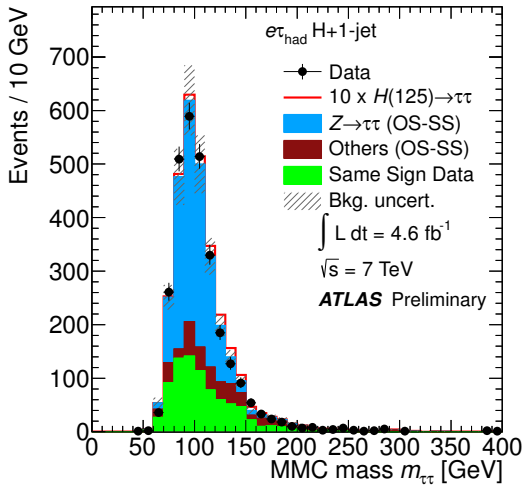

(c)

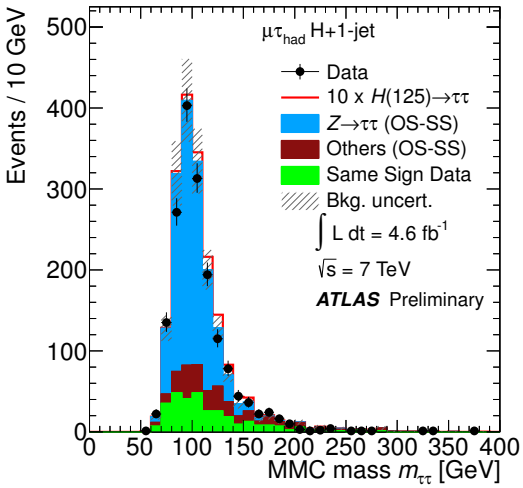

(d)

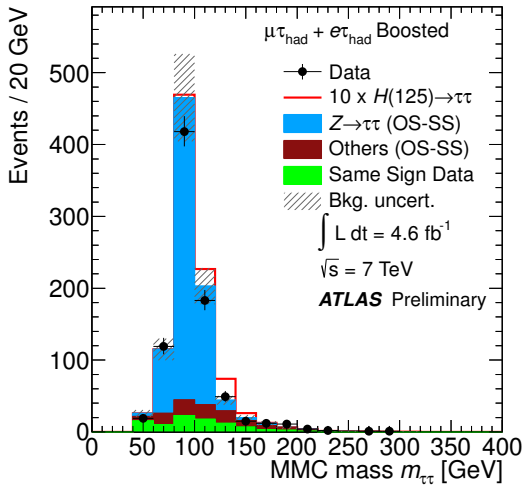

(e)

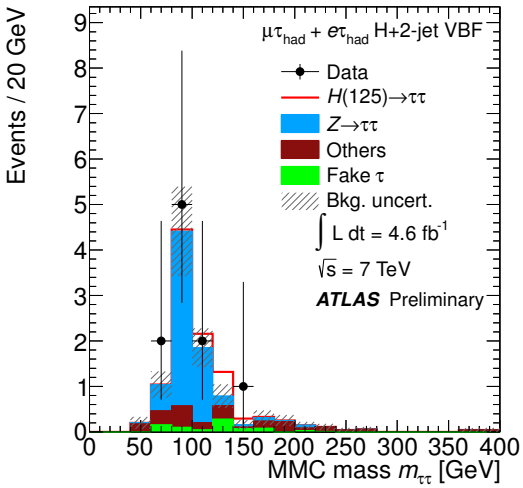

(f)

Figure C.1: MMC mass distributions of the selected events in the (a,b) Zero- (c,d) One-Jet (e) Boosted and (f) VBF Categories of the $H \to \tau_{\text{lep}}\tau_{\text{had}}$ channel for the 7 TeV analysis. The selected events in data are shown together with the predicted Higgs boson signal ($m_H = 125$ GeV, scaled by a factor 10) stacked above the background contributions [97].

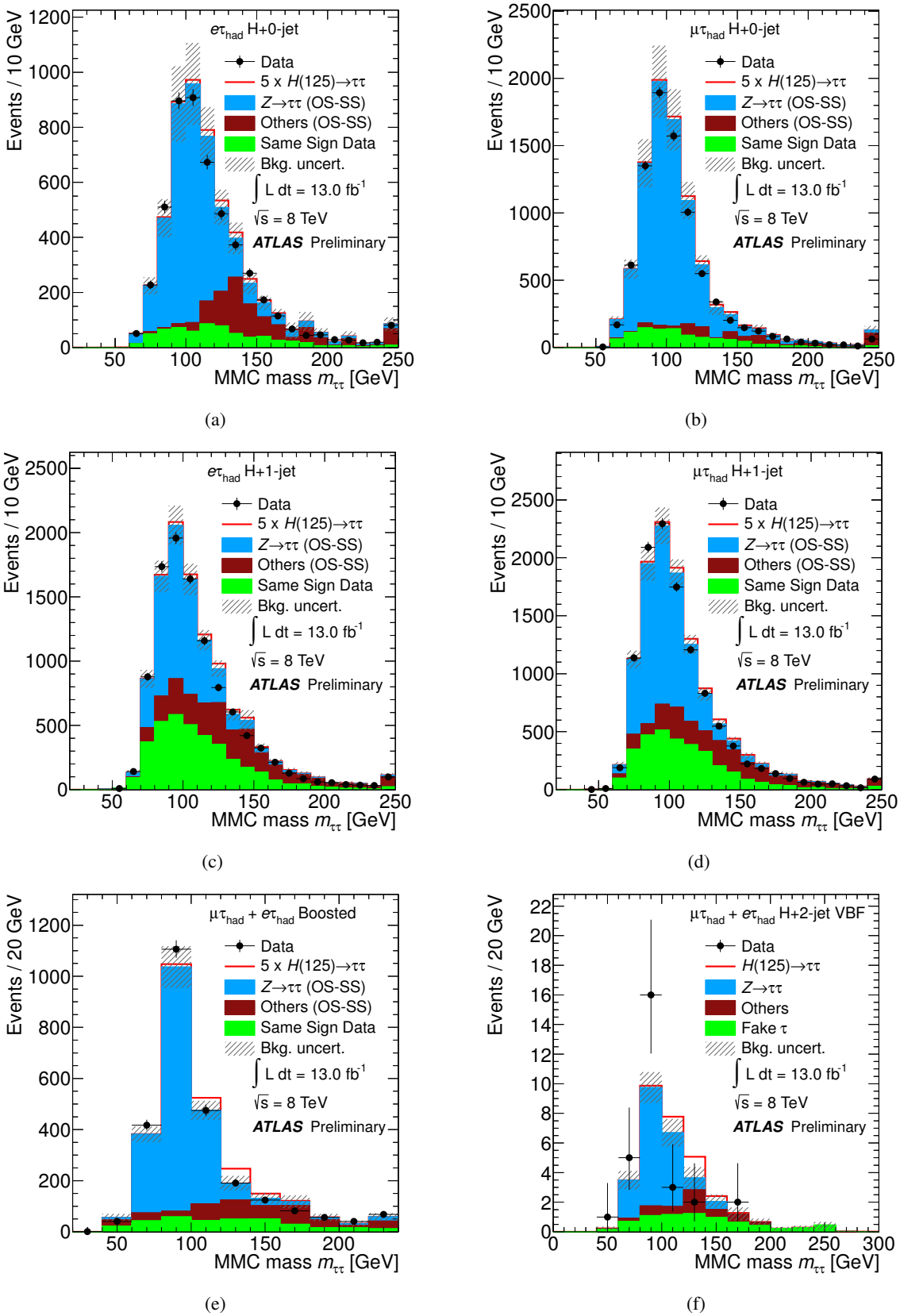

Figure C.2: MMC mass distributions of the selected events in the (a,b) Zero- (c,d) One-Jet (e) Boosted and (f) VBF Categories of the $H \to \tau_{\text{lep}}\tau_{\text{had}}$ channel for the 8 TeV analysis. The selected events in data are shown together with the predicted Higgs boson signal (m_H = 125 GeV, scaled by a factor 10) stacked above the background contributions [97].

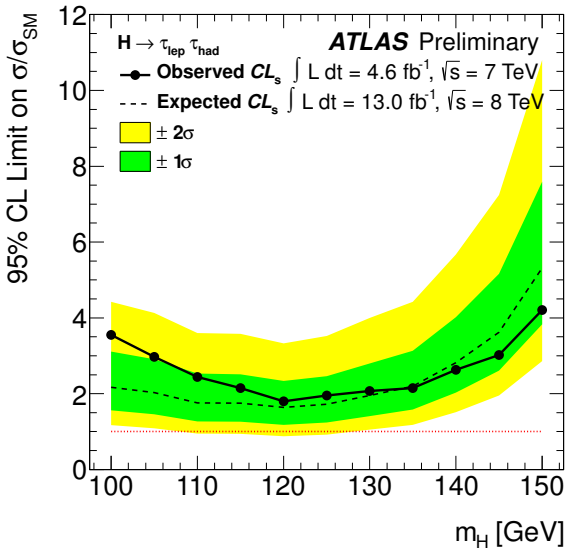

Figure C.3: Observed (solid line) and expected (dashed line) upper limits on the signal cross section times branching ratio relative to the Standard Model expectation at 95% CL as a function of m_H. The green and yellow bands indicate the $\pm 1\sigma$ and $\pm 2\sigma$ uncertainty on the expected upper limit. The results are based on the analysis of the $H \to \tau_{\text{lep}}\tau_{\text{had}}$ decay channel with 13.0 fb^{-1} at $\sqrt{s} = 8$ TeV and 4.6 fb^{-1} at $\sqrt{s} = 7$ TeV [97].

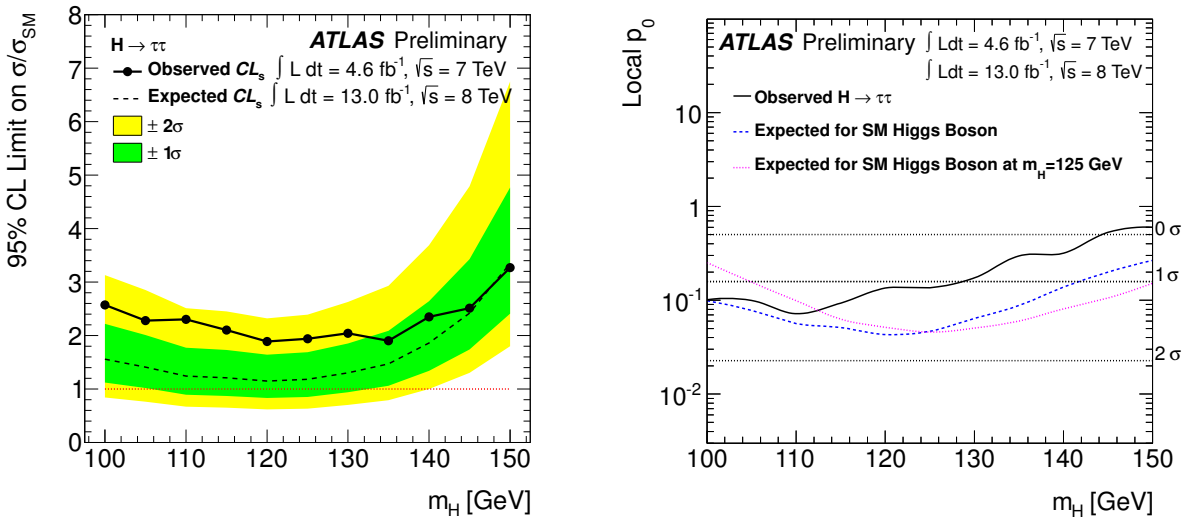

(a) (b)

Figure C.4: (a) Observed (solid line) and expected (dashed line) upper limits on the signal cross section times branching ratio relative to the Standard Model expectation at 95% CL as a function of m_H. The green and yellow bands indicate the $\pm 1\sigma$ and $\pm 2\sigma$ uncertainty on the expected upper limit. (b) Observed (solid line) and expected (dashed line) p_0 values and the corresponding signal significances in units of standard deviation as a function of m_H. The expected p_0 value obtained under the assumption of a presence with a Higgs boson at $m_H = 125$ GeV is also included (dotted line). The results are shown for the combination of all three decay channels of $H \to \tau\tau$ based on 13.0 fb^{-1} at $\sqrt{s} = 8$ TeV and 4.6 fb^{-1} at $\sqrt{s} = 7$ TeV [97].

APPENDIX D

Details on Systematic Uncertainties in the $H \to \tau_{\text{lep}}\tau_{\text{had}}$ Analysis

Tables D.1 summarises all theory uncertainties and Tabs. D.2 and D.3 list experimental and background estimation systematic uncertainties affecting the $H \to \tau_{\text{lep}}\tau_{\text{had}}$ analysis (Chaps. 7 and 7.7).

Nuisance parameter	Physics process	Rel. $\pm 1\sigma$ variation	
		Boosted Cat.	VBF Cat.
QCDscale_ggH1in	ggF signal	$^{+0.28}_{-0.22}$	-
QCDscale_ggH2in	ggF signal	∓ 0.03	$^{+0.23}_{-0.19}$
QCDscale_ggH3in	ggF signal	-	$^{-0.28}_{+0.38}$
QCDscale_VH	VH signal	± 0.04	-
QCDscale_qqH	VBF signal	± 0.02	
QCDscale_VV	diboson	± 0.05	
QCDscale_V	$Z \to \ell\ell(\ell \to \tau_{\text{had}})$	± 0.01	
pdf_Higgs_gg	ggF signal	$^{+0.08}_{-0.07}$	
pdf_Higgs_qq	VBF/VH signal	± 0.03	
pdf_qq	diboson/$Z \to \ell\ell(\ell \to \tau_{\text{had}})$	± 0.04	
UE_gg	ggF signal	-	± 0.3
UE_qq	VBF signal	-	± 0.06
Gen_Qmass_ggH	ggF signal	± 0.29	± 0.18
BR_tautau	ggF/VBF/VH signal	$^{+0.069/+0.03}_{-0.067/-0.031}$	

Table D.1: Theory systematic uncertainties in the $H \to \tau_{\text{lep}}\tau_{\text{had}}$ analysis. The uncertainty on the branching ratio depends on the Higgs mass, the maximal and minimal uncertainties that are found are given in this table.

	Backgr. est.	*EL_EFF*	*EL_SCALE*	*EL_RES*	*MU_EFF*	*MU_SCALE*	*TAU_TRIG*	*TAU_ID*	*TAU_EFAKE*	*TAU_MUFAKE*	*TES*
ggF($H \to \tau_{\text{lep}}\tau_{\text{had}}$)	$^{+0.0}_{-0.0}$	$^{+0.8}_{-0.8}$	$^{+0.1}_{-0.1}$	$^{+0.2}_{-0.1}$	$^{+1.2}_{-0.8}$	$^{+0.1}_{-0.0}$	$^{+1.0}_{-1.3}$	$^{+3.4}_{-3.4}$	$^{+0.0}_{-0.0}$	$^{+0.0}_{-0.0}$	$^{+0.0}_{-1.1}$
VBF($H \to \tau_{\text{lep}}\tau_{\text{had}}$)	$^{+0.0}_{-0.0}$	$^{+0.8}_{-0.8}$	$^{+0.1}_{-0.1}$	$^{-0.1}_{-0.0}$	$^{+1.2}_{-0.7}$	$^{+0.0}_{-0.0}$	$^{+1.3}_{-1.8}$	$^{+3.3}_{-3.3}$	$^{+0.0}_{-0.0}$	$^{+0.0}_{-0.0}$	$^{+0.9}_{-1.3}$
WH($H \to \tau_{\text{lep}}\tau_{\text{had}}$)	$^{+0.0}_{-0.0}$	$^{+0.8}_{-0.8}$	$^{+0.2}_{-0.1}$	$^{+0.2}_{-0.0}$	$^{+1.2}_{-0.8}$	$^{+0.0}_{-0.0}$	$^{+0.9}_{-1.3}$	$^{+3.3}_{-3.3}$	$^{+0.0}_{-0.0}$	$^{+0.0}_{-0.0}$	$^{+1.2}_{-1.2}$
ZH($H \to \tau_{\text{lep}}\tau_{\text{had}}$)	$^{+0.0}_{-0.0}$	$^{+0.8}_{-0.8}$	$^{+0.1}_{-0.1}$	$^{+0.0}_{-0.1}$	$^{+1.2}_{-0.8}$	$^{+0.0}_{-0.0}$	$^{+1.0}_{-1.3}$	$^{+3.3}_{-3.3}$	$^{+0.0}_{-0.0}$	$^{+0.0}_{-0.0}$	$^{+1.1}_{-0.5}$
$Z \to \tau\tau$	$^{+6.1}_{-6.2}$	$^{+0.1}_{-0.1}$	$^{+0.4}_{-0.4}$	$^{-0.1}_{-0.0}$	$^{+0.1}_{-0.1}$	$^{+0.0}_{-0.0}$	$^{+0.1}_{-0.5}$	$^{+0.1}_{-0.1}$	$^{+0.0}_{-0.0}$	$^{+0.0}_{-0.0}$	$^{+0.5}_{-2.0}$
W + jets	$^{+17.8}_{-19.0}$	$^{+0.2}_{-0.1}$	$^{+1.2}_{-1.0}$	$^{-0.6}_{-0.2}$	$^{+0.2}_{-0.3}$	$^{+1.3}_{-0.2}$	$^{+0.3}_{-0.4}$	$^{+0.5}_{-0.5}$	$^{-0.4}_{-0.4}$	$^{-0.3}_{-0.3}$	$^{+10.7}_{-1.3}$
$Z \to \ell\ell(j \to \tau_{\text{had}})$	$^{+0.0}_{-0.0}$	$^{+0.0}_{-0.0}$	$^{+0.0}_{-0.0}$	$^{+0.0}_{-0.0}$	$^{+0.0}_{-0.0}$	$^{+0.0}_{-0.0}$	$^{+0.0}_{-0.0}$	$^{+0.0}_{-0.0}$	$^{+0.0}_{-0.0}$	$^{+0.0}_{-0.0}$	$^{+0.0}_{-0.0}$
$Z \to \ell\ell(\ell \to \tau_{\text{had}})$	$^{+0.0}_{-0.0}$	$^{+1.1}_{-1.1}$	$^{+1.3}_{-1.3}$	$^{-1.1}_{-0.3}$	$^{+0.8}_{-0.8}$	$^{+0.1}_{-0.0}$	$^{+0.4}_{-0.4}$	$^{+0.0}_{-0.0}$	$^{+15.9}_{-16.5}$	$^{+5.4}_{-5.4}$	$^{-4.2}_{-2.7}$
Top	$^{+5.6}_{-5.7}$	$^{+0.1}_{-0.0}$	$^{+0.3}_{-1.0}$	$^{-0.5}_{-1.6}$	$^{+0.1}_{-0.1}$	$^{+0.5}_{-0.0}$	$^{+0.3}_{-0.3}$	$^{+0.1}_{-0.1}$	$^{+0.0}_{-0.0}$	$^{+0.0}_{-0.0}$	$^{+2.3}_{-5.8}$
Diboson	$^{+2.0}_{-2.0}$	$^{+0.8}_{-0.8}$	$^{+0.1}_{-0.0}$	$^{-0.9}_{-0.3}$	$^{+1.2}_{-1.0}$	$^{+0.3}_{-0.0}$	$^{+0.4}_{-0.6}$	$^{+2.6}_{-2.6}$	$^{+0.1}_{-0.1}$	$^{+0.0}_{-0.0}$	$^{+1.7}_{-3.1}$
SS	$^{+12.4}_{-12.4}$	$^{+0.0}_{-0.0}$	$^{+0.0}_{-0.0}$	$^{+0.0}_{-0.0}$	$^{+0.0}_{-0.0}$	$^{+0.0}_{-0.0}$	$^{+0.0}_{-0.0}$	$^{+0.0}_{-0.0}$	$^{+0.0}_{-0.0}$	$^{+0.0}_{-0.0}$	$^{+0.0}_{-0.0}$

	b-tag	JES in-situ	JES η	JES Flav.	JES *b*-jet	JES PileUp	*JER_2012*	*JVF_2012*	*MET_RESO*	*MET_SCALE*
ggF($H \to \tau_{\text{lep}}\tau_{\text{had}}$)	$^{+0.4}_{-0.5}$	$^{+3.7}_{-3.8}$	$^{+3.3}_{-3.4}$	$^{+5.0}_{-5.7}$	$^{+0.0}_{-0.1}$	$^{+1.6}_{-1.9}$	$^{-1.9}_{-1.9}$	$^{+0.0}_{-0.0}$	$^{-0.2}_{-0.3}$	$^{+0.2}_{-0.6}$
VBF($H \to \tau_{\text{lep}}\tau_{\text{had}}$)	$^{+0.4}_{-0.5}$	$^{+2.4}_{-2.5}$	$^{+2.5}_{-2.6}$	$^{+3.3}_{-3.9}$	$^{+0.0}_{-0.0}$	$^{+0.9}_{-1.0}$	$^{-0.5}_{-0.5}$	$^{+0.0}_{-0.0}$	$^{+0.1}_{-0.2}$	$^{+0.2}_{-0.2}$
WH($H \to \tau_{\text{lep}}\tau_{\text{had}}$)	$^{+1.2}_{-1.3}$	$^{+1.9}_{-2.1}$	$^{+1.3}_{-1.4}$	$^{+2.6}_{-3.3}$	$^{+0.0}_{-0.0}$	$^{+0.9}_{-1.1}$	$^{-0.2}_{-0.2}$	$^{+0.0}_{-0.0}$	$^{+0.3}_{-0.2}$	$^{-0.1}_{-0.1}$
ZH($H \to \tau_{\text{lep}}\tau_{\text{had}}$)	$^{+1.1}_{-1.1}$	$^{+2.1}_{-2.4}$	$^{+2.0}_{-2.1}$	$^{+2.8}_{-4.3}$	$^{+0.1}_{-0.1}$	$^{+0.5}_{-1.4}$	$^{+0.9}_{-0.9}$	$^{+0.0}_{-0.0}$	$^{+0.1}_{-0.2}$	$^{+0.1}_{-0.1}$
$Z \to \tau\tau$	$^{+0.1}_{-0.1}$	$^{+0.1}_{-0.1}$	$^{+0.1}_{-0.1}$	$^{+0.0}_{-0.1}$	$^{+0.0}_{-0.0}$	$^{+0.1}_{-0.1}$	$^{+0.1}_{-0.1}$	$^{+0.0}_{-0.0}$	$^{+0.1}_{-0.0}$	$^{+0.0}_{-0.0}$
W + jets	$^{+4.5}_{-4.5}$	$^{+2.7}_{-2.9}$	$^{+2.8}_{-2.8}$	$^{+0.0}_{-2.2}$	$^{+0.0}_{-0.2}$	$^{+3.4}_{-3.4}$	$^{-11.2}_{-11.2}$	$^{+-0.1}_{-0.1}$	$^{-2.2}_{-1.3}$	$^{+0.0}_{-1.7}$
$Z \to \ell\ell(j \to \tau_{\text{had}})$	$^{+0.0}_{-0.0}$	$^{+0.0}_{-0.0}$	$^{+0.0}_{-0.0}$	$^{+0.0}_{-0.0}$	$^{+0.0}_{-0.0}$	$^{+0.0}_{-0.0}$	$^{+0.0}_{-0.0}$	$^{+0.0}_{-0.0}$	$^{+0.0}_{-0.0}$	$^{+0.0}_{-0.0}$
$Z \to \ell\ell(\ell \to \tau_{\text{had}})$	$^{+0.5}_{-0.6}$	$^{+6.2}_{-6.8}$	$^{+2.8}_{-2.9}$	$^{+12.6}_{-20.0}$	$^{+0.2}_{-0.2}$	$^{+1.6}_{-2.9}$	$^{+4.9}_{-4.9}$	$^{+0.1}_{-0.1}$	$^{-0.7}_{-0.0}$	$^{-0.6}_{-0.3}$
Top	$^{+15.4}_{-15.4}$	$^{+0.9}_{-5.3}$	$^{+2.9}_{-3.0}$	$^{+6.7}_{-9.8}$	$^{+1.0}_{-2.4}$	$^{+1.3}_{-1.7}$	$^{+2.2}_{-2.2}$	$^{+0.6}_{-0.0}$	$^{+2.6}_{-1.4}$	$^{-1.4}_{-2.0}$
Diboson	$^{+0.7}_{-0.8}$	$^{+1.6}_{-1.7}$	$^{+2.5}_{-2.5}$	$^{+4.4}_{-6.1}$	$^{+0.0}_{-0.4}$	$^{+1.0}_{-1.3}$	$^{-0.5}_{-0.5}$	$^{+0.0}_{-0.0}$	$^{+1.1}_{-0.1}$	$^{+0.9}_{-0.1}$
SS	$^{+0.0}_{-0.0}$	$^{+0.0}_{-0.0}$	$^{+0.0}_{-0.0}$	$^{+0.0}_{-0.0}$	$^{+0.0}_{-0.0}$	$^{+0.0}_{-0.0}$	$^{+0.0}_{-0.0}$	$^{+0.0}_{-0.0}$	$^{+0.0}_{-0.0}$	$^{+0.0}_{-0.0}$

Table D.2: Systematic variation (in %) of the background estimation and experimental uncertainties for all samples in the Boosted Category. The signal samples are simulated with a mass $m_H = 125$ GeV.

	Backgr. est.	*EL_EFF*	*EL_SCALE*	*EL_RES*	*MU_EFF*	*MU_SCALE*	*TAU_TRIG*	*TAU_ID*	*TAU_EFAKE*	*TAU_MUFAKE*	*TES*
ggF($H \to \tau_{\text{lep}}\tau_{\text{had}}$)	$^{+0.0}_{-0.0}$	$^{+0.9}_{-0.9}$	$^{+0.0}_{-0.3}$	$^{-1.1}_{-0.5}$	$^{+1.1}_{-1.1}$	$^{+0.4}_{-0.0}$	$^{+0.0}_{-0.0}$	$^{+3.4}_{-3.4}$	$^{+0.0}_{-0.0}$	$^{+0.0}_{-0.0}$	$^{+0.7}_{-1.2}$
VBF($H \to \tau_{\text{lep}}\tau_{\text{had}}$)	$^{+0.0}_{-0.0}$	$^{+0.9}_{-0.9}$	$^{+0.1}_{-0.2}$	$^{+0.1}_{-0.2}$	$^{+1.1}_{-1.1}$	$^{+0.1}_{-0.0}$	$^{+0.0}_{-0.0}$	$^{+3.4}_{-3.4}$	$^{+0.0}_{-0.0}$	$^{+0.0}_{-0.0}$	$^{+1.8}_{-2.0}$
WH($H \to \tau_{\text{lep}}\tau_{\text{had}}$)	$^{+0.0}_{-0.0}$	$^{+1.3}_{-1.3}$	$^{+0.0}_{-0.0}$	$^{-0.1}_{-0.1}$	$^{+0.6}_{-0.6}$	$^{+0.0}_{-0.0}$	$^{+0.0}_{-0.0}$	$^{+3.7}_{-3.7}$	$^{+0.0}_{-0.0}$	$^{+0.0}_{-0.0}$	$^{-8.5}_{-0.0}$
ZH($H \to \tau_{\text{lep}}\tau_{\text{had}}$)	$^{+0.0}_{-0.0}$	$^{+0.8}_{-0.8}$	$^{+0.1}_{-0.0}$	$^{+0.0}_{-0.0}$	$^{+1.3}_{-1.3}$	$^{+0.0}_{-0.0}$	$^{+0.0}_{-0.0}$	$^{+4.0}_{-4.0}$	$^{+0.0}_{-0.0}$	$^{+0.0}_{-0.0}$	$^{+1.4}_{-0.0}$
$Z \to \tau\tau$	$^{+7.1}_{-8.9}$	$^{+0.2}_{-0.2}$	$^{+0.6}_{-0.9}$	$^{+0.4}_{-0.1}$	$^{+0.2}_{-0.2}$	$^{+0.0}_{-0.1}$	$^{+0.1}_{-0.1}$	$^{+0.3}_{-0.3}$	$^{+0.0}_{-0.0}$	$^{+0.0}_{-0.0}$	$^{+0.5}_{-4.7}$
$Z \to \ell\ell(j \to \tau_{\text{had}})$	$^{+11.9}_{-11.9}$	$^{+1.0}_{-1.0}$	$^{+2.8}_{-0.4}$	$^{-0.9}_{-2.4}$	$^{+0.8}_{-0.8}$	$^{+0.0}_{-0.0}$	$^{+0.0}_{-0.0}$	$^{+0.0}_{-0.0}$	$^{+0.0}_{-0.0}$	$^{+0.0}_{-0.0}$	$^{-2.5}_{-0.1}$
$Z \to \ell\ell(\ell \to \tau_{\text{had}})$	$^{+10.0}_{-10.0}$	$^{+1.2}_{-1.2}$	$^{+1.3}_{-0.0}$	$^{-1.8}_{-0.0}$	$^{+0.6}_{-0.6}$	$^{+0.0}_{-0.0}$	$^{+0.0}_{-0.0}$	$^{+0.0}_{-0.0}$	$^{+20.7}_{-20.7}$	$^{+4.1}_{-4.1}$	$^{-3.7}_{-1.8}$
Top	$^{+1.3}_{-1.5}$	$^{+0.6}_{-0.6}$	$^{+0.4}_{-0.5}$	$^{-0.1}_{-0.0}$	$^{+0.8}_{-0.9}$	$^{+0.1}_{-0.0}$	$^{-0.2}_{-0.2}$	$^{+0.2}_{-0.2}$	$^{+0.0}_{-0.0}$	$^{+0.0}_{-0.0}$	$^{-0.5}_{-0.2}$
Diboson	$^{+0.0}_{-0.0}$	$^{+1.4}_{-1.4}$	$^{+0.0}_{-20.3}$	$^{-0.2}_{-20.0}$	$^{+0.3}_{-0.3}$	$^{+0.0}_{-0.0}$	$^{+0.0}_{-0.0}$	$^{+2.8}_{-2.8}$	$^{+0.0}_{-0.0}$	$^{+0.0}_{-0.0}$	$^{+26.6}_{-2.1}$
Fake τ_{had}	$^{+50.0}_{-50.0}$	$^{+0.2}_{-0.2}$	$^{+0.2}_{-0.3}$	$^{-0.8}_{-0.0}$	$^{+0.2}_{-0.2}$	$^{+0.0}_{-0.0}$	$^{+0.0}_{-0.0}$	$^{+0.0}_{-0.0}$	$^{+0.0}_{-0.0}$	$^{+0.0}_{-0.0}$	$^{-2.4}_{-1.9}$

	b-tag	JES in-situ	JES η	JES Flav.	JES *b*-jet	JES PileUp	*JER_2012*	*JVF_2012*	*MET_RESO*	*MET_SCALE*
ggF($H \to \tau_{\text{lep}}\tau_{\text{had}}$)	$^{+0.3}_{-0.4}$	$^{+2.3}_{-2.7}$	$^{+12.0}_{-12.1}$	$^{+1.6}_{-4.5}$	$^{+0.0}_{-0.0}$	$^{+0.8}_{-3.0}$	$^{-0.1}_{-0.1}$	$^{-1.0}_{-0.0}$	$^{+0.0}_{-1.4}$	$^{+0.6}_{-0.5}$
VBF($H \to \tau_{\text{lep}}\tau_{\text{had}}$)	$^{+0.3}_{-0.4}$	$^{+2.4}_{-2.6}$	$^{+5.3}_{-5.3}$	$^{+2.6}_{-3.9}$	$^{+0.0}_{-0.0}$	$^{+0.8}_{-1.4}$	$^{-0.5}_{-0.5}$	$^{-0.2}_{-0.1}$	$^{+0.0}_{-0.1}$	$^{+0.0}_{-0.0}$
WH($H \to \tau_{\text{lep}}\tau_{\text{had}}$)	$^{+0.5}_{-0.6}$	$^{+26.8}_{-27.0}$	$^{+38.3}_{-38.5}$	$^{+28.2}_{-28.2}$	$^{+0.0}_{-0.0}$	$^{+12.3}_{-12.3}$	$^{-7.5}_{-6.5}$	$^{+1.6}_{-0.0}$	$^{+0.0}_{-3.3}$	$^{+0.0}_{-0.0}$
ZH($H \to \tau_{\text{lep}}\tau_{\text{had}}$)	$^{+0.4}_{-0.4}$	$^{+32.1}_{-32.1}$	$^{+26.5}_{-26.5}$	$^{+37.4}_{-37.4}$	$^{+0.0}_{-0.0}$	$^{+27.0}_{-27.0}$	$^{-2.1}_{-2.1}$	$^{+0.2}_{-0.0}$	$^{+0.0}_{-0.0}$	$^{+0.0}_{-0.0}$
$Z \to \tau\tau$	$^{+0.1}_{-0.1}$	$^{+0.1}_{-0.1}$	$^{+0.2}_{-0.2}$	$^{+0.1}_{-0.1}$	$^{+0.0}_{-0.0}$	$^{+0.1}_{-0.1}$	$^{+0.1}_{-0.1}$	$^{+0.0}_{-0.0}$	$^{+0.1}_{-0.0}$	$^{-0.1}_{-0.0}$
$Z \to \ell\ell(j \to \tau_{\text{had}})$	$^{+0.2}_{-0.2}$	$^{+8.4}_{-8.9}$	$^{+20.9}_{-21.2}$	$^{+7.7}_{-8.1}$	$^{+0.0}_{-0.0}$	$^{+2.8}_{-5.1}$	$^{-2.1}_{-2.1}$	$^{+0.0}_{-0.5}$	$^{-1.3}_{-7.3}$	$^{+0.9}_{-0.4}$
$Z \to \ell\ell(\ell \to \tau_{\text{had}})$	$^{+0.3}_{-0.4}$	$^{+28.6}_{-28.7}$	$^{+27.1}_{-27.2}$	$^{+32.4}_{-32.6}$	$^{+0.0}_{-0.0}$	$^{+24.3}_{-24.3}$	$^{+1.7}_{-1.7}$	$^{+0.0}_{-0.0}$	$^{+0.0}_{-0.0}$	$^{-1.6}_{-0.0}$
Top	$^{+7.6}_{-7.7}$	$^{+4.1}_{-4.1}$	$^{+8.6}_{-8.6}$	$^{+0.2}_{-5.1}$	$^{+3.7}_{-6.6}$	$^{+3.8}_{-6.6}$	$^{-2.2}_{-2.2}$	$^{+0.6}_{-0.2}$	$^{-0.1}_{-0.1}$	$^{+0.0}_{-0.0}$
Diboson	$^{+0.3}_{-0.5}$	$^{+1.9}_{-1.9}$	$^{+20.5}_{-28.8}$	$^{+1.9}_{-2.6}$	$^{+0.0}_{-0.0}$	$^{+0.0}_{-1.7}$	$^{+16.1}_{-16.1}$	$^{+0.0}_{-0.0}$	$^{+1.7}_{-18.5}$	$^{+0.0}_{-0.0}$
Fake τ_{had}	$^{+0.5}_{-0.5}$	$^{+1.4}_{-1.4}$	$^{+2.8}_{-2.9}$	$^{+0.9}_{-1.5}$	$^{+0.5}_{-0.5}$	$^{+1.1}_{-1.1}$	$^{-2.2}_{-2.2}$	$^{+0.3}_{-0.0}$	$^{+0.0}_{-0.9}$	$^{+0.4}_{-0.1}$

Table D.3: Systematic variation (in %) of the background estimation and the experimental uncertainties for all samples in the VBF Category. The signal samples are simulated with a mass $m_H = 125$ GeV.

APPENDIX E

Normalisation Studies for $H \rightarrow \tau_{\text{lep}}\tau_{\text{had}}$ Pre-Fit Distributions

The variation of the kinematic distributions in the $H \rightarrow \tau_{\text{lep}}\tau_{\text{had}}$ analysis (Chap. 7) under different τ energy scales is studied. The distributions of the $m_{\tau\tau}$ mass at preselection, in the Zero- and the One-Jet Category for the 1σ up- and downwards variation of the TES systematic uncertainty are shown in Figs. E.1–E.3. In all distributions data is most conform with a downwards variation of TES.

Figures E.4a and E.4b show the distribution of the selection variable $\Delta\Delta R^{\ell,\tau_{\text{had}}}$ and the distance between lepton and τ_{had} ($\Delta R^{\ell,\tau_{\text{had}}}$) defined in Eq. 7.10 for events contained in the Boosted Category. All selection criteria are applied except for the $\Delta\Delta R^{\ell,\tau_{\text{had}}}$ criterion (Tab. 7.5). A small discrepancy (within statistical uncertainties) in the shape of both distributions can be seen. The selection criterion on $\Delta\Delta R^{\ell,\tau_{\text{had}}} < 0.8$ enhances this discrepancy, resulting in a slight underestimation of the number of expected background events in the final Boosted signal region.

In order to exclude the mismodelling of a certain background process, these kinematic variables are investigated in the different background control regions. In Figs. E.4c and E.4d for instance the $\Delta\Delta R^{\ell,\tau_{\text{had}}}$ and $\Delta\eta$ distribution in the W control region of the Boosted Category are shown. The variables are well modelled. The same conclusion is drawn from other regions. For this region and since the discrepancies are covered by the statistical uncertainties, the slight discrepancy seen in the Boosted signal region is not considered a problem for the analysis.

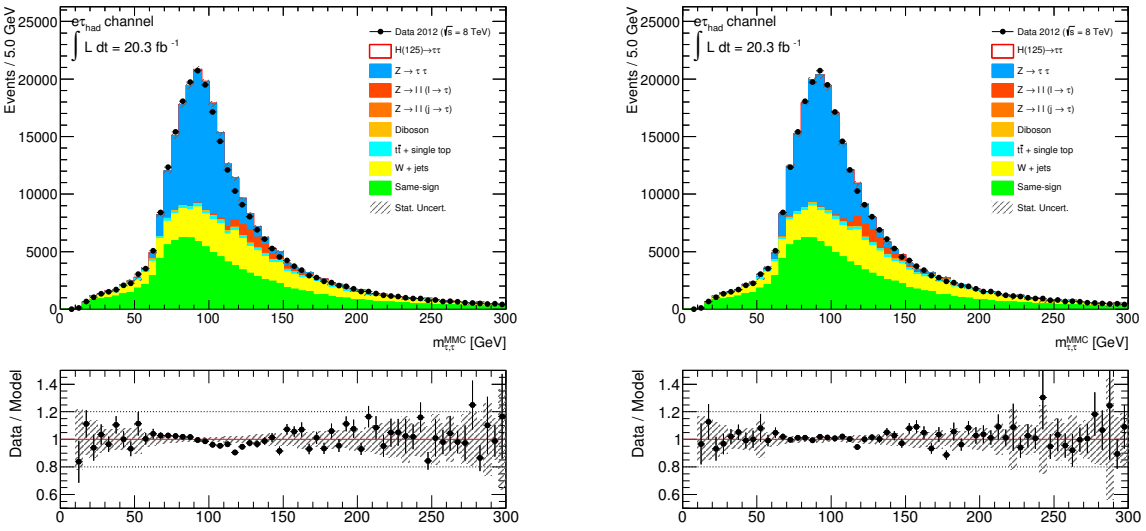

Figure E.1: Kinematic distributions of the invariant $m_{\tau\tau}$ mass calculated with the MMC algorithm at preselection for data (black points), the stack of the expected distribution if all background processes (estimated according to Sec. 7.5) for (top) the $e\tau_{\text{had}}$ channel and (bottom) the $\mu\tau_{\text{had}}$ channel with an (a,c) upwards variation of the TES and (b,d) a downwards variation of TES.

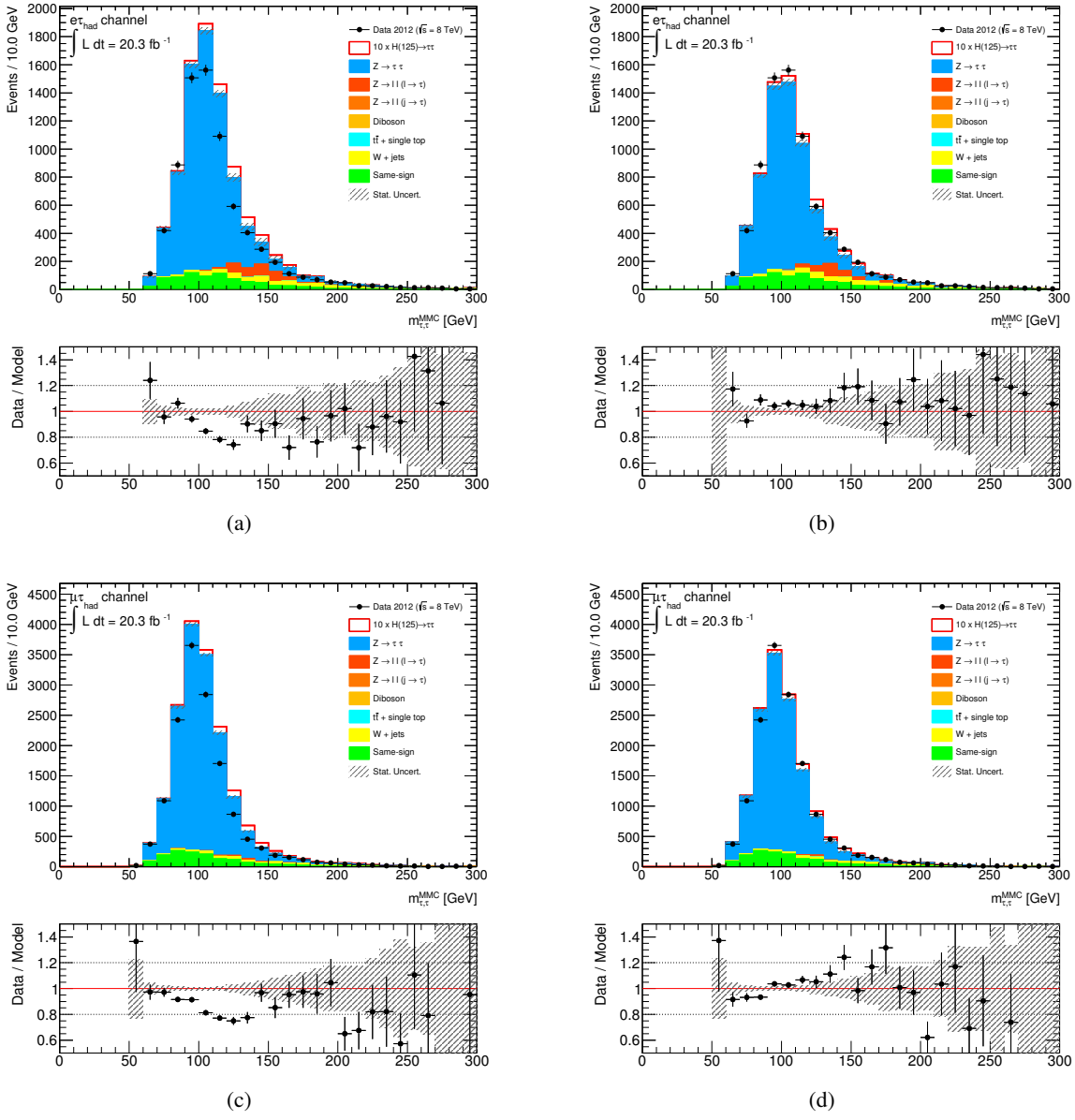

Figure E.2: Kinematic distributions of the invariant $m_{\tau\tau}$ mass calculated with the MMC algorithm in the Zero-Jet Category for data (black points), the stack of the expected distribution if all background processes (estimated according to Sec. 7.5) for (top) the $e\tau_{\text{had}}$ channel and (bottom) the $\mu\tau_{\text{had}}$ channel with an (a,c) upwards variation of the TES and (b,d) a downwards variation of TES.

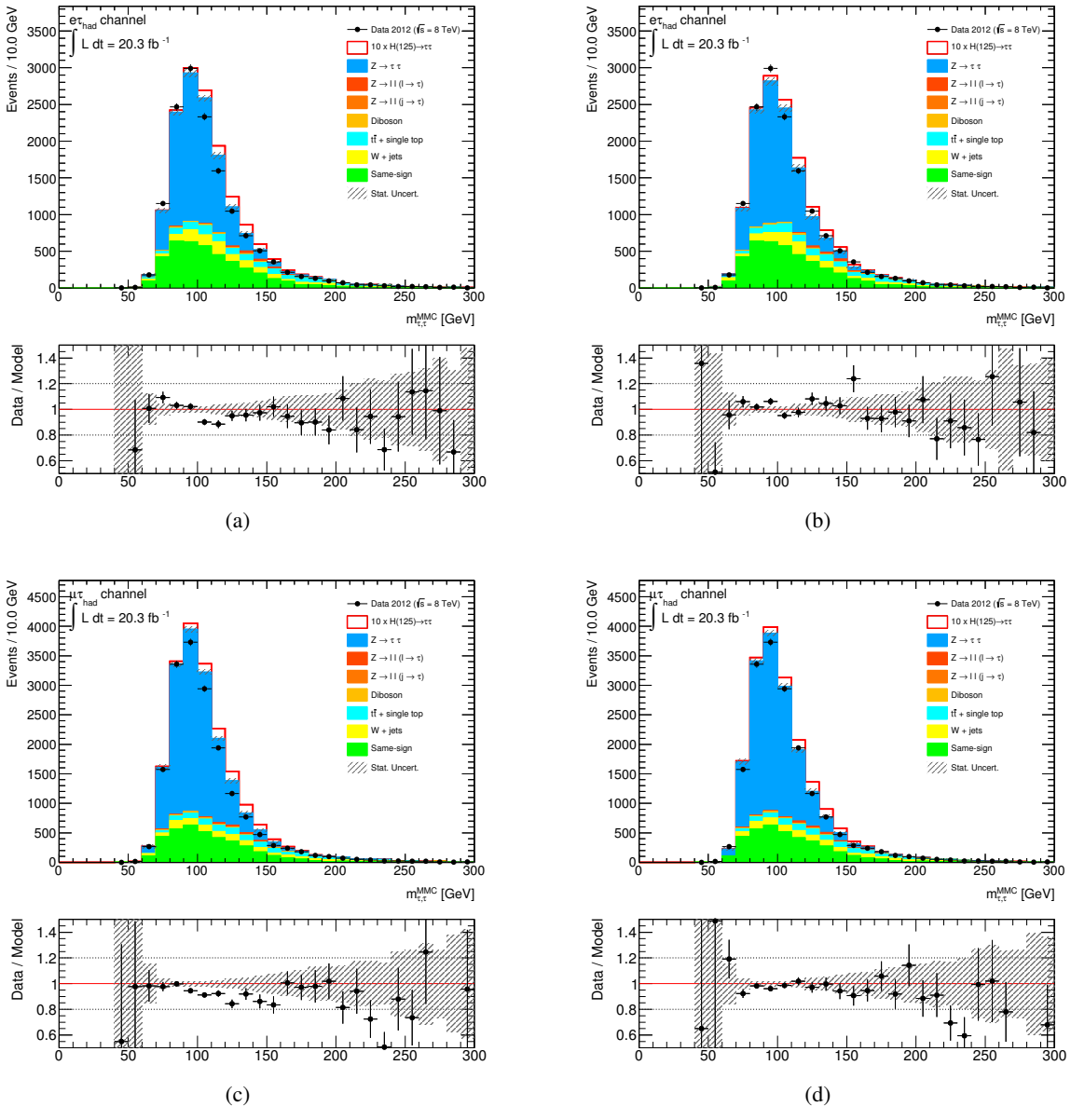

Figure E.3: Kinematic distributions of the invariant $m_{\tau\tau}$ mass calculated with the MMC algorithm in the One-Jet Category for data (black points), the stack of the expected distribution if all background processes (estimated according to Sec. 7.5) for (top) the $e\tau_{\text{had}}$ channel and (bottom) the $\mu\tau_{\text{had}}$ channel with an (a,c) upwards variation of the TES and (b,d) a downwards variation of TES.

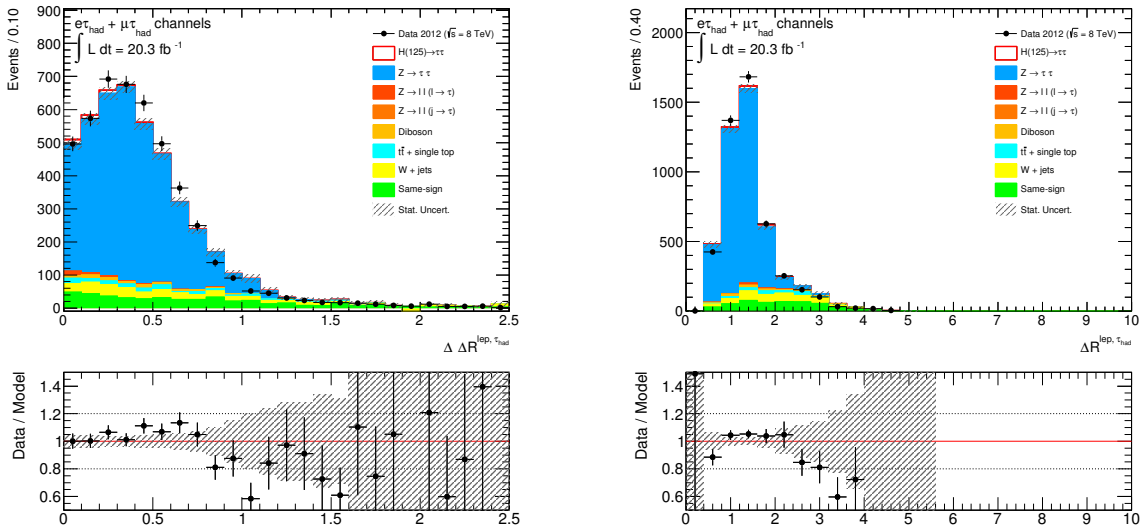

(a)

(b)

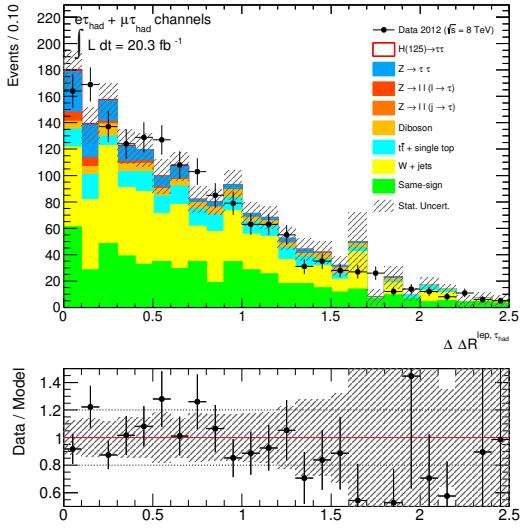

(c)

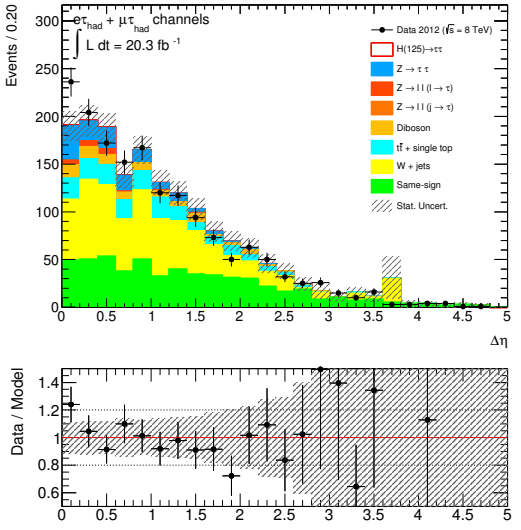

(d)

Figure E.4: Top: (a) $\Delta\Delta R^{\ell,\tau_{\text{had}}}$ and (b) $\Delta R^{\ell,\tau_{\text{had}}}$ distribution in the Boosted Category, after all selection criteria except for the $\Delta\Delta R^{\ell,\tau_{\text{had}}}$ have been applied. Bottom: (c) $\Delta\Delta R^{\ell,\tau_{\text{had}}}$ and (d) $\Delta\eta$ distribution in the W control region of the Boosted Category.

APPENDIX F

New $H \rightarrow \tau_{\text{lep}}\tau_{\text{had}}$ Analysis Categorisation

In Sec. 8.3 it was concluded, that the multivariate analysis is more flexible in utilising the correlation of variables to include multiple phase space regions where signal can be found with different purity. Due to the sequential application of event selection criteria in the cut-based analysis it is more limited in the selection of phase space regions. This can be improved by splitting the defined cut-based categories further: In some sub-categories very tight selection criteria are applied to achieve a very high signal-to-background ratio. In other sub-categories looser criteria are applied to include signal events in a larger phase space region, but with a less high signal-to-background ratio.

Here an example is given for a splitting of the VBF Category as defined in Sec. 7.4. Figure F.1a shows the m_{jj} distribution as a function of $\Delta\eta_{jj}$ of the two tagging jets for a loose selection of VBF events for signal compared to background. With the nominal VBF selection ($m_{jj} > 500$ GeV, $\Delta\eta_{jj} > 3$) a quite large amount of signal can be collected. If both criteria are tightened, the purity of the selected sample gets higher, but also a larger fraction of signal events is not included. In Fig. F.1b the distribution of p_{T}^{H} (Eq. 7.4) as a function of the $m_{\tau\tau}$ mass is investigated for signal and background processes. Clearly, the signal-to-background ratio and also mass resolution increases towards a higher boost of the Higgs boson.

Based on these observations two new VBF Categories are defined: For the *Tight VBF Category* events with $m_{jj} > 700$ GeV, $\Delta\eta_{jj} > 4$ and $p_{\text{T}}^{\text{H}} > 100$ GeV in addition to the old VBF selection criteria (Tab. 7.5) are selected. The *Loose VBF Category* contains all events selected for the old VBF Category that fail the Tight VBF Category. Table F.1 lists the number of expected signal and background events. The $m_{\tau\tau}$ distributions are shown in Fig. F.2. Based on this categorisation the expected p_0 values can be derived as a function of m_H [1]. The result is shown in Fig. F.3 for the combined and individual fit of the unchanged Boosted and the new VBF Categories. At $m_H = 125$ GeV the expected significance for the VBF Categories alone is 1.5σ and in the combined fit it is 1.8σ. This is a 15% improvement of the VBF Category result and a 6% improvement of the combined fit result.

A similar splitting of $H \rightarrow \tau_{\text{lep}}\tau_{\text{had}}$ categories has been implemented for the combination with other $H \rightarrow \tau\tau$ channels, as explained in Sec. 8.1, and a similar improvement of the expected significance is seen [136].

[1] The binning of $m_{\tau\tau}$ distributions for the fit is adjusted by merging marginal bins to avoid empty bins. The theory uncertainty to account for the modelling uncertainty of the Higgs transverse momentum in the Tight VBF Category is assumed to be the same as in the Boosted Category, since the same p_{T}^{H} selection is used (Sec. 7.7).

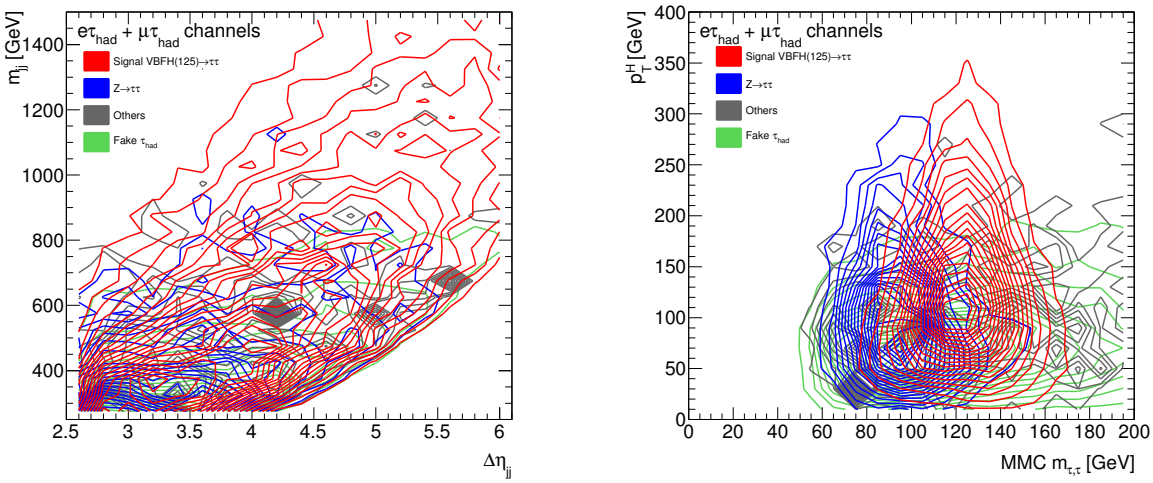

(a) (b)

Figure F.1: Two-dimensional correlations of observables in the VBF Category (with a loose VBF selection) for VBF signal with $m_H = 125$ GeV (red), $Z \to \tau\tau$ (blue), the $j \to \tau_{\text{had}}$ background estimated with the fake factor method (green) and the rest of background processes $Z \to \ell\ell$, top and diboson (grey) in the $\sqrt{s} = 8$ TeV samples with 20.3 fb^{-1}. (a) Mass and pseudorapidity difference of the tagging jets, (b) Higgs momentum (Eq. 7.4) and $m_{\tau\tau}$ mass.

Process	Loose VBF	Tight VBF
ZH($H \to \tau_{\text{lep}}\tau_{\text{had}}$) ($m_H = 125$ GeV)	0.003 ± 0.002	0.001 ± 0.001
WH($H \to \tau_{\text{lep}}\tau_{\text{had}}$) ($m_H = 125$ GeV)	0.013 ± 0.004	< 0.001
VBF($H \to \tau_{\text{lep}}\tau_{\text{had}}$) ($m_H = 125$ GeV)	3.13 ± 0.05	3.41 ± 0.05
ggF($H \to \tau_{\text{lep}}\tau_{\text{had}}$) ($m_H = 125$ GeV)	1.06 ± 0.09	0.43 ± 0.06
$Z \to \tau\tau$	39.0 ± 3.7	17.3 ± 3.3
$Z \to \ell\ell(\ell \to \tau_{\text{had}})$	1.0 ± 0.5	0.3 ± 0.2
$Z \to \ell\ell(\text{j} \to \tau_{\text{had}})$	2.2 ± 0.4	0.3 ± 0.1
Diboson	1.1 ± 0.6	0.4 ± 0.3
Top	2.8 ± 1.3	2.6 ± 0.9
Fake τ_{had}	9.9 ± 0.8	2.8 ± 0.5
Total background	55.9 ± 4.1	23.6 ± 3.5

Table F.1: Number of expected signal and background events in the signal region of the Loose and Tight VBF Categories in the combined $e\tau_{\text{had}}$ and $\mu\tau_{\text{had}}$ channel including the statistical uncertainties.

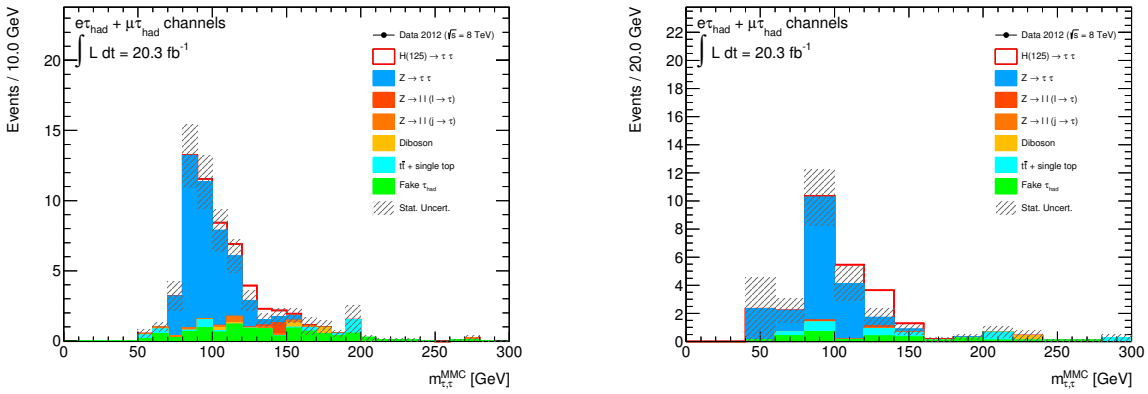

(a) (b)

Figure F.2: Expected signal and background distribution of the invariant $m_{\tau\tau}$ mass in the (a) Loose and (b) Tight VBF Categories. Included are also the statistical uncertainties of the background model.

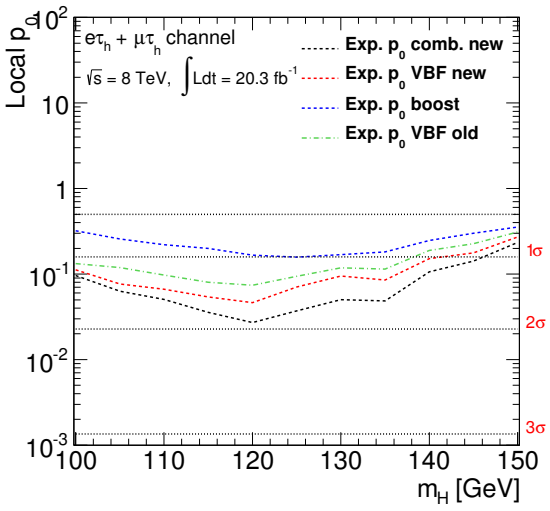

Figure F.3: Expected p_0 values as a function of m_H for the combined fit of the Boosted and new VBF Categories (black). The expected p_0 values for the Boosted Category (blue) and combined new Loose and Tight VBF Categories (red) are also shown. For comparison the expected p_0 values for the old VBF Category are also included (green).

Bibliography

[1] D. Griffiths, *Introduction to Elementary Particles*, John Wiley & Sons, 1987.

[2] K. A. Olive et al., "Review of Particle Physics", *Chin. Phys. C* 38 (2014) 090001.

[3] M. Herrero, "The Standard model", *NATO Sci.Ser.C* 534 (1999) 1–59, arXiv: hep-ph/9812242.

[4] A. Djouadi, "The Anatomy of electro-weak symmetry breaking. I: The Higgs boson in the standard model", *Phys.Rept.* 457 (2008) 1–216, arXiv: hep-ph/0503172.

[5] P. Aurenche, "The Standard model of particle physics" (1997), arXiv: hep-ph/9712342.

[6] P. W. Higgs, "Broken symmetries, massless particles and gauge fields", *Phys.Lett.* 12 (1964) 132–133.

[7] G. S. Guralnik, C. R. Hagen and T. W. B. Kibble, "Global Conservation Laws and Massless Particles", *Phys. Rev. Lett.* 13 (20 Nov. 1964) 585–587.

[8] P. W. Higgs, "Spontaneous Symmetry Breakdown without Massless Bosons", *Phys. Rev.* 145 (4 May 1966) 1156–1163.

[9] J. F. Gunion et al., *The Higgs Hunter's Guide*, Perseus Books, 2000.

[10] J. Goldstone, A. Salam and S. Weinberg, "Broken Symmetries", *Phys. Rev.* 127 (3 Aug. 1962) 965–970.

[11] T. Binoth, C. Buttar and P. Clark, eds., *LHC Physics*, CRC Press, 2012.

[12] G. P. Salam, "Elements of QCD for hadron colliders" (2010), arXiv: 1011.5131 [hep-ph].

[13] J. M. Campbell, J. Huston and W. Stirling, "Hard Interactions of Quarks and Gluons: A Primer for LHC Physics", *Rept.Prog.Phys.* 70 (2007) 89, arXiv: hep-ph/0611148.

[14] P. Skands, "Introduction to QCD" (2013), arXiv: 1207.2389 [hep-ph].

[15] T. Plehn, *Lectures on LHC Physics*, Springer Verlag Berlin Heidelberg, 2012.

[16] R. K. Ellis, W. J. Stirling and B. R. Webber, *QCD and Collider Physics*, Cambridge University Press, 1996.

[17] A. Martin et al., "Parton distributions for the LHC", *Eur. Phys. J.* C63 (2009) 189–285, arXiv: 0901.0002 [hep-ph].

[18] V. Radescu, "Hera Precision Measurements and Impact for LHC Predictions" (2011), arXiv: 1107.4193 [hep-ex].

[19] L. Evans and P. Bryant, "LHC Machine", *JINST* 3 (2008), ed. by L. Evans S08001.

[20] Deutsches Elektronen-Synchrotron DESY, *Weltmaschine*, URL: http://www.weltmaschine.de.

[21] K. Aamodt et al., "The ALICE experiment at the CERN LHC", *JINST* 3 (2008) S08002.

[22] A. Augusto Alves, Jr. et al., "The LHCb Detector at the LHC", *JINST* 3 (2008) S08005.

[23] G. Aad et al., "The ATLAS Experiment at the CERN Large Hadron Collider", *JINST* 3 (2008) S08003.

[24] S. Chatrchyan et al., "The CMS experiment at the CERN LHC", *JINST* 3 (2008) S08004.

[25] H. Burkhardt and P. Grafström, "Absolute Luminosity from Machine Parameters", CERN-LHC-PROJECT-Report-1019, 2007.

[26] The ATLAS Collaboration, *Luminosity public results*, 2011, URL: https://twiki.cern.ch/twiki/bin/view/AtlasPublic/LuminosityPublicResults.

[27] G. Aad et al., "Luminosity Determination in pp Collisions at $\sqrt{s}$ =7 TeV Using the ATLAS Detector at the LHC", *Eur.Phys.J.* C71 (2011) 1630, arXiv: 1101.2185 [hep-ex].

[28] G. Aad et al., "Improved luminosity determination in pp collisions at $\sqrt{s}$ = 7 TeV using the ATLAS detector at the LHC", *Eur.Phys.J.* C73 (2013) 2518, arXiv: 1302.4393 [hep-ex].

[29] C. Grupen and B. A. Shwartz, *Particle Detectors*, Cambridge University Press, 2008.

[30] ATLAS Inner Detector Community, "ATLAS Inner Detector Technical design report", CERN/LHCC/97-16, 1997.

[31] The ATLAS Collaboration, "ATLAS Calorimeter Performance Technical design report", CERN/LHCC/96-14, 1997.

[32] The ATLAS Collaboration, "ATLAS Muon Spectrometer Technical design report", CERN/LHCC/97-22, 1997.

[33] G. Aad et al., "Expected Performance of the ATLAS Experiment - Detector, Trigger and Physics" (2008), CERN-OPEN-2008-020.

[34] M. Krämer and F. J. P. Soler, ed., *Large Hadron Collider Phenomenology, Proceedings of the Fifty Seventh Scottish Universities Summer School in Physics St Andrews*, IoP Publishing, Bristol and Philadephia, 2014.

[35] ATLAS Level-1 Trigger Group, "Level-1 Trigger Technical Design Report", ATLAS-TDR-12, 1998.

[36] The ATLAS Collaboration, "Performance of the ATLAS tau trigger in 2011", ATLAS-CONF-2013-006, CERN, Jan. 2013.

[37] The ATLAS Collaboration, *Public Trigger System Plots for Collision Data*, 2014, URL: https://twiki.cern.ch/twiki/bin/view/AtlasPublic/TriggerPublicResults.

[38] T. Cornelissen et al., "Concepts, Design and Implementation of the ATLAS New Tracking (NEWT)", ATL-SOFT-PUB-2007-007, CERN, Mar. 2007.

[39] The ATLAS Collaboration, "Performance of the ATLAS Inner Detector Track and Vertex Reconstruction in the High Pile-Up LHC Environment", ATLAS-CONF-2012-042, CERN, Mar. 2012.

[40] W. Lampl et al., "Calorimeter Clustering Algorithms: Description and Performance", ATL-LARG-PUB-2008-002, CERN, Apr. 2008.

[41] The ATLAS Collaboration, "Electron efficiency measurements with the ATLAS detector using the 2012 LHC proton-proton collision data", ATLAS-CONF-2014-032, CERN, June 2014.

[42] The ATLAS Collaboration, "Improved electron reconstruction in ATLAS using the Gaussian Sum Filter-based model for bremsstrahlung", ATLAS-CONF-2012-047, CERN, May 2012.

[43] G. Aad et al., "Electron and photon energy calibration with the ATLAS detector using LHC Run 1 data" (2014), arXiv: 1407.5063 [hep-ex].

[44] G. Aad et al., "Electron reconstruction and identification efficiency measurements with the ATLAS detector using the 2011 LHC proton-proton collision data", *Eur.Phys.J.* C74 (2014) 2941, arXiv: 1404.2240 [hep-ex].

[45] G. Aad et al., "Electron performance measurements with the ATLAS detector using the 2010 LHC proton-proton collision data", *Eur.Phys.J.* C72 (2012) 1909, arXiv: 1110.3174 [hep-ex].

[46] G. Aad et al., "Measurement of the muon reconstruction performance of the ATLAS detector using 2011 and 2012 LHC proton-proton collision data" (2014), arXiv: 1407.3935 [hep-ex].

[47] The ATLAS Collaboration, "Muon reconstruction efficiency and momentum resolution of the ATLAS experiment in proton-proton collisions at $\sqrt{s}$=7 TeV in 2010" (2014), arXiv: 1404.4562 [hep-ex].

[48] M. Cacciari, G. P. Salam and G. Soyez, "The anti-k_t jet clustering algorithm", *JHEP* 04 (2008) 063, arXiv: 0802.1189 [hep-ph].

[49] G. Aad et al., "Jet energy measurement and its systematic uncertainty in proton-proton collisions at $\sqrt{s}$ = 7 TeV with the ATLAS detector" (2014), arXiv: 1406.0076 [hep-ex].

[50] The ATLAS Collaboration, "Jet energy scale and its systematic uncertainty for jets produced in proton-proton collisions at $\sqrt{s}$ = 7 TeV and measured with the ATLAS detector", ATLAS-CONF-2010-056, CERN, July 2010.

[51] The ATLAS Collaboration, "Pile-up subtraction and suppression for jets in ATLAS", ATLAS-CONF-2013-083, CERN, Aug. 2013.

[52] The ATLAS Collaboration, "Commissioning of the ATLAS high-performance b-tagging algorithms in the 7 TeV collision data", ATLAS-CONF-2011-102, CERN, July 2011.

[53] The ATLAS Collaboration, "Calibration of the performance of b-tagging for c and light-flavour jets in the 2012 ATLAS data", ATLAS-CONF-2014-046, CERN, July 2014.

[54] T. Sjöstrand, S. Mrenna and P. Z. Skands, "PYTHIA 6.4 Physics and Manual", *JHEP* 0605 (2006) 026, arXiv: hep-ph/0603175.

[55] T. Sjöstrand, S. Mrenna and P. Z. Skands, "A Brief Introduction to PYTHIA 8.1", *Comput. Phys. Commun.* 178 (2008) 852, arXiv: 0710.3820 [hep-ph].

[56] G. Corcella et al., "HERWIG 6.5 release note" (2002), arXiv: hep-ph/0210213.

[57] M. Dobbs et al., "Les Houches guidebook to Monte Carlo generators for hadron collider physics" (2004) 411–459, arXiv: hep-ph/0403045.

[58] A. Buckley et al., "General-purpose event generators for LHC physics", *Phys.Rept.* 504 (2011) 145–233, arXiv: 1101.2599 [hep-ph].

[59] J. M. Butterworth, J. R. Forshaw and M. H. Seymour, "Multiparton interactions in photoproduction at HERA", *Z. Phys. C* 72 (1996) 637, arXiv: hep-ph/9601371.

[60] M. Mangano et al., "ALPGEN, a generator for hard multiparton processes in hadronic collisions", *JHEP* 07 (2003) 001, arXiv: hep-ph/0206293.

[61] M. Mangano et al., "Multijet matrix elements and shower evolution in hadronic collisions: $Wb\bar{b}$ + n jets as a case study", *Nucl. Phys. B* 632 (2002) 343, arXiv: hep-ph/0108069.

[62] S. Alioli et al., "A general framework for implementing NLO calculations in shower Monte Carlo programs: the POWHEG BOX", *JHEP* 1006 (2010) 043, arXiv: 1002.2581 [hep-ph].

[63] S. Frixione and B. R. Webber, "Matching NLO QCD computations and parton shower simulations", *JHEP* 06 (2002) 029, arXiv: hep-ph/0204244.

[64] S. Jadach et al., "The tau decay library TAUOLA: Version 2.4", *Comput. Phys. Commun.* 76 (1993) 361.

[65] N. Davidson, T. Przedzinski and Z. Was, "PHOTOS Interface in C++: Technical and Physics Documentation" (2010), arXiv: 1011.0937 [hep-ph].

[66] P. M. Nadolsky et al., "Implications of CTEQ global analysis for collider observables", *Phys.Rev.* D78 (2008) 013004, arXiv: 0802.0007 [hep-ph].

[67] J. Pumplin et al., "New generation of parton distributions with uncertainties from global QCD analysis", *JHEP* 07 (2002) 012, arXiv: hep-ph/0201195.

[68] G. Aad et al., "The ATLAS Simulation Infrastructure", *Eur. Phys. J.* C70 (2010) 823–874, arXiv: 1005.4568 [physics.ins-det].

[69] S. Agostinelli et al., "GEANT4: A simulation toolkit", *Nucl. Instrum. Meth.* A506 (2003) 250–303.

[70] W. J. Stirling, private communication, *Parton luminosity and cross section plots*, URL: http://www.hep.ph.ic.ac.uk/~wstirlin/plots/plots.html.

[71] A. D. Martin et al., "Parton distributions and the LHC: W and Z production", *Eur.Phys.J.* C14 (2000) 133–145, arXiv: hep-ph/9907231.

[72] R. Hamberg, W. van Neerven and T. Matsuura, "A Complete calculation of the order α_s^2 correction to the Drell-Yan K factor", *Nucl.Phys.* B359 (1991) 343–405.

[73] G. Aad et al., "Measurement of the inclusive $W^{\pm}$ and Z/γ cross sections in the electron and muon decay channels in pp collisions at $\sqrt{s}$ = 7 TeV with the ATLAS detector", *Phys.Rev.* D85 (2012) 072004, arXiv: 1109.5141 [hep-ex].

[74] S. Chatrchyan et al., "Measurement of the Inclusive W and Z Production Cross Sections in pp Collisions at $\sqrt{s}$ = 7 TeV", *JHEP* 1110 (2011) 132, arXiv: 1107.4789 [hep-ex].

[75] C. Albajar et al., "Events with large missing transverse energy at the CERN collider: $W \to \tau\nu$ decay and test of $\tau - \mu - e$ universality at $Q^2 = m_W^2$", *Phys.Lett.* B185 (1987) 233–240.

[76] B. Abbott et al.,
"A measurement of the $W \to \tau\nu$ production cross section in $p\bar{p}$ collisions at $\sqrt{s} = 1.8$ TeV", *Phys.Rev.Lett.* 84 (2000) 5710–5715, arXiv: hep-ex/9912065.

[77] F. Abe et al.,
"Measurement of the ratio B(W→τν)/B(W→eν) in $p\bar{p}$ collisions at $\sqrt{s}$=1.8 TeV", *Phys. Rev. Lett.* 68 (23 June 1992) 3398–3402.

[78] S. Protopopescu, "$W \to \tau\nu_\tau$ at the Tevatron", *Nucl.Phys.Proc.Suppl.* 76 (1999) 91–97.

[79] LHC Higgs Cross Section Working Group et al.,
"Handbook of LHC Higgs Cross Sections: 3. Higgs Properties",
CERN-2013-004 (CERN, Geneva, 2013), arXiv: 1307.1347 [hep-ph].

[80] R. Barate et al., "Search for the standard model Higgs boson at LEP",
Phys.Lett. B565 (2003) 61–75, arXiv: hep-ex/0306033.

[81] The CDF and D0 Collaborations, "Combined CDF and D0 Upper Limits on Standard Model Higgs Boson Production with up to 8.6 fb^{-1} of Data" (2011), arXiv: 1107.5518 [hep-ex].

[82] G. Aad et al., "Observation of a new particle in the search for the Standard Model Higgs boson with the ATLAS detector at the LHC", *Phys.Lett.* B716 (2012) 1–29,
arXiv: 1207.7214 [hep-ex].

[83] S. Chatrchyan et al.,
"Observation of a new boson at a mass of 125 GeV with the CMS experiment at the LHC", *Phys.Lett.* B716 (2012) 30–61, arXiv: 1207.7235 [hep-ex].

[84] T. Aaltonen et al., "Evidence for a Particle Produced in Association with Weak Bosons and Decaying to a Bottom-Antibottom Quark Pair in Higgs Boson Searches at the Tevatron", *Phys. Rev. Lett.* 109 (7 Aug. 2012) 071804.

[85] G. Aad et al., "Measurements of Higgs boson production and couplings in diboson final states with the ATLAS detector at the LHC", *Phys.Lett.* B726 (2013) 88–119,
arXiv: 1307.1427 [hep-ex].

[86] The CMS Collaboration, "Combination of standard model Higgs boson searches and measurements of the properties of the new boson with a mass near 125 GeV",
CMS-PAS-HIG-13-005, CERN, 2013.

[87] G. Aad et al., "Evidence for the spin-0 nature of the Higgs boson using ATLAS data", *Phys.Lett.* B726 (2013) 120–144, arXiv: 1307.1432 [hep-ex].

[88] S. Chatrchyan et al., "Study of the Mass and Spin-Parity of the Higgs Boson Candidate Via Its Decays to Z Boson Pairs", *Phys.Rev.Lett.* 110 (2013) 081803, arXiv: 1212.6639 [hep-ex].

[89] K. Cranmer et al.,
"HistFactory: A tool for creating statistical models for use with RooFit and RooStats", CERN-OPEN-2012-016, New York U., Jan. 2012.

[90] The ATLAS Collaboration, *ATLAS Statistics Forum*, 2014, URL:
https://twiki.cern.ch/twiki/bin/viewauth/AtlasProtected/StatisticsTools.

[91] The ATLAS Collaboration,
"Procedure for the LHC Higgs boson search combination in summer 2011",
ATL-PHYS-PUB-2011-011, CERN, Aug. 2011.

[92] G. Cowan et al., "Asymptotic formulae for likelihood-based tests of new physics",
Eur.Phys.J. C71 (2011) 1554, arXiv: 1007.1727 [physics.data-an].

[93] N. Möser, "A Sensitivity Study for Higgs Boson Production in Vector Boson Fusion in the $H \to \tau\tau \to \ell h + 3\nu$ Final State with ATLAS", PhD thesis: University of Bonn, 2011.

[94] M. Schmitz, "Higgs production in Vector Boson Fusion in the $H \to \tau\tau \to \ell\ell + 4\nu$ final state with ATLAS: a sensitivity study", PhD thesis: University of Bonn, 2011.

[95] N. Möser et al., "Estimation of $Z \to \tau\tau$ Background in VBF $H \to \tau\tau$ Searches from $Z \to \mu\mu$ Data using an Embedding Technique", ATL-PHYS-INT-2009-109, CERN, Dec. 2009.

[96] J. Liebal,
"Development an analysis of a data-driven method to characterize $W \to \tau\nu$ decays in ATLAS",
Master's Thesis: University of Bonn, 2009.

[97] The ATLAS Collaboration, "Search for the Standard Model Higgs boson in $H \to \tau\tau$ decays in proton-proton collisions with the ATLAS detector", ATLAS-CONF-2012-160,
CERN, Nov. 2012.

[98] Z. Zinonos et al.,
"Search for the Standard Model Higgs boson $H \to \tau\tau$ decays with the ATLAS detector",
ATL-COM-PHYS-2013-722, CERN, June 2013.

[99] The ATLAS Collaboration, "Identification of the Hadronic Decays of Tau Leptons in 2012 Data with the ATLAS Detector", ATLAS-CONF-2013-064, CERN, July 2013.

[100] The ATLAS Collaboration,
"Determination of the tau energy scale and the associated systematic uncertainty in proton-proton collisions at $\sqrt{s} = 8$ TeV with the ATLAS detector at the LHC in 2012",
ATLAS-CONF-2013-044, CERN, Apr. 2013.

[101] The ATLAS Collaboration, "Reconstruction, Energy Calibration, and Identification of Hadronically Decaying Tau Leptons", ATLAS-CONF-2011-077, CERN, May 2011.

[102] L. Breiman et al., *Classification and Regression Trees*, Chapman & Hall, 1984.

[103] Y. Freund and R. E. Schapire,
"A Decision-Theoretic Generalization of On-Line Learning and an Application to Boosting",
Journal of Computer and System Sciences 55.1 (1997) 119–139.

[104] The ATLAS Collaboration, "Performance of the Reconstruction and Identification of Hadronic Tau Decays in ATLAS with 2011 Data", ATLAS-CONF-2012-142, CERN, Oct. 2012.

[105] The ATLAS Collaboration, *ATLAS Tau Recommendations*, 2013, URL: https://twiki.cern.ch/twiki/bin/view/AtlasProtected/TauRecommendationsWinterConf2013.

[106] The ATLAS Collaboration, "Measurement of the Mis-identification Probability of τ Leptons from Hadronic Jets and from Electrons", ATLAS-CONF-2011-113, CERN, Aug. 2011.

[107] The ATLAS Collaboration,
"Performance of the Reconstruction and Identification of Hadronic Tau Decays with ATLAS",
ATLAS-CONF-2011-152, CERN, Nov. 2011.

[108] Z. Czyczula and M. Dam,
"Cut-based electron veto algorithm for the track-seeded part of tauRec",
ATL-PHYS-INT-2009-023, CERN, Feb. 2009.

[109] S. Bedikian et al., "Determination of the Electron-Tau Mis-identification Probability with a Tag-and-Probe Method", ATL-PHYS-INT-2011-069, CERN, Sept. 2011.

[110] The ATLAS Collaboration,
"Performance of the Missing Transverse Energy Reconstruction and Calibration in Proton-Proton Collisions at a Center-of-Mass Energy of 7 TeV with the ATLAS Detector",
ATLAS-CONF-2010-057, CERN, July 2010.

[111] The ATLAS Collaboration, "Reconstruction and Calibration of Missing Transverse Energy and Performance in Z and W events in ATLAS Proton-Proton Collisions at 7 TeV",
ATLAS-CONF-2011-080, CERN, June 2011.

[112] G. Aad et al., "Performance of Missing Transverse Momentum Reconstruction in Proton-Proton Collisions at 7 TeV with ATLAS", *Eur.Phys.J.* C72 (2012) 1844,
arXiv: 1108.5602 [hep-ex].

[113] The ATLAS Collaboration, "Performance of Missing Transverse Momentum Reconstruction in ATLAS studied in Proton-Proton Collisions recorded in 2012 at 8 TeV",
ATLAS-CONF-2013-082, CERN, Aug. 2013.

[114] The ATLAS Collaboration, "Performance of Missing Transverse Momentum Reconstruction in ATLAS with 2011 Proton-Proton Collisions at $\sqrt{s} = 7$ TeV", ATLAS-CONF-2012-101,
CERN, July 2012.

[115] The ATLAS Collaboration, "Observation of $W \to \tau\nu_\tau$ Decays with the ATLAS Experiment",
ATLAS-CONF-2010-097, CERN, Nov. 2010.

[116] G. Nunes Hanninger, N. Wermes and J. Kroseberg,
"Observation of $W \to \tau\nu_\tau$ Decays with the ATLAS Experiment", Presented 29 Apr 2011,
PhD thesis: Bonn U., 2011.

[117] G. Aad et al., "Measurement of the $W \to \tau\nu$ Cross Section in pp Collisions at $\sqrt{s} = 7$ TeV with the ATLAS experiment", *Phys.Lett.* B706 (2012) 276–294, arXiv: 1108.4101 [hep-ex].

[118] C. Anastasiou et al., "High precision QCD at hadron colliders: Electroweak gauge boson rapidity distributions at NNLO", *Phys.Rev.* D69 (2004) 094008, arXiv: hep-ph/0312266.

[119] G. Aad et al., "Measurement of the $W \to \ell\nu$ and $Z/\gamma^* \to \ell\ell$ production cross sections in proton-proton collisions at $\sqrt{s} = 7$ TeV with the ATLAS detector", *JHEP* 1012 (2010) 060,
arXiv: 1010.2130 [hep-ex].

[120] A. Sherstnev and R. S. Thorne, "Parton Distributions for LO Generators",
Eur. Phys. J. C55 (2008) 553–575, arXiv: 0711.2473 [hep-ph].

[121] The ATLAS Collaboration,
"Charged particle multiplicities in pp interactions at $\sqrt{s} = 0.9$ and 7 TeV in a diffractive limited phase-space measured with the ATLAS detector at the LHC and new PYTHIA6 tune",
ATLAS-CONF-2010-031, CERN, July 2010.

[122] The ATLAS Collaboration, "A combined measurement of the top quark pair production cross-section using dilepton and single-lepton final states", ATLAS-CONF-2011-040,
CERN, Mar. 2011.

[123] The ATLAS Collaboration, *ATLAS Metadata Interface*, 2006, URL: https://ami.in2p3.fr/index.php/en/.

[124] The ATLAS Collaboration, "Performance of the ATLAS tau trigger in p-p collisions at $\sqrt{s}$ = 7 TeV", ATLAS-CONF-2010-090, CERN, Oct. 2010.

[125] The ATLAS Collaboration, "Performance of the ATLAS transverse energy triggers with initial LHC runs at $\sqrt{s}$ = 7 TeV", ATLAS-CONF-2011-072, CERN, May 2011.

[126] The ATLAS Collaboration, "Data-Quality Requirements and Event Cleaning for Jets and Missing Transverse Energy Reconstruction with the ATLAS Detector in Proton-Proton Collisions at a Center-of-Mass Energy of $\sqrt{s}$ = 7 TeV", ATLAS-CONF-2010-038, CERN, July 2010.

[127] A. Andreazza et al., "Measurement of the $W \to \tau\nu_\tau$ Production Cross Section in pp Collisions at $\sqrt{s}$ = 7 TeV with the ATLAS Experiment", ATL-COM-PHYS-2011-778, CERN, June 2011.

[128] A. Ahmed et al., "Supporting Document: Measurement of the W cross section and asymmetry in the electron and muon decay channels at $\sqrt{s}$=7 TeV", ATL-PHYS-INT-2010-116, CERN, Sept. 2010.

[129] P. Z. Skands, "Tuning Monte Carlo Generators: The Perugia Tunes", *Phys.Rev.* D82 (2010) 074018, arXiv: 1005.3457 [hep-ph].

[130] The ATLAS Collaboration, "Updated Luminosity Determination in pp Collisions at $\sqrt{s}$=7 TeV using the ATLAS Detector", ATLAS-CONFf-2011-011, CERN, Mar. 2011.

[131] The CMS Collaboration, "Measurement of $W \to \tau\nu$", CMS-PAS-EWK-11-019, CERN, 2011.

[132] G. Aad et al., "Search for the Standard Model Higgs boson in the H to $\tau^+\tau^-$ decay mode in $\sqrt{s}$ = 7 TeV pp collisions with ATLAS", *JHEP* 1209 (2012) 070, arXiv: 1206.5971 [hep-ex].

[133] G. Aad et al., "Search for neutral MSSM Higgs bosons decaying to $\tau^+\tau^-$ pairs in proton-proton collisions at $\sqrt{s}$ = 7 TeV with the ATLAS detector", *Phys.Lett.* B705 (2011) 174–192, arXiv: 1107.5003 [hep-ex].

[134] The ATLAS Collaboration, "Search for neutral MSSM Higgs bosons decaying to $\tau^+\tau^-$ pairs in proton-proton collisions at $\sqrt{(s)}$ = 7 TeV with the ATLAS detector", ATLAS-CONF-2011-132, CERN, Sept. 2011.

[135] T. Schwindt, "Evidence for the Higgs Bosons Decay to τ^+ τ^- in the Lepton + Hadrons Final State with ATLAS", PhD thesis: University of Bonn, 2015.

[136] G. Aad et al., "Evidence for the Higgs-boson Yukawa coupling to τ leptons with the ATLAS detector" (2015), arXiv: 1501.04943 [hep-ex].

[137] The ATLAS Collaboration, "Evidence for Higgs Boson Decays to the $\tau^+\tau^-$ Final State with the ATLAS Detector", ATLAS-CONF-2013-108, CERN, Nov. 2013.

[138] S. Alioli et al., "NLO Higgs boson production via gluon fusion matched with shower in POWHEG", *JHEP* 0904 (2009) 002, arXiv: 0812.0578 [hep-ph].

[139] P. Nason and C. Oleari,
"NLO Higgs boson production via vector-boson fusion matched with shower in POWHEG",
JHEP 1002 (2010) 037, arXiv: 0911.5299 [hep-ph].

[140] G. Bozzi et al.,
"Transverse-momentum resummation and the spectrum of the Higgs boson at the LHC",
Nucl. Phys. B737 (2006) 73–120, arXiv: hep-ph/0508068.

[141] T. Gleisberg et al., "Event generation with SHERPA 1.1", *JHEP* 0902 (2009) 007,
arXiv: 0811.4622 [hep-ph].

[142] B. P. Kersevan and E. Richter-Was, "The Monte Carlo event generator AcerMC version 2.0
with interfaces to PYTHIA 6.2 and HERWIG 6.5" (2004), arXiv: hep-ph/0405247.

[143] T. Binoth et al., "Gluon-induced W-boson pair production at the LHC",
JHEP 0612 (2006) 046, arXiv: hep-ph/0611170.

[144] The ATLAS Collaboration, *PileUp Reweighting in 2012 data*, 2012, URL: https:
//twiki.cern.ch/twiki/bin/view/AtlasProtected/ExtendedPileupReweighting.

[145] A. Elagin et al., "A New Mass Reconstruction Technique for Resonances Decaying to di-tau",
Nucl.Instrum.Meth. A654 (2011) 481–489, arXiv: 1012.4686 [hep-ex].

[146] The ATLAS Collaboration, "Performance of the ATLAS Electron and Photon Trigger in pp
Collisions at $\sqrt{s} = 7$ TeV in 2011", ATLAS-CONF-2012-048, CERN, May 2012.

[147] G. Aad et al., "Performance of the ATLAS muon trigger in pp collisions at $\sqrt{s} = 8$ TeV"
(2014), arXiv: 1408.3179 [hep-ex].

[148] The ATLAS Collaboration, *HiggsToTauTauToLH Analysis Twiki (Winter 2013)*, 2014,
URL: https://twiki.cern.ch/twiki/bin/viewauth/AtlasProtected/
HiggsToTauTauToLH2013Winter8TeV.

[149] S. Asai et al., "Prospects for the search for a standard model Higgs boson in ATLAS using
vector boson fusion", *Eur.Phys.J.* C32S2 (2004) 19–54, arXiv: hep-ph/0402254.

[150] A. Andreazza et al., "Search for Standard Model $H \to \tau^+\tau^- \to \ell\tau_h$ with the ATLAS Detector
in 8 TeV Proton-Proton Collisions", ATL-COM-PHYS-2013-1494, CERN, Nov. 2013.

[151] The ATLAS Collaboration, *Uncertainty on PileUp Reweighting procedure in 2012 data*, 2012,
URL: https://twiki.cern.ch/twiki/bin/viewauth/AtlasProtected/
InDetTrackingPerformanceGuidelines#Analyses_based_on_Athena_release.

[152] G. Aad et al., "Jet energy resolution in proton-proton collisions at $\sqrt{s} = 7$ TeV recorded in
2010 with the ATLAS detector", *The European Physical Journal C* 73.3, 2306 (2013).

[153] The ATLAS Collaboration, *JES uncertainties in 2012 data*, 2013, URL: https://twiki.
cern.ch/twiki/bin/view/AtlasPublic/JetEtmissApproved2013JESUncertainty.

[154] The ATLAS Collaboration, "Tagging and suppression of pileup jets with the ATLAS detector",
ATLAS-CONF-2014-018, CERN, May 2014.

[155] The ATLAS Collaboration, "ATLAS tunes of PYTHIA 6 and Pythia 8 for MC11",
ATL-PHYS-PUB-2011-009, CERN, July 2011.

[156] R. D. Ball et al.,
"Impact of heavy quark masses on parton distributions and LHC phenomenology",
Nucl. Phys. B849 (2011) 296–363, arXiv: 1101.1300 [hep-ph].

[157] LHC Higgs Cross Section Working Group et al.,
"Handbook of LHC Higgs Cross Sections: 2. Differential Distributions",
CERN-2012-002 (CERN, Geneva, 2012), arXiv: 1201.3084 [hep-ph].

[158] I. W. Stewart and F. J. Tackmann,
"Theory Uncertainties for Higgs and Other Searches Using Jet Bins",
Phys.Rev. D85 (2012) 034011, arXiv: 1107.2117 [hep-ph].

[159] W. Verkerke and D. Kirkby, "The RooFit toolkit for data modeling",
ArXiv Physics e-prints (2003), arXiv: physics/0306116 [hep-ex].

[160] L. Moneta et al., "The RooStats Project", *PoS* ACAT2010 (2010) 057,
arXiv: 1009.1003 [physics.data-an].

[161] R. Brun and F. Rademakers, "{ROOT} — An object oriented data analysis framework",
Nuclear Instruments and Methods in Physics Research Section A: Accelerators, Spectrometers, Detectors and Associated Equipment 389.1–2 (1997), New Computing Techniques in Physics Research V 81–86.

[162] I. M. Chakravarti, R. G. Laha and J. Roy, *Handbook of methods of applied statistics*,
Wiley, 1967.

[163] J. H. Friedman, "Data Analysis Techniques for High-Energy Particle Physics, CERN Computing School, 1974", SLAC-0176 (1974) 271.

[164] The ATLAS Collaboration, *New implementation of the τ energy scale*, 2014,
URL: https://twiki.cern.ch/twiki/bin/viewauth/AtlasProtected/TauRecommendationsWinterConf2013.

[165] Z. Czyczula, T. Przedzinski and Z. Was,
"TauSpinner Program for Studies on Spin Effect in tau Production at the LHC",
Eur.Phys.J. C72 (2012) 1988, arXiv: 1201.0117 [hep-ph].

[166] B. Efron and C. Stein, "The Jackknife Estimate of Variance",
The Annals of Statistics 9.3 (1981) 586–596.

[167] S. Chatrchyan et al., "Evidence for the 125 GeV Higgs boson decaying to a pair of τ leptons",
JHEP 1405 (2014) 104, arXiv: 1401.5041 [hep-ex].

[168] G. N. Hanninger, "VH Status Report", 2014, URL:
https://indico.cern.ch/event/298360/contribution/0/material/slides/0.pdf.

Acknowledgements

This thesis could not have been finalised without the help and guidance of many people and I would like to express my deep gratitude for their support.

First of all, I would like to thank Prof. Dr. Norbert Wermes for giving me the opportunity to join his working group in such an exciting period of research. He provided a lot of support during the whole time and I am very thankful that he gave me the opportunity to work at CERN for two years, which was an outstanding experience.

Special thanks also go to Jürgen Kroseberg, who supervised me throughout my entire PhD and was prepared to listen, discuss and consult at any time of the day and at any place. I could always count on his support.

The funding and support of the Bonn Cologne Graduate School and the Deutsche Telekom Stiftung significantly contributed to the success of my PhD. Moreover they offered me the possibility to visit conferences and summer schools and get into contact with many interesting people. In particular I would like to thank my DTS mentor Timotheus Höttges for many new impulses and perspectives for my future career.

Several other people helped me in these years of research, I hope I don't forget to mention anyone in the following.

Particular gratitude I owe my Bonn colleagues and co-analysts Guilherme Nunes Hanninger and Thomas Schwindt. Guilherme helped me to get on track with the $W \rightarrow \tau\nu_\tau$ analysis. Thomas was always available to discuss and give advice in technical as well as physical issues of the $H \rightarrow \tau\tau$ analysis.

Moreover, I would like to thank the other ATLAS colleagues with whom I worked closely together: With Susie Bedikian and Patrick Czodrowski I searched for electrons in disguise with the first ATLAS data. Jessica Liebal, Sebastian Johnert, Mathias Uhlenbrock and most importantly Lidia Dell'Astra were of special help to crack every detail of the $W \rightarrow \tau\nu_\tau$ cross section measurement. Together with Dimitris Varouchas I investigated the connection of $E_{\mathrm{T}}^{\mathrm{miss}}$ and (pink cone) τ leptons. Thanks also to the members of the HSG4 group, in particular Keita Hanawa, with whom I participated in the hunt for the Higgs decaying to τ leptons.

I would like to thank all colleagues in Bonn, their friendliness contributed significantly that I always felt comfortable in our group. In particular my thanks go to Dennis Hellmich, Elisabeth Schopf, Stephan Hageböck, Jan Therhaag and Duc Bao Ta for sharing many fun activities in Bonn and Geneva including skiing and cooking sessions and always providing me with sweets in emergency cases.

A special thanks goes to Cécile Lapoire and Agnieszka Leyko who turned from colleagues to best friends. They were with me in funny and sad times and all the adventures we had together are unforgetable. To Aga goes also a special thanks for the last minute thesis corrections.

Also my other dear friends in Geneva, Bonn/Cologne, Prague, Landau and elsewhere I want to thank for all their support and belief in me and their patience, when I again postponed a meeting “because I finally want to finish the thesis”.

A big thanks also goes to my family, my parents and my sister, whom I can rely on in every situation and who are always prepared to move every stone out of my way.

Finally, I would like to thank Alex for being the most patient boyfriend and for supporting me on all possible levels: as thesis corrector, manager, host, chauffeur, engineer and most important emotionally. I am grateful to have him at my side.